SPECTROSCOPY OF NEUTRON UNBOUND STATES IN ^{24}O AND ^{23}N.

By

Michael David Jones

A DISSERTATION

Submitted to
Michigan State University
in partial fulfillment of the requirements
for the degree of

Physics – Doctor of Philosophy.

2015

ABSTRACT

SPECTROSCOPY OF NEUTRON UNBOUND STATES IN ^{24}O AND ^{23}N.

By

Michael David Jones

Unbound states in ^{24}O and ^{23}N were populated from an ^{24}O beam at 83.4 MeV/u via inelastic excitation and proton knockout on a liquid deuterium target. Using the MoNA-LISA-Sweeper setup, the decay of each nucleus could be fully reconstructed. The two-body decay energy of ^{23}N exhibits two prominent peaks at $E = 100 \pm 20$ keV and $E = 960 \pm 30$ keV with respect to the neutron separation energy. However, due to the lack of γ-ray detection, a definitive statement on the structure of ^{23}N could not be made. Shell model calculations with the WBP and WBT interactions lead to several interpretations of the spectrum. Both a single state at 2.9 MeV in ^{23}N, or two states at 2.9 MeV and 2.75 MeV are consistent with the shell model and data.

In addition, a two-neutron unbound excited state of ^{24}O, populated by $(d, d^{'})$, was observed with a three-body excitation of $E = 715 \pm 110$ (stat) ± 45 (sys) keV, placing it at $E = 7.65 \pm 0.2$ MeV with respect to the ground state. Three-body correlations for the decay of $^{24}\text{O} \rightarrow ^{22}\text{O} + 2\text{n}$ show clear evidence for a sequential decay through an intermediate state in ^{23}O. Neither a di-neutron nor phase-space model were able to describe the observed correlations. This measurement constitutes the first observation of a two-neutron sequential decay through three-body energy and angular correlations, and provides valuable insight into few-body physics at the neutron dripline.

ACKNOWLEDGMENTS

During my time at MSU, I received a tremendous amount of support from my advisor, the MoNA group, the NSCL staff, and my fellow graduate students. Without them, I could not have completed my degree. First and foremost, I would like to thank my advisor, Michael Theonnessen, for his wisdom, guidance, and mentorship. He was always there to answer my questions and discuss ideas. It has been a great opportunity and a pleasure to work with him. I also thank the other members of my committee, Remco Zegers, Alex Brown, Norman Birge, and Phillip Duxbury for their time, advice, and guidance during our meetings.

Working with the MoNA Collaboration has been a tremendously joyful experience. The entire collaboration has been incredibly supportive and receptive to my questions since the day I joined. I always looked forward to the yearly meeting and will certainly miss it. Many thanks to Nathan Frank, Paul DeYoung, and Thomas Baumann for helping with everything from simple calibration questions to fixing the DAQ in the middle of the night, to discussing and assisting in the analysis of our data.

I would also like to thank the other graduate students and members of the local group: Greg Christian, Shea Mosby, Jenna Smith, Jesse Snyder, Krystin Stiefel, Zach Kohley, Anthony Kuchera, and Artemis Spyrou for all their help and support. They, and many others, provided insightful and valuable discussions that made these past few years productive and very enjoyable.

The Liquid Hydrogen Target was critical to the success of this experiment and I would like to thank Remco Zegers, Andy Thulin, and Jorge Pereira, as well as Paul Zeller, for their support and assistance in installing and operating the target. Without their support, the support of the MoNA Collaboration, and the staff of the Coupled Cyclotron Facility as well

as the A1900 group, the experiment in this work would not have been a success.

Many thanks to Mike Bennet, Vincent Bader, Daniel Winklehner, Dan Alt, and Eric Deleeuw – my office-mates and fellow members of the Technical Institute of Procrastination in the Physical Sciences (TIPPS). Friday evening won't be the same without the blaring dubstep of Muse and nerf-gun fights. I would like to thank the trio of Chrises: Chris Morse, Chris Sulivan, and Chris Prokop, for putting up with my stupid questions. I would also like to thank Sam Lipschutz for being an outstanding Rockport salesman, and Kenneth Whitmore for never being wrong.

I would like thank my family for their continuous loving support, and in particular, my grandfather, who sparked my interest in physics at an early age.

Finally, I am grateful for the opportunity to work with the great faculty, staff, post-docs, and graduate students of the NSCL, without whom this work would not have been possible.

TABLE OF CONTENTS

LIST OF TABLES

LIST OF FIGURES

Chapter 1

Introduction

1.1 Chart of the Nuclides

The atomic nucleus consists of two types of composite particles with similar mass: protons and neutrons. Protons carry one unit of positive charge e and neutrons are charge-neutral. A nuclear species is characterized by the number of protons it contains, Z, and a mass number A so defined such that the mass of a single nucleon is nearly one. In the nucleus we encounter length scales on the order of 10^{-15}m, densities on the order of $\sim 2.3 * 10^{17}$ kg/m^3, and energies typically in the keV to MeV range. The time-scales for nuclear processes vary over an enormous range. β and α decay can take place on the order of milliseconds to hours, or even thousands or millions of years. Electromagnetic decays typically occur within lifetimes of 10^{-15}s, and the breakup of particle-unbound resonances, like ^{25}O, are extremely short – occurring on timescales of 10^{-21}s [1, 2].

Similar to the periodic table, which arranges elements, the chart of nuclides arranges all known nuclear species by the number of protons (Y -axis), and number of neutrons (X-axis), shown in Fig. 1.1. For example, plotting the neutron separation energy S_n, the energy required to remove a single neutron, immediately reveals a global trend evidenced by a staggering pattern in Fig. 1.1. This even-odd oscillation between separation energies can be explained by two-body pairing $(n - n)$ which can increase/decrease the binding. The same trend is observed for protons. The chart of nuclides at present is far from being

completely explored, and the limits for existence are unknown. Of the approximately 3000 known nuclei there is an estimated 4000 more that may exist [3]. The proton dripline is unknown for the heaviest elements and the neutron dripline is only known up to ^{24}O[4]. There are also predictions for an "island of stability," a region in the superheavies of stable nuclei yet unobserved but expected to occur around $Z = 114$, $N = 184$ [5].

The over-arching goal of nuclear physics is to understand, with predictive power, the interactions between neutrons and protons and the properties of the complex many-body systems they can create when arranged together. So strictly speaking, nuclear physics is strong interaction physics and based upon the Standard Model, we should be concerned with gluon exchange between the constituent quarks. However the typical energy scale characteristic of nuclear physics is in the low-energy regime of QCD where the theory is non-perturbative, so direct calculation is difficult. Although the problem can be approached on a discretized lattice (lattice QCD), this method is still limited by computational power and has so far only been implemented in the lightest nuclei (^{3}He, ^{4}He) [6]. In addition, in 1979, Weinberg [7] pointed out that any effective theory for nucleons and mesons that obeys the same symmetries as QCD is equivalent to QCD, which allows us to consider nucleons and mesons as our starting point instead of quarks. Even this reduction can be untractable computationally. If one starts with a bare two-nucleon NN interaction, then any nuclear many-body problem can be exactly defined, but the problem grows factorially and these microscopic calculations are limited to only the lightest nuclei. A nucleus like ^{238}U is simply impossible to compute from a bare NN potential, and will likely be for some time. At present there is no single theoretical formulation that allows us to interpret all nuclear phenomena in a fundamental way, and so nuclear physics is approached phenomenologically. The appropriate model depends on where one is in the nuclear chart and what phenomenon

is being discussed. It is from these models that we gain insight into nuclear structure.

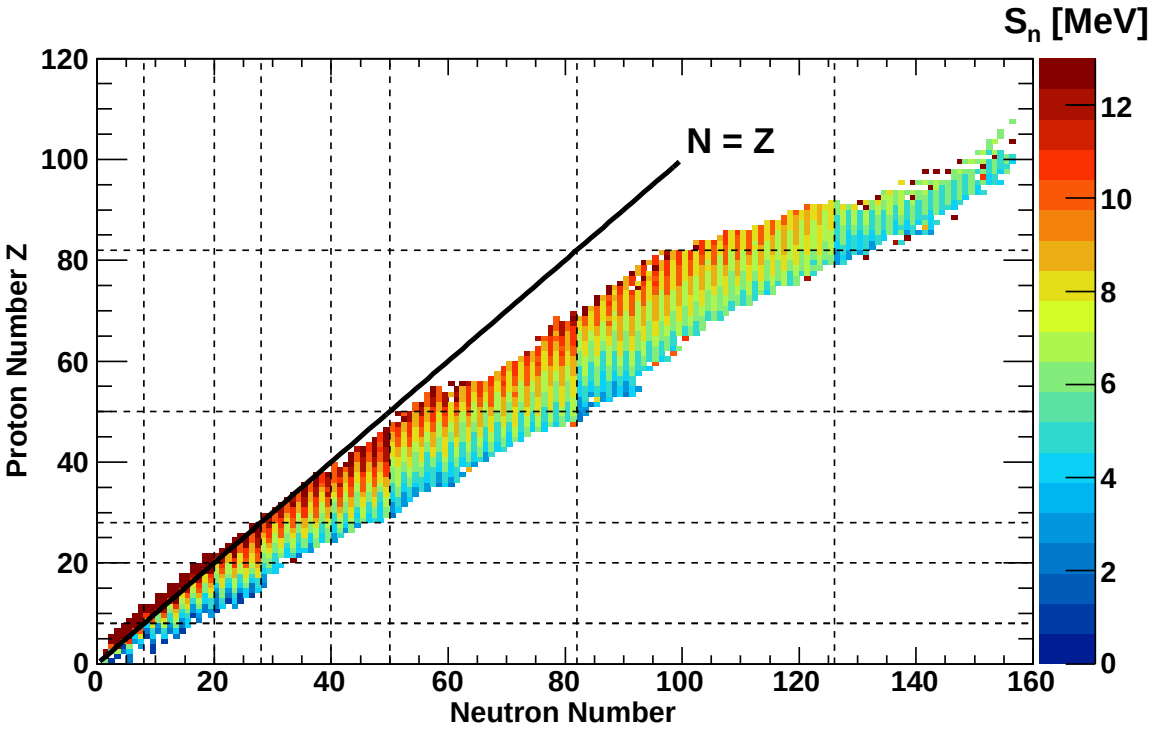

Figure 1.1: Chart of the Nuclides. On the color axis is the neutron separation energy S_n in MeV. Data taken from AME2012 [8]

1.2 Shell Model

One successful model is the Shell Model. Early electron and Rutherford scattering experiments showed, surprisingly, that the charge and matter radii of nuclei *are nearly equal to within about 0.1 fm* [1, 9] – implying that the nuclear force is the same between neutrons and protons. (Although not quite true as the symmetry is broken by the slight difference in quark masses). Both have an A dependence as:

$$r \sim r_0 A^{1/3}$$

with $r_0 = 1.2$ fm. From these measurements, the density profile as a function of r was found to be largely constant within the nucleus, with a smooth fall-off as one approaches the surface. Because of the short range of the nuclear interaction, nucleons mainly interact with their neighbors and saturation occurs where nucleons on the surface do not interact strongly with those in the core. This observation first lead to the liquid-drop model, proposed by Gamov, where the nucleus was thought of like a droplet of liquid. The binding energy can be expressed in the following way:

$$BE(N,Z) = \alpha_1 A - \alpha_2 A^{2/3} - \alpha_3 \frac{Z^2}{A^{1/3}} - \alpha_4 \frac{(N-Z)^2}{A}$$

Where the four terms refer to the volume, surface, Coulomb, and symmetry terms, respectively. The first is a result of constant density, while the second accounts for the fact that the nucleons on the surface have less neighbors to interact with. The third results from Coulomb repulsion between the protons, and the fourth term can be understood as an effect of the Pauli principle.

While a good estimator of the average binding energy, the liquid drop model does not account for any shell or pairing effects. Similar to nobel gases, which have full electron shells, there are certain numbers of neutrons and protons that are more tightly bound than others. Fig. 1.2 shows the difference between the liquid drop model prediction for binding energy and what is observed in experiment. Large peaks appear at what are called the "magic numbers," 28, 50, 82, 126, where one observes more binding in nature than predicted by the liquid drop-model. This is strikingly similar to spikes in the electron ionization energy occurring in the nobel gasses. Thus inspired by the atomic shell model, Maria Goppert Mayer, Haxel, Jensen, and Suess all sought to explain the enhanced binding with a similar

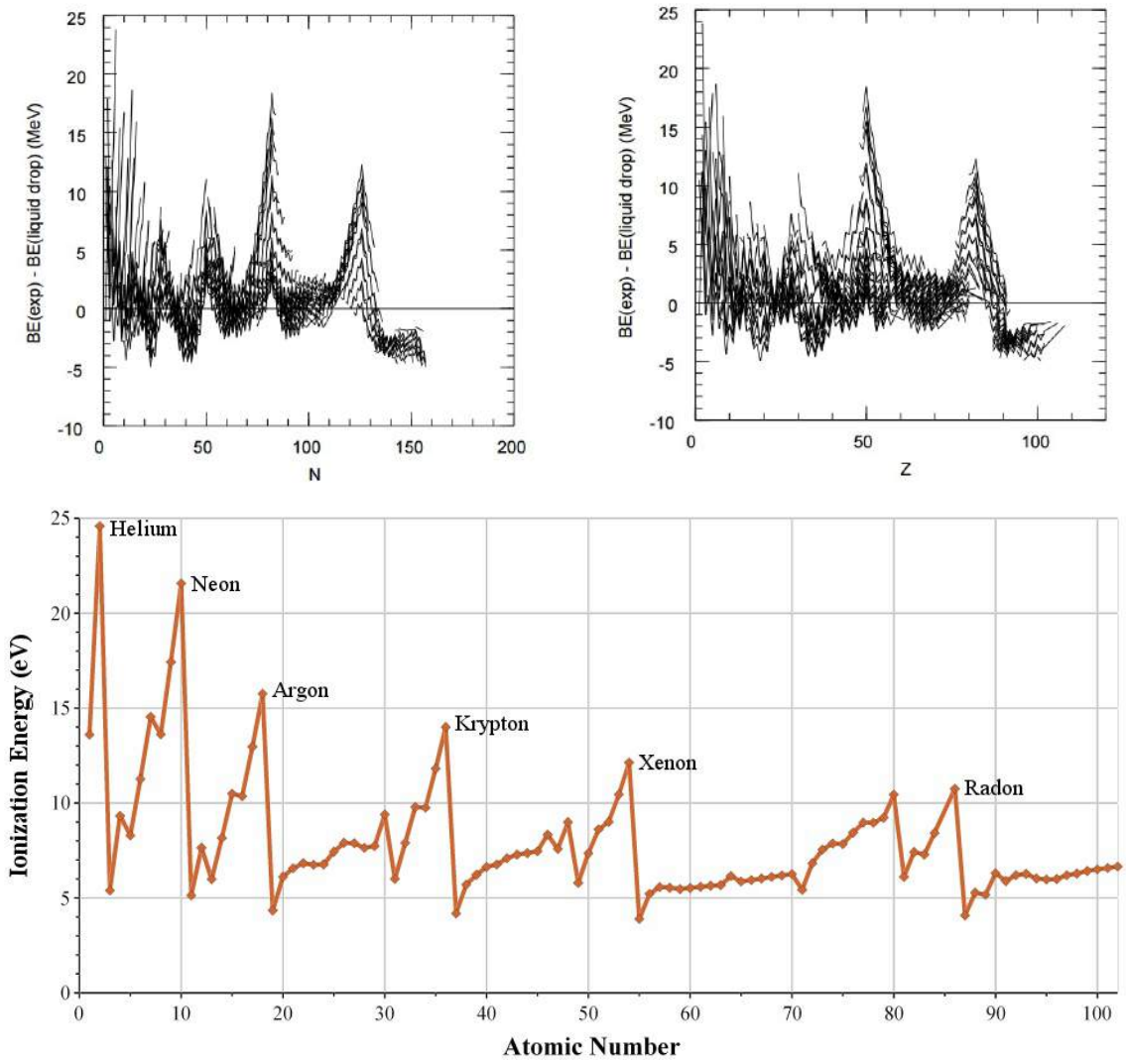

Figure 1.2: (Top) Difference in binding energy between the liquid drop model and experimental observation. On the left is the difference as a function of neutron number N. On the right is as a function of the proton number Z. (Bottom) Electron Ionization energy for all elements with $Z < 104$ on the periodic table. Note the similarity in closed electron shells and closed neutron/proton shells. Image sources: [10], [11]

approach [12, 13]. This idea is particularly attractive because now spatial orbits for nucleons can be discussed in analogy to electron orbitals.

The first step in developing a shell model is to choose a potential. Due to the short-range interaction and constant density, a nucleon in the middle of the nucleus will interact with approximately the same number of nucleons regardless of it's position. Thus the potential

should be flat inside the nucleus, and negative so that the nucleus is bound, $V(r) < 0$. As the nucleon moves towards the surface the number of neighbors it can interact with decreases leading to a shallower potential. Finally, outside the nucleus, we exceed the short-interaction range, and so $V(r)$ should approach zero. This behavior is often parameterized with a Woods-Saxon shape, which can be further approximated by a harmonic oscillator. By adding a spin-orbit term, Mayer and Jensen were able to reproduce the observed gaps in orbital energy, corresponding to the magic numbers, for which they were awarded the Nobel Prize (1963).

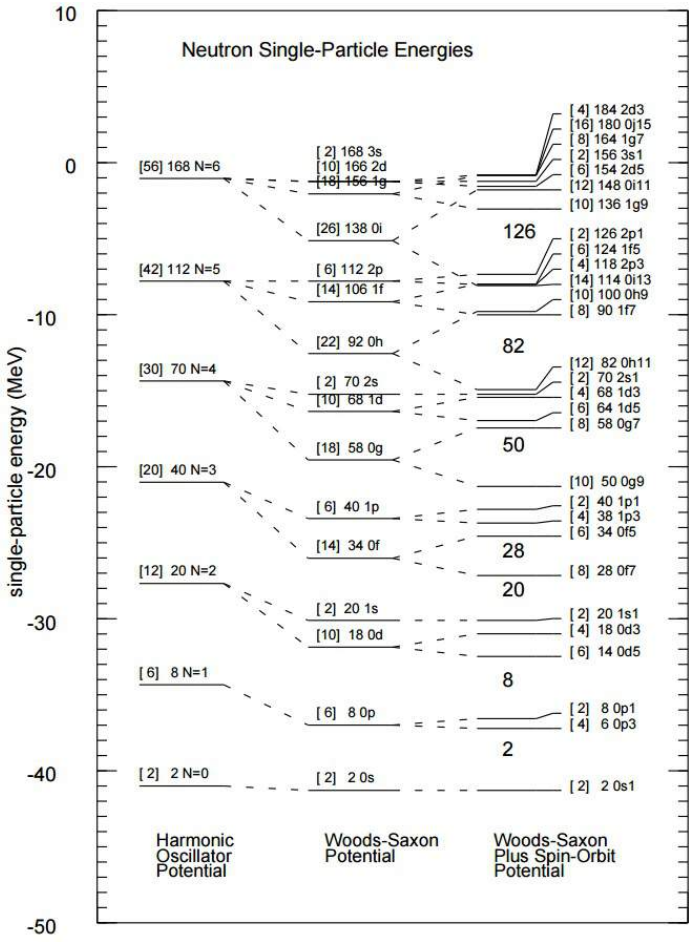

Figure 1.3: Single particle orbits in the nuclear shell model. Energies are shown for a harmonic oscillator potential, woods-saxon, and woods-saxon with spin orbit. Image Source: [10]

The nuclear shell model shares some properties with the atomic shell model. A single particle is placed in a mean-field $V(r)$, and the eigenstates are characterized by orbitals with quantum numbers n, l, j, and an energy E. Like atomic orbitals, the eigenstates are filled separately with neutrons and protons beginning with the lowest energy while obeying the Pauli principle. However, unlike the atomic shell model, the spin-orbit term is greater and of opposite sign, so the ordering of the orbitals and the placement of shell gaps (magic numbers) is different.

Since Mayer and Jensen's work, the Shell Model has become much more sophisticated. A more modern calculation will write the Hamiltonian as a sum of one- and two-body operators, with an effective two-body interaction typically derived phenomenologically from experimental measurements in a particular mass-range of interest. The problem then becomes one of matrix-diagonalization to determine the eigenvalues of a particular few-body system. It is a good simplification to assume that at the shell-closures the nucleons in a filled shell can be approximated as a single core. This approach also has computational limitations, as the number of basis states increases factorially with the addition of more orbitals and/or particles and truncations are often made to simplify the calculation.

1.2.1 Islands of Inversion

It has been shown that Mayer and Jensen's magic numbers break down as one moves towards neutron rich nuclei. The conventional magic numbers for nuclei in the valley of stability are not necessarily magic for nuclei with extreme N/Z ratios. For example ^{24}O is doubly magic with the appearance of a new shell closure at $N = 16$, as evidenced by trends in $E(2^+)$ energies [14, 15, 16]. One striking example is the "Island of Inversion," located around the mass region of $A \sim 32$ [17, 18]. Here, the $N = 20$ shell gap is quenched and nuclei that

should occupy ground states in the *sd* shell instead occupy orbitals in the *pf* shell. This shift has been attributed to the NN tensor force [19], three-body forces [20], and continuum effects in cases where nuclei approach the driplines [21]. The discovery of the island of inversion caused a paradigm shift, as it was previously thought that the magic numbers were immutable [20]. It has since been found that there are multiple such islands of inversion, and the effect of nuclear forces on the shell structure of nuclei, particular in neutron-rich regions, is an ongoing area of research.

1.2.2 Tensor Force

The tensor force is the result of one-pion exchange and is the most prominent spin-isospin interaction between nucleons. In recent years it has been shown to have systematic effects on the single-particle energies of exotic nuclei [19, 22]. Depending on the angular momenta of the particles involved, the tensor force can be either attractive or repulsive. The tensor force is written as:

$$V_T = (\vec{\tau_1} \cdot \vec{\tau_2}) S_{12} V(r)$$

where $\vec{\tau_i}$ denotes the isospin operators of nucleons 1 and 2, $V(r) > 0$ is a function of the distance r between the nucleons, and S_{12} is:

$$S_{12} = 3(\vec{s_1} \cdot \hat{r})(\vec{s_2} \cdot \hat{r}) - (\vec{s_1} \cdot \vec{s_2})$$

where $\vec{s_i}$ are the spin of the nucleons. For simplicity, take $\vec{s_1} = \vec{s_2} = +\hat{z}$, and let ℓ and ℓ' denote the angular momentum of a proton and neutron respectively. Their total angular momentum will be $j_\pm = \ell \pm 1/2$, and $j'_\pm = \ell' \pm 1/2$.

For "spin-flip" partners, $(j_{\pm}, j'_{\mp})$ the tensor force is attractive. When the nucleons collide, they will have large relative momentum causing the spatial wavefunction to be narrowly distributed in the direction of the collision like that illustrated in the left of Fig. 1.4. This results in a wavefunction similar to the deuteron. In this case, $\vec{s_1} \cdot \vec{s_2} = +1$, and $\vec{s_1} \cdot \hat{r} = \vec{s_2} \cdot \hat{r} = 1$, thus $S_{12} = 2$. Since $(\vec{\tau_1} \cdot \vec{\tau_2}) = 2(\hat{T}^2 - 3/2) = -3$ for opposite isospins, $(\hat{T} = \hat{\tau_1} + \hat{\tau_2} = 0)$, V_T becomes negative and thus the interaction is attractive.

In the opposite case with $(j_{\pm}, j'_{\pm})$, the wave function is stretched along the direction of motion as illustrated in the right of Fig. 1.4. In this case $\vec{s_i} \cdot \hat{r} = 0$ and we obtain $S_{12} = -1$ making the interaction repulsive.

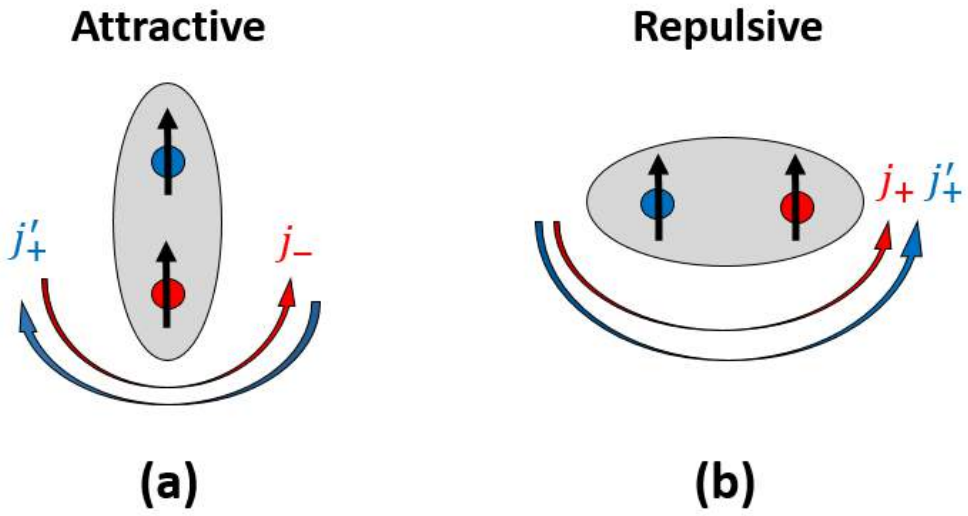

Figure 1.4: (a) Diagram for wave function of relative motion for collision of a "spin-flip" pair. Note that this case is deuteron-like and attractive. (b) In the non spin-flip case the wave function of relative motion is stretched perpendicular to the spin (denoted by black arrows), and is repulsive.

The role of the tensor force in driving shell evolution is illustrated in Figure 1.5. For stable nuclei near $N = Z = 20$, the proton $\pi 0d_{5/2}$ orbital (j_+) is full and has an attraction with the neutrons in the $\nu 0d_{3/2}$ orbital (j'_-), as well as a repulsion with $\nu 0f_{7/2}$ orbital (j'_+). This results in the normal shell-ordering at stability, as the $\nu 0f_{7/2}$ orbital is raised and the

$\nu 0d_{3/2}$ orbital is lowered creating a large gap at $N = 20$. If one removes protons and travels down the isotones, the $\pi 0d_{5/2} - \nu 0d_{3/2}$ attraction is weakened causing the the $\nu 0d_{3/2}$ orbital to rise in energy relative to nuclei at stability. This creates a gap between the $\nu 0d_{3/2}$ and $\nu 1s_{1/2}$ orbitals leading to a quenching of the $N = 20$ gap, and the appearance of a new magic number at $N = 16$.

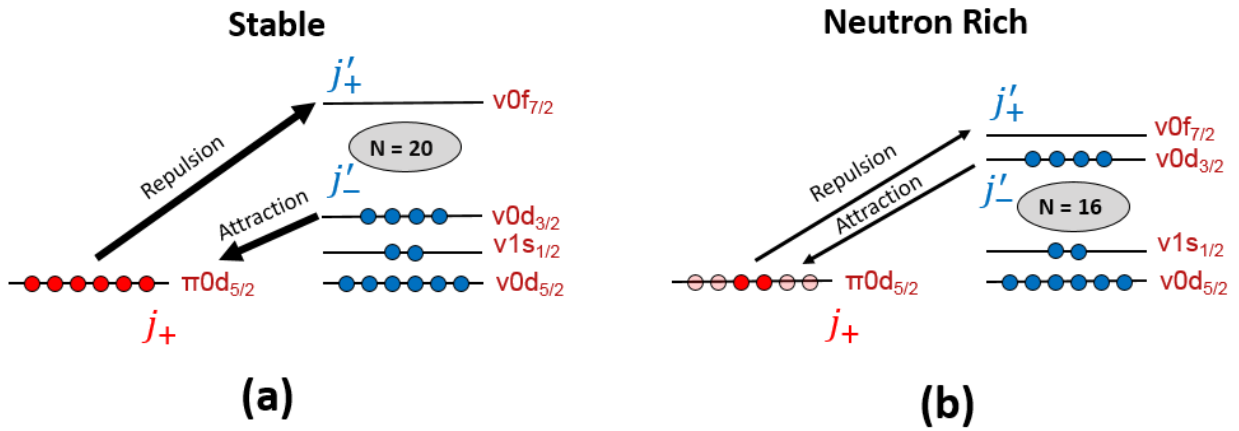

Figure 1.5: Schematic for illustrating shell evolution due to the tensor force. The width of the arrows denotes the strength of the interaction. (Left) A configuration in nuclei near stability with $N = 20$ being magic. (Right) As protons are removed the attraction with the $\nu 0d_{3/2}$ orbital weakens causing it to rise in energy relative to the $\nu 1s_{1/2}$ orbital creating a new shell gap at $N = 16$

1.3 Three-body Correlations and Decays

In a three-body decay there are three particles in the final state. Nuclei which undergo 2n or 2p emission, such as ^{10}He(2n) [23, 24, 25], ^{13}Li(2n) [23, 26], ^{12}O(2p)[27, 28], ^{19}Mg(2p)[29, 30, 31]), and many others discussed in this section, fall into this category. Correlations between the two nucleons as well as the heavy core can provide insight into the decay mechanism. In general, there are several broad categories used to classify the different decay modes: (1) Di-neutron/proton emission, (2) a sequential decay, or (3) a three-body decay wherein it

is necessary to solve the three-body schrodinger equation. The latter is a true three-body processes and can be complex. It is also useful to introduce the concept of a phase-space decay (which is distinct from a three-body interaction), where the phase volume (M^2_{fn} vs. M^2_{n-n}) is uniformly populated. The dineutron, phase-space, and sequential decay modes are discussed in detail in Section 2.2.

In the two-body decay, a resonance can be characterized by just an energy and a width. The addition of a third particle however allows for 9 degrees of freedom in the final state if we neglect spin. Three of them describe the center-of-mass motion, and another three describe the Euler rotations that define the decay plane. Thus for a given three-body energy E_T, there are two free parameters left. In the Jacobi coordinate systems, discussed in detail in section 3.10, it is convenient to choose the relative energy ϵ and angle θ_k between the Jacobi momenta. These correlations are sensitive to the decay mechanism, and can in principle be reproduced with the three-body wavefunction. Thus they are a powerful tool to discern the decay mechanism, as well as connect directly with few-body kinematics. Measurement of 2p and 2n decays and their three-body correlations near the driplines provide an opportunity to benchmark our theoretical understanding of few-body quantum mechanics as well potentially observe new phenomena.

1.3.1 Two-Proton Decay

The first mention of true two-proton emission is in the work of Zeldovich [32], with a more explicit and detailed description given by V.I. Goldansky soon after [33]. Although first predicted by Goldansky in 1960, it took nearly 40 years to confirm the existence of two-proton radioactivity in ^{45}Fe [34], and since then many other nuclei have been found to have lifetimes long-enough to fall into the regime of radioactivity ($\tau > 10^{-14}$ s) including ^{17}Ne

[35], ^{19}Mg [36], ^{48}Ni [37], and ^{54}Zn [38]. While a stringent limit for radioactivity does not exist, one definition suggested by Pfutzner [2] is "A process of emission of particles by an atomic nucleus which occurs with characteristic time (half-life) much longer than the K-shell vacancy half-life in a carbon atom ($2 * 10^{-14}$ s)." Hence a nuclear process whose duration exceeds this limit could be considered radioactive, including the decay of unbound ground states.

Experimental attempts to search for 2p emission started in the lightest nuclei as they are relatively easier to access experimentally, with the first systems studied being ^{6}Be [39, 40], ^{12}O [28, 41] and ^{16}Ne [42].

The decay of ^{6}Be falls into the class of "democratic decays", where there is no strong energy focusing of the particles and their momenta are smoothly distributed. Even in Geesaman's work [39] it was evident that a simple phase-space decay, di-proton decay, or even simultaneous emission of two p-wave protons could not describe the energy distribution of α particles they observed. It was concluded that a full three-body calculation was necessary. More recently, the full picture of the three-body correlations in ^{6}Be was experimentally measured and shown to be in very good agreement with a three-body calculation by Grigorenko. Fig. 1.6 shows the the $\mathbf{T}$ and $\mathbf{Y}$ Jacobi correlations for the breakup of ^{6}Be $\rightarrow p + p + \alpha$ from Ref. [43], compared to the theoretical model [44]. A full three-body approach was also shown to be necessary to understand the $p - p$ correlations in ^{16}Ne [30], ^{19}Mg [30], and ^{45}Fe [44].

In the case of ^{12}O the opening angle between the emitted protons was measured and was inconsistent with models for di-proton emission [28]. It was later found that the intermediate nucleus, ^{11}N, has a ground state below ^{12}O. The state is broad – implying that ^{12}O cannot be a Goldansky-like true 2p emitter. Initial measurements interpreted the decay as sequential

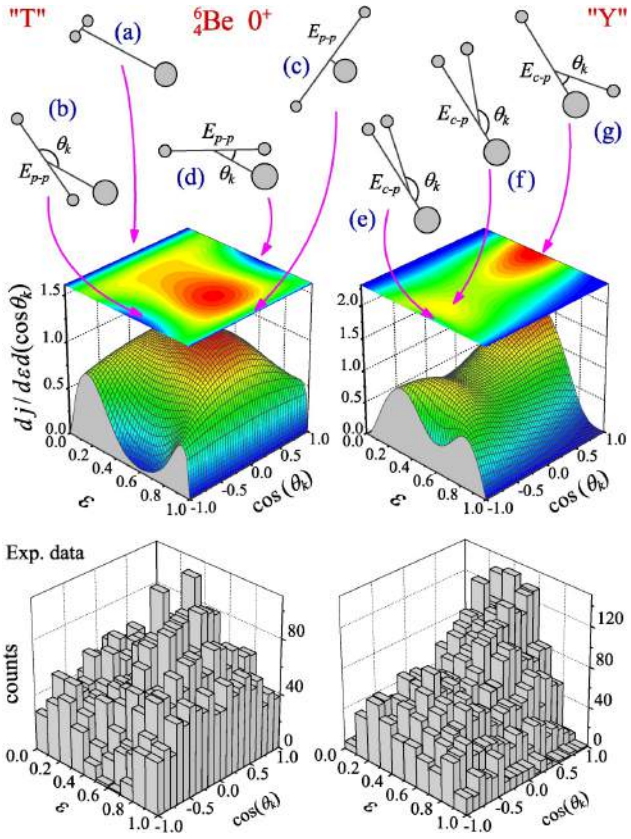

Figure 1.6: (Top) Theoretical prediction for the Jacobi **T** (left) and **Y** (right) system relative energy and angular correlations in the breakup of ^{6}Be based on a full three-body calculation[44] The data are shown on the bottom panels. Image Source: [43]

[28], however more recent work has shown that ^{12}O more appropriately falls in the category of ^{6}Be, as the three-body energy E_T is comparable to the width of the intermediate state [27]. A study of ^{14}O [45] also found evidence for sequential emission, and although not a 2p decay, there is evidence for sequential decay in the three-body exit channel of ^{9}B$\rightarrow p + 2\alpha$ which passes through an intermediate state in ^{5}Li [46].

There are several cases of β-delayed 2p emission, further discussed by Blank and Borge in 2008 [47]. The most studied case, ^{31}Ar [48] appears to decay only by sequential emission, and it is currently believed that all studied $\beta 2p$ processes are sequential [2].

In general, for 2p emitting nuclei, the mechanism is either a true three-body process or sequential, although there are some cases with evidence for di-proton emission. For

example, the breakup of ^{8}C $\rightarrow$ 2p+^{6}Be$\rightarrow$ 4$p + \alpha$ was measured recently at the National Superconducting Cyclotron Laboratory [46]. In this study, it was found that this decay can be described as two 2p decays with the first step ^{8}C $\rightarrow$ 2p+^{6}Be showing some di-proton characteristics, and the second being a three-body decay. In addition, there are studies on the 1^{-} resonance in ^{18}Ne populated by ^{17}F + ^{1}H [49] and by Coulomb excitation [50] where the $p - p$ correlation spectra are explained with a di-proton component. However the statistical claims in both cases are weak.

1.3.2 Two-Neutron Decay

Compared to 2p decays along the proton dripline, the neutron dripline is less studied. Analogous to the 2p emitters, several two-neutron unbound systems have been measured including ^{5}H [51], ^{10}He [52, 25, 23, 24], ^{13}Li [23, 26], ^{14}Be [53], ^{16}Be [54], and ^{26}O [55, 56]. Several of the three-body correlations in these system have been interpreted as di-neutron emission [26, 54]. In addition, ^{26}O has potential to exhibit two-neutron radioactivity [57]. Despite observing 2p radioactivity approximately a decade ago, up until recently there has been "no theoretical treatise" (Grigorenko, 2011) [58] for neutron radioactivity. This is partly due to the fact that neutron radioactivity is yet unobserved, but also that 2n unbound systems are challenging from both an experimental and theoretical point of view. The Coulomb interaction plays a major role in understanding the dynamics of 2p emission, especially in heavier systems like ^{45}Fe, and extending these models to the neutron drip line is not as simple as removing Coulomb effects [59]. In addition, it is difficult to identify two independent neutrons within a single event experimentally.

Contrary to the 2p decays, many of the three-body correlations in 2n emitters indicate di-neutron emission, or a strong $n-n$ final state interaction (FSI). Fig. 1.7 shows the relative

$n-n$ energy, E_x compared to the total three-body energy E_T in the Jacobi **T** system for ^{5}H [51], ^{13}Li [26], and ^{16}Be [60]. All three spectra are similar and peak at low $n-n$ energy which can be interpreted as the wavefunction having a di-neutron component, or $n-n$ FSI effects. Correlations for ^{26}O have also been measured and potentially show di-neutron like character as well [61]. However, in this case the statics are low and the data are indistinguishable from a model where the neutrons are emitted back-to-back rather than a cluster [62]. In these nuclei, the intermediate nucleus is energetically inaccessible and the level structure mimics a "Goldansky true 2p" emitter illustrated in Fig.2.3.

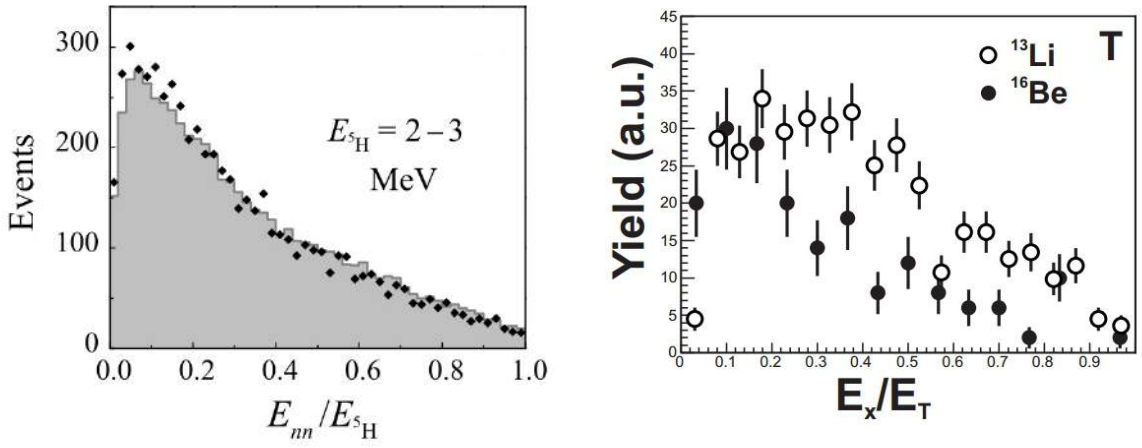

Figure 1.7: Jacobi relative energy correlations in the **T** system for the unbound systems (Left) ^{5}H [51], (Right) ^{13}Li, and ^{16}Be [60]. Peaks at low E_x/E_T indicate that the neutron-neutron energy is low relative to the total three-body energy and is interpreted as either a di-neutron emission or final state interaction.

Sequential correlations along the neutron drip-line have been least observed. There is a measurement of the decay of highly excited states in ^{14}Be [53] where the three-body energy correlations show some evidence for decays through intermediate states. However this work did not publish angular correlations. There is also indication that excited states in ^{24}O can decay by sequential emission, as evidenced by Hoffman [63] but the statistics were insufficient to extract three-body correlations.

β-delayed multineutron emission, while dominant in the very neutron-rich nuclei, is not well studied and correlations have not been measured in these systems. This is in part due to the difficulty of neutron detection, and the fact that few cases are known. The first β-delayed neutron decays were discovered in 1979 [64] and 1980 [65], both $\beta 2n$ and $\beta 3n$ processes were observed in ^{11}Li. In addition, there is a report of $\beta 4n$ emission in ^{17}B [66], however this work is unconfirmed.

1.3.3 Transition from 3-body to 2-body

The level structure of the nuclei involved in either 2p or 2n emission strongly influence, although do not appear to completely determine, the mechanism of the decay. Just because a sequential decay is energetically viable, does not guarantee it will occur. In the democratic decay of ^{6}Be the transition from three-body to sequential was examined by looking at the $p-\alpha$ energy in the Jacobi $\mathbf{Y}$ system for different slices of the total three-body energy E_T [43]. Fig.1.8 shows the level structure of ^{6}Be and the intermediate nucleus ^{5}Li. Because the intermediate state in ^{5}Li is broad, the sequential decay mechanism is *suppressed* in favour of three-body dynamics.

In this study it was found that sequential correlations were not visible until the decay energy E_T was greater than twice the intermediate state plus its width. This is shown in Fig.1.8 by the double-hump structure in the $E_{\alpha-p}/E_T$ spectrum, indicating a high-energy and a low-energy proton coming from discrete states. Contrast this with the three-body bell-curve at lower E_T, which peaks at 1/2 and is symmetric. The symmetry is a result of the two protons being indistinguishable, and the maximum at 1/2 can be understood as a result of the maximum probability for barrier penetration occurring when the proton energies are equal. Goldanksy proposed an exponential factor $w(\epsilon)$ as the product of two

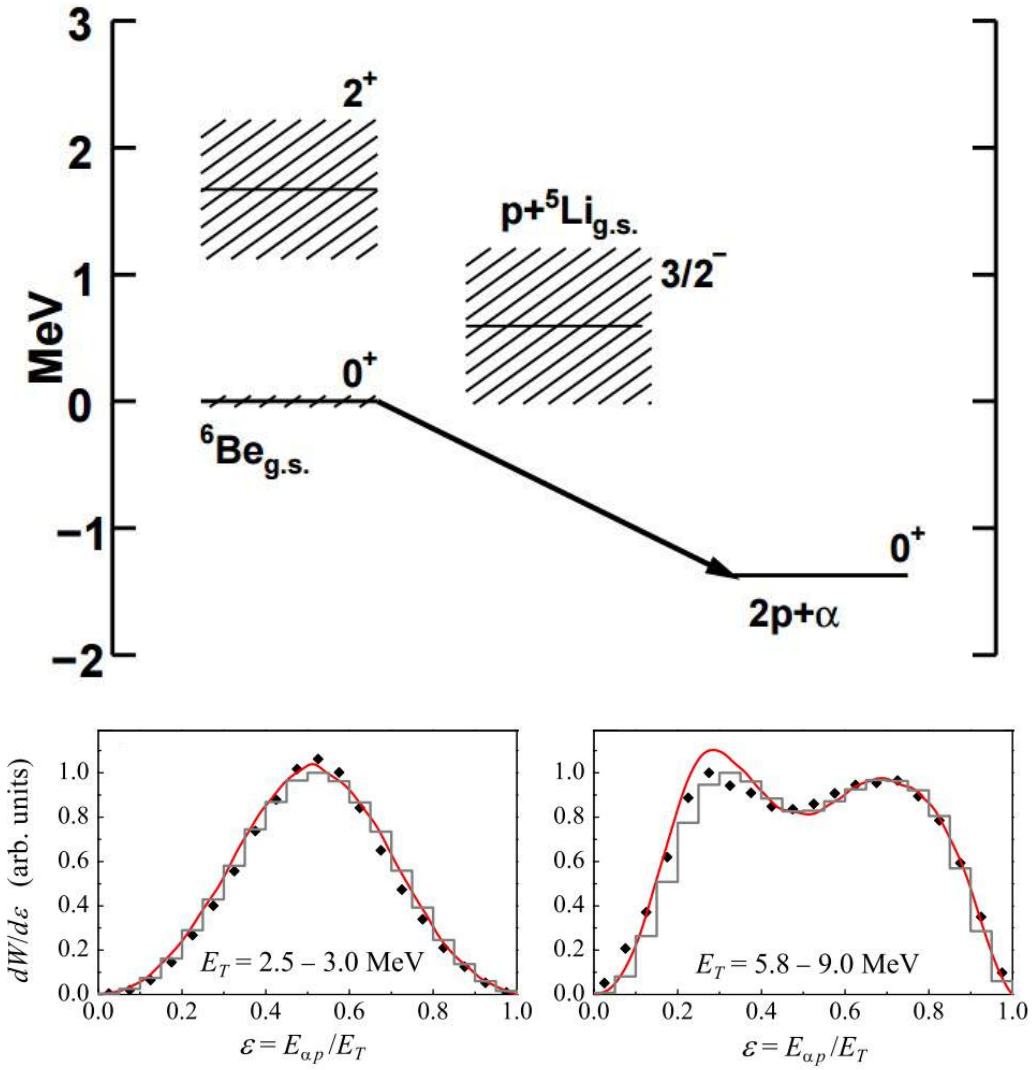

Figure 1.8: (Top) Level structure for the three-body decay of ^{6}Be [67]. (Bottom) Relative energy plots in the Jacobi **Y** system (proton-core) for different slices in the total three-body energy. On the left, the energy region is slightly above the 2^+ state and the correlation indicate a three-body decay. On the right, the energy is much greater than the intermediate state and correlations indicating sequential emission begin to emerge [43]

usual barrier factors [33]:

$$w(\epsilon) = exp\left[\frac{-2\pi(Z-2)\alpha\sqrt{M}}{\sqrt{E_T}}\left(\frac{1}{\sqrt{\epsilon}} + \frac{1}{\sqrt{1-\epsilon}}\right)\right]$$

Here E_T is the total three-body energy, and ϵ and (1-ϵ) the fraction of energy given to each

proton and $\alpha = e^2/\hbar$. This expression is maximum when the two proton energies are the same ($\epsilon = 0.5$).

However, sequential correlations in ^{19}Mg were observed in the decay of excited states once they were energetically available because the intermediate 1^- state in ^{18}Na is narrow giving a well defined proton energy and longer life-time [30, 29]. The transition from the three-body to the two-body regime was examined for ^{12}O (democratic), and ^{19}Mg (democratic g.s. sequential excited) within the context of a full three-body calculation [2]. Plotted in Fig. 1.9 are the predictions for the $p-core$ energy in the Jacobi $\mathbf{Y}$ system from Grigorenko's three-body model for ^{12}O and ^{19}Mg with increasing energy E_T. In the case of ^{12}O, which is similar to ^{6}Be, even though the energy is high enough to undergo a sequential decay a full three-body process is favoured due to the large width of the intermediate state. This is evidenced by the three-body bell-curve, which simply becomes narrower. In contrast, as the energy in the ^{19}Mg system is increased large "horns" begin to appear around 0 and 1 indicating two discrete proton energies. As the energy increases further, the horns begin to dominate more of the spectrum. The exact limits for transitioning from a three-body decay to a sequential decay are not known. Empirical estimates from Grigorenko's three-body model give the requirement:

$$\epsilon_0 E_T < E_{2r}$$

Which is derived from finding the point where the probabilities from the three-body bell-curve equal that of the sequential horns. In addition, ϵ_0 varries between $\epsilon_0 \sim 0.3 - 0.84$ depending on the life-time of the decay [2]. This is less restrictive than the original condition

proposed by Goldansky:

$$E_T + \Gamma_{2r}/2 < E_{2r}$$

Nevertheless, if we wish to observe sequential correlations in 2n unbound nuclei, we need to look for systems with narrow states in the intermediate nucleus.

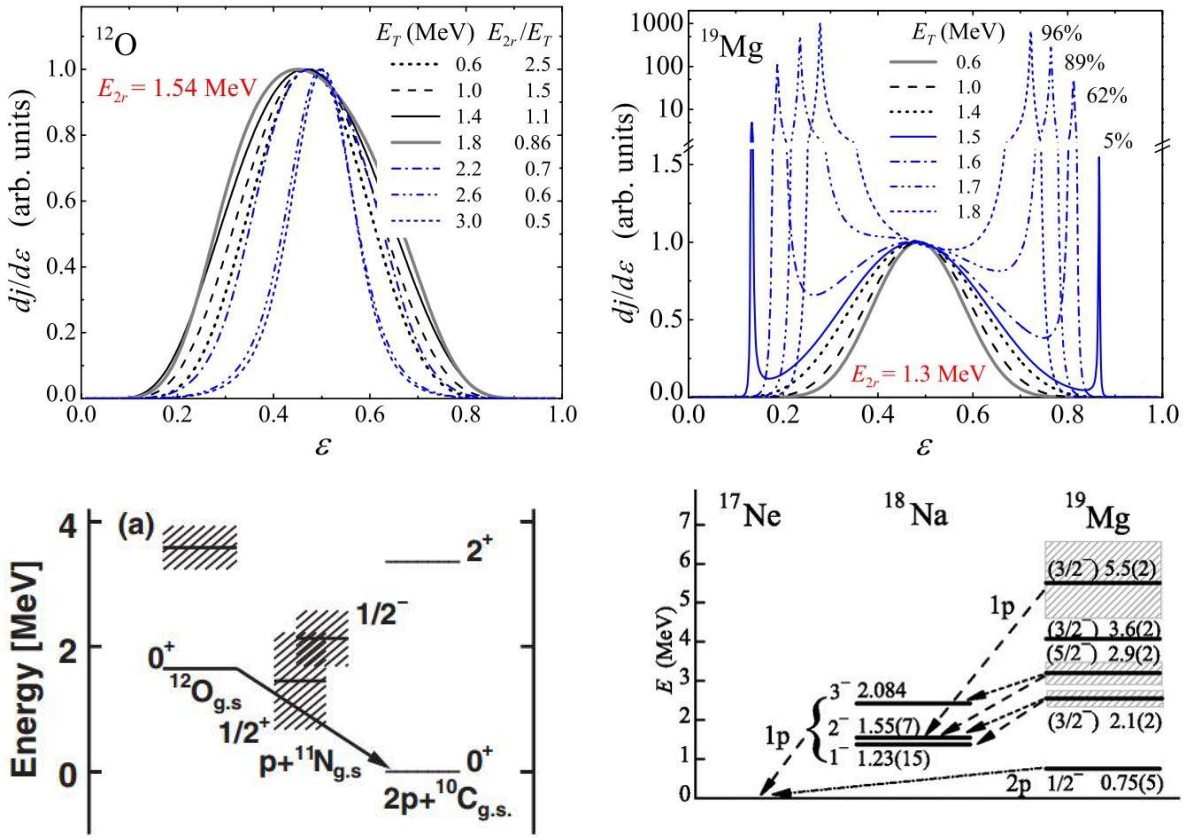

Figure 1.9: (Top) The transition from the three-body to the two-body regime as studied within Grigorenko's model for ^{12}O and ^{19}Mg. Plotted are the relative energies in the Jacobi **Y** system [2] . (Bottom) Level structure for the decays of ^{12}O [27] and ^{19}Mg. [29]. Note the widths of the intermediate states.

1.3.4 Previous Experiments

^{24}O, the last bound isotope for which the neutron drip-line is established, is an ideal candidate for observing a two-neutron sequential decay. It's structure has been well studied as well as the intermediate nucleus ^{23}O. There is substantial evidence for the appearance of a new magic number $N = 16$ [16, 68, 15, 69], and two unbound resonances have been observed below the two-neutron separation energy at 4.7 MeV and 5.3 MeV, with respective spin-parity assignments 2^+ and 1^+ [70, 63, 71]. There is also evidence for a state above the two-neutron separation energy $S_{2n} = 6.93 \pm 0.12$ MeV, at approximately 7.5 MeV [63]. In addition, the intermediate nucleus ^{23}O, has a low-lying narrow $5/2^+$ resonance at 45 keV above the $1n$ separation energy [72, 73, 68]. The next excited state, a $3/2^+$, lies at 1.3 MeV [74]. The level structures of these nuclei are ideal to observe sequential emission and is summarized in Fig. 1.10. The condition found in the ^{6}Be study [43]:

$$E_{3body} > 2 * E_{2body} + \Gamma_{2body}$$

is well satisfied if the decay proceeds from the 7.5 MeV state through the $5/2^+$ state. First tentative evidence that this resonances decays by sequential emission of two neutrons was deduced from a measurement of two discrete neutron energies in coincidence similar to a γ-ray cascade [63]. Since the three-body state is at roughly ~ 600 keV relative to the ground state of ^{22}O and the intermediate state in ^{23}O low-lying and narrow, this state is the optimum case for observing sequential correlations. This is the goal of the current experiment, as full three-body correlations demonstrating a sequential decay have not yet been observed on the neutron drip-line.

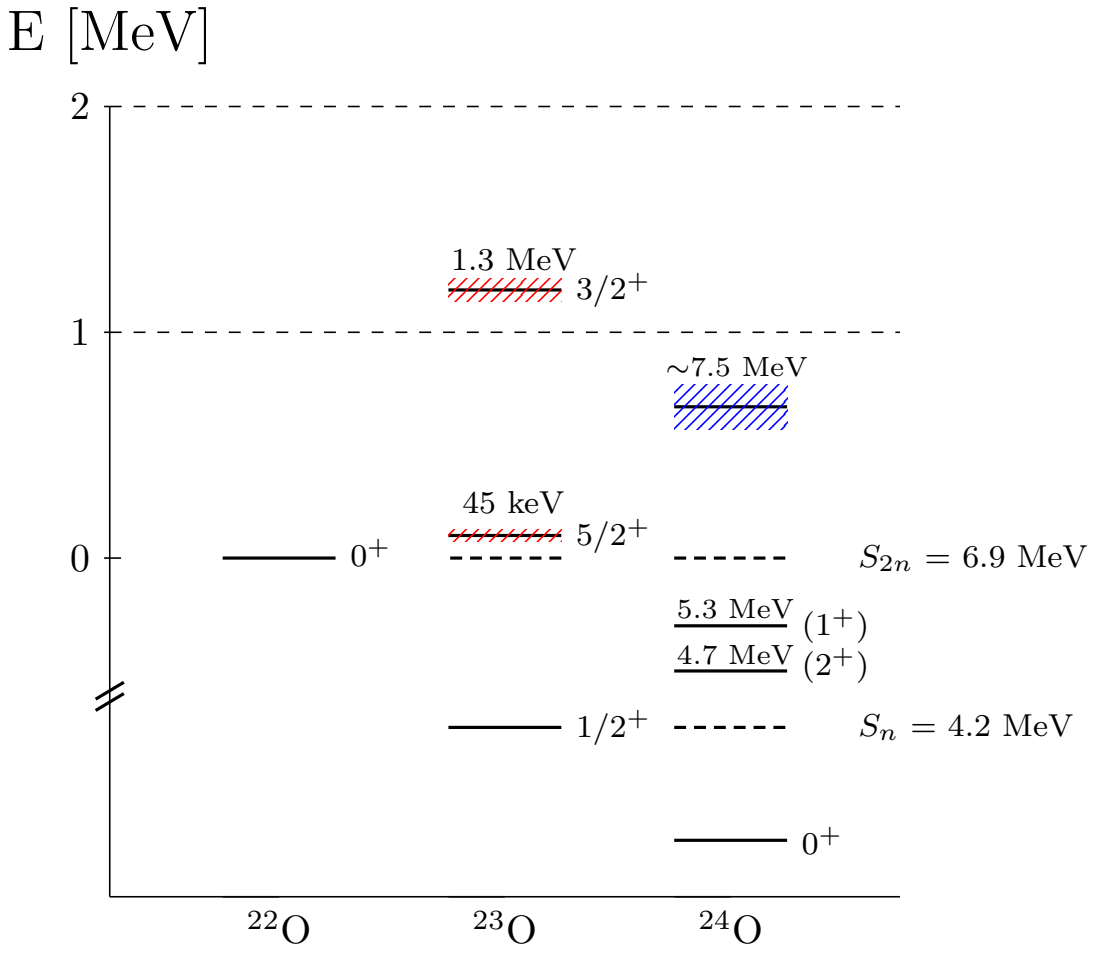

Figure 1.10: Level structure of the most neutron rich bound oxygen isotopes. Hatched areas indicate approximate widths.

Chapter 2

Theoretical Background

2.1 One Neutron Decay

This section gives a derivation of the energy-dependent Breit-Wigner lineshape that is used to model an unbound resonance in the case of 1n decay using the **R** matrix formalism. Models for two-neutron decays use lineshapes that depend on the decay mechanism and are discussed in later sections.

2.1.1 R-Matrix deriviation

One-neutron unbound states can be populated in a number of ways. In this experiment unbound states in ^{23}N and ^{23}O were populated via one-proton/neutron removal from an ^{24}O beam. The resulting nuclei then proceeded to decay by emitting a neutron and a charged fragment. This process is taken to be a direct reaction which populates the unbound state and then promptly decays. The decay of the unbound nucleus can be interpreted as an inelastic scattering problem in the context of R-matrix theory. However, rather than make predictions based on the Hamiltonian, here we use R-matrix phenomenlogy to derive a resonance lineshape that will be fit to the data based on a pole energy e_p and width amplitude $\gamma_{p\alpha}$. Only a summary is presented here, additional details can be found in Thompson and Nunes [75] and Lane and Thomas [76]

The problem we want to consider involves different entrance and exit channels as we want to describe the unbound resonance, not just elastic scattering. In this context this can be considered as inelasticly scattering from channel α to another α'. The method for the multi-channel problem uses as basis states, the eigenfunctions of the real part of the diagonal potential in each channel w_α, where α denotes the channel. It can be shown that the generalization in this case for channel α and pole p, the $\mathbf{R}$ matrix is: [75]

$$\mathbf{R}_{\alpha'\alpha} = \sum_{p=1}^{P} \frac{\gamma_{p\alpha}\gamma_{p\alpha'}}{e_p - E}$$

Where E is the incident particle energy, e_p is the pole energy (resonance), and $\gamma_{p\alpha}$ are the reduced width amplitudes. In general the $\gamma_{p\alpha}$ are constructed from an expansion of w_α [75]. We wish to describe the cross section σ, which is proportional to the absolute squre of the $\mathbf{S}$ matrix. In terms of the $\mathbf{R}$ matrix, the $\mathbf{S}$ matrix can be written as:

$$\mathbf{S} = (\mathbf{t}^{1/2}\mathbf{H}^{+}) \frac{1 - a\mathbf{R}(\mathbf{H}^{-'}/\mathbf{H}^{-} - \beta)}{1 - a\mathbf{R}(\mathbf{H}^{+'}/\mathbf{H}^{+} - \beta)}$$

Where $\mathbf{H}^{\pm}$ are diagonal matricies whose elements are the Hankel functions which are constructed from the regular Coulomb functions, $H_l^{\pm} = G_l \pm iF_l$. The matrix $\mathbf{t}$ is diagonal with elements $t_\alpha \equiv \hbar^2/2\mu_\alpha$ and β is the logarithmic derivative of the $\mathbf{R}$ matrix evalulated at the channel radius a, which is an arbiratry cut-off point past which only long-range interactions play a role. μ_α is the reduced mass. It is useful to define a "logarithmic" matrix $\mathbf{L}$:

$$\mathbf{L} = \mathbf{H}^{+'}/\mathbf{H}^{+} - \beta = \frac{1}{a}(S + iP - a\beta)$$

Where we have introduced the penetrability P and shift function S, which are diagonal

matrices with elements:

$$P_\alpha = \frac{k_\alpha a}{F_\alpha^2 + G_\alpha^2} \tag{2.1}$$

$$S_\alpha = (\dot{F}_\alpha F_\alpha + \dot{G}_\alpha G_\alpha) P_\alpha \tag{2.2}$$

The dot denotes a derivative with respect to $\rho = kR$, where k is the quantum mechanical wavenumber, and R the radial coordinate. Since $\mathbf{H}^{-'}/\mathbf{H}^- = \mathbf{L}^*$, the scattering matrix $\mathbf{S}$ can be put in the following form:

$$\mathbf{S} = \mathbf{\Omega}(\mathbf{t}\mathbf{H}^-\mathbf{H}^+)^{-1/2}\frac{1 - a\mathbf{R}\mathbf{L}^*}{1 - a\mathbf{R}\mathbf{L}}(\mathbf{t}\mathbf{H}^-\mathbf{H}^+)^{1/2}\mathbf{\Omega}$$

Where we have introduced Ω, yet another diagonal matrix with elements $\Omega_\alpha = e^{i\phi_\alpha}$ with ϕ_α being hard-sphere phase shifts. The matrix product $\mathbf{t}\mathbf{H}^-\mathbf{H}^+$ is diagonal with elements:

$$\mathbf{H}_\alpha^-\mathbf{H}_\alpha^+\mathbf{t}_\alpha = \frac{\hbar v_\alpha a}{2P_\alpha}$$

Where $v = \hbar k/\mu$ is the channel velocity.

The cross section is proportional to the absolute square of the symmetric matrix $\widetilde{\mathbf{S}}$, which is constructed from $\mathbf{S}$ via a similarity transformation $\widetilde{\mathbf{S}} \equiv \mathbf{v^{1/2}S v^{-1/2}}$ and can be written as:

$$\widetilde{\mathbf{S}} = \mathbf{\Omega}[1 + 2iP^{1/2}(1 - a\mathbf{R}\mathbf{L})^{-1}\mathbf{R}P^{1/2}]\mathbf{\Omega}$$

Which is powerful, as we now have an expression for the $\mathbf{S}$ matrix from the $\mathbf{R}$ matrix in

terms of the penetrabilities and shift functions (Eqs. 2.1 and 2.2). This expression can be greatly simplified by making several assumptions. First suppose that there are only *two* channels, the elastic and inelastic resonance where the mass is partitoned differently. We also assume that there is only one energy level in the unbound nucleus, i.e. a single pole e_p. Note that $\tilde{\mathbf{S}}_{\mathbf{12}} = \tilde{\mathbf{S}}_{\mathbf{21}}$, we obtain in this case:

$$\begin{aligned}\tilde{\mathbf{S}}_{\mathbf{12}} &= e^{i\phi_1}\left[\frac{2iP_\alpha^{1/2}\gamma_\alpha\gamma_{\alpha'}P_{\alpha'}^{1/2}}{(e_p-E)(1-aR_{11}L_1-aR_{22}L_2)}\right]e^{i\phi_2} \\ &= e^{i\phi_1}\left[\frac{2iP_\alpha^{1/2}\gamma_\alpha\gamma_{\alpha'}P_{\alpha'}^{1/2}}{e_p-E-\gamma_1^2(S_1-a\beta)-i\gamma_1^2P_1-\gamma_2^2(S_2-a\beta)-i\gamma_2^2P_2}\right]e^{i\phi_2}\end{aligned} \tag{2.3}$$

Define the formal width Γ_α:

$$\Gamma_\alpha = 2\gamma_\alpha^2 P_\alpha \tag{2.4}$$

As well as S_α^0, the energy shift Δ_α, and total energy shift Δ_T in addition to the total formal width Γ_T:

$$\begin{aligned}S_\alpha^0 &= S_\alpha - a\beta \\ \Delta_\alpha &= -\gamma_\alpha^2 S_\alpha^0 \\ \Delta_T &= \sum_\alpha \Delta_\alpha = -\gamma_1^2 S_1^0 - \gamma_2^2 S_2^0 \\ \Gamma_T &= \sum_\alpha = 2\gamma_1^2 P_1 + 2\gamma_2^2 P_2\end{aligned}$$

The value of $-a\beta$ can be set to any constant. Lane and Thomas [76] suggest using $-a\beta = S_\alpha(e_0)$. Substitution of these definitions into Eq. 2.3 reduces the form of $\widetilde{\mathbf{S}}_{\mathbf{12}}$ considerably.

It already begins to take on the shape of a Breit-Wigner distribution:

$$\tilde{\mathbf{S}}_{\mathbf{12}} = e^{i\phi_1}\left[\frac{i\Gamma_1^{1/2}\Gamma_2^{1/2}}{(e_p - E + \Delta_T) + i\Gamma_T/2}\right]e^{i\phi_2}$$

Recall that the cross-section is related to the symmetric $\mathbf{S}$ matrix by the following relation:

$$\sigma_{\alpha\alpha'}(E) = \frac{\pi}{k_i^2} g J_{tot} |\widetilde{\mathbf{S}}_{\alpha\alpha'}|^2$$

Where k_i is the wavenumber of the entrance channel and the spin weighting factor gJ_{tot} is:

$$gJ_{tot} \equiv \frac{2J_{tot}+1}{(2I_{p_i}+1)(2I_{t_i}+1)}$$

J_i is the total spin of the populated state and I_{p_i}, I_{t_i} are the spins of the projectile and target-like fragments respectively. Substitution of $\widetilde{\mathbf{S}}_{\mathbf{12}}$ into this expression yields:

$$\sigma_{12} = \frac{\pi}{k_i} g J_{tot} \frac{\Gamma_1\Gamma_2}{(E - e_p + \Delta_T)^2 + \Gamma_T^2/4} \tag{2.5}$$

We are only interested in describing the decay of an unbound state. It is assumed that the population mechanism is unimportant. Eq. 2.5 can be factored into two expressions:

$$\sigma_{12} = \left(\frac{\pi}{k_i} g J_{tot}\Gamma_1\right)\left(\frac{\Gamma_2}{(E - e_p + \Delta_T)^2 + \Gamma_T^2/4}\right)$$

The first describes the population of the unbound state which we are unconcerned with. We only wish to know the E dependence of σ for the unbound state, and so this term is treated as a constant. In addition, the probability to decay through the entrance channel is small,

$\Gamma_2 >> \Gamma_1$, thus $\Gamma_T \sim \Gamma_2$ and $\Delta_T \sim \Delta_2$. The lineshape for the neutron decay reduces to:

$$\sigma_l(E; e_p, \Gamma_0) \propto \frac{\Gamma_l(E; e_p; \Gamma_0)}{\left[e_p - E + \Delta_l(E; e_p, \Gamma_0)\right]^2 + \frac{1}{4}\left[\Gamma_l(E; e_p, \Gamma_0)\right]^2} \tag{2.6}$$

Here we have dropped the subscripts for the channels and explicitly state the angular momentum dependences. Γ_0, the width of the decay at e_p, is used as a substitute for the partial width γ^2 (Eq. 2.4):

$$\Gamma_0 = 2\gamma^2 P_l(e_p)$$

Equation 2.6 is used to define the probability distribution for the decay energy E_{decay} in simulation.

2.2 Two Neutron Decay

In two-body kinematics, the masses of the particles and the decay energy completely determine the system by conservation of energy and momentum. The addition of a third particle increases the number of degrees of freedom and adds complexity. The energies are no longer monochromatic, but E and P conservation still place kinematic boundaries on what momenta are possible, and all three particles are emitted in the same plane. In modelling the two-neutron decay of an unbound state three simple models are used: (1) A phase space decay, (2) a di-neutron model, and (3) a sequential decay. The choice of model determines the energy of each neutron as well as whether the decay proceeds as a true three-body breakup, or multiple two-body processes.

2.2.1 Phase space decay

The phase space model assumes no correlations between the outgoing particles by uniformly sampling the phase space of the invariant mass pairs m_{12}^2 and m_{23}^2 while applying kinematic constraints to conserve energy and momentum. This model is used as a baseline for simulating the detector response for observing no three-body correlations.

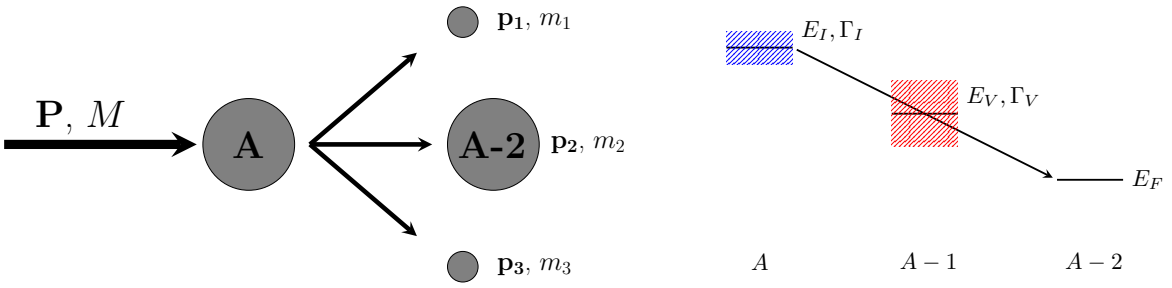

Figure 2.1: (Left) Schematic for phase-space breakup. (Right) A hypothetical level scheme where one would expect to observe a phase-space decay. E_I denotes the three-body energy, E_V the intermediate state, and $E_F = 0$, the final state. The hatched areas indicate widths. Note that the intermediate state is broad.

Consider the decay of a particle of mass M and momentum P into three products denoted by m_i, p_i, and energy E_i as illustrated in Fig. 2.1. Take $c = 1$, and define $p_{ij} = p_i + p_j$, and $m_{ij}^2 = p_{ij}^2$. Then we obtain the relations:

$$m_{12}^2 + m_{23}^2 + m_{13}^2 = M^2 + m_1^2 + m_2^2 + m_3^2$$

And

$$m_{12}^2 = (P - p_3)^2 = M^2 - 2ME_3 + m_3^2$$

Where E_3 is the energy of the third particle in the rest frame of M. In this frame all particles lie within a plane and their relative orientation can be fixed if their energies are

known. Define the quantities:

$$E_2^* = \frac{(m_{12}^2 - m_1^2 + m_2^2)}{2m_{12}}$$

$$E_3^* = \frac{(M^2 - m_{12}^2 - m_3^2)}{2m_{12}}$$

For a given value of m_{12}^2, m_{23}^2 is maximum or minimum when p_2 is parallel or anti-parallel to p_3. Setting $\vec{p_2} = \pm\vec{p_3}$ we obtain the limits:

$$(m_{23}^2)_{max} = (E_2^* + E_3^*)^2 - \left(\sqrt{E_2^{*2} - m_2^2} - \sqrt{E_3^{*2} - m_3^2}\right)^2$$

$$(m_{23}^2)_{min} = (E_2^* + E_3^*)^2 - \left(\sqrt{E_2^{*2} - m_2^2} + \sqrt{E_3^{*2} - m_3^2}\right)^2$$

The phase-space mechanism can then be simulated by uniformly sampling m_{12}^2 and m_{23}^2 under the constraint that $(m_{23}^2)_{min} < m_{23}^2 < (m_{23}^2)_{max}$. The energy and momenta of all three particles is then completely determined since $p^2 = E^2 - m^2$:

$$E_1 = (M^2 + m_1^2 - m_{23}^2)/2M$$

$$E_2 = (M^2 + m_2^2 - m_{13}^2)/2M$$

$$E_3 = (M^2 + m_3^2 - m_{12}^2)/2M$$

As well as their relative angles:

$$cos(\theta_{ij}) = \frac{m_i^2 + m_j^2 + 2E_iE_j - m_{ij}^2}{2|p_i||p_j|}$$

If we now take M to be the mass of a three-body system consisting of a core and two-neutrons, we can add the decay energy E_{decay} to this system and distribute it amongst the daughter products $A-2$, n, and n. In this case, the three-body resonant lineshape for the decay is taken to be an energy dependent Breit-Wigner, Eq. 2.6, and the energy is distributed according to the above relations. For more than three products, a recursive relation can be used to determine the momenta of the ith particle.

2.2.2 Sequential decay

The sequential model used in this analysis is based on the work of A. Volya [77, 78], which uses the formalism of the Continuum Shell Model. Additional details beyond this outline can be found in Ref. [77].

The sequential decay mechanism consists of multiple two-body processes. Consider a level scheme like that in Figure 2.2. A nucleus with mass A has an unbound three-body state with central energy E_1 and width Γ_1 relative to the ground state of the isotope with mass $A-2$. The intermediate nucleus has a state defined with an energy E_2 and and a width Γ_2 sufficiently narrow that its life-time is long enough to form the intermediate state. Let ϵ_1 be the kinetic energy of the first neutron, and ϵ_2 the energy of the second. Note that $\epsilon_{1,2}$ are distributions and correspond to the decay energies in each step of the sequential mechanism and are not necessarily equal to the energy difference between E_1 and E_2. Let $E = \epsilon_1 + \epsilon_2$, denote an arbitrary three-body energy – distinct from E_1 which is the centroid of the intial state. For simplicity take $E_3 = 0$.

In this formalism, a distribution for the relative energy of the two neutrons $E_r = \epsilon_1 - \epsilon_2$ is calculated as a function of the total decay energy E. The first neutron, with kinetic energy ϵ_1 decays from an initial state E_1 to an intermediate unbound state E_2, which also decays

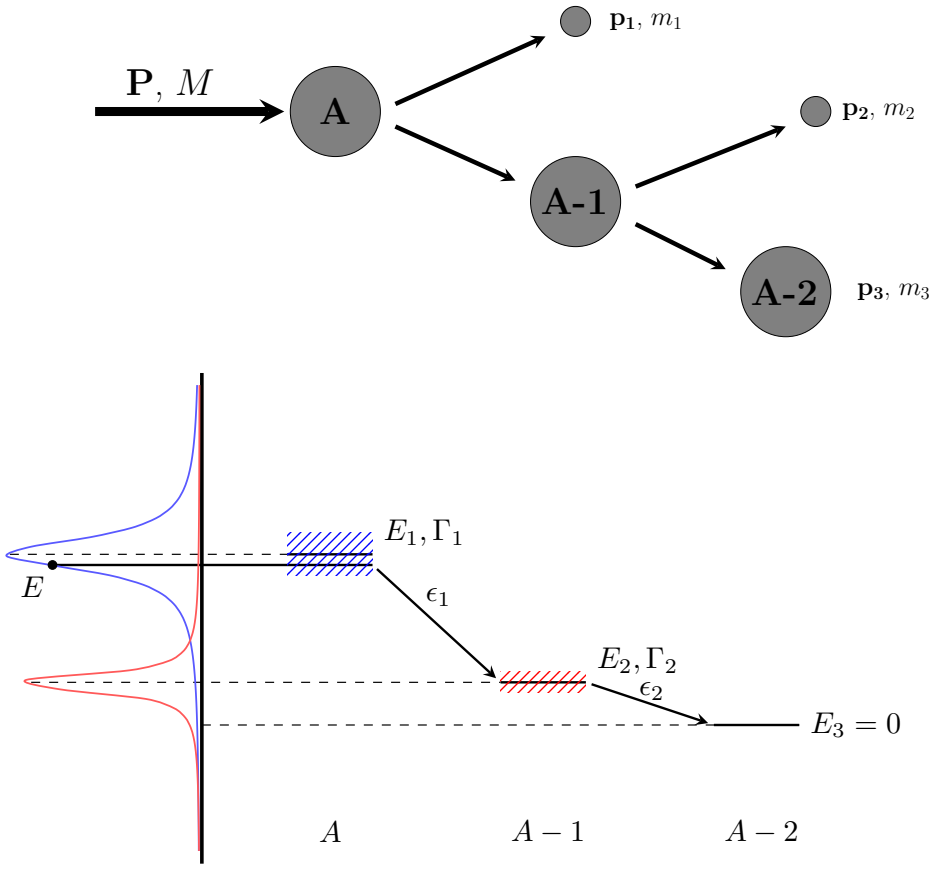

Figure 2.2: (Top) Schematic for a sequential decay. (Bottom) A hypothetical level scheme where one would expect to observe a sequential decay. The hatched areas indicate widths. Note that the intermediate state is narrow and well separated from E_1.

emitting another neutron with kinetic energy ϵ_2. Assuming a spin anti-symmetric pair of neutrons, the total amplitude for the decay becomes:

$$A_T(\epsilon_1, \epsilon_2) = \frac{1}{\sqrt{2}} \left(\frac{A_1(\epsilon_1)A_2(\epsilon_2)}{(\epsilon_2 - (E_2 - \frac{i}{2}\Gamma_2(\epsilon_2))} + \frac{A_1(\epsilon_2)A_2(\epsilon_1)}{(\epsilon_1 - (E_2 - \frac{i}{2}\Gamma_2(\epsilon_1))} \right) \tag{2.7}$$

Where A_1 and A_2 are the single-particle decay amplitudes.

Recall that the three-body energy is $E = \epsilon_1 + \epsilon_2$. We introduce $S = E_2 - E$, the difference between the intermediate state and the three-body energy. If $S > 0$, then the level structure is like that illustrated in Fig. 2.3. For $S < 0$, the intermediate state is not

classically forbidden and we have a heirarchy like that illustrated Fig. 2.2. Eq. 2.7 can now be rewritten as:

$$A_T(\epsilon_1,\epsilon_2) = \frac{1}{\sqrt{2}}\frac{A_1(\epsilon_1)A_2(\epsilon_2)[S+\epsilon_2-\frac{i}{2}\Gamma_2(\epsilon_1)] + A_1(\epsilon_1)A_2(\epsilon_2)[S+\epsilon_1-\frac{i}{2}\Gamma_2(\epsilon_2)]}{[S+\epsilon_1-\frac{i}{2}\Gamma_2(\epsilon_2)][S+\epsilon_2-\frac{i}{2}\Gamma_2(\epsilon_1)]} \quad (2.8)$$

The single particle decay amplitudes are related to their widths by the following relation:

$$\Gamma_i = 2\pi|A_i(\epsilon)|^2$$

Which can be equated with the single-particle decay width $\gamma_l(\epsilon)$ multiplied by a spectroscopic factor S_i:

$$\Gamma_i = 2\pi|A_i(\epsilon)|^2 = \gamma_l(\epsilon)S_i$$

The single-particle width can be estimated for a neutron in a square well using the expression derrived in Bohr-Mottleson Vol. I [79]:

$$\gamma_l = \frac{2\hbar^2}{\mu R}(kR)\left|\frac{2l-1}{2l+1}\right| T_l(kR)$$

Here $T_l(x)$ is the tranmission probability through the centrifugal barrier. For s and p waves, $T_0 = 1$ and $T_1 = x^2/(1+x^2)$. $R \sim 1.3(A+1)^{1/3}$ is the nuclear radius in fm, and $k = \sqrt{2\mu\epsilon}$. μ is the reduced mass and ϵ the incident neutron energy. To get to a decay rate and a cross section, we need to utilize the Fermi Golden Rule which gives the partial decay width as:

$$\frac{d\Gamma(E)}{d\epsilon_1 d\epsilon_2} = 2\pi\delta(E-\epsilon_1-\epsilon_2)|A_T(\epsilon_1,\epsilon_2)|^2 \quad (2.9)$$

Putting the decay amplitudes in terms of the single-particle widths and applying Fermi's Rule 2.9, we obtain the following expression for the differential width in terms of the relative energy $E_r = \epsilon_1 - \epsilon_2$:

$$\frac{d\Gamma(E)}{dE_r} = \frac{1}{8\pi}\gamma_l(\epsilon_1)\gamma_l(\epsilon_2)\left[\frac{E + 2S - \frac{i}{2}[\Gamma_2(\epsilon_1) + \Gamma_2(\epsilon_2)]}{[S + \epsilon_1 - \frac{i}{2}\Gamma_2(\epsilon_2)][S + \epsilon_2 - \frac{i}{2}\Gamma_2(\epsilon_1)]}\right]^2$$

The cross-section then follows the familiar Breit-Wigner form with the differential written in terms of the relative energy:

$$\frac{d\sigma}{dE_r} \propto \frac{1}{(E - E_1)^2 + \Gamma_T^2(E)/4}\frac{d\Gamma(E)}{dE_r}$$

Where the total width $\Gamma_T(E)$ is obtained from:

$$\Gamma_T = \int dE_r \frac{d\Gamma(E)}{dE_r}$$

In this manner, the relative energy distributions for the two neutrons are calculated depending on the energy and widths of the states involved. Once the distribution for each neutron is calculated, the process is treated as two two-body decays. In cases where $S > 0$, the intermediate state is higher in energy than the three-body state and the decay proceeds through it's width.

It should be noted, that this formalism assumes that the two neutrons come from the same single-particle orbital and are coupled to $J^\pi = 0^+$. In addition, although the Breit-Wigner lineshape for the relative energies depends on the ℓ value of the three-body and intermediate state, the angular distributions of the neutrons are assummed to be isotropic in the rest frame of each two-body decay.

2.2.3 Di-neutron decay

The di-neutron model used in this analysis is also based on the work of A. Volya [77, 78]. In this model the di-neutron cluster breaks away from the core before decaying into two separate neutrons.

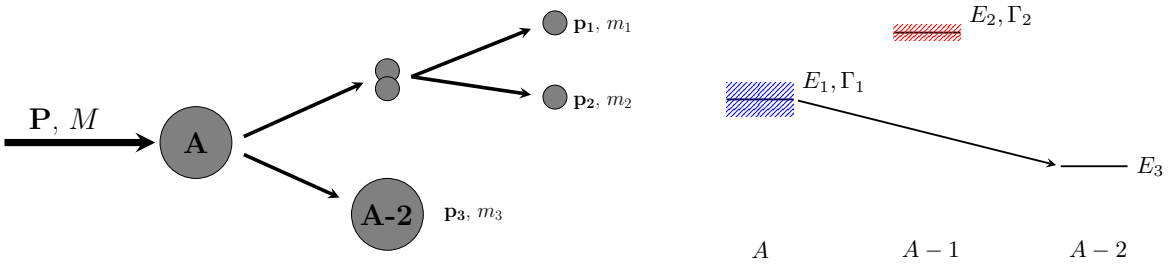

Figure 2.3: (Left) Schematic for dineutron emission. (Right) A hypothetical level scheme where one would expect to observe a dineutron. The hatched areas indicate widths.

Let the dineutron have mass $m_D = 2m$, and reduced mass $\mu = m/2$. Define ϵ_K as the kinetic energy of the dineutron. Let ϵ_I be the intrinsic energy of the dineutron - or neutron-neutron energy, and E_2 be the energy of the "intermediate state" which may be classically forbidden. The total three-body energy is denoted by $E_1 = \epsilon_K + \epsilon_I$. For simplicity take $E_3 = 0$. The decay is treated as a two-step process where the dineutron first separates from the core and then decays into two neutrons. The amplitude for the decay is given by:

$$A_T(\epsilon_K, \epsilon_I) = \frac{A_1(\epsilon_K)A_2(\epsilon_I)}{\epsilon_I - (E_2 - \frac{i}{2}\Gamma_2(\epsilon_I))}$$

Where, A_1 is the amplitude for the di-neutron emission and A_2 is the amplitude for the di-neutron breakup. Substituting this expression into Fermi's Golden Rule 2.9, we obtain the following for the differential width:

$$\frac{d\Gamma}{d\epsilon_K d\epsilon_I} = \frac{1}{2\pi}\delta(E_1 - \epsilon_K - \epsilon_I)\frac{\Gamma_1(\epsilon_K)\Gamma_2(\epsilon_I)}{[(\epsilon_I - E_2)^2 + \Gamma_2^2(\epsilon_I)/4]} \tag{2.10}$$

Next, it is assumed that both the emission of the dineutron, and the subsequent breakup, can be parameterized as an s-wave decay. In this case, the decay width for $\Gamma_2(\epsilon_I)$ becomes:

$$\Gamma_2(\epsilon_I) = \frac{2\hbar^2}{\mu r_0} k_I$$

Where μ is the reduced mass of the dineutron and r_0 is the channel radius, approximated as $r_0 = 1.4(2^{1/3}) \sim 1.7$ fm. Likewise, the decay width for $\Gamma_1(\epsilon_K)$ becomes:

$$\Gamma_1(\epsilon_K) = \frac{2\hbar^2}{m_D R} k_K$$

Here m_D is the mass of the dineutron, and the channel radius R includes the size of the core, $R = 1.4[(A-2)^{1/3} + 2^{1/3}]$. To determine the intermediate energy E_2, or virtual state, we require consistency with the effective range approximation. Recall that in the s-wave decay the decay width is proportional to $\sqrt{\epsilon_I}$. As $\epsilon_I \to 0$ the denominator of the scattering amplitude A_T must behave like $1/a_s + ik_I$ where a_s is the $n-n$ scattering length, [78] (Note: $\hbar^2/\mu r_0 = \Gamma_2/2k_I$) thus:

$$\begin{aligned} \lim_{\epsilon_I \to 0} \left[\epsilon_I - \left(E_2 - \frac{i}{2}\Gamma_2(\epsilon_I) \right) \right] &= \frac{\hbar^2}{\mu r_0} \left(\frac{1}{a_s} + ik_I \right) \\ -E_2 + \cancel{\frac{i}{2}\Gamma_2(\epsilon_I)} &= \frac{\Gamma_2(\epsilon_I)}{2k_I} \left(\frac{1}{a_s} + \cancel{ik_I} \right) \\ E_2 &= -\frac{\Gamma_2(\epsilon_I)}{2k_I a_s} \end{aligned} \tag{2.11}$$

Substituting $\Gamma_2(\epsilon_I) = \frac{2\hbar^2}{\mu r_0} k_I$, it follows that:

$$E_2 = -\frac{\hbar^2}{\mu r_0 a_s}$$

For a given scattering length, we can associate an energy:

$$\epsilon_0 = \frac{\hbar^2}{2\mu a_s^2}$$

So we may write:

$$E_2 = -\epsilon_0 \frac{2a_s}{r_0}$$

Recall that ϵ_I and ϵ_K are defined as the following:

$$\epsilon_K = \frac{\hbar^2 k_K^2}{2m_D}$$

$$\epsilon_I = \frac{\hbar^2 k_I^2}{2\mu}$$

And we may express the widths as:

$$\Gamma_1(\epsilon_K) = 2\frac{|a_s|}{R}\sqrt{\epsilon_0 \epsilon_K}$$

$$\Gamma_2(\epsilon_I) = 4\frac{|as|}{r_0}\sqrt{\epsilon_0 \epsilon_I}$$

Setting the masses to $\mu = m/2$ and $m_D = 2m$, substituting the widths into Eq. 2.10 and integrating over ϵ_K we obtain:

$$\frac{d\Gamma(E_1)}{d\epsilon_1} = \frac{1}{\pi}\frac{\sqrt{(E_1 - \epsilon_I)\epsilon_I}}{\left(1 + \frac{r_0}{2a_s}\frac{\epsilon_I}{\epsilon_0}\right)^2 \epsilon_0 + \epsilon_I}\frac{r_0}{R} \tag{2.12}$$

Which defines the distribution for the intrinsic energy of the dineutron. We can make an approximation if $\epsilon_I << |2a_s\epsilon_0/r_0|$. The n-n scattering length is $a_s = -18.7$ fm [80]. Using $r_0 \sim 1.7$ fm, and $\epsilon_0 \sim 0.15$ MeV gives us $\epsilon_I << 3$ MeV. In this regime, we can approximate

the integral of Eq. 2.12 with the expression:

$$\Gamma(E_1) = \frac{r_0}{R}\left(\frac{E_1}{2} + \epsilon_0 - \sqrt{\epsilon_0(\epsilon_0 + E_1)}\right)$$

However, integration of Eq. 2.12 is still performed numerically in simulation to determine the energy distributions of the dineutron and its intrinsic energy.

Chapter 3

Experimental Technique

3.1 Experimental Setup

This section gives an overview of the experimental setup at the National Superconducting Cyclotron Laboratory (NSCL) using the Modular Neutron Array (MoNA), the Large-area multi-Institutional Scintillator Array (LISA), and the Sweeper magnet. The overall setup is described here while the details of each detector are discussed in the following sections.

The experiment was performed at the NSCL, where a 140 MeV/u ^{48}Ca beam impinged upon a 1363 mg/cm^2 ^{9}Be target to produce an ^{24}O beam at 83.3 MeV/u with a purity of $\sim$ 30%. The A1900 fragment separator was used to select the ^{24}O beam from the other fragments in the secondary beam. The ^{24}O beam continued on to the experimental area where it impinged upon the Ursinus College Liquid Hydrogen Target [81], which was filled with liquid deuterium (LD_2). The average beam rate was approximately 30 particles per second.

After the beam reacted in the target the resulting charged fragments were swept 43.3° by a 4-Tm superconducting sweeper magnet [82] into a series of position and energy-sensitive charged particle detectors. Inside the sweeper focal plane were two cathode-readout drift chambers (CRDCs), separated by 1.55 m, an ion-chamber, a thin timing scintillator, and an array of CsI(Na) crystals called the hodoscope. Fig. 3.1 shows a diagram of the experimental setup.

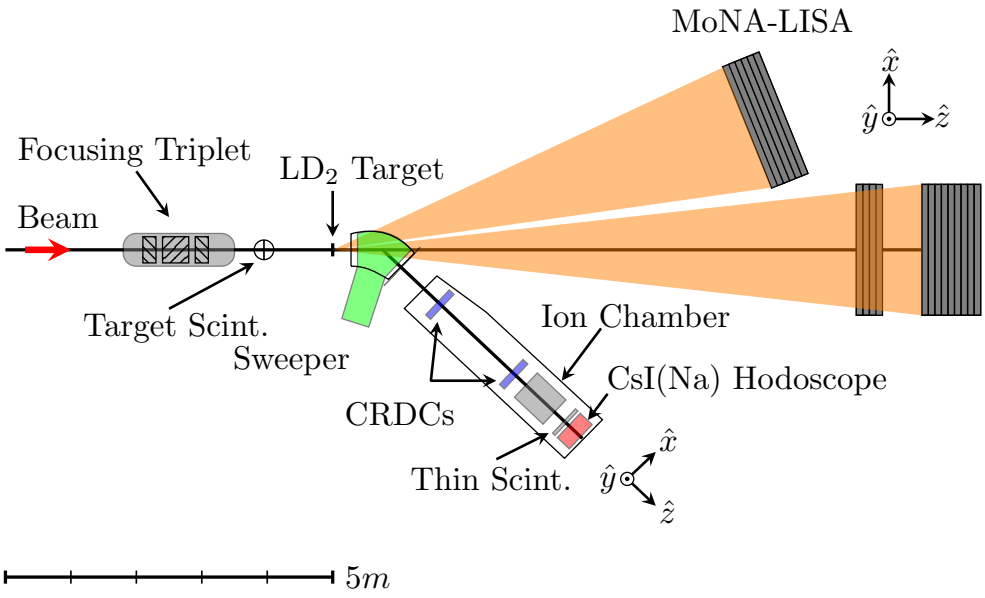

Figure 3.1: Layout of the detectors in the N2 Vault.

The neutrons produced from the decay of unbound states traveled undisturbed 8m towards MoNA and LISA [83]. MoNA and LISA each contain 9 vertical layers with 16 bars per layer and the combined array was configured into three blocks of detector bars. LISA was split into two tables 4 and 5 layers thick, with the 4 layer table placed at 0° in front of MoNA, while the remaining portion of LISA was placed off-axis centered at 22°. The resulting angular coverage in the lab frome was from $0° \leq \theta \leq 10°$ for the detectors placed at 0°, and $15° \leq \theta \leq 32°$ for the off-axis portion.

Together, MoNA-LISA and the sweeper magnet provide a kinematically complete measurement of the neutrons and the charged particles from which the decays of unbound states can be reconstructed. With the full 4-vector information of each particle, three-body correlations can also be examined in cases where nuclei decay by emission of two-neutrons.

3.2 Beam Production (K500, K1200)

An ^{24}O beam was provided by the Coupled Cyclotron Facility (CCF) [84] and A1900 Fragment Separator at the NSCL [85]. The facility provides intense heavy ion beams, both stable and unstable via fast fragmentation [86]. Since ^{24}O has a half-life of 64 ms [87] it cannot be accelerated directly. A diagram of the beam production process is shown in Figure 3.2.

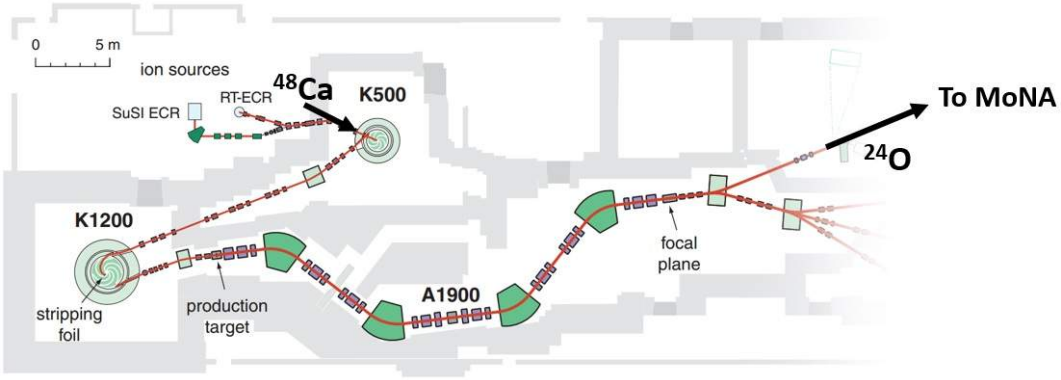

Figure 3.2: Beam production at the Coupled Cyclotron Facility [84]. ^{48}Ca is heated up in an ion-source and accelerated by the K500 and K1200 cyclotrons. After impinging on a Be target, the fragments are filtered by the A1900 to provide the desired beam.

A beam of stable ^{48}Ca was first accelerated to 140 MeV/u in the coupled K500 and K1200 cyclotrons. After emerging from the K1200, the beam impinged upon a 1363 mg/cm^2 ^{9}Be target where the fragmentation process occured. A wide variety of nuclei are made simultaneously by this process. In order to isolate the ^{24}O beam the A1900 separator was used. The A1900 has four dipoles with focusing elements inbetween, to filter the fragmentation products by their rigidty $B\rho = p/q$ to select a specific momentum to charge ratio. An achromatic aluminum wedge with thickness 1050 mg/cm^2 was placed inbetween the second and third dipoles to improve separation. The energy loss through the wedge is proportional to square of the nuclear charge, Z^2. Hence different elements with the same rigidity entering the wedge will have different rigidities upon exit. The ^{24}O was delivered to the experimental

vault with an energy of 83.4 MeV/u corresponding to a rigidity of 4.0344 Tm at a rate of $\sim$ 0.6 pps/pnA. The largest contaminant was ^{27}Ne which arrived with the same rigidity at an energy of 122.4 MeV/u. In addition to the ^{24}O beam, an ^{20}O beam of much higher intensity ($\sim$ 700 pps/pnA) was also provided for calibration and diagnostics.

3.3 A1900 & Target Scintillator

At the end of the A1900 is a plastic timing scintillator located 10.579 m upstream from the liquid deuterium (LD_2) target in the N2 vault. It is made of 0.125 mm thick BC-404 and is optically coupled to a PMT. The target scintillator, also made of BC-404, is 0.254mm thick and was placed 1.0492 m upstream from the LD_2 target and was coupled to a PMT. When a particle passes through the plastic, it creates electron-hole pairs that recombine emitting photons. These photons are then collected in the PMTs and converted to an electronic signal. The signals from these detectors can be used to help separate beam contaminants by time-of-flight measurement. In addition to the timing scintillators, the cyclotron radio-frequency (RF) is also recorded to provide additional separation.

3.4 Liquid Deuterium (LD_2) Target

This experiment opted to use a cryogenic deuterium target over deuterated plastics such as CD_2 for two main reasons: (1) a reduced carbon background, and (2) it provides higher density of D_2 for the same overall target thickness. The Ursinus-NSCL Liquid Hydrogen/Deuterium Target (LD_2) offers a high-density, low-background deuteron target for a variety of experiments including elastic scattering, secondary fragmentation, charge exchange, and nucleon transfer. The basic principle of the LD_2 target is simple: fill a volume with D_2

gas and cool it so the liquid collects at the bottom of a target cell. The LD_2 target consists of five main components, described in the following sub-sections:

1.) Target Cell: Holds the liquid deuterium. Cylindrical in shape.

2.) Refrigerator System: A Sumitomo 205D Cryocooler.

3.) Vacuum Chamber: Houses the target cell, cold finger, refrigerator and heat shield.

4.) Temperature Control System: Monitors the temperature of the target cell and regulates the temperature of the heater block.

5.) Gas handling system: Regulates the flow of neon, hydrogen or deuterium to the refrigerator.

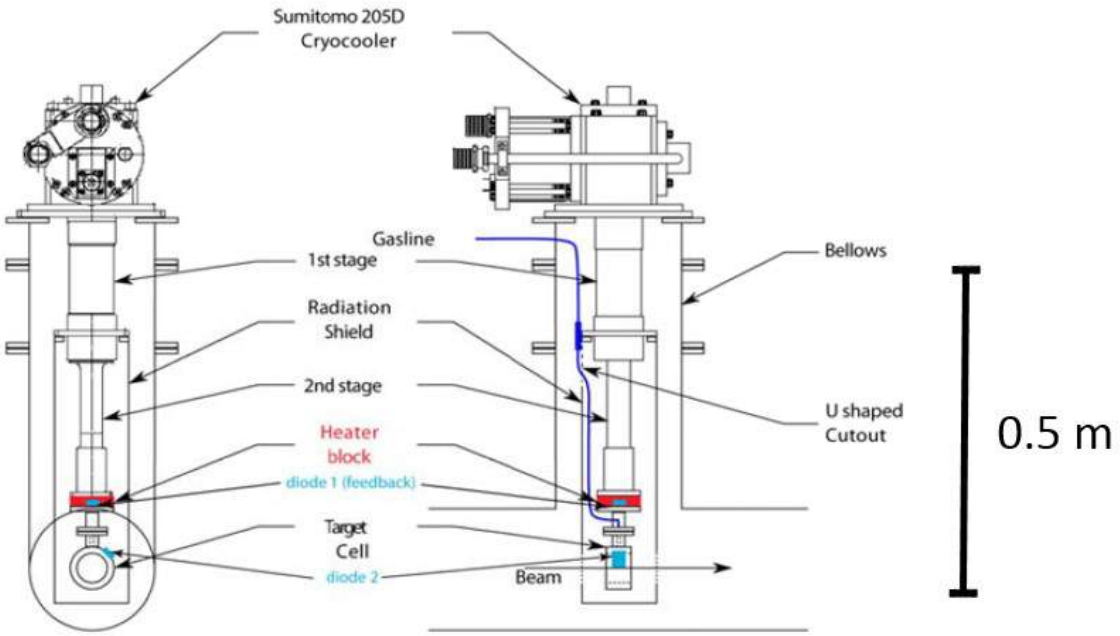

Figure 3.3: Schematic of the Ursinus College Liquid Hydrogen Target. (Left) A head on view along the beam axis. (Right) Side view.

Gas	Boiling Point	Triple Point
Hydrgoen	(20.35 K, 760 Torr)	(13.85 K, 54 Torr)
Deuterium	(23.50 K, 760 Torr)	(18.70 K, 128 Torr)
Neon	(27.07 K, 760 Torr)	(24.56 K, 323 Torr)

Table 3.1: Boiling and triple points of hydrogen, deuterium, and neon.

Including the resevoir in the gas handling system, a total of 100 L of hydrogen or deuterium at STP is contained in the entire apparatus. The target operates by filling the target cell with an appropriate amount of gas and cooling it to near the triple point, where the gas condenses to the liquid state. Table 3.1 documents the triple points for neon, hydrogen, and deuterium. For deuterium, the triple point is at approximately 18.7 K and 128 Torr. During operation, the target was held at roughly 20 K and ∼850 torr. This lies in the window between the solid-liquid, and liquid-gas phase transitions of D_2 as seen in Fig. 3.4.

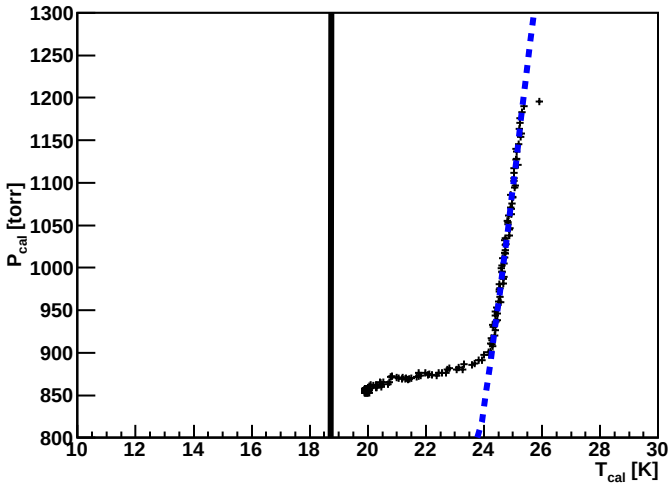

Figure 3.4: Phase diagram for deuterium. The solid line marks the liquid/solid transition, while the blue dotted line denotes the liquid/gas transition. The plus marks are data obtained during the initial filling of the target.

As seen by the schematic of the target in Fig 3.3, the deuterium fills the entire volume of the gas line which is connected to the target cell resting in the beam path. The cryocooler, which sits on top, cools the deuterium gas until it condenses and drips down the gas line

into the target cell. However, since the cooler is operated by a closed liquid He cycle, it will cool the D_2 to 4 K, which would cause the liquid to freeze and clog the gas line. For this reason the target cell is coupled to a heater block which counter-acts the cryocooler to maintain the temperature of the liquid at a desired point. The temperature is read out by two silicon diodes, one attached to the target cell, and another attached to the heater block. The pressure is read out by a monometer in the gas handling system, which is connected to the target cell line.

3.4.1 Target Cell

The target cell is cylindrical with a diameter of 5.4 cm and a length of about 3.0 cm, and consists of an aluminum frame with Kapton windows 125 μm thick on both ends. It is designed to hold the liquid deuterium in place. For the cell used in this experiment, the design thickness for deuterium was 400 mg/cm^2, or 200 mg/cm^2 for hydrogen. The cell couples to a commercial refrigerator, and has a diode attached to the frame for reading out the temperature. A photo of the cell along side a mechanical drawing can be found in Fig. 3.5

The cell is designed to withstand an outward pressure gradient of about 2 atm as it sits in a vacuum. When the target cell is filled, the kapton foils bulge outward increasing the actual thickness of the deuterium. The cell is surrounded by a heat shield to reduce the thermal load and enable cooling from room temperature to the triple point. To ensure temperature stability during the experiment, the openings in the heat shield were covered with 5 μm thick aluminized reflective mylar film.

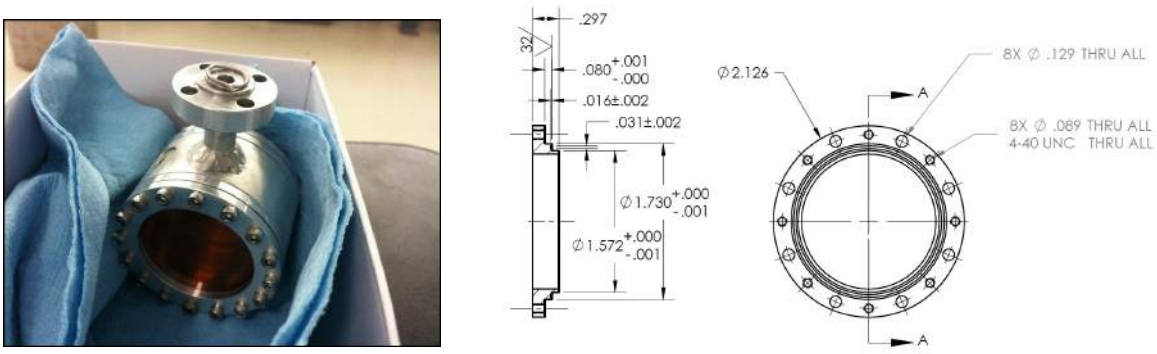

Figure 3.5: (Left) Photo of the target cell used to contain the Liquid Deuterium. The liquid drips down through the center hole seen on the target flange. The iridium seal can be seen surrounding it before being pressed. (Right) Drawing of the inner ring where the Kapton foil is glued. The ring is then clamped to the target by an outer ring visible in the left photo.

3.4.2 Temperature Control System

The temperature of the target cell is regulated by the heater block. Since the target cell sits in a vacuum during operation, heat can only be transfered by thermal radiation or conduction. The heater block is controlled by a Lakeshore 331S temperature controller unit which is operatated manually by a PC running LabView. The Lakeshore 331S controller reports the diode temperature as a voltage which is then read out by the Experimental Physics and Industrial Control System (EPICS) [88] and later converted to Kelvin. Details of the LabView programming and operation of the temperature control system can be found in the Liquid Deuterium Target users manual [89].

The temperature controller unit relies on a feedback loop to maintain a desired equillibrium. Because the heater block is not in direct contact with the target cell, there is thermal lag between it and the target cell. The time it takes for the heater block to affect the cell is too long to use the diode at the target cell in a feedback loop. Instead the temperature of the cell must be monitored, and controlled from a separate diode attached to the heater block. This often means that the "set point", or desired temperature, of the heater block

is different from the desired temperature in the cell. However, during liqufication, the cell temperature is closely monitored to determine an appropriate set point.

3.4.3 Gas Handling System

The gas handling system controls the flow of air, deuterium and dry nitrogen when evacuating and filling the target. It is designed with safety as a priority, and its purpose is to regulate the flow of these gases to insure that the mixture of deuterium and nitrogen/air stays well below the flammabilty limit, and that there is never an over-pressure on the target cell which may cause it to implode. A schematic of the gas handling system is shown in Fig. 3.6. Table 3.2 describes each of the components. The full operation of this system and the LD_2 target is describted in the LHDT Users Manual [89]. The target pressure is read out by a manometer attached to the target cell line. This manometer reports a voltage which is then read out by EPICS.

3.4.4 Vacuum Chamber

The vacuum chamber holds the target assembly in the beam line and interfaces with the existing beam-line structure. It was connected directly to the flange of the sweeper magnet, and to the target-scintillator. Due to the height of the target, and the geometry of the sweeper magnet, the entire target had to operated at a 30° angle. This resulted in only a portion of the target cell being filled. However the target itself was much larger than the beam-spot, ensuring that the tilt had no effect.

The bellows beneath the cryocooler, illustrated in Fig. 3.3, allow for adjusting the target cell position in the beam line. Using a laser alignment, the cell was centered on the beam-

Component	Function
Target Cell	Cell containing LH_2 or LD_2.
Reservoir	100 L tank which serves as H_2 or D_2 reservoir.
H_2	Pressurized gas bottle with H_2 or D_2.
T (B141TP)/ B141GV	Turbo-pump / Turbo gate valve.
P	Pascal C2 series 2015 C2 rotary pump.
$V_{1,3,4,5,10}$	Manual valves.
V_2	Needle valve.
$V_{6,7}$	Manual needle valves on flowmeter F_1 and F_2.
V_8 (B141FV)	Fore valve.
V_{11} (B141VV)	Venting valve.
F_1	Flowmeter for H_2/D_2 gas (always open).
F_2	Flowmeter for dry nitrogen (always open).
R_1	Regulator for gas bottle.
$M_{1,3}$	Manometers with a range of 1 - 5000 Torr.
	M_1 reads the cell pressure, and M_3 the pressure in the reservoir.
M_2	Manometer for the gas cell with a range of 0.001 - 1 Torr.
M_4 (B142PG)	Pirani gauge and ion gauge for beam-chamber vacuum.
N2 Exhaust Line	Exhaust line for discharging the H_2/D_2 gas.
Dry Nitrogen (DN)	Dry Nitrogen Supply.
Dry Nitrogen/Vent	Vent line for the target system with dry nitrogen.

Table 3.2: List of components in the gas handling system. Table adopted from Ref. [89].

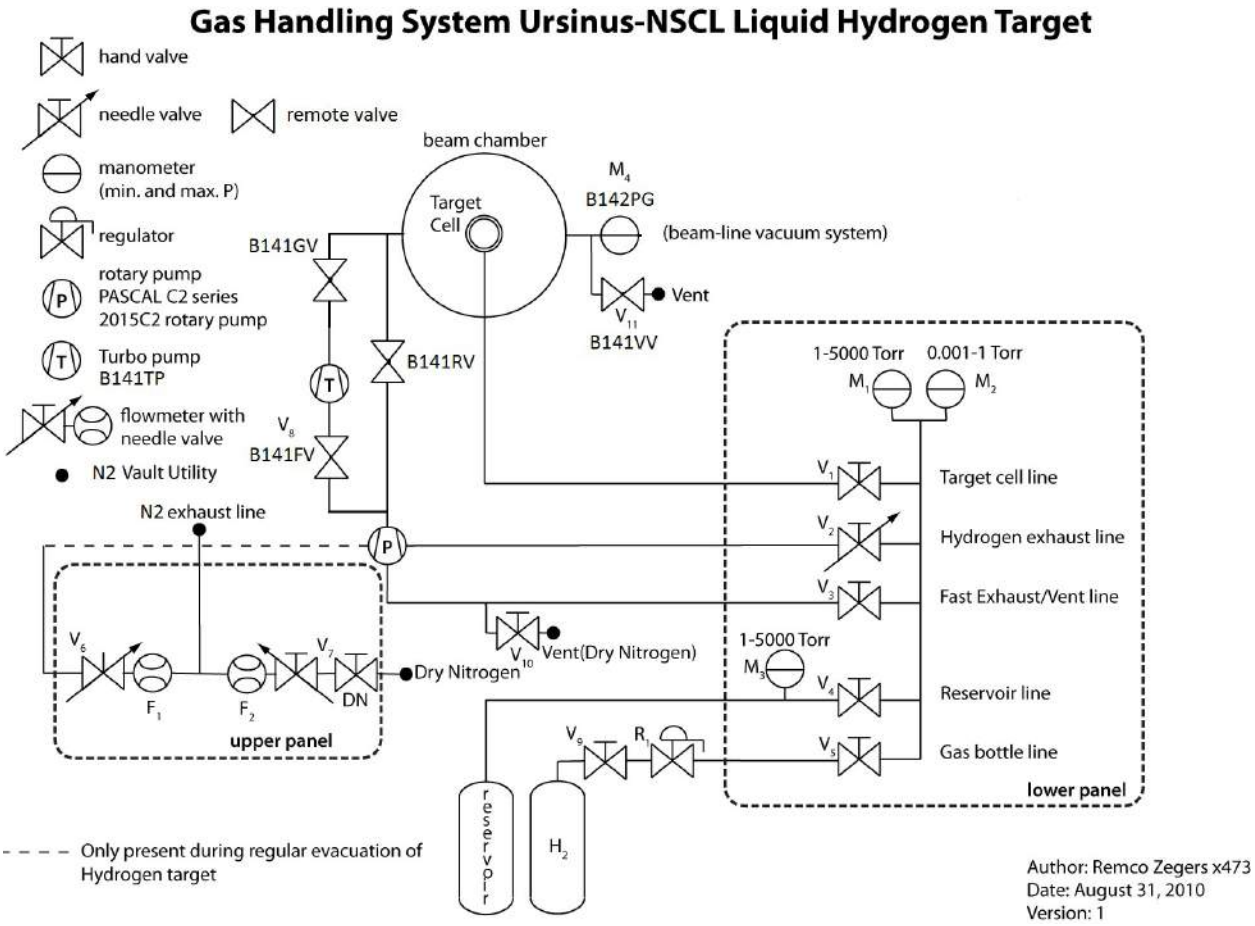

Figure 3.6: A diagram of the gas handling system used to control the flow of deuterium in and out of the target cell. Figure adopted from [89]

axis and the foils were aligned perpendicular to the beam by lining up the reflection of the laser off the back of the second foil with the impinging beam-spot.

3.5 Sweeper Magnet

The sweeper magnet is a large-gap superconducting dipole magnet with a bending angle of 43.3° and a radius of 1 meter [82]. It's purpose is to sweep charged particles and unreacted beam away from MoNA-LISA and towards a suite of charged-particle detectors described in the following sections. The charged reaction products exiting the target are swept away while

the neutrons continue straight through a vertical gap of 14 cm towards MoNA-LISA. The maximum rigidity of the sweeper is 4 Tm. The magnetic field in the sweeper is monitered with a Hall probe and the dipole field has been mapped in previous work [90]. For reactions with the ^{24}O beam, the magnet was set to a current of 320 A, corresponding to a central rigidity of 3.524 Tm. To measure the background induced by the kapton foils of the target, as well as diagnose the sweeper, the LD_2 target was put in a gaseous state by warming it to 50 K. This reduces the thickness of the deuterium to ~ 1 mg/cm^2. For the settings with the warm gaseous target, the current was raised to 360 A to account for the more rigid beam. The central rigidity on those setting was 3.85 Tm.

3.6 Charged Particle Detectors

Immediately following the sweeper magnet was a collection of charged particle detectors residing in a vacuum box. The position of the reaction products deflected by the magnet was measured with two Cathode Readout Drift Chambers (CRDCs) separated by 1.55 m. Following the CRDCs was an ion-chamber which provided a measurement of energy loss, and a thin (5 mm) dE plastic scintillator which triggered the system readout and gave a time-of-flight measurement. Finally, an array of CsI(Na) detectors consisting of 25 crystals, each 80 x 80 x 25 mm^3 was installed behind the thin scintillator and stopped the fragments while measuring their total energy.

3.6.1 CRDCs

The first CRDC was placed approximately 1.56 m from the target, where the distance is measured along the central track of the dipole, and the second CRDC was placed 1.55 m

downstream of the first. The CRDCs measure the X and Y position, from which the angle of the particles can be determined and their path traced backward to the target. A schematic of the detector can be found in Figure 3.7.

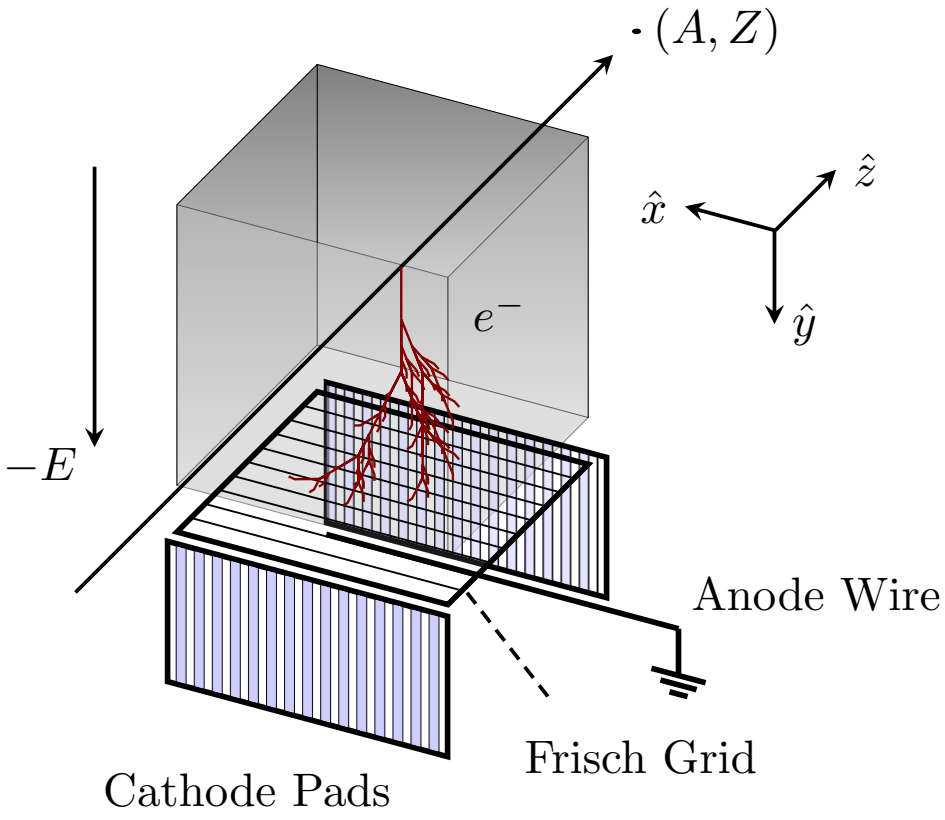

Figure 3.7: Schematic of a Cathode Readout Drift Chamber (CRDC) where the z-direction has been expanded. The field shaping wires are not drawn for visibility. Note that the electron avalance is does not begin until the electrons encounter the Frisch grid.

The CRDC is similar to an ion-chamber. It is filled with a 1:4 mixture of isobutane and CF_4 gas at a pressure of 40 torr and sealed with two windows. When a particle passes through the gas it creates ionization pairs which drift apart due to a uniform applied electric field. This field is created by the application of a drift voltage of 1000 V between a plate at the top of the detector, and a Frish grid near the bottom of the detector. Field shaping wires are placed at specific intervals along each face of the detector parrallel with the X direction.

Under the Frisch grid is an anode wire (parallel with the X direction) and a collection of 116 aluminum cathode pads with a pitch of 2.54 mm in width segmented along the X direction.

When electrons drift into the Frisch grid they enter a strong electric field created by the anode wire causing an avalanche of electrons. The Y-position of the interaction is determined by the drift time of the electron, which is defined as the difference between a signal in the thin timing scintillator and a signal on the anode wire. The X-position is determed from the induced charge distribution on the cathode pad caused by an avalanche of electrons. The peak of this distribution gives the X-position of the particle. The Z-position is assumed to be the center of the detecting volume along the beam axis since there is no segmentation in this direction. The active area of each CRDC is 30 x 30 cm^2 in the XY plane.

3.6.2 Ion Chamber

The ion-chamber is a gas-filled detector similar to the CRDCs but segmented in the Z-direction with 16 pads. The active volume of the detector is 40 x 40 x 65 cm^3. The ion-chamber is filled with P-10 gas (10% CH4 and 90% Ar_2) and held at 300 torr. The windows are made of Kevlar filament and 12 μm PPTA and are mounted with epoxy. They allow particles to pass through with neglible energy loss. The upstream window has an active area of 30 x 30 cm^2 to match the acceptance of the CRDC, while the downstream window is 40 x 40 cm^2 to allow for dispersion of the beam.

The ion-chamber has a plate on top and 16 charge collecting pads on the bottom biased to create a drift voltage of 800 V. When a charged particle enters the gaseous volume of the detector, ionization pairs are created and the electrons are collected on the 16 pads. The energy loss in the gas can be calculated from the total charge collected on all 16 pads.

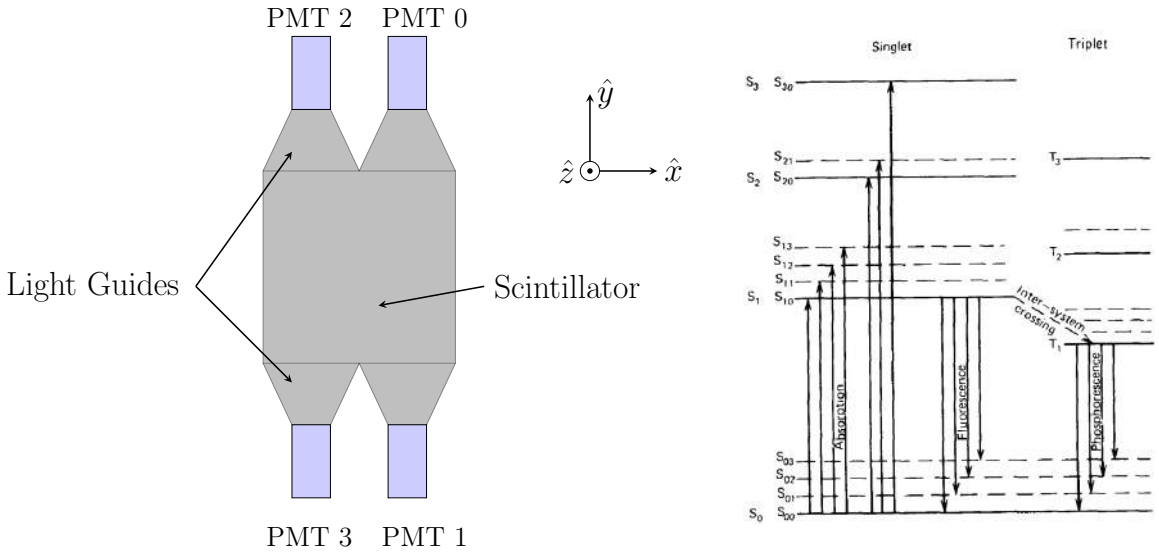

Figure 3.8: (Left) Head-on view (looking into the beam) of the thin timing scintillator. (Right) An example level scheme for transitions in the organic material with a π-electron structure. Source: [91]

3.6.3 Timing Scintillators

The thin timing detector rests inbetween the ion-chamber and the hodoscope. It is a plastic scintillator (EJ-204) with dimensions of 55 cm x 55 cm x 5mm and has pairs of photomultiplier tubes attached via light guides on the top and bottom of the detector. It measures the time-of-flight and triggers the data aquisition system. A schematic of the detector is shown in Fig. 3.8. The light guides are trapezoidal and optically connected to the PMTs.

When a charged particle passes through the organic scintillator it deposits energy into the material. A small portion of this kinetic energy is converted into flourescent light, while the majority is dissapated non-radiatively through lattice vibrations or heat. The flouresence arises from transitions in the energy level structure of a specific molecule, in this case Polyvinyl-toluene doped with antracene. Plastic scintillators such as these take advantage of the π-electron structure of these molecules. The typical spacing of vibrational states in organic scintillators is on the order of 0.15 eV, which is much greater than the average ther-

mal energy at room temperature $kT = 0.025$ eV, meaning nearly all the molecules are in the ground state. The typical spacing of the singlet states is on the order of a few eV. Fig. 3.8 shows a level scheme for an organic molecule with a π-electron structure. When a charged particle passes by, it excites the molecule to one of the singlet states. The principle source of flourescence comes from the de-excitation of the first-excited singlet state S_1 by internal conversion to one of the vibrational states of the ground state S_{0x}. Any state with excess vibrational energy quickly loses that energy as it is no longer in equillibrium with its neighbors. This decay is called prompt flourescence and is typically on the order of nanoseconds. For EJ-204, the decay constant is 1.8 ns.

It is also possible to decay to a triplet state which can be longer lived, with lifetimes up to 10^{-3} s, causing a delayed emission of light with a longer-wavelength since the triplet state is a lower energy than the singlet. This, along with multiple available excited states, causes a spectrum of light to be emitted. The emission spectrum for EJ-204 is shown in Fig. 3.9, and peaks around 410 nm [92]. The light emitted in the de-excitation of the organic molecules scatters within the plastic until it is collected in the PMTs [91].

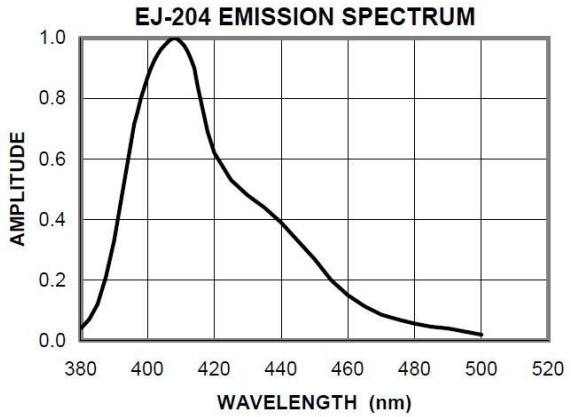

Figure 3.9: Emission spectrum for EJ-204. The peak wavelength is around 410 nm [92].

3.6.4 Hodoscope

The last detector in the sweeper focal plane is the hodoscope. The hodoscope is an array of CsI(Na) detectors consisting of 25 3.25" x 3.25" x 2.16" crystals oriented in a 5 x 5 square. A mechanical design of the detector is shown in Figure 3.10. The array is assembled with 5 rows which each contain 5 crystals and is centered on the central track through the sweeper. Each crystal is wrapped in reflective material 0.2 mm thick, and optically coupled to a Hamamatsu PMT R1307 with magnetic shielding. There is no light guide between the PMT and the crystal. The hodoscope fully stops the charged particles due to its thickness and measures their remaining energy.

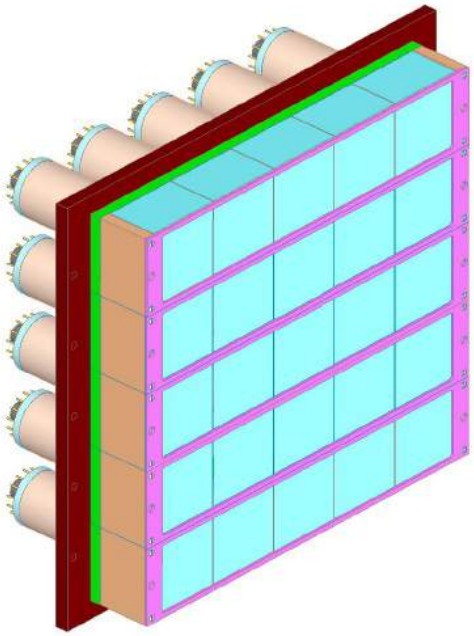

Figure 3.10: Schematic of the Hodoscope, which is an array of CsI(Na) crystals arranged in a 5x5 configuration.

The scintillation mechanism depends on the energy states determined by the crystal lattice of CsI. Electrons only have available discrete bands of energy in insulators or semiconductors. When a charged particle passes through the lattice, electrons are excited from

the valence band across the forbidden region into the conductance band which leaves an electron hole. A return of an electron to the valence band can cause the emission of a photon. However for pure crystals this is an inefficient process so often a dopant or impurity is introduced. The added impurity can create available states in the forbidden band of the crystal which increases the probability of populating and de-excitating from these states since their energies are less than the full forbidden gap. CsI(Na) typically has a slow decay time which consists of two components with mean lives of 0.46 μs and 4.18 μs. In addition, CsI(Na) is hydroscopic so care must be taken to avoid exposure to the ambient atmosphere. A four-sided gas cover surrounds the crystals and an inlet allows dry nitrogen to flow over the face of the crystals whever the detector box is not under vacuum.

3.7 MoNA LISA

The Modular Neutron Array (MoNA), and the Large-area multi-Institutional Scintillator Array (LISA) each consist of 144 200 x 10 x 10 cm^3 plastic scintillator bars. Each bar in MoNA is made of BC-408, while LISA is made of EJ-200. The bars are wrapped in reflective material and black plastic to reduce light loss and prevent ambient light from leaking in. Each bar is also coupled to two PMTs on either end by light guides. The MoNA-LISA bars serve to measure the position and time-of-flight of neutrons that interact in the plastic. When a neutron scatters off hydrogen or carbon nuclei in the bar, scintillation light is produced and the photons internally reflect until they are collected by the PMTs. The position along the bar is determined by the time difference of the two PMTs, and the interaction time is determined from their average. The Y and Z coordinates are given by the discretization of the bars.

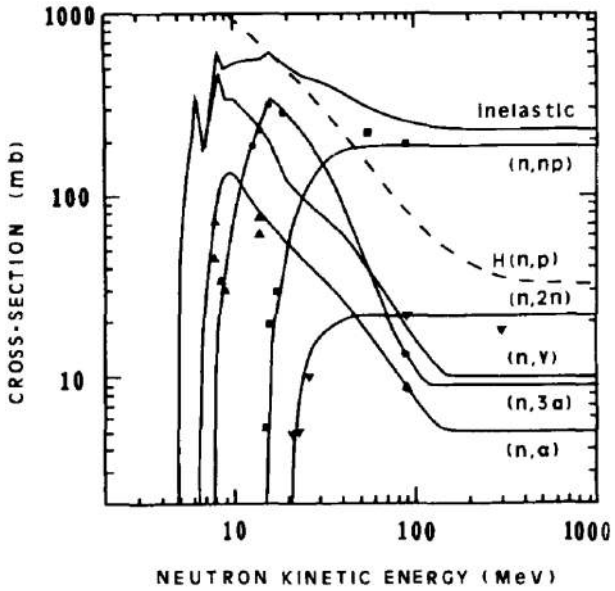

Figure 3.11: ^{12}C(n,*) cross sections for neutron energies ranging from 1 - 100 MeV for several different reactions. Each of the cross sections listed here are included in MENATE_R and used to model the neutron interactions in MoNA-LISA. Image source: [93]

When a neutron enters the plastic it interacts with carbon or hydrogen nuclei causing them to scatter which excites the plastic causing flouresence in a manner described in section 3.6.3. Figure 3.11 shows different cross sections as a function of neutron kinetic energy. At typical beam energies, it is most likely for neutrons to interact inelasticlly with carbon since the elastic cross section for H(n,p) drops as the neutron energy increases. However, since the mass of a carbon nucleus is much larger than that of hydrogen, the recoil is much smaller, and so less light is produced in the plastic compared to scattering on hydrogen. Thus the dominant signal comes from scattering on hydrogen. The emitted light scatters towards the ends where it is collected by a PMT. MoNA and LISA use Photonis XP2262/B PMTs and Hamamatsu R329-02 PMTs respectively.

3.8 Electronics and DAQ

The data acquisition (DAQ) system for MoNA, LISA, and the sweeper magnet is described in detail in References [90, 94, 95, 96]. An overview is presented here, with an abbreviated schematic in Fig. 3.12. Each detector subsystem runs an independent acquisition system connected by a "Level 3" system which generates a system trigger and a timestamp to be relayed to each detector. After the data are written to disk, the seperate files for each subsystem are merged by matching timestamps event-by-event. The system trigger in this experiment was the left-upper PMT of the thin scintillator (PMT 0), and the timestamp was a 64-bit word generated by the clock of the Level 3 system.

The trigger logic was handled by Xilinx Logic Modules (XLMs), divided into 3 levels. The Level 1 and Level 2 XLMs determine weather or not an event in MoNA or LISA is valid, with a valid event being defined by a good timing signal in the CFD channels for both PMTs in a single bar. Level 3 contains a clock which runs when the system is not busy processing an event, and handles the coincidence trigger logic between MoNA-LISA and the Sweeper. Upon recieving a signal from the system trigger, the Level 3 system opens a coincidence gate of 35 ns and waits for a valid signal from either MoNA or LISA. If one is recieved a "system trigger" signal is sent to each subsystem and the event is processed. If no such signal is recieved, then the coincidence gate will close and the system will fast clear. If MoNA-LISA trigger but not the sweeper, then they will send a trigger and busy signal to Level 3 causing it to go busy and reject signals from the sweeper. Without a signal from the sweeper, the system trigger cannot be produced, and the coincidence gate is never opened. Since MoNA and LISA do not recieve a system trigger in this case, they fast clear.

MoNA and LISA each consist of identical but independent electronic set-ups. Each PMT

has two outputs, an anode and a dynode. The anode signal is used for local triggering and for timing, while the dynode is used to measure the charge collected in the PMT. The timing signal proceeds to a constant fraction discriminator (CFD). The timing signals from both PMTs then go from the CFD to a time-to-digital converter (TDC) and an XLM module. The TDC modules are run in common stop mode, meaning a trigger in MoNA/LISA will signal the start, with the stop coming from the Level 3 system trigger. Finally, the charge signal from the dynode goes to a charge-to-digital converter (QDC) for integration. This process is duplicated for every bar in MoNA and LISA.

In the sweeper, the electronics are set up for three timing scintillators, two CRDCs, an ion-chamber, and a CsI(Na) array. Each timing signal from the thin PMTs, target scintillator, and A1900 scintillator goes to a CFD and then a TDC. In the case of the thin, the timing signal from PMT 0 is sent to Level 3 to act as the system trigger. Where charge signals are available, they are sent to amptlitude-to-digital converters (ADCs). All TDCs in the sweeper operated in common start mode. The Level 3 trigger began the measurement, and the timing signal itself provided the stop. The pads of the CRDCs were digitized by Front-End-Electronics (FEE) modules that sampled the pulse and sent it to an XLM. For the ion chamber, the signals from each pad were sent directly to a shaper and then to an ADC. Finally, the PMT signals from the CsI(Na) array, or Hodoscope, went through shaping amplifiers and then ADCs. Every time the system recieved a trigger from Level 3, all TDC, ADC, QDC and XLMs were read out and processed.

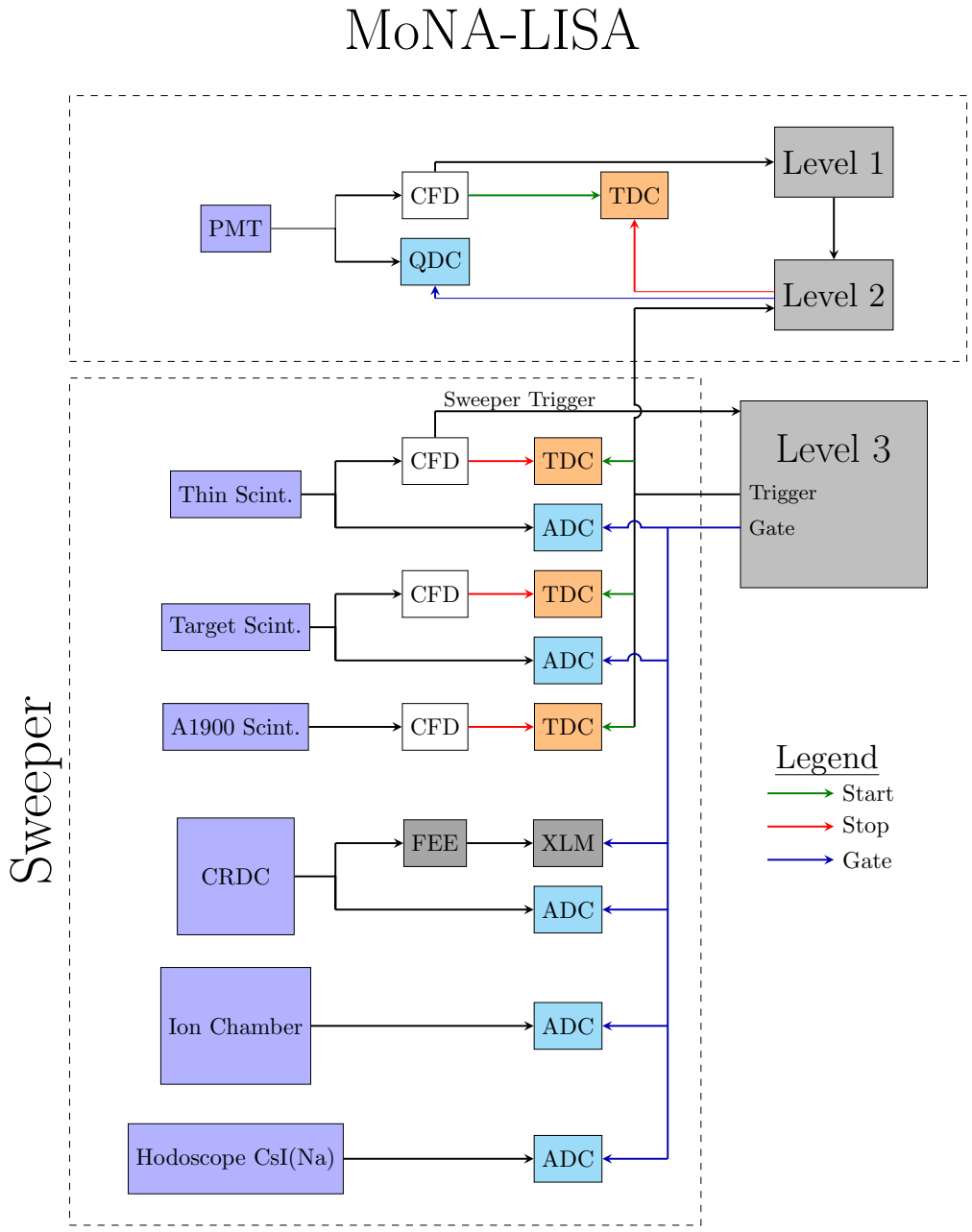

1

Figure 3.12: Schematic of the electronics for MoNA-LISA and the Sweeper. Dashed lines encompases each subsystem. Green arrows indicate start signals, red stop signals, and blue arrows indicate the QDC/ADC gate for integration. Upon receiving the system trigger from level 3, all TDCs, QDCs, and ADCs read out and are processed.

3.9 Invariant Mass Spectroscopy

Consider the decay of a particle with mass M into a large fragment A and N neutrons, with masses M_A and m_n respectively. Energy and momentum are conserved, thus:

$$E_M = E_A + \sum_{i=1}^{i=N} E_n$$

and

$$P^{\nu}_{initial} = P^{\nu}_{final}$$

The quantity $M^2 = (P^{\nu})^2$ is lorentz invariant, and therefore independent of reference frame. The decay energy of an unbound nucleus is defined as the energy difference between the initial nucleus and it's decay products:

$$E_{decay} = M_{A+n} - M_A - \sum_{i=1}^{i=N} m_n \tag{3.1}$$

where M_{A+n} is the invariant mass of the initial nucleus, M_A the rest mass of the fragment, and m_n the rest mass of a neutron. The 4-vector of the initial nucleus is obtained by summing the 4-vectors of all daughter products, which determines M_{A+n}. In the case of a one-neutron decay this expression becomes:

$$E_{decay} = \sqrt{M_A^2 + M_n^2 + 2(E_A E_n - \vec{p_A} \cdot \vec{p_n})} - M_A - m_n \tag{3.2}$$

For two-neutron emission, the expression becomes slightly more complicated:

$$E_{decay} = \sqrt{M_T^2 + 2(E_T - \vec{p_T}^2)} - M_A - 2m_n$$

Where

$$M_T^2 = M_A^2 + 2m_n^2$$

$$E_T^2 = E_A E_{n1} + E_A E_{n2} + E_{n1} E_{n2}$$

and

$$\vec{p_T}^2 = \vec{p_A} \cdot \vec{p_{n1}} + \vec{p_A} \cdot \vec{p_{n2}} + \vec{p_{n1}} \cdot \vec{p_{n2}}$$

While the decay energy simplifies to a single algebraic expression in the case of one, or even two neutrons, an expression like 3.1 can become cumbersome in cases of 3 or 4 neutron emission due to an abundance of cross-terms. It is much easier in those cases to handle the 4-vectors of each particle numerically to calculate dot products.

3.10 Jacobi Coordinates

In the case of three-body decays, or two-neutron emission, one can utilize Jacobi coordinates to examine correlations between the neutron pair and the core. The Jacobi coordinate system has the advantage of removing the center-of-mass motion so that the relative motion is exposed. Given three particles, there are three unique coordinate systems that can be chosen. However, since the neutrons are indistinguishable this reduces to two choices: the **T** and the **Y** systems illustrated in figure Fig. 3.13. The vector $\vec{k_x}$ is drawn from the second particle to the first, and the second vector $\vec{k_y}$ from the third particle to the center-of-mass of the two-body subsystem. The relative motion of the three-body system can be described by an energy ϵ, and angle θ_k defined as [2]:

$$\epsilon = E_x / E_T$$

$$cos(\theta_k) = \vec{k_x} \cdot \vec{k_y}/(k_x k_y)$$

where ϵ is the energy of the two-body subsystem relative to the total three-body energy, and $cos(\theta_k)$ the angle between the vectors k_x and k_y. More explicitly:

$$E_T = E_x + Ey = \frac{(m_1 + m_2)k_x^2}{2m_1 m_2} + \frac{(m_1 + m_2 + m_3)k_y^2}{2(m_1 + m_2)m_3}$$

where $\vec{k_x}$ and $\vec{k_y}$ are defined as:

$$\vec{k_x} = \frac{m_2\vec{k_1} - m_1\vec{k_2}}{m_1 + m_2}$$

$$\vec{k_y} = \frac{m_3(\vec{k_1} + \vec{k_2}) - (m_1 + m_2)\vec{k_3}}{m_1 + m_2 + m_3}$$

And m_i and k_i denote the mass and momentum of each particle in the three-body system. In the **T** system ϵ is the energy of the neutron-neutron pair relative to the total three-body energy, whereas in the **Y** system it is the neutron-core energy. Additional information on Jacobi coordinates can be found in Ref.[2] and Ref.[75]. The Jacobi Coordinates are a

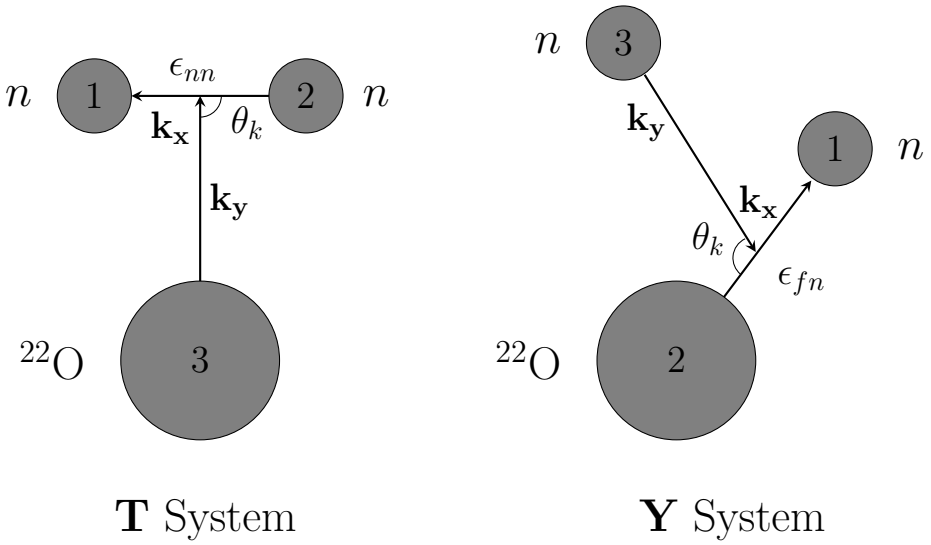

Figure 3.13: Jacobi **T** and **Y** coordinates for the three-body system ^{22}O + 2n.

powerful experimental tool as they distinguish between the different decay modes a two-neutron (or two-proton) unbound system can undergo. For example, in a di-neutron-like correlation the two-neutrons are clustered together and so the angle θ_k is close to π in the **Y** system and $cos(\theta_k)$ peaks at -1. In addition, the neutron-neutron energy is low relative to the total three-body energy causing ϵ to peak at 0 in the **T** system.

For a sequential decay it is neccessary to make the distinction between the limiting cases of "even" and "uneven", as they have very different correlations. In an even sequential decay, the intermediate state is at half the total three-body energy, and so both neutrons decay with similar energy. Whereas in an uneven decay, the intermediate state is either close to the three-body state or the final state, resulting in a high and a low energy neutron. Due to the varying energies between the two cases, the corresponding three-body correlations are dramatically different, as illustrated in Fig. 3.14.

Since a measurement of the decay energy is kinematically complete, the Jacobi spectra can also be constructed from the measured 4-vectors of the two neutrons and the core. Measuring the three-body correlations allow one to connect to the three-body wavefunction as the few-body Schrodinger equation can be solved in the same coordinate system and predictions made for the three-body decay. Three-body correlations in both the **T** and **Y** are shown in Fig. 3.14 for the different cases of sequential (uneven/even), di-neutron, and phase space decays. Effects from neutron scattering have been removed, illustrating the stark difference between the different decay modes.

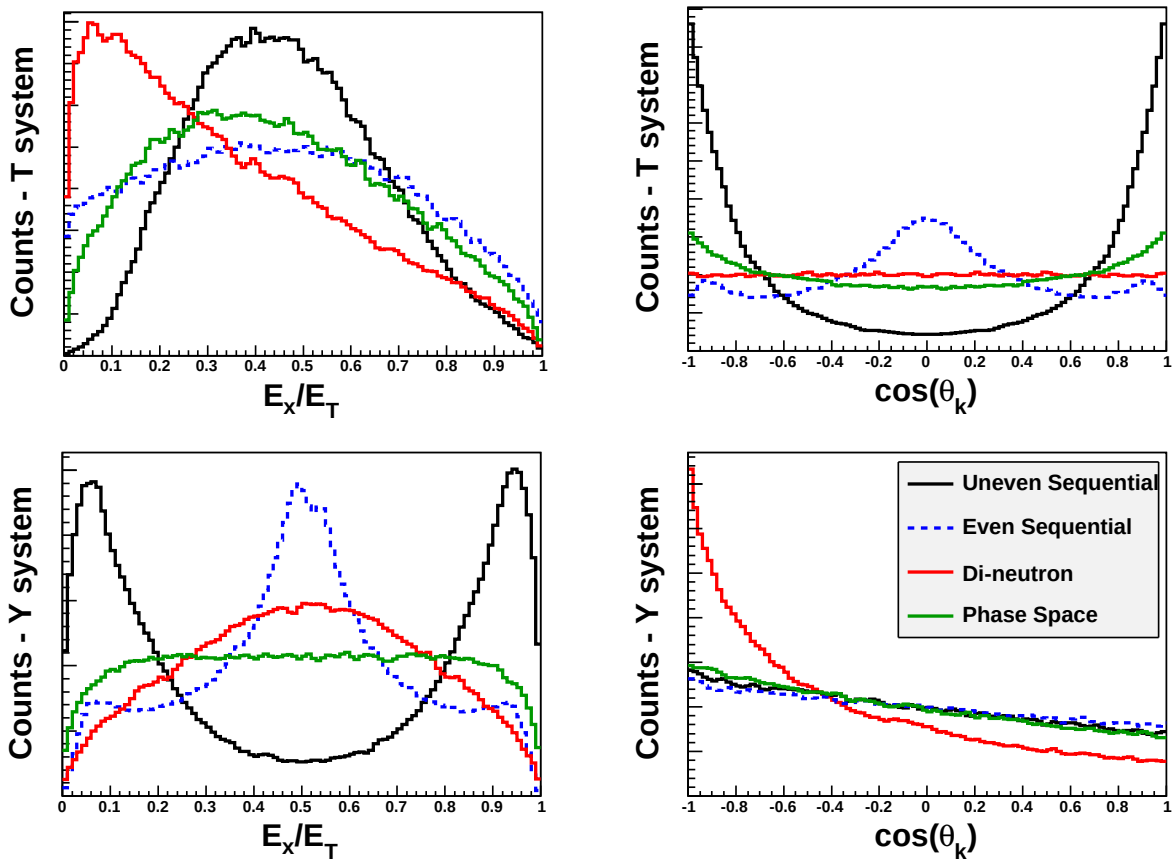

Figure 3.14: Simulated Jacobi **T** and **Y** coordinates for the three-body system ^{22}O + 2n with E_T = 750 keV. Effects from neutron scattering have been removed. Acceptances and efficiencies are applied. The different colors indicate different decay mechanisms. All spectra are normalized to $2 * 10^6$ events.

Chapter 4

Data Analysis

This chapter details the procedures and methods used to calibrate MoNA, LISA, and the detectors in the Sweeper setup and how meaningful data are obtained from the raw signals in each detector. After the calibrations are complete, event selection is discussed in addition to modeling and simulation.

4.1 Calibrations and Corrections

4.1.1 Charged Particle Detectors

Following the sweeper magnet are several charged-particle detectors: two CRDCs, an ion-chamber, a thin scintillator and a hodoscope. The following sections detail the calibration procedures for these detectors including the timing scintillators upstream of the target.

4.1.1.1 CRDCs

The Cathode Readout Drift Chambers (CRDCs) provide a measurement of the X and Y position of charged particles passing through the detector. They are used to track the reaction products for isotope separation and to determine their energy and momentum at the target. Hence, good tracking is essential for a successful reconstruction. There are two CRDCs in the sweeper focal plane. CRDC1 was placed roughly 1.56 m from the center of the LD_2 target (along the center track), and CRDC2 was placed 1.55 m behind CRDC1.

	CRDC1	CRDC2
Bad Pad	96-100	24
	104	121
	106	

Table 4.1: Bad pads in the CRDCs which are removed from analysis.

The X position is determined by charge collection along 116 segmented pads with a pitch of 2.54 mm in width. First, the quality of each pad must be examined. Bad pads that show poor charge collection and give erroneous signals must be removed. Small leakage currents in the CRDCs can be read out in the electronics, even with no beam. This signal is called the pedestal and must be subtracted to properly determine the total charge collected. The pedestal subtraction for CRDC1 and CRDC2 is shown in Figure 4.1, a gaussian fitting algorithm is used to determine the pedestal for each pad. From the subtraction several pathological pads can be identified; they are listed in Table 4.1.

After the pedestal-subtraction the pads need to be gainmatched. This is accomplished using a "continuous sweep" run where the beam is moved across the detector to illuminate all pads within acceptance. An ^{20}O beam with 99% purity was used for this purpose. The pad with the maximum charge deposited was selected event-by-event. The charge distribution of each pad, when it registered as the maximum pad, was then gainmatched to a reference (pad 64) with the following relation:

$$m = \frac{\mu_{ref}}{\mu_i}$$

where μ_i is the centroid of the charge distribution on the ith pad. Figure 4.2 shows a comparison before and after the gainmatching procedure. The total charge collected on the

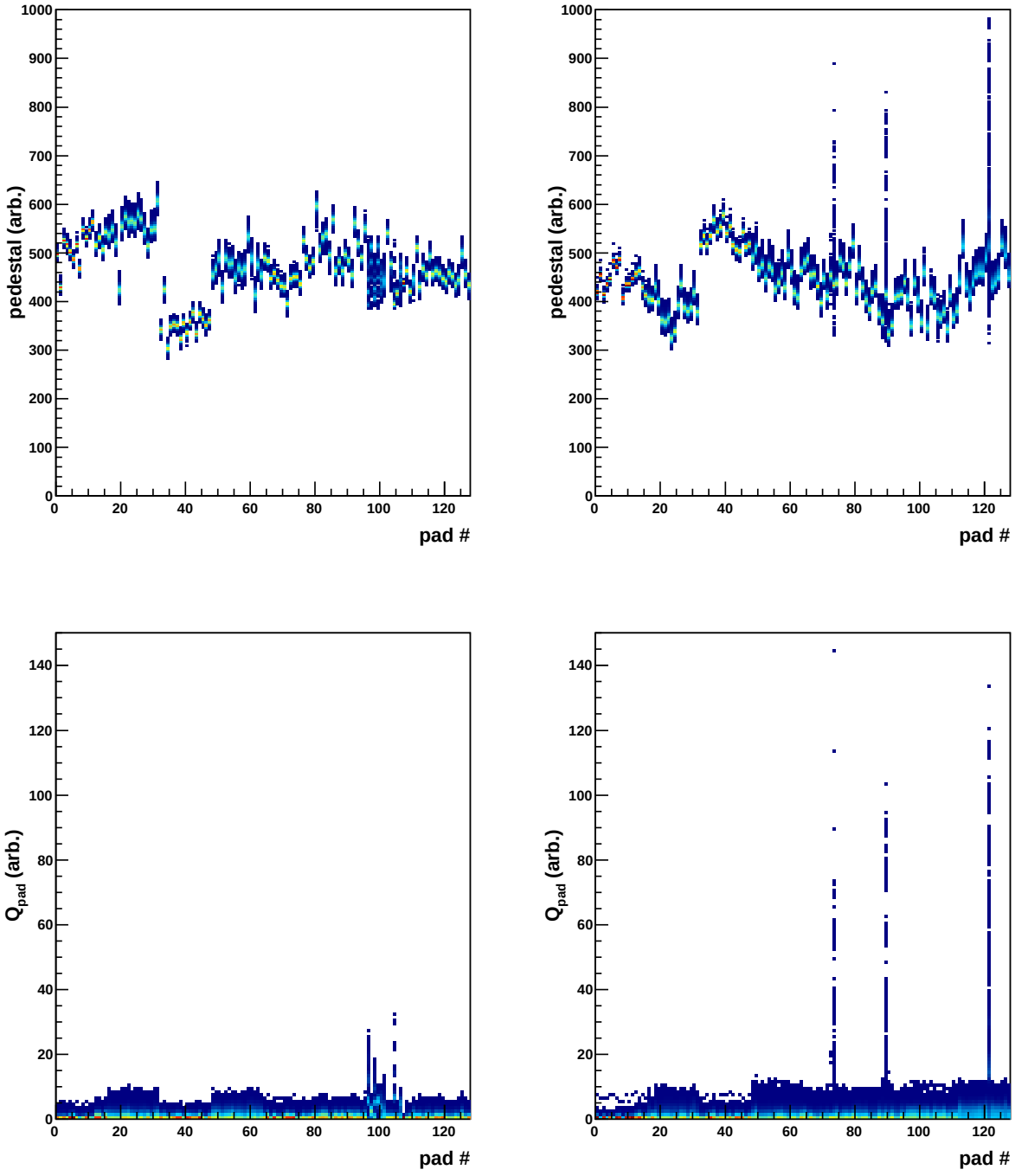

Figure 4.1: Pedestal subtraction in the CRDCs. The raw pads for CRDC1 (left) and CRDC2 (right) are shown in the first and second panels from the left, while the subtraction is shown in the third and fourth panels.

pad is determined by a Riemann-sum:

$$Q_{pad} = \frac{1}{n}\sum_{i=0}^{n} q_i - q_{pedestal}$$

where n is the number of samples and q_i is the amount of charge per sample. The gain-matched signal is then:

$$Q_{cal} = m * Q_{pad}$$

The X-position is then determined by the charge distribution across all pads. A gaussian line-shape is fit to this distribution to determine the central value.

The Y-position is determined by the drift-time of the charge carriers in the active volume of the detector. Thus, the drift time and pad-distribution need to be converted into physical X and Y positions in the lab-frame. This is accomplished using tungsten masks with specific hole-patterns drilled into them. The mask is placed in front of the detector and the known hole-pattern can be used to determine a linear transformation from charge/time to X/Y position.

It should be noted that the CRDCs are placed in opposite orientations in the x direction. For CRDC1 the pad number increases in the $+x$ direction in the lab frame, while for CRDC2 increasing pad numbers are in the $-x$ direction. This results in their X slopes having opposite sign.

The tungsten masks are put in place by a hydraulic drive. During the experiment, the drive for CRDC2 was unable to fully lift the mask into position thus not covering the full face of the detector. The X-slope is determined by the pitch of the pads, and the offset found from the mask. The Y-slope is found from the spacing of the vertical holes, and likewise the offset from the absolute position of the holes. However, since the mask did not fully insert,

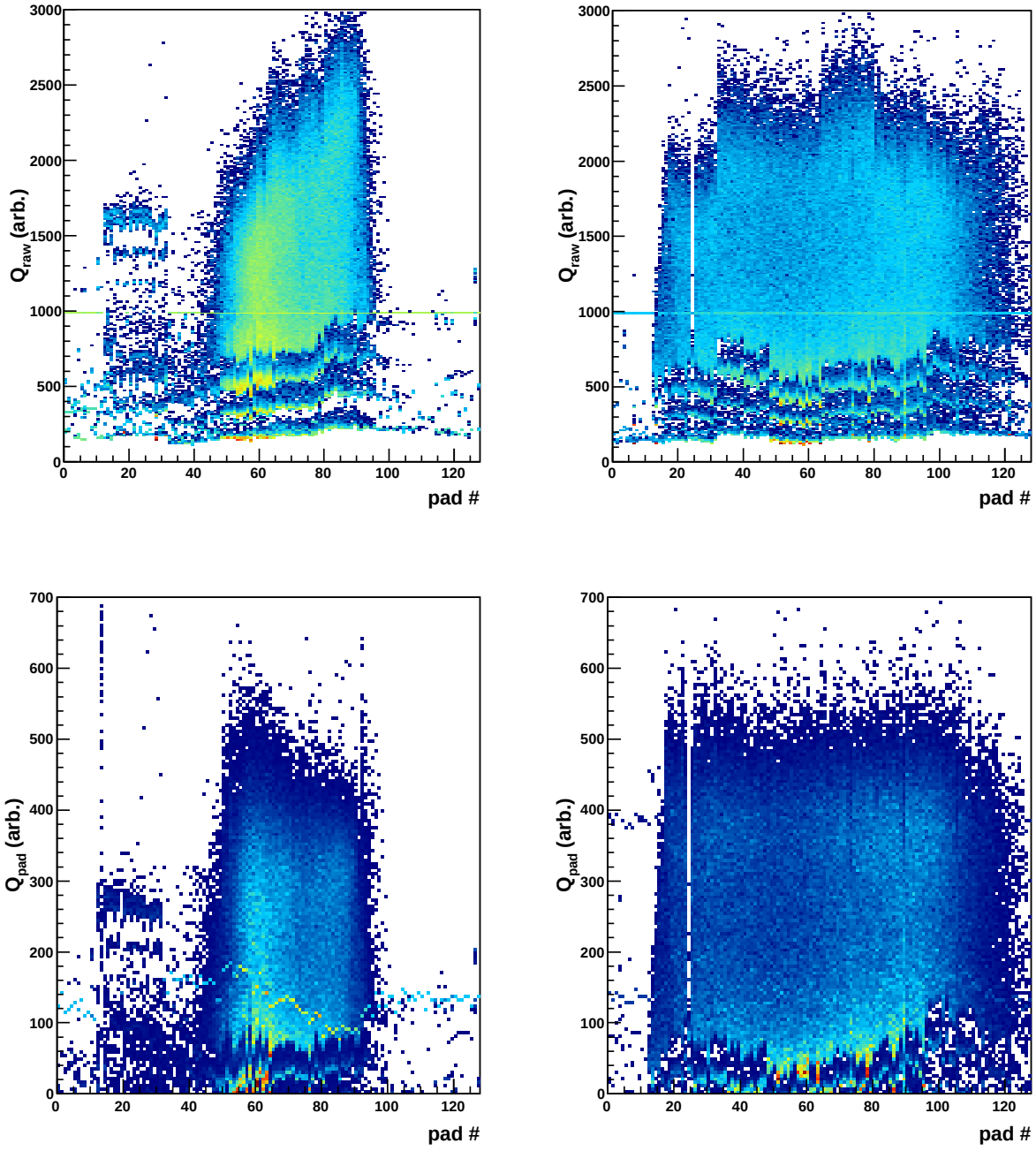

Figure 4.2: Before (left) and after (right) gainmatching of CRDC1 and CRDC2. CRDC1 is shown in the first and third panel, and CRDC2 in the second and fourth.

	X_{slope} [mm/pad]	X_{offset} [mm]	Y_{slope} [mm/ns]	Y_{offset} [mm]
CRDC1	2.54	-171.3	-0.1953	98.5
CRDC2	-2.54	187.3	-0.2043	103.7

Table 4.2: Slopes and offsets for the CRDC calibration.

this means that the y-offset for CRDC2 cannot be determined by this method. Figure 4.3 shows 3 different mask-calibration runs taken at different points during the experiment, the upper edge of the mask becomes visible, and it is evident the mask did not fully insert. There was no indication of this occurring for the mask of CRDC1.

The y-offset of CRDC2 was determined by examining the decay-kinematics of ^{23}O $\rightarrow$ ^{22}O + 1n, since the offset will not prevent isotope separation but will affect the fragment energy. This offset was constrained by lining up the reconstructed fragment angles with the neutron cone and matching the fragment and neutron energies. This procedure is iterative since an offset must first be guessed. The parameters for this decay are shown in Sections 4.3 and 4.4. The slopes and offsets for both CRDCs can be found in Table 4.2.

The CRDCs can exhibit a drift in the measured Y position. The apparent Y-position can fluctuate if the gas-pressure changes, or if the drift voltage fluctuates. This is corrected by gain-matching the raw drift time to a reference run (Run1035), and performing a run-by-run correction. The correction factor is determined by:

$$m = \frac{\mu_{TACref}}{\mu_i}$$

where μ_{TACref} and μ_i are the centroids of the TAC signal in the CRDC for the reference run and an arbitrary run respectively. The corrected drift-time is simply:

$$t_{corr} = m * t_{drift}$$

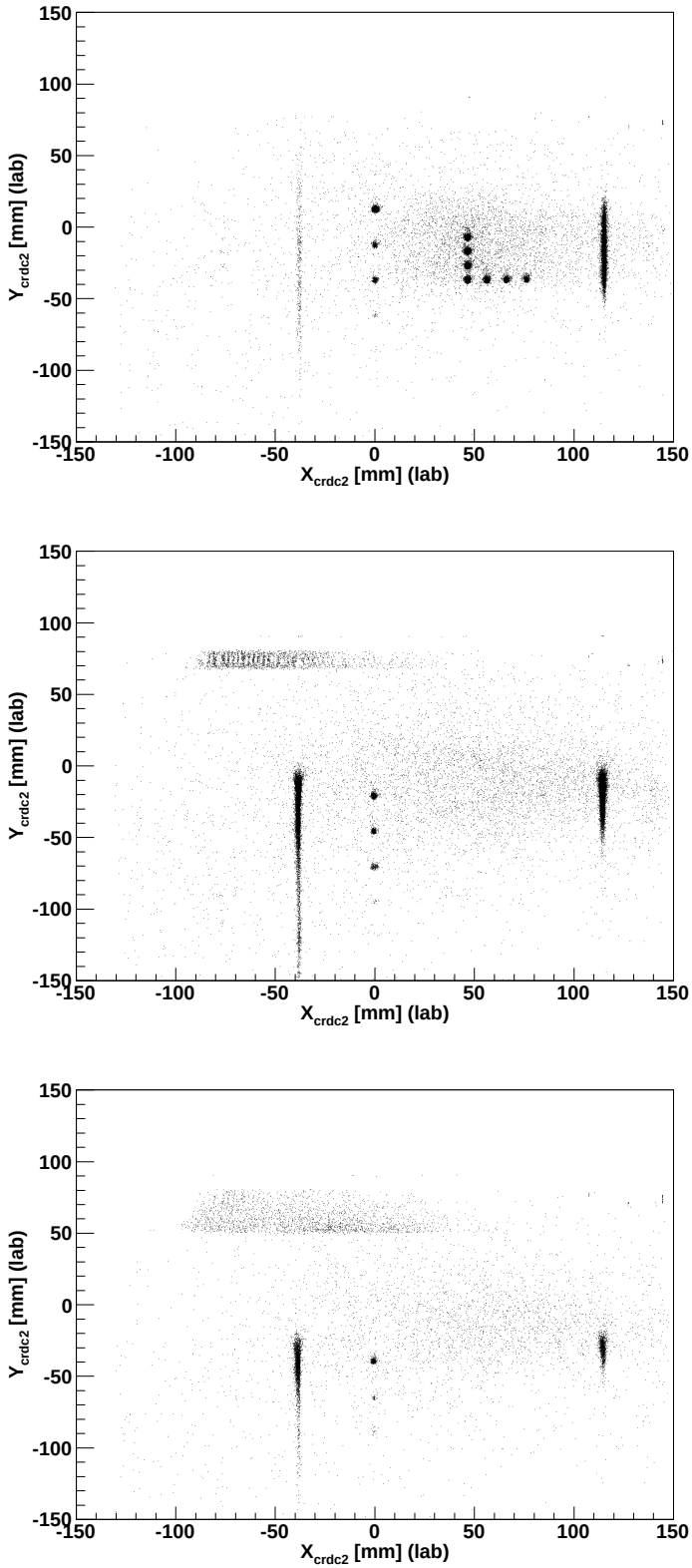

Figure 4.3: (From left to right) Mask runs 3023, 3078, and 3142 for CRDC2. Particles that illuminate an area above the mask indicate that the mask did not fully insert.

Figure 4.4 and 4.5 shows this correction for CRDC1 and CRDC2. The drift in the CRDCs is correlated because the two detectors are connected to the same gas-handling system.

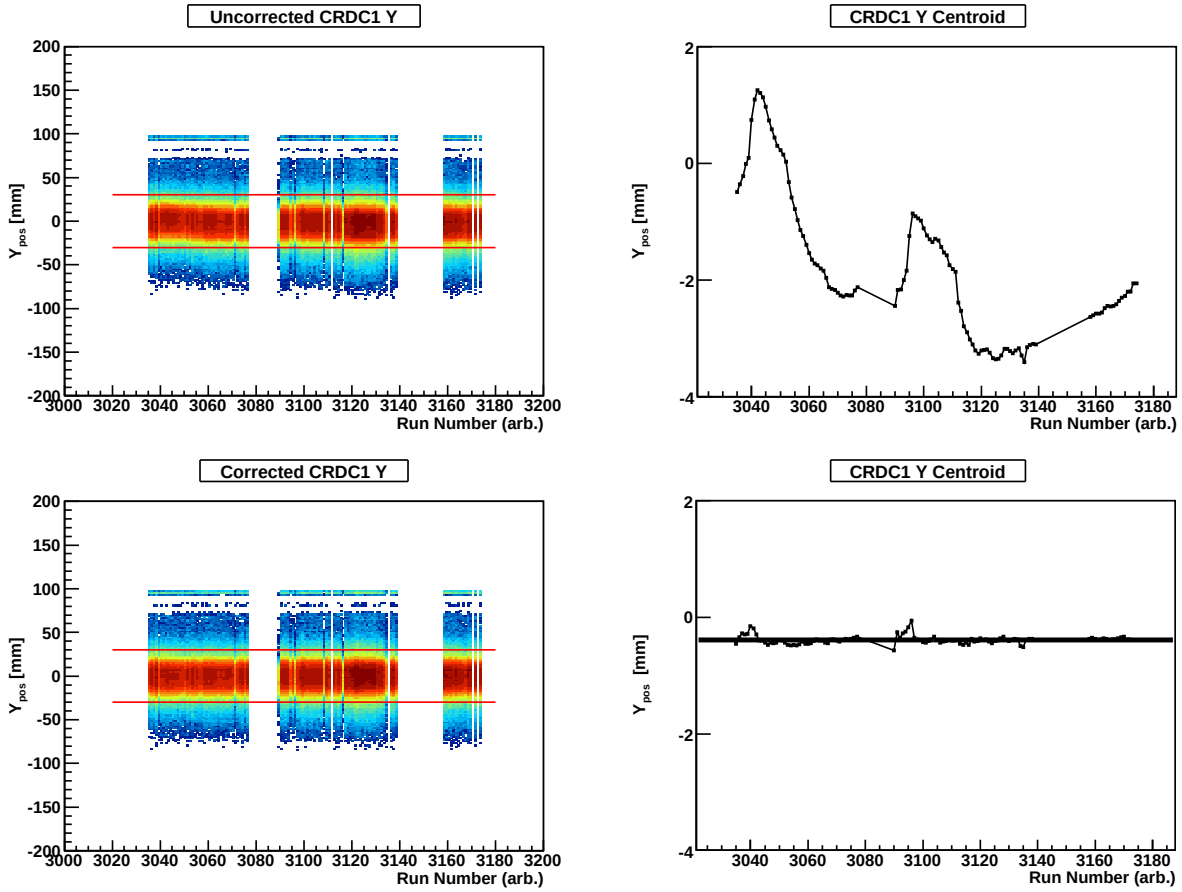

Figure 4.4: Drift correction for CRDC1 Y position. (Top left), Uncorrected Y distribution in CRDC1 as a function of Run Number. (Top right), Uncorrected centroids of CRDC1 Y position as a function of Run Number. (Bottom left). Corrected Y distribution in CRDC1. (Bottom right) Centroids of corrected Y distribution in CRDC1 as a function of run number.

4.1.1.2 Ion Chamber

The ion chamber is segmented into 16 pads along the z-axis, or beam direction. The raw charge collected on each pad can be used for element separation, however each pad needs to be gainmatched and any X or Y-position dependencies removed. To gainmatch the ion chamber a beam was sent down the center of the detector. For this experiment, an ^{20}O

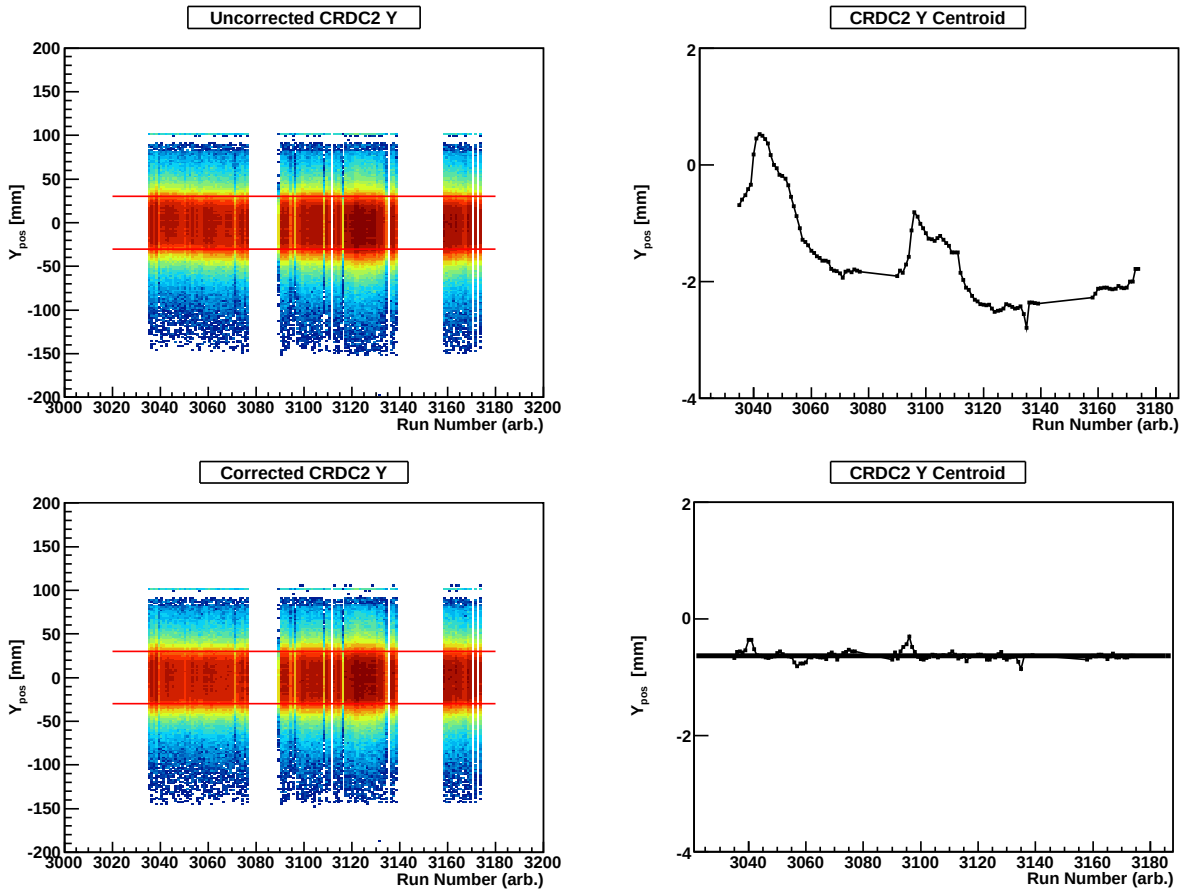

Figure 4.5: Drift correction for CRDC2 Y position. (Top left), Uncorrected Y distribution in CRDC2 as a function of Run Number. (Top right), Uncorrected centroids of CRDC2 Y position as a function of Run Number. (Bottom left). Corrected Y distribution in CRDC2. (Bottom right) Centroids of corrected Y distribution in CRDC2 as a function of run number.

beam was used for this purpose since the ^{24}O beam was not intense enough.

In order to ensure that each pad gives the same signal for the same amount of charge collected it is necessary to gainmatch them. For this procedure, the incoming ^{20}O beam is selected to remove impurities. In addition, a gate is placed on a good response in the CRDCs to remove events with strange trajectories. It is also assumed that the beam loses a negligible amount of energy in the first half of the detector compared to the second half. If we approximate the detector as 65 cm of pure Ar gas ($\rho = 1.66 * 10^{-3} g/cm^3$), the total energy loss for ^{20}O at 118 MeV/u in the first half of the detector is 16 MeV, and 16.1 MeV

in the second half.

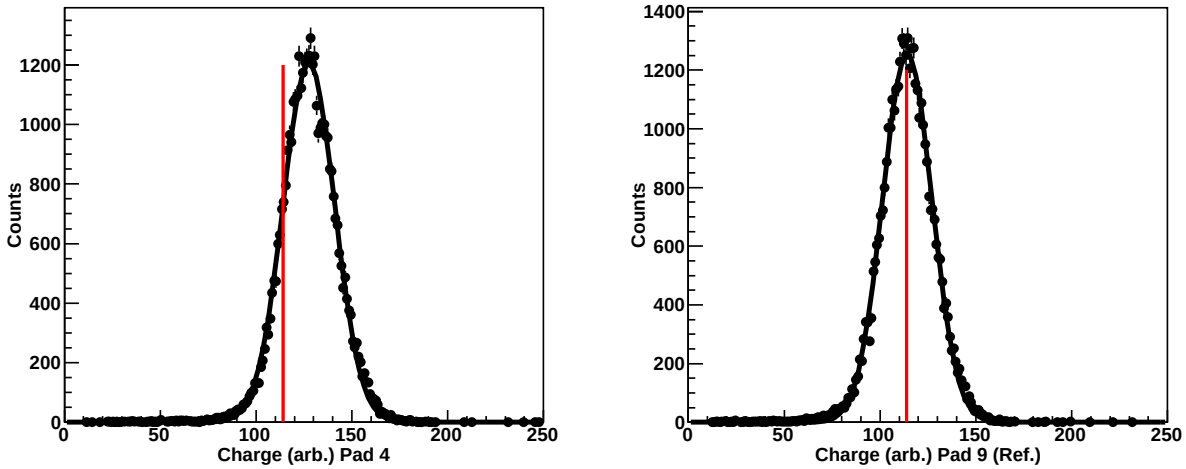

Figure 4.6: Example of gaussian fitting procedure for gainmatching of the IC pads. Pad 4 is shown on the left, and the reference pad, pad 9 on the right.

The gainmatching is performed by determining a slope for each pad:

$$q_{cal} = m_i * q_{raw}$$

Where q_{raw} is the raw charge collected on each pad, and m_i is the slope defined as:

$$m_i = c_{ref}/c_i$$

Here c_{ref} is the centroid of the reference pad, and c_i is the centroid of the ith pad determined by a gaussian fit. Example fits are shown in Fig. 4.6 for pad 4 and pad 9. Pad 9 was chosen as the reference pad, as it is in the middle of the detector and displayed a signal that was roughly in the middle of the variation from all other pads.

The results of the gainmatching procedure are shown in Fig. 4.7. It is apparent that pad 1 and 8 show abnormally low charge collection, and thus are excluded from analysis. For

the remaining good pads, the peaks line up and the widths are approximately the same.

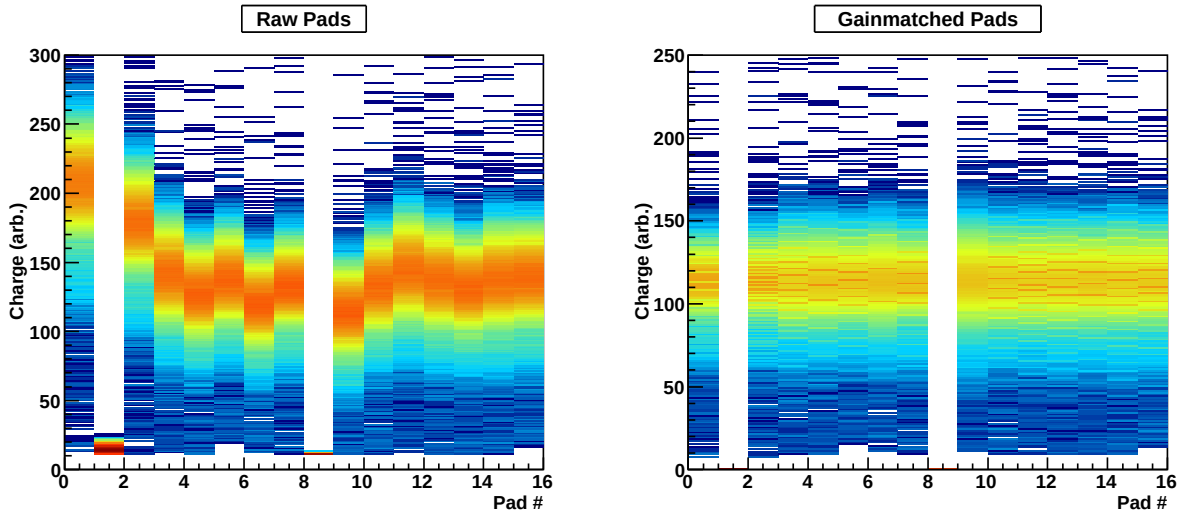

Figure 4.7: Results of applying the gainmatching calibration for the IC. Raw pads on shown on the left and calibrated pads on the right.

There is some variation in the charge collected in each pad as a function of the X position due to inefficient charge collection. Each pad has a different position dependence, and so each pad must be corrected independently to achieve the best resolution. To accomplish this, a "sweep run" was used where the beam was swept back and forth across the focal plane to illuminate the detector at different X-positions. Since magnetic fields do no work, the beam has the same energy despite the varying sweeper setting and so the same amount of charge is being deposited at each X position. Using 5 mm wide slices in X, the centroid of the charge deposited on each pad is determined by a gaussian fit and plotted as a function of the X position. The dependence is then fit with a polynomial of appropriate order and removed by the following expression:

$$q_{pos} = \frac{q_{cal}}{\sum a_i x^i}$$

where q_{cal} is the gainmatched charge, and a_i represent the polynomial coefficients.

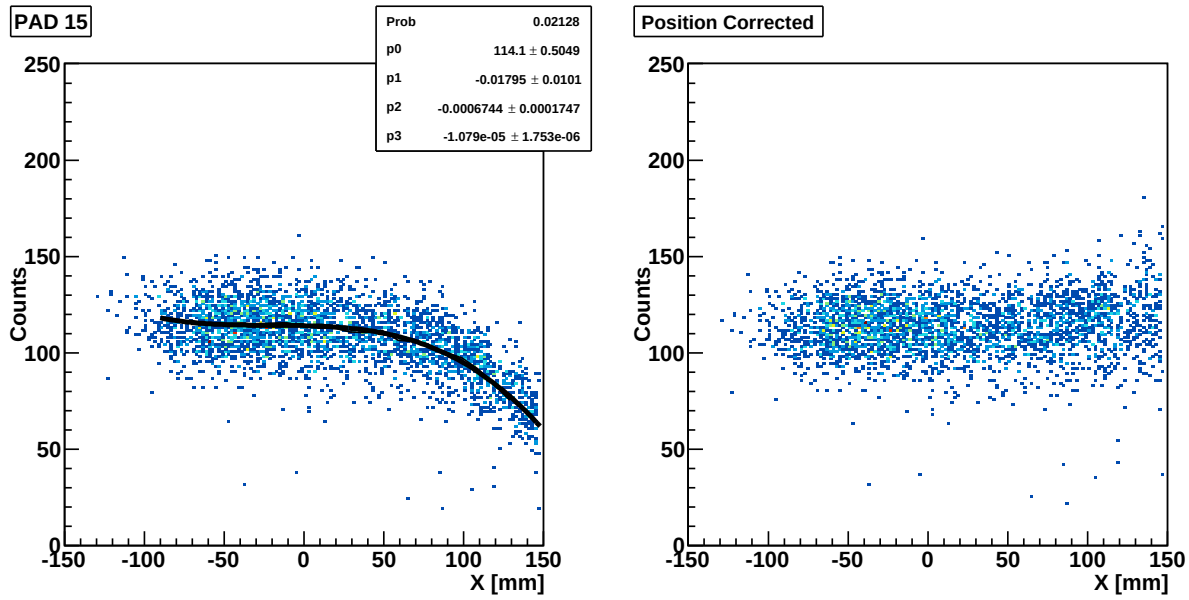

Figure 4.8: Example of position correction in the ion chamber for pad 15. The raw signal as a function of X position is shown in the left panel, with the best-fit super-imposed. The right panel shows the result of the correction.

This method was only applied for the X position correction, as there was no noticeable Y-dependence. After each pad has been gainmatched and position-corrected, the total energy loss is determined by the sum of all pads:

$$Q_{tot} = \sum q_{pos}$$

The results for the position correction are shown for pad 15 as an example in Fig. 4.8.

The ion chamber exhibited a slow drift over the course of the experiment. This is shown in Fig. 4.9 for the reaction products from the ^{24}O beam. The drift was fit with the functional form:

$$dE(t) = p_0 + \frac{p_1}{t + p_2}$$

The final drift-corrected energy loss then becomes:

$$dE_{corr} = Q_{tot}/dE(t)$$

To determine the coefficients for the drift correction, a gate is placed on the selection of ^{24}O beam, good CRDCs, and on oxygen in the ion chamber (denoted by the red lines in Fig. 4.9). The coefficients for the drift correction are summarized in Table 4.3.

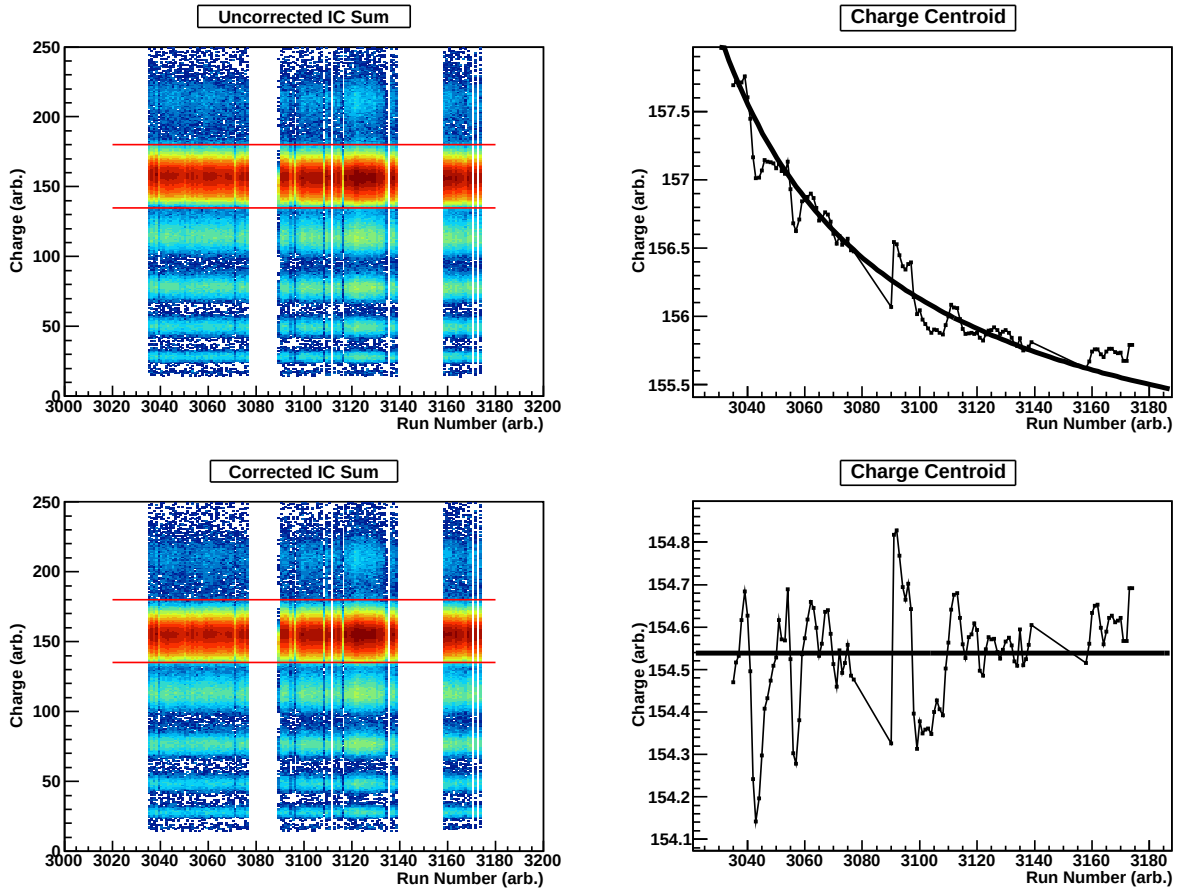

Figure 4.9: Drift correction for IC sum. (Top left), Uncorrected charge distribution in the IC as a function of Run Number. (Top right), Uncorrected centroids of the charge distribution as a function of Run Number. (Bottom left). Drift Corrected charge distribution in the IC. (Bottom right) Centroids of the drift corrected charge distribution.

Drift Correction	
p_0	154.8
p_1	210.9
p_2	-2971.2

Table 4.3: Drift correction parameters for the Ion Chamber.

4.1.1.3 Thin Scintillator

The thin scintillator is located after the ion chamber in the sweeper focal plane and provides an additional measurement of the energy loss in addition to time-of-flight information. The detector has four PMTs mounted on light-guides as illustrated in Fig. 3.8, and are labeled 0 through 3. The signal from each PMT gives a time and a charge measurement which are combined to give a total energy loss and the interaction time. Due to inhomogeneities and attenuation in the plastic, there is variation in the charge-collection efficiency for each PMT based on the interaction position in the detector. Thus, each PMT needs to be gainmatched and position corrected.

An ^{20}O beam was sent down the center of the focal plane for gainmatching of the PMTs. This ensured that the middle of the thin scintillator was illuminated and that the distance from the interaction point to each PMT was roughly equal. The sweeper was set to $I = 350$A with a central rigidity of $B\rho_0 = 3.767$ Tm for this run. Due to the logistics of warming and cooling the liquid deuterium target, it was more time-efficient to use a 670 mg/cm^2 Be degrader while the target was kept in a gaseous state (50 K) instead of waiting for the target to liquefy. The choice of 670 mg/cm^2 of beryllium was to mimic the expected energy-loss through the deuterium target. In addition, a selection was made on oxygen isotopes in the ion chamber, and each event was required to fall within a 20 mm x 20 mm square centered on the thin scintillator. The position on the thin scintillator was determined by projection

from the CRDCs.

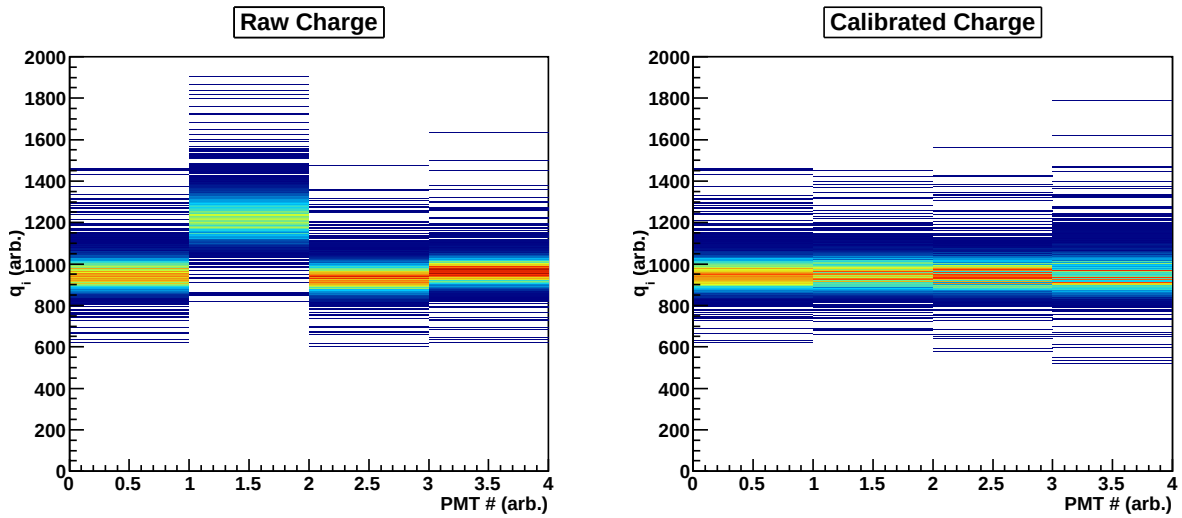

Figure 4.10: Before (left) and after (right) the gainmatching of the PMTs in the thin scintillator.

The charge signals from each PMT are calculated in a similar manner to the ion chamber, and gainmatched in the same way:

$$q_{cal} = m_i * q_{raw} + q_0$$

Where the slope are determined by a ratio of gaussian widths with respect to a reference PMT (PMT 0, see Fig. 3.8), and the offset is set to line up the peaks:

$$m_i = \frac{\sigma_{ref}}{\sigma_i}$$

Fig. 4.10 shows the charge collected in each PMT before and after gainmatching. Once all four PMTS are gain-matched, their signals are combined to provide a measurement of

the total charge deposited in the plastic, which is defined as follows:

$$q_{top} = \frac{q_{LU} + q_{RU}}{2}$$

$$q_{bot} = \frac{q_{LD} + q_{RD}}{2}$$

$$q_{tot} = \frac{\sqrt{q_{top}^2 + q_{bot}^2}}{2}$$

Where $q_{LU,LD,RU,RD}$ are the gainmatched signals from the left-upper (lower) and right-upper (lower) detectors respectively. The total charge signal q_{tot} exhibited both a positional dependence inherent in each PMT signal as well as an overall time dependence as the detector drifted over the course of the experiment. These effects were corrected by using the same method as the ion chamber. The position dependence was removed by a sixth-order polynomial:

$$q_{poscorr} = \frac{q_{tot}}{\sum a_i x^i}$$

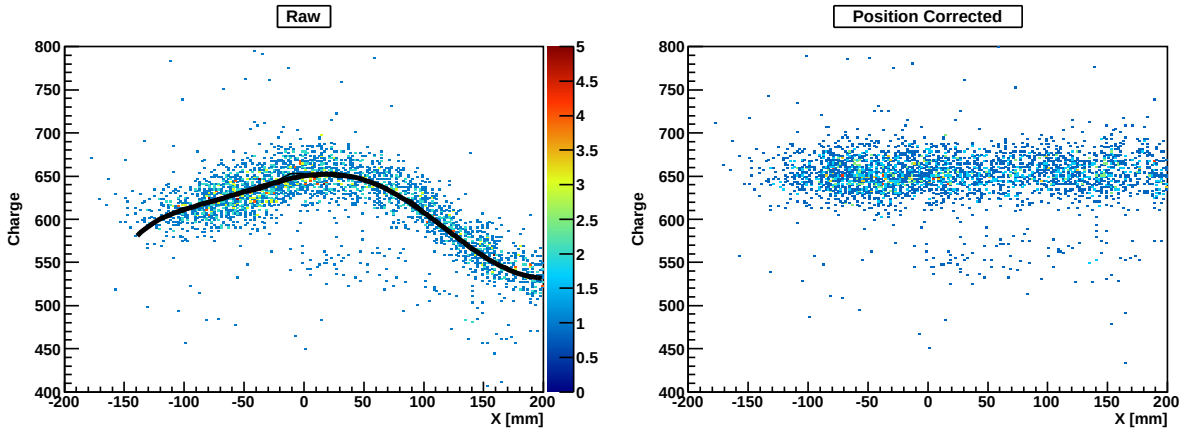

Figure 4.11: Correction of the position dependence in the thin scintillator. (Left) the raw charge signal as a function of X position with the best-fit superimposed. (Right) Result of position correction.

Position Correction		Drift Correction	
a_0	651.7	p_0	742.7
a_1	0.2001	p_1	-43364
a_2	-4.71*10^{-3}	p_2	-2374
a_3	-2.31*10^{-5}		
a_4	7.55*10^{-8}		
a_5	3.08*10^{-10}		
a_6	4.63*10^{-15}		

Table 4.4: Coefficients for position correction (left) and drift correction (right) of the Thin scintillator.

Figure 4.11 shows the energy-loss in the thin scintillator as a function of the X position determined by the CRDCs. To map out this dependence, a "sweep run" was used as described in previous sections. No significant Y dependence was observed, and thus was not corrected. The detector drift was handled the same way as the ion-chamber:

$$dE(t)_{thin} = p_0 + \frac{p_1}{t + p_2}$$

With the final energy signal being:

$$dE_{corr} = q_{tot}/dE(t)_{thin}$$

The drift-corrected energy signal can be seen in Fig. 4.12. The slight correlation is removed. The coefficients for the position and energy-drift correction can be found in Table 4.4.

Only an offset is used to calibrate the timing signal of each PMT. The slope of the TDC is assumed to be 0.1 ns/ch since the range of the TDC is fixed. In addition, there is about a 20 ns jitter introduced the Field Programmable Gate Array (FPGA) in the sweeper electronics. Since the TDCs receive a start from the individual PMTS and the stop is generated by the FPGA, the amount of jitter can vary event-by-event. However, the same stop signal is

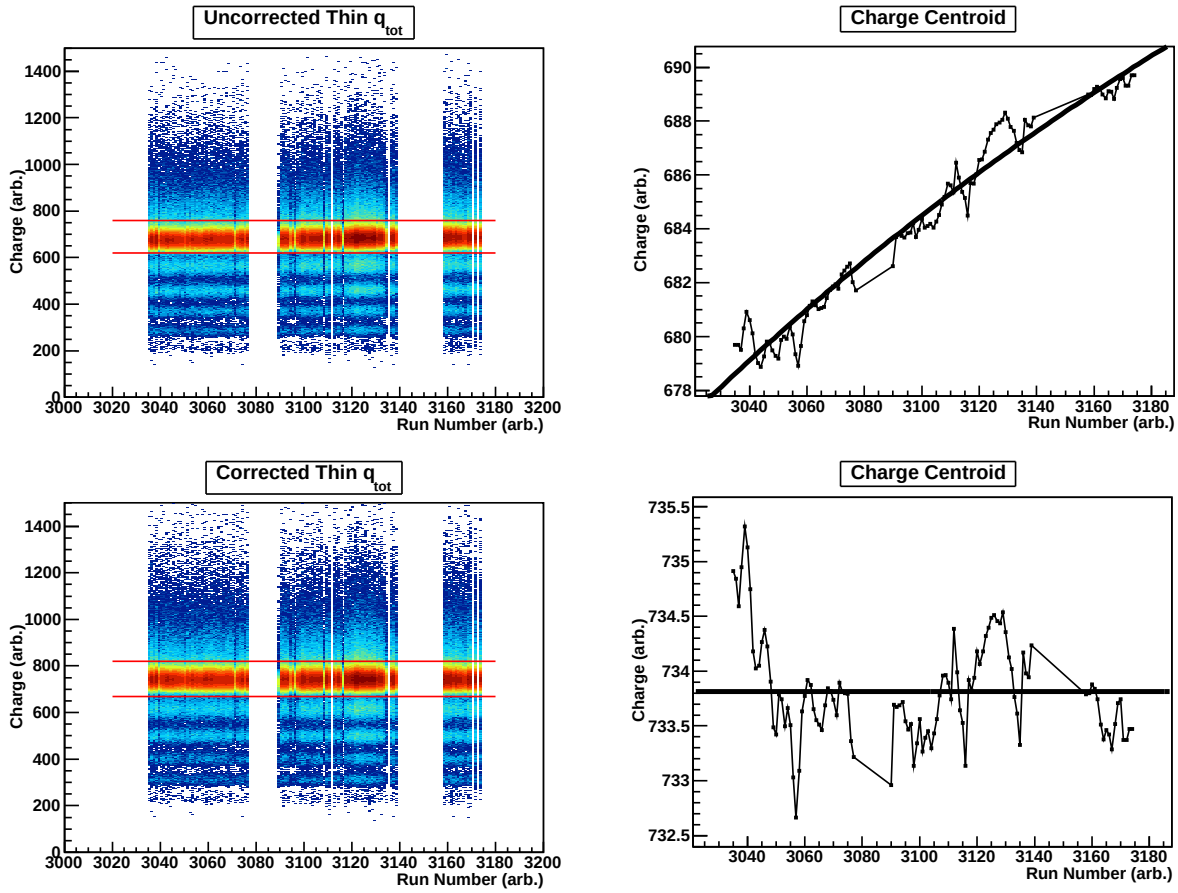

Figure 4.12: Drift correction for charge collection in the thin scintillator. (Top left), Uncorrected charge distribution in the thin as a function of Run Number. (Top right), Uncorrected centroids of the charge distribution as a function of Run Number. (Bottom left). Drift Corrected charge distribution in the thin. (Bottom right) Centroids of the drift corrected charge distribution.

used for all PMTs so the jitter is the same for each timing signal. The jitter is eliminated by subtracting one timing signal from the remaining others after applying the slope of 0.1 ns/ch. In the past the reference signal has been Thin PMT0, however in this experiment this signal would drop out intermittently and so a more stable copy of the signal passing through different electronics was used, called "sweeper trigger". This did not affect the q_{tot}, as the charge signal was always present.

The individual offsets for each PMT were determined using the same method as the gainmatching. Events which hit the center of the detector were selected and the centroid

PMT	Offset [ns]
0	31.3
1	-24.0
2	-74.9
3	-5.94

Table 4.5: Time offsets for the Thin scintillator.

of each PMT was aligned with that of Thin PMT0. The overall offset for Thin PMT0 was determined by the expected time-of-flight for the beam. For this calibration, the beam was ^{20}O at 118 MeV/u impinging upon a 670 mg/cm^2 Be degrader with a flight path of 417.86 cm from the target to the thin. This gives a calculated time-of-flight of $t_0 = 31.28$ ns, and determines the offset of Thin PMT, and hence the offset of the other PMTs. These offsets are listed in Table 4.5. Once the offsets are determined, the calibrated timing signal for the entire detector is formed from the average of each PMT:

$$t_{thin} = \frac{1}{n}\sum_{i=0}^{n} t_i$$

Where n is the number of PMTs that fired for a given event and t_i are the timing signals of each PMT. The individual timing signals of each PMT drifted over the course of the experiment with the worst case being about a 1 ns drift in timing. Because the trends for each PMT are different they were corrected individually. Instead of a global function for the drift, like in the case of the ion-chamber, the offsets for each PMT were varied run-by-run to eliminate this drift. This was done by selecting a reference run, Run3030, and finding the change in timing relative to the reference, $\delta t = t - t_{ref}$, and subtracting δt from the observed time. A list of δt was then stored in a hash-table so that the calibration could be performed run-by-run. Figure 4.13 shows the drift in the combined signal and the effect of the correction. The gradual shift in timing is removed.

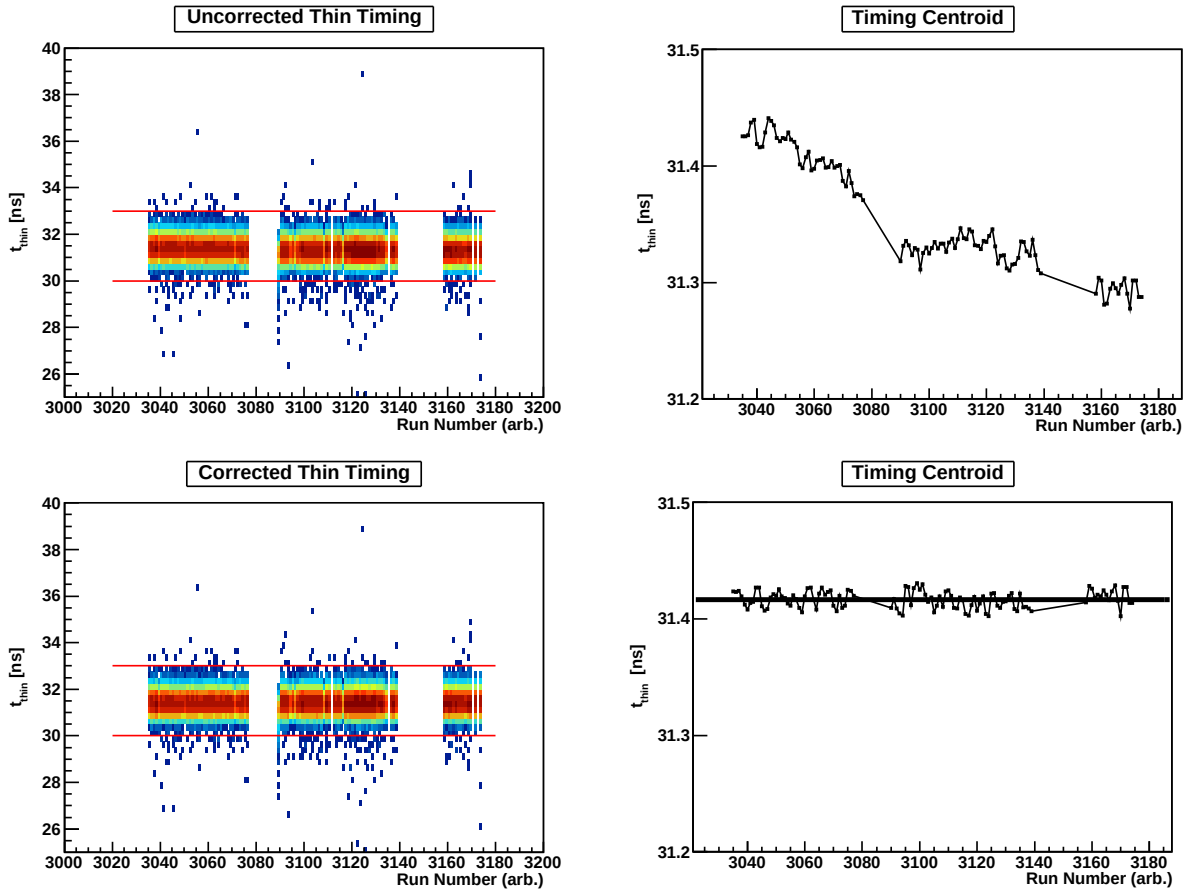

Figure 4.13: Drift correction for the timing of the thin scintillator. (Top-left) The average time t_{thin} is shown as a function of run number. (Top-right) The centroid of the timing signal as a function of run number. (Bottom-left) Drift corrected thin timing as a function of run number. (Bottom-right) Corrected timing centroids using the offset method.

4.1.1.4 Target and A1900 Timing Scintillator

There are two other timing scintillators in the beam-line. The A1900 scintillator was placed immediately after the A1900, and the target scintillator was placed 105.92 cm upstream from the center of the LD_2 target. The target scintillator has a single PMT attached to it that records both time and charge. The A1900 scintillator was located 10.579 m upstream and only the timing signal was recorded. Both TDCs for the scintillators have a fixed slope of 0.1 ns/ch, and their calibration follows the same method as the individual thin PMTs. After the TDC channel is converted to ns, the FPGA jitter is subtracted. This leaves a global

A1900 and Target Scint.	Offset [ns]
A1900	-123.6
Target	52.61

Table 4.6: Timing offsets for the Target and A1900 Scintillators.

offset to be determined. To find the offset, a "beam down center" run was used with the an ^{20}O beam and a ^{9}Be degrader. The offsets are set so that the velocity of the unreacted beam is properly reproduced between the two scintillators. They can be found in Table 4.6.

Both the target scintillator and the A1900 exhibited a gradual time dependence. This is corrected in the same manner as the thin PMTs. A reference offset is chosen and a δt calculated relative to that offset on a run-by-run basis. The calibrated time is then shifted δt to remove the drift. The drift correction for the target scintillator is shown in Fig. 4.14, and for the A1900 scintillator in Fig. 4.15.

4.1.1.5 Hodoscope

The CsI(Na) array, or Hodoscope, did not function properly during this experiment due to a smoothing of the crystal surface, likely due to the formation of water droplets which caused the teflon wrapping to come in contact with the crystal face. The detectors rely on total internal reflection to direct the light produced from an event to a PMT at the end of the CsI(Na) crystal. Normally the surface of the CsI is sanded so that the surface is rough leaving gaps between it and the teflon covering. For total internal reflection to occur, the interface of the crystal and the teflon must have a gap so that the when the light is incident on the medium in between the crystal and its wrapping it is not transmitted. When the angle of incidence exceeds a critical angle, the amplitude of the transmitted wave becomes zero. The critical angle depends on the index of refraction of the materials:

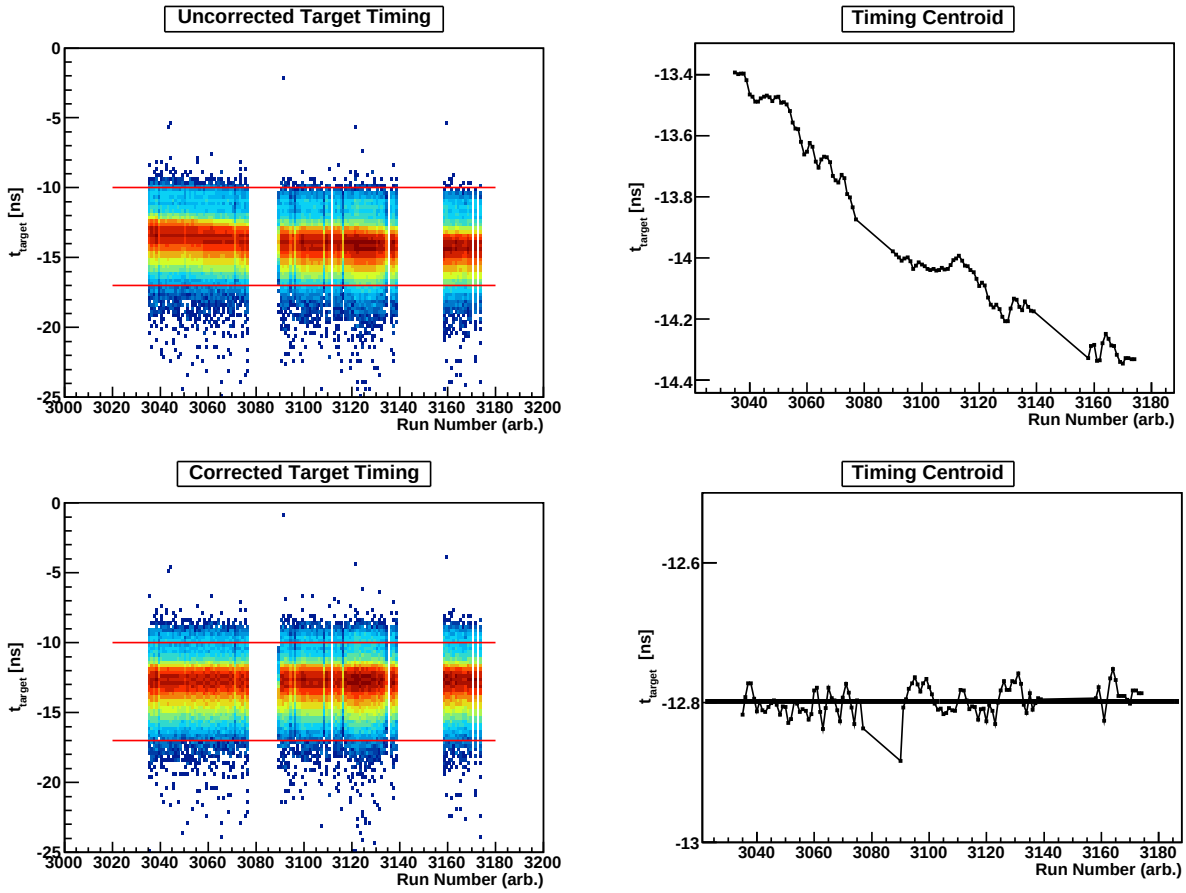

Figure 4.14: Drift correction for the timing of the target scintillator. (Top-left) The timing signal is shown as a function of run number. (Top-right) The centroid of the timing signal as a function of run number. (Bottom-left) Drift corrected target scintillator timing as a function of run number. (Bottom-right) Corrected timing centroids using the offset method.

$$sin(\theta_c) = n_{medium}/n_{CsI}$$

However, if the size of gap between the teflon and CsI becomes comparable to the wavelength of the light, it can be transmitted through the teflon resulting in poor resolution. CsI(Na) crystals are hydroscopic. If the crystals were exposed to a humid environment during their manufacture then water droplets could have formed in between the teflon and the surface of the crystal. The resulting condensation can cause the surface to become smooth allowing teflon to stick to the crystal leading to light leaks.

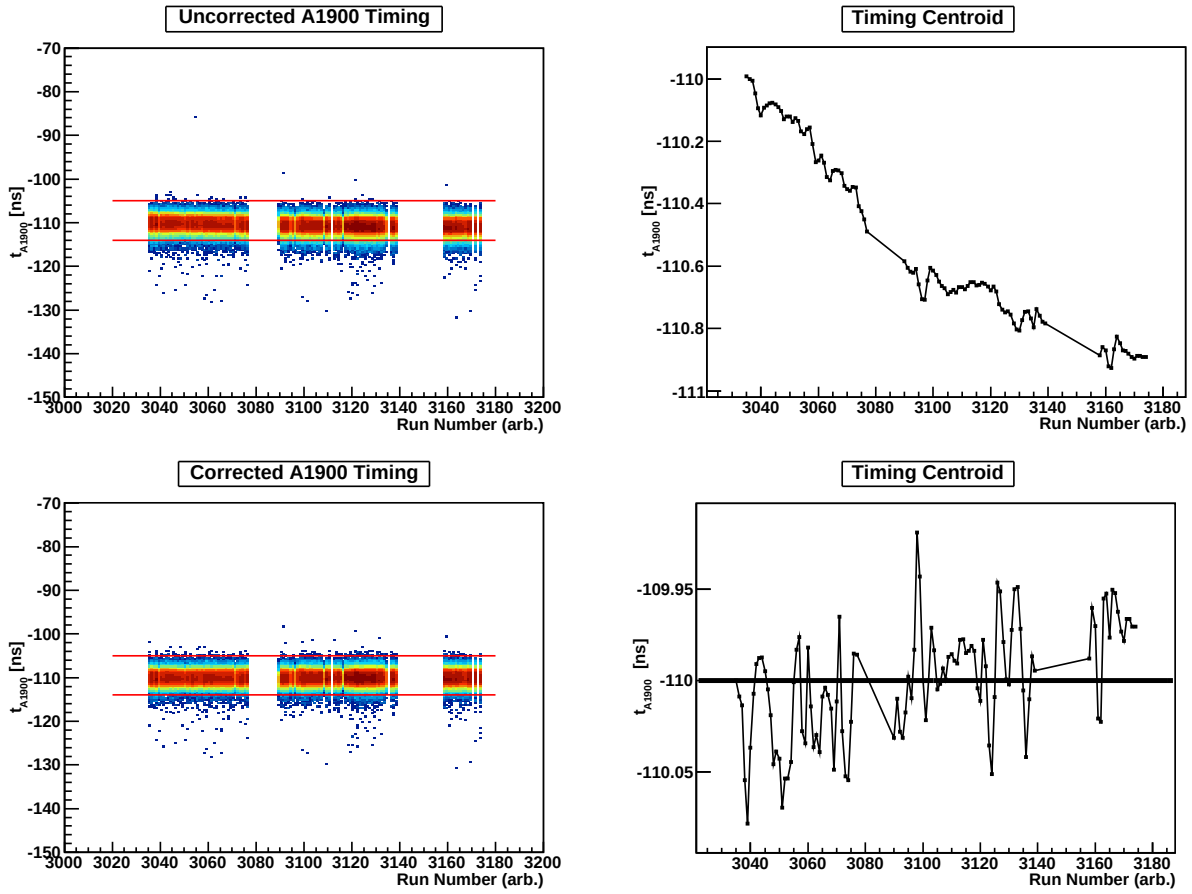

Figure 4.15: Drift correction for the timing of the A1900 scintillator. (Top-left) The timing signal is shown as a function of run number. (Top-right) The centroid of the timing signal as a function of run number. (Bottom-left) Drift corrected A1900 timing as a function of run number. (Bottom-right) Corrected timing centroids using the offset method.

A ^{20}O beam was used to map-out the position dependence of the crystals. By sweeping the beam back and forth the middle row (modules 10-14) of the hodoscope was illuminated. The position on the crystal face can be determined with the CRDCs to $\sim$1 mm resolution. Plotting the total charge collected on the z-axis and the X and Y position in the crystal on the X and Y axis shows unique patterns for each crystal (Figure 4.16.)

It is evident that the signal quality is degraded in areas with low light collection, causing the overal resolution of the array to be significantly worsened. Large portions of the crystals are un-usable. Upon removing the middle-row after the experiment, an inspection confirmed

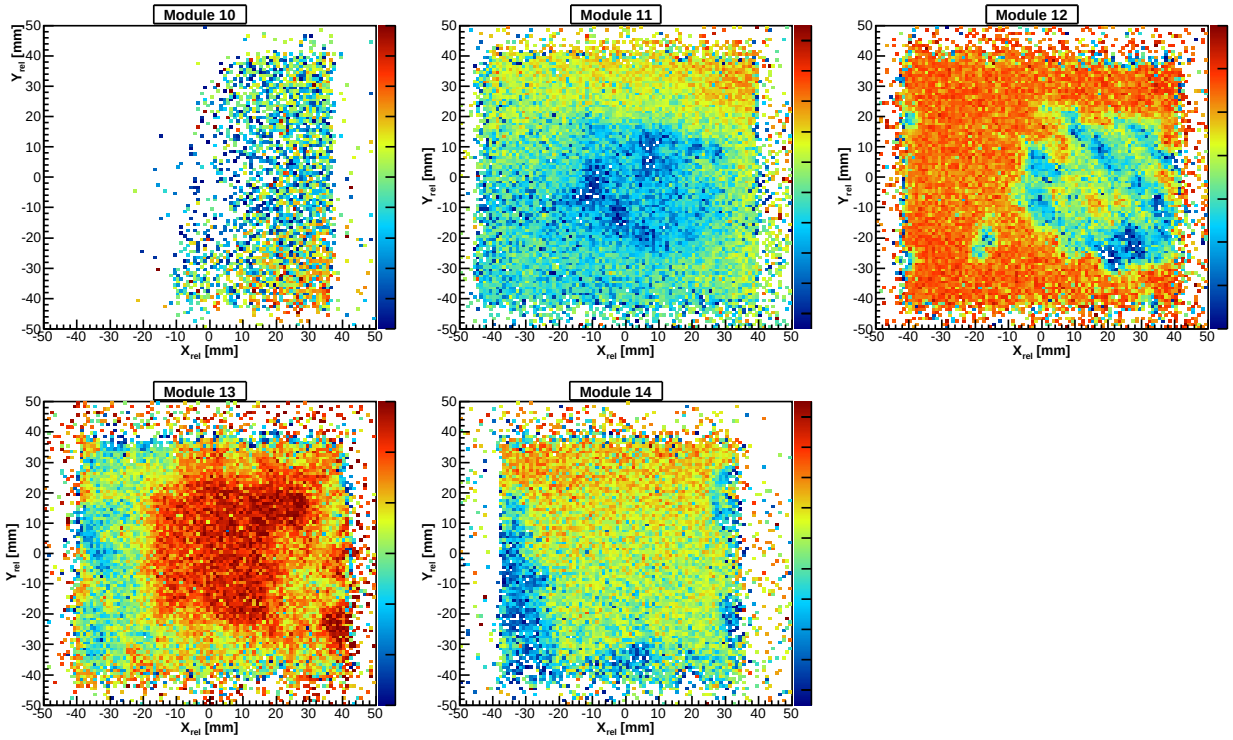

Figure 4.16: Light collection in the middle row of the Hodoscope for Run 3002 where an ^{20}O beam was swept across the focal plane. Ideal behaviour would be a uniform response. On the X and Y axis are the X and Y positions relative to each crystal, the color axis is the total energy deposited.

that the teflon was sticking to the surface. Due to a significant degradation of the hodoscope resolution, this detector remains unused in this analysis.

4.1.2 LD_2 Target

The Ursinus College Liquid Deuterium Target has two quantities that were monitored during the experiment: pressure and temperature. It is important to monitor these quantities during operation of the target to ensure the safety of the target as well track any fluctuations that may occur. The pressure was monitored by a manometer in the gas-handling system that provided a measurement of the target cell pressure. The manometer was controlled by a MKS PDR 200 unit [97], which outputs a raw voltage signal with a resolution of 1 mV that

must be converted into a pressure. The temperature is monitored by a silicon diode which is read-out by a Lake Shore Model 331S temperature controller that outputs an analog signal with a resolution of < 1 mV. The uncertainty on this system is around $\sim$0.25 K according to the manufacturer [98]. (The IEEE-488 analog interface has an accuracy of $\pm$ 2.5 mV, which corresponds to 0.75 K. Factory settings for diodes are between 0.25 - 1 K uncertainty).

To calibrate the temperature and pressure of the cell, the raw signal is converted to the appropriate quantity assuming the following functional forms (as recommended by the manufacturers). For pressure the relation is:

$$P = p_0 * 10^{2*V} \text{ [Torr]}$$

And for temperature:

$$T = t_0 * V \text{ [K]}$$

The coefficients p_0 and t_0 can be constrained simultaneously by fitting the phase-transition of a particular gas. For this experiment, two types of gas were liquefied and data recorded for the phase transition. A neon test gas was used to initially check the target system while deuterium was used for the actual experiment. This provides a method of cross checking, as a calibration to the phase transition of one gas must reproduce the phase transition of the other. The phase transitions of neon and deuterium have been measured and can be parameterized with the following forms.

For neon, data can be obtained from NIST [99, 100]:

$$log_{10}(P) = 3.75641 - \frac{95.599}{T - 1.503}$$

where the units for P are bar, and Kelvin for T. The vapor pressure for deuterium has also been measured [101]:

$$log_{10}(P) = 5.8404 - 70.044/T + \frac{4.59 * 10^{-4}}{(T-23)^2}$$

where P is in mm of Hg and T in Kelvin.

These parameterizations of the vapor pressure are only valid for a specific temperature regime as they are an approximation. For the neon data this interval is from 15.9 - 27 K, and for deuterium it is 14 - 24.5 K. The coefficients p_0 and t_0 can be determined by fitting directly to a known phase-transition. Figure 4.17 shows the fit to the raw phase diagram for D_2 gas observed during liquefaction. From this calibration we see that the D_2 gas did not cross into a region where it would have frozen. The best fit parameters are:

$$p_0 = 9.621 * 10^{-6} \text{ [Torr]}$$

$$t_0 = 30.34 \text{ [K/V]}$$

The calibration can be verified by applying it to the data the neon phase-transition, and is shown in Fig. 4.18. The calibrated data are shown in black, while the NIST data are shown in red. The dashed-lines give an error band. This is determined by systematically shifting the temperature by the uncertainty reported in the neon measurement ($\delta T = 0.5K$ [100]) used to constrain the NIST parameterization. The data fall within the uncertainty of the previous measurement confirming the calibration.

Once the temperature and pressure have been calibrated the target can be checked for any drifts during its operation. Figures 4.19 shows the temperature and pressure over the

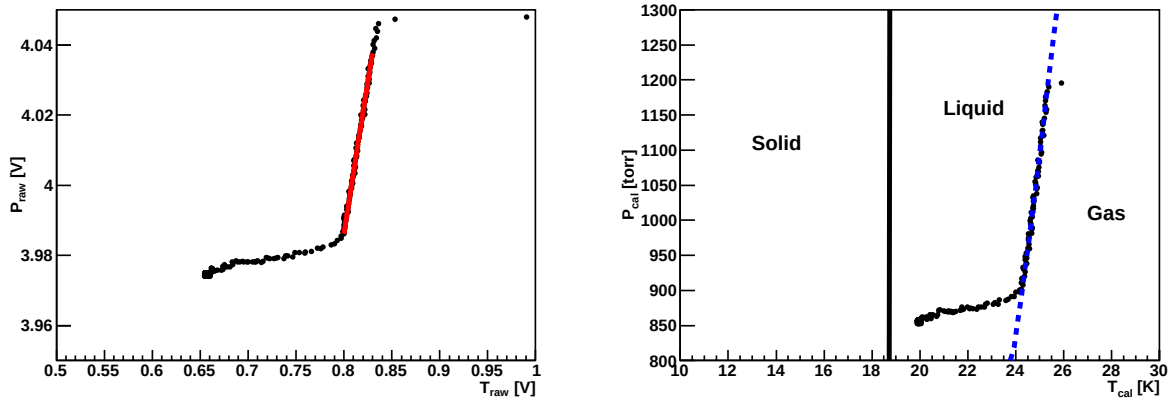

Figure 4.17: Temperature and Pressure calibration of the LD_2 target. (Left) Raw voltages from the EPICS readout from the temperature controller and manometer. The data are in black, the region used to fit the phase transition is highlighted in red. (Right) Calibration to phase-transition (blue line) in deuterium.

course of the experiment. The temperature fluctuation is less than 0.15 K which is well below the uncertainty of the temperature controller. In addition, the pressure is very stable except for a slow drop of about 5 Torr in the middle of the experiment. The pressure equalized for the remaining duration and no further change was detectable. It is not likely a leak or a failure of the target cell. Since this change is less than 1% of the pressure it is neglected.

It is crucial to determine the target thickness. Although the cell is designed to contain 200 mg/cm^2 of LH_2, the Kapton windows can deform under pressure causing the nominal thickness of the target to increase. In addition, the heat-shield of the LD_2 target was wrapped in 5 μm of aluminized mylar to help keep the temperature stable, which adds aditional energy loss, albeit small. The target thickness is determined by measuring the kinetic energy of the unreacted ^{24}O beam in the focal plane and determining the total energy loss. To measure the kinetic energy of the unreacted beam, it is necessary to calibrate the CRDCs and perform the inverse tracking. Details on those calibrations and the inverse tracking can be found in sections 4.1.1.1 and 4.3.

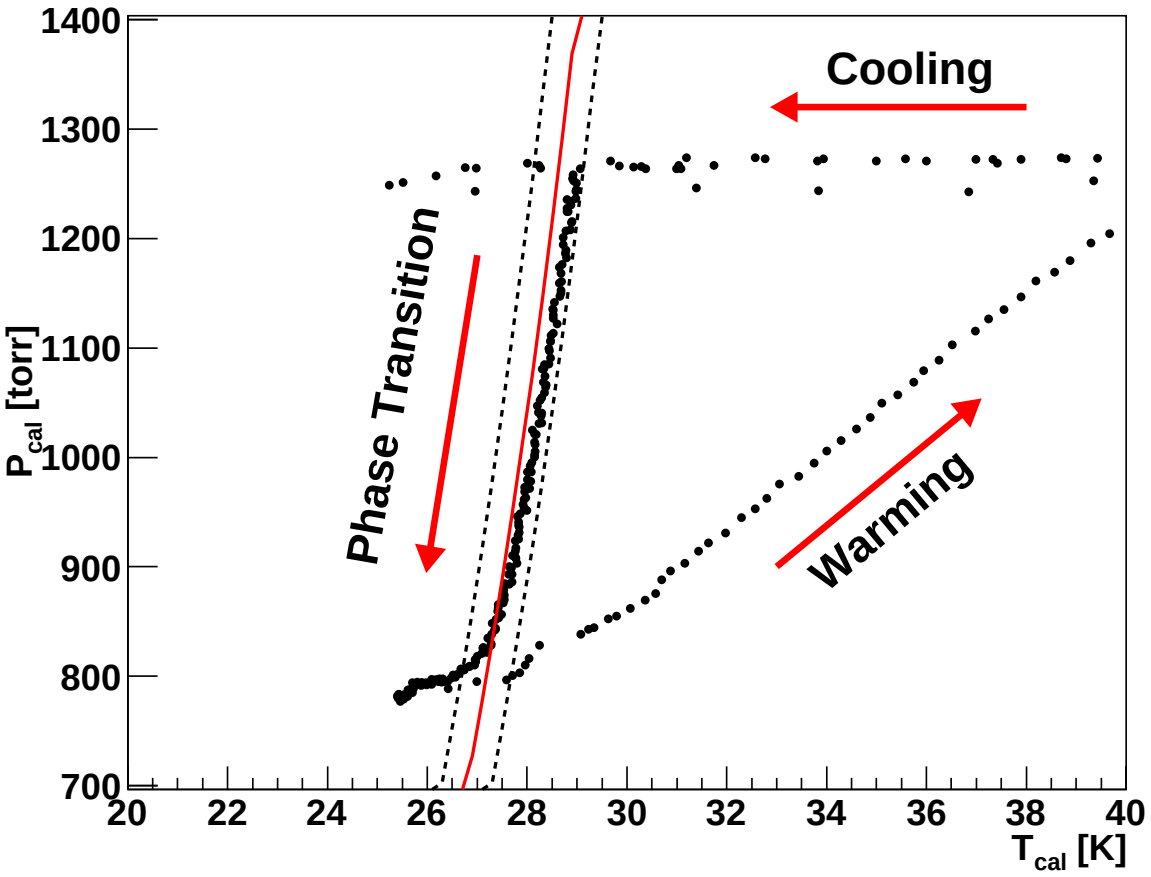

Figure 4.18: Measured phase transition with a neon test gas using the calibration parameters from fitting the deuterium transition. The red line corresponds to data from Ref [100], and the dashed lines are the uncertainty bands given a $\pm 0.5K$ fluctuation. The red arrows indicate data taken during initial cooling, liquefaction, and warming of the target. The events around 26 K and 1200 Torr are a result of a sensor error.

The incoming beam energy is known since the focusing quadrupole triplet before the target was set to a $B\rho$ of 4.03146 Tm thus giving an energy of $E_{beam} = 83.25 \pm 1$ MeV/u for the ^{24}O beam. A measurement on an empty cell gives a reconstructed beam energy of $E_{beam} = 83.4$ MeV/u, which agrees well with the triplet setting.

The kinetic energy of the unreacted ^{24}O is shown after the inverse reconstruction in Fig. 4.20. The peak of the distribution is at $E_0 = 66.4$ MeV/u giving a total energy loss of $E_{loss} = 17.1$ MeV/u. The target thickness can be determined by estimating the energy

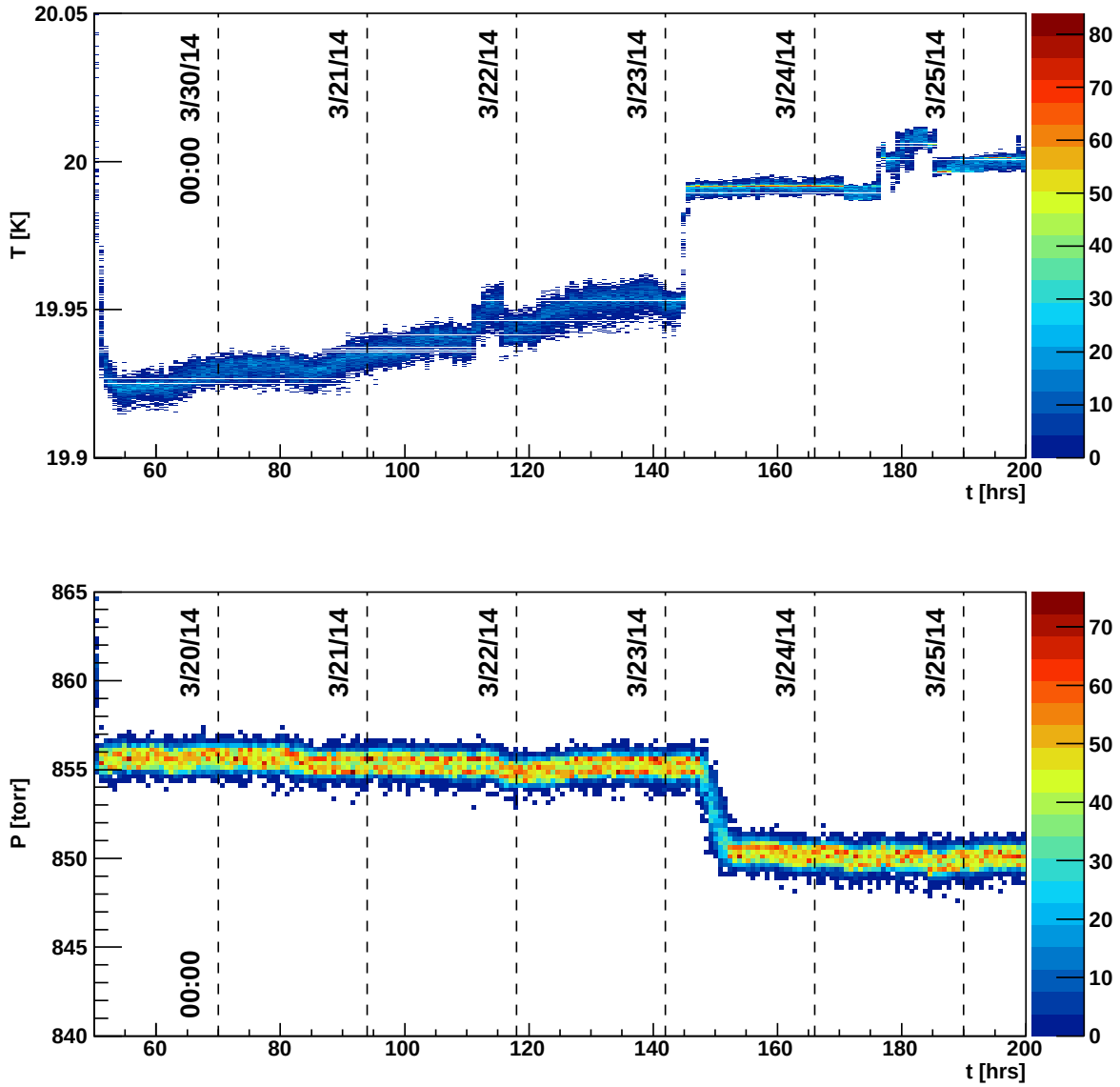

Figure 4.19: Temperature and Pressure fluctuations over the course of the experiment starting from 4:00 AM 3/19/14. Time is measured in hours.

loss with LISE++ [102]. However, this requires knowing the density of liquid deuterium which changes with the temperature. A parametrization of the density as a function of the temperature can be found from data taken at NIST [103]:

$$\rho(T) = 0.1596 + 3.395 * 10^{-3}T - 1.4086 * 10^{-4}T^2$$

Given the observed temperature fluctuations, the average density is $\rho = 0.1712$ g/cm^3 with an uncertainty of about $\pm 1.4 * 10^{-3}$ g/cm^3. This results in an uncertainty in the target thickness of about 10 mg/cm^2, corresponding to about 0.2 MeV/u in the energy loss of the beam. At this density, the nominal thickness of the target is 514 mg/cm^2.

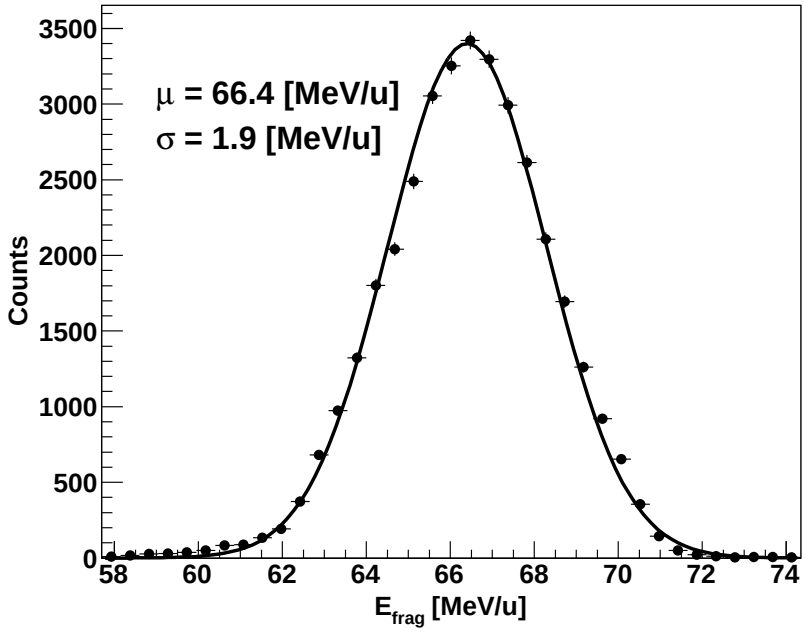

Figure 4.20: Measured kinetic energy of the ^{24}O beam after passing through the full LD_2 target.

Using a density of $\rho = 0.1712$ g/cm^3 for LD_2, the resulting energy after passing through the mylar, kapton, and deuterium can be calculated and compared to experiment. The target thickness was determined to be $t = 630^{+45}_{-40}$ mg/cm^2, where the error arises from the uncertainty in the beam energy ($\sigma_{beam} = 1$MeV/u). This is significantly larger than the nominal thickness. Repeating this process with the ^{27}Ne contaminant beam yields a thickness of $t = 650 \pm 30$ mg/cm^2. There is approximately a 40 mg/cm^2 uncertainty from the beam energy, 5 mg/cm^2 systematic uncertainty in the choice of beam, and 10 mg/cm^2 due to the density fluctuation of the target, giving a combined thickness of $t = 640 \pm 45$

mg/cm^2.

Additionally, this uncertainty in the target thickness results in approximately a $0.5 - 1$ MeV/u uncertainty in the energy loss which ultimately broadens any decay energy measurement.

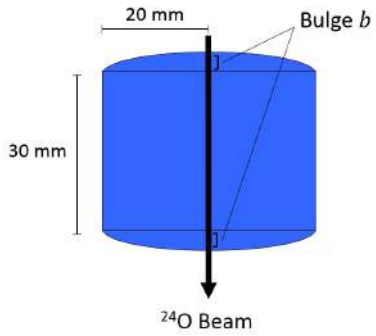

Figure 4.21: A 3.4 mm bulge in the LD_2 drawn to scale.

The excess thickness of the target is a result of the bulging of the Kapton windows. To account for the observed thickness, this bulge would have to be approximately $b = 3.4$ mm which is roughly 10% the length of the target cell. Figure 4.21 shows a diagram of the bulge drawn to scale. The size of the bulge can be estimated using an empirical result derived for clamped windows. From the BNL OSHA safety guide (June 7, 1999) "Glass and plastic window design for pressure vessels," [104], the bulge b can be expressed in terms of the pressure gradient ΔP, the Young's Modulus of Kapton, E, the window thickness $t = 125$ μm, and window diameter (d = 38 mm):

$$\frac{\Delta P d^4}{E t^4} = K_1 * \left(\frac{b}{t}\right) + K_2 * \left(\frac{b}{t}\right)^3$$

The constants K_1 and K_2 are derived for windows which are clamped along their edge, and are $K_1 = 23$ and $K_2 = 55$ respectively. Using the measured 850 Torr pressure differential gives a value of $b = 2.5mm$ which is less than the bulge needed to explain the observed

thickness, however this expression is only an estimate.

4.1.3 MoNA-LISA

The raw output from the PMTs in MoNA and LISA provide a charge and a time measurement that reflects the total light collected by the PMT and the time of its arrival. Several calibrations are needed to convert these measurements into deposited charge, position, and interaction time. First, each PMT must be gainmatched and the QDC channels calibrated. Then the corresponding TDCs calibrated, and a conversion from time-difference to position within a bar determined. Each bar must then be placed in time relative to the first bar in each table. Finally each table is placed in time relative to the target. The majority of calibrations can be done with cosmic rays. Cosmic data was taken both before and after the experiment. Cosmic muons deposit roughly 2.05 MeV/cm [105] in each detector as they pass through with a velocity close to the speed of light. Thus approximately 20 MeV electron-equivalent (MeVee) of light is deposited into each bar. Because of the dependence of the light yield in organic scintillators on the type of particle, the MeVee is used to quantify the absolute amount of light produced. 1 MeVee is defined as the amount of light produced by an electron with 1 MeV of kinetic energy. Since the speed of the muons is close to c they can be used to determine the relative timing of the bars.

4.1.3.1 Charge Calibration (QDC)

Each PMT was gainmatched by changing the voltages until the peak from cosmic muons appeared in roughly the same channel for all PMTs. This process was repeated until the cosmic peak was at roughly channel 900, and until the individual fluctuations in a PMTs voltage were below 10 V. Typical voltages range from 1300-1950 V in MoNA and LISA.

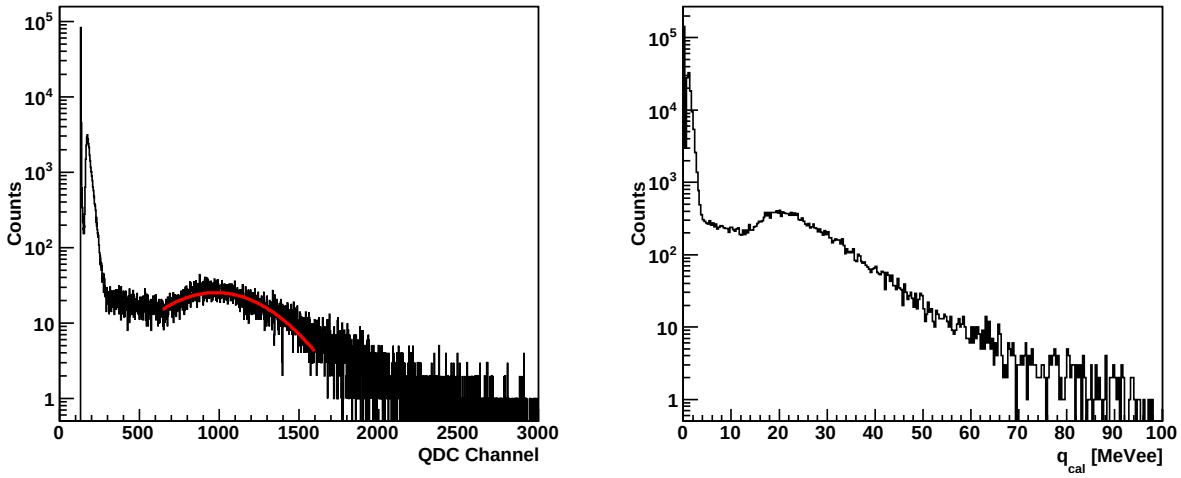

Figure 4.22: Example spectra used for QDC calibration in MoNA-LISA. (Left.) Raw QDC channels for data taken with cosmic rays. The red curve is a gaussian fit to the cosmic-ray peak. (Right) Pedestal subtracted and calibrated charge spectrum. The cosmic ray peak appears around 20-30 MeVee.

The QDC calibration is done by taking cosmic data after having gainmatched all PMTs and determining a linear relation between raw channels and MeVee by finding the pedestal peak and the cosmic peak:

$$q_{cal} = (q_{raw} - q_{ped}) * m_q$$

Where m_q is the QDC slope in MeVee/ch and q_{raw} is the raw QDC channel and q_{ped} the pedestal (ch). A threshold is placed above the pedestal, determined by:

$$Q_{thresh} = q_{ped}/16 + 2$$

The slope is given by the difference between the cosmic peak and the pedestal. The factor of 16 is necessary to convert the pedestal channel from 12 bits to 8 bits, as the pedestal and threshold are stored as 12 and 8 bit numbers respectively. The 2 assures that the threshold is placed above the pedestal.

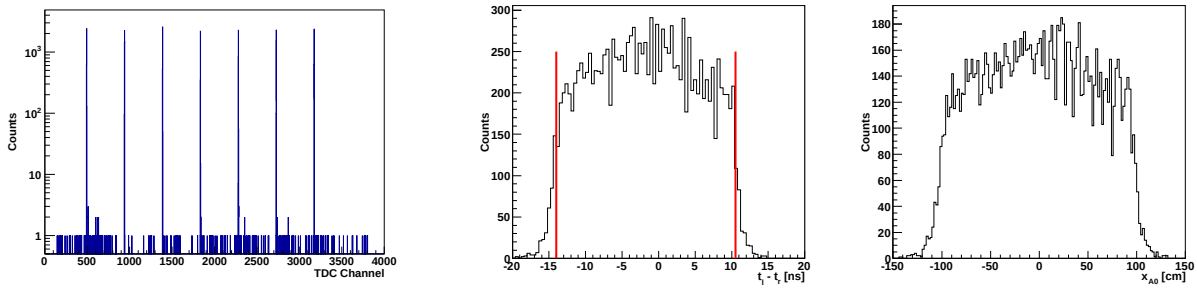

Figure 4.23: TDC and X-position calibration spectra. (Left) Raw TDC channels for a run taken with a time calibrator with a fixed interval of 40 ns, this determines the TDC slope. (Middle) Raw time-difference spectrum used to calculate the X-position. The red lines indicate the physical ends of the bar. (Right) Conversion of time-difference into X-position. Data taken with cosmics which fully illuminate the array.

This process is automated with a procedure that finds the location of the pedestal and cosmic peak via gaussian fitting. An example fit is shown in Figure 4.22.

4.1.3.2 Position Calibration (TDC)

MoNA and LISA use time-to-digital converters (TDCs) to measure timing differences of events within the array. When a TDC channel receives a pulse from the anode of a PMT it begins charging a capacitor until it receives a delayed stop signal from the logic of the electronics. The amount of charge on the capacitor corresponds to the time the TDC was charging. There is slight variation in the capacitors of each TDC and so a slope must be determined for each TDC. This is done by pulsing the system with an Ortec NIM Time Calibrator module (Model 462), which provides pulses at specific intervals to the TDCs. For this experiment, the pulse rate was set to 40 ns intervals and the TDC range was 350 ns. Figure 4.23 shows an example TDC spectra for this calibration. The "picket-fence" is spaced in 40 ns intervals, and can be used to calculate a slope for the TDC. A slope is determined for every TDC channel in MonA and LISA. They are typically around 0.09 ns/ch.

Once the slope of each TDC is calibrated, the time differences between the left and right

PMTs of a bar can be used to determine the position of an event. Using cosmic rays, the full length of each MoNA/LISA bar was illuminated and spectra of left-right time differences were generated. A fermi-function is used to find the edge of each bar, from which the time-difference is converted to a position via a linear relationship. Figure 4.23 shows an example raw bar-position in a LISA and the corresponding calibrated position. The slope is determined by the edge of the time-difference, and the offset is such that the bar is centered in its own reference frame.

4.1.3.3 Time calibration (tmean + global)

It is important to know the relative timing between each detector in the array, so that the neutron time-of-flight can be accurately determined. While the time of an event is determined by the average of the PMTs, a timing offset needs to be determined to place each bar relative to a reference bar. Finally, the reference bar needs an absolute offset to place it relative to the target. The timing offset between bars is determined using cosmic ray data, while γ-rays from the target are used to determine the offset relative to the target. The known velocity of cosmic-ray muons can be used to determine the timing between events which pass through all 16 bars in a layer, either vertically or diagonally. Only events which triggered a majority of the bars in a layer and deposited approximately 20 MeV in each bar were used.

Except for the first layer, the top bar of each layer is used as a reference and each subsequent bar in a given layer is placed relative in time to the top bar. For events which pass vertically through the array the travel time is:

$$t = \frac{d}{v_\mu}$$

Where d the distance between interactions, and $v_\mu = 29.8$ cm/ns is the speed of the muon. The difference between the expected and observed time determines the offset. Once each vertical layer is placed in time, the layers themselves need to be placed relative to the bottom bar of the front layer in each "table". This is done using diagonal tracks which travel from the top of each layer to the bottom bar of the front layer. Figure 4.24 illustrated the muon tracks used to perform this calibration.

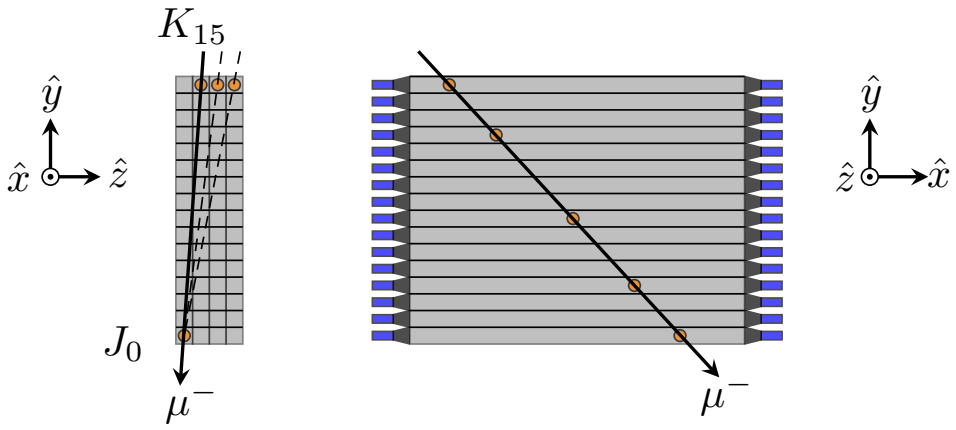

Figure 4.24: Schematic of a cosmic ray tracks used to determine the relative offsets between each bar. Offsets within a table are with respect to the bottom bar in the front layer. J_0 and K_{15} are example bars in the first and second layer of LISA.

Once each table (1 for MoNA, 2 for LISA) is placed in time relative to the bottom bar of the front layer, a final offset must be determined to place that bar with respect to the target. To accomplish this, γ-rays emitted from interactions in the target are used since their velocity is well-defined and the positions of the bars are well-known. The offset is set such that the reconstructed speed of the γ-rays is the speed of light.

Due to the low beam rate (< 200 pps), the entire set of production data was necessary in order to gain enough statistics. In addition, a gate was placed on ^{22}O fragments coming from the ^{24}O beam because the unreacted ^{24}O produces a large background when it stops at

LISA ($\Theta = 0$)	LISA ($\Theta = 22°$)	MoNA [ns]
411.66	410.53	434.54

Table 4.7: Global tmean offset in nanoseconds for each table in MoNA-LISA.

the end of the sweeper focal plane. Fig. 4.25 shows the results of the calibration, the γ-ray peaks show up at 29.97 cm/ns for each table. Table 4.7 lists the final time offsets for MoNA and LISA.

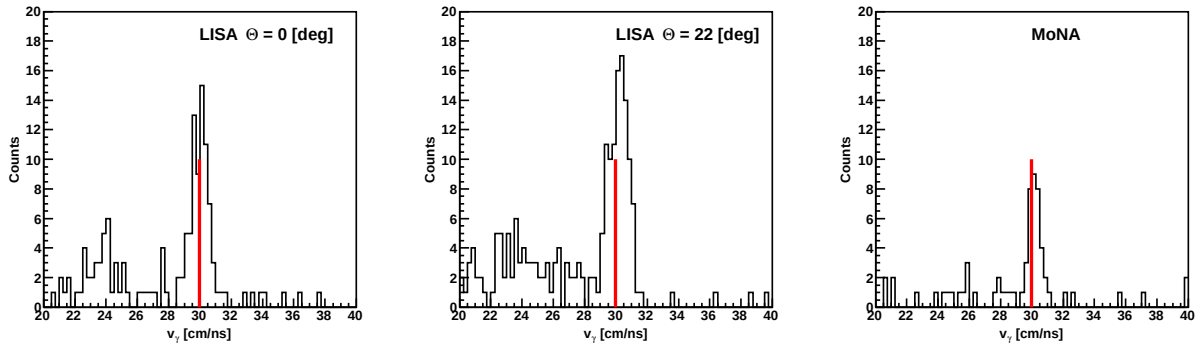

Figure 4.25: Reconstructed velocity of γ-rays coming from the target in coincidence with ^{22}O fragments. The global timing offset is varied for each table to align the centroids at $v = 29.97$ cm/ns.

4.2 Event Selection

This section details how the data are reduced to the physics events of interest. Over the course of the experiment, there are many events that are recorded that are unrelated to the physical process one may wish to study. This may include background, contaminant beam, or events that do not create a big enough signal to be useful and are of poor quality. For example, some of the CRDC or ion chamber pads malfunctioned and produced data that are not useful. The physical processes of interest are ^{24}O(d,d')^{24}O* $\rightarrow^{22}$O + 2n and ^{24}O(-1p)^{23}N $\rightarrow^{22}$N + 1n, which require selection of the beam and reaction products in coincidence

with neutrons.

4.2.1 Beam Selection

The coupled cyclotrons provided an ^{24}O beam with 32% purity at an intensity of 0.6 pps/pnA at 83±1 MeV/u, with the major contaminant being ^{27}Ne. There are however a significant amount of contaminants created in the wedge of the A1900. The magnet before the target was set to a central rigidity of $B\rho = 4.03146$ Tm corresponding to a beam velocity of 11.89 cm/ns. Ideally, to identify the beam components, one would send the beam into the focal plane without a target. However due to the nature of the setup of the Liquid Hydrogen Target, it was impossible to have a data set with no material in the beam-pipe. The closest approximation that could be achieved was to warm the target to 50 K where it would be in a gaseous less-dense state and send the beam through the foils, which cause an energy loss of around 1 MeV/u. Using a warm-target run, the beam was sent into the focal plane and element identification was achieved by looking at dE vs. $ToF_{target \rightarrow thin}$.

One can remove the wedge fragments by correlating the time-of-flight from the end of the A1900 to the target with the time difference between the RF signal from the cyclotrons and the A1900. Fragments with the same $B\rho$, but different Z and A will have different velocities, and so separation can be achieved. Here, the RF signal from the K1200 cyclotron is used. The selection of ^{24}O is shown in Figure 4.26, along with the Z identification of the beam-components in the ion chamber.

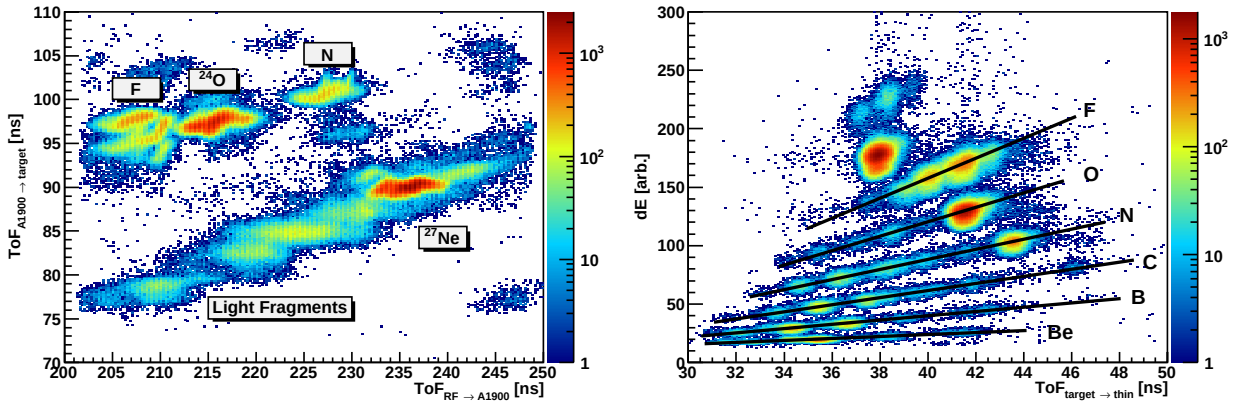

Figure 4.26: (Left) Separation of the ^{24}O beam by time-of-flight from the other beam contaminates. (Right) Energy loss vs. time-of-flight spectrum for all beams and reaction products. Lines are drawn to guide the eye for each element.

4.2.2 Event Quality Gates

To separate isotopes and reconstruct their energies and momenta, it is necessary to have accurate position information in the CRDCs. Occasionally the CRDCs failed to collect all the charge deposited by an event resulting in an unreliable position determination. These events can be removed by applying quality gates to the CRDCs, as events that have a pathological charge distribution will give an unreliable position. These events can be identified by looking at the σ of the gaussian fitting algorithm for the X position as a function of the padsum – or integrated total charge. The CRDC quality gates for CRDC1 and CRDC2 are shown in Figure 4.27. An additional quality gate is made between the CRDCs. There are some events that deposit low charge in one detector, but high charge in the other. The tracking of these events can be unreliable. A gate is placed around events that behave linearly in the charge deposition between the two detectors. This cut is shown in Figure 4.28.

Since the Y-position in the CRDCs is determined by a time difference between an interaction in the thin scintillator and the collection of charge carriers in the anode of the CRDC, there are some events where the charge carriers were unable to be fully collected resulting

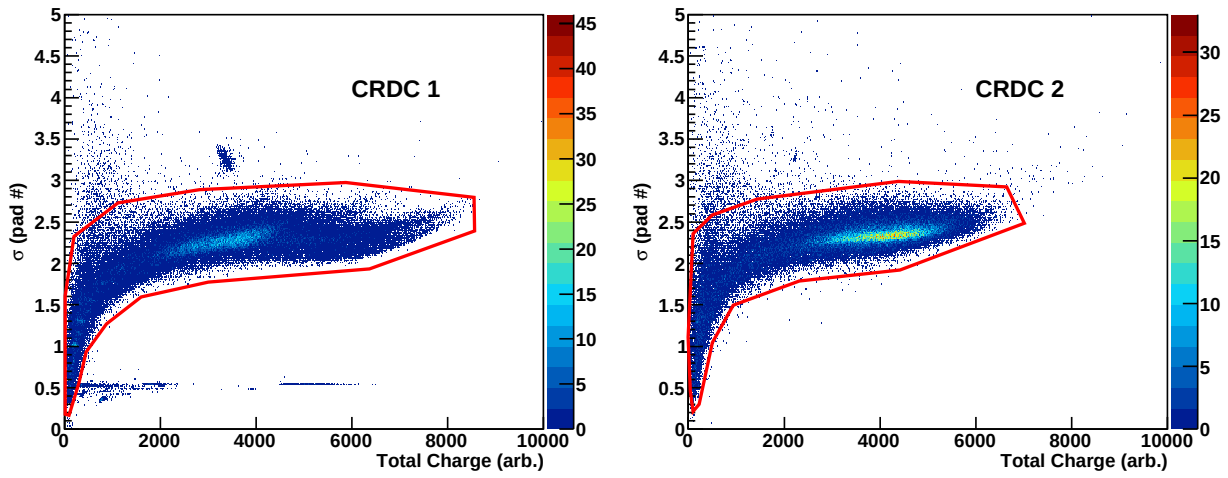

Figure 4.27: σ vs. total integrated charge in the CRDCs. Quality gates are drawn in red.

in a poor determination of the Y-position. These events are removed by requiring a valid Y-position in the calibration algorithm.

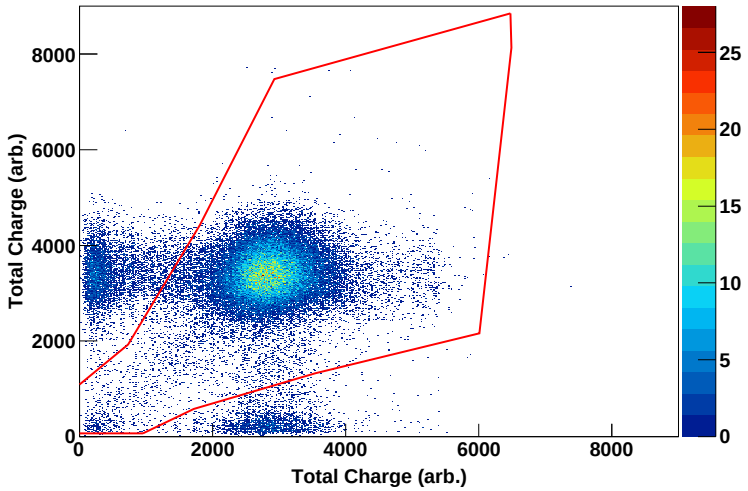

Figure 4.28: Total integrated charge of CRDC1 (Y-axis) vs. CRDC2 (X-axis). A gate, shown in red, is drawn around events that deposite a similar charge in both detectors. A gate is applied to select the ^{24}O beam.

Additional cuts are made on proper charge collection in the PMTs of all timing scintillators. A good signal is required in the RF, A1900, target scintillator, and the thin scintillator. This ensures that the events of interest have a good signal throughout the entire system.

4.2.3 Element and Isotope Identification

Several reaction products were expected from the ^{24}O beam on the LD_2 target. The sweeper was set to a central $B\rho = 3.524$ Tm (320 A), corresponding to the expected energy of (d,p) reaction products. The acceptance of the sweeper is approximately $\pm 8\%$ in rigidity, and so only a fraction of the isotopes produced made it into the focal plane. For this experiment, the reaction products include $^{22-24}$O, $^{18-22}$N, $^{16-18}$C, $^{13-15}$B, and $^{10-12}$Be.

Element separation is achieved by the correlation between the energy loss dE in the ion chamber and the time-of-flight from the target to the thin scintillator. The Bethe-Bloch relation gives the energy loss as a function of several parameters, including the density of the material, mean excitation potential, but most importantly the charge Z and the velocity β:

$$-\frac{dE}{dx} \propto \frac{Z^2}{\beta^2} * f(\beta)$$

The full explicit formula can be found in Ref. [91] (pg. 31). Element separation can be achieved by plotting the energy loss as a function β, or the time-of-flight. A $dE - E$ measurement could not be cleanly made due to poor resolution of the hodoscope. Figure 4.29 shows the element idenfication for products from the ^{24}O beam.

The next step is isotope separation. Ideally, a dipole magnet will separate isotopes by their rigidity. Given a set of isotopes with the same $B\rho$, their velocity can be written as:

$$v = \frac{\Delta L}{\Delta t} = \frac{B\rho q}{m} = \frac{B\rho q}{A m_u} \propto \frac{1}{A}$$

Where q is the charge, L the flight path and t the time-of-flight. Thus the time-of-flight and mass are proportional.

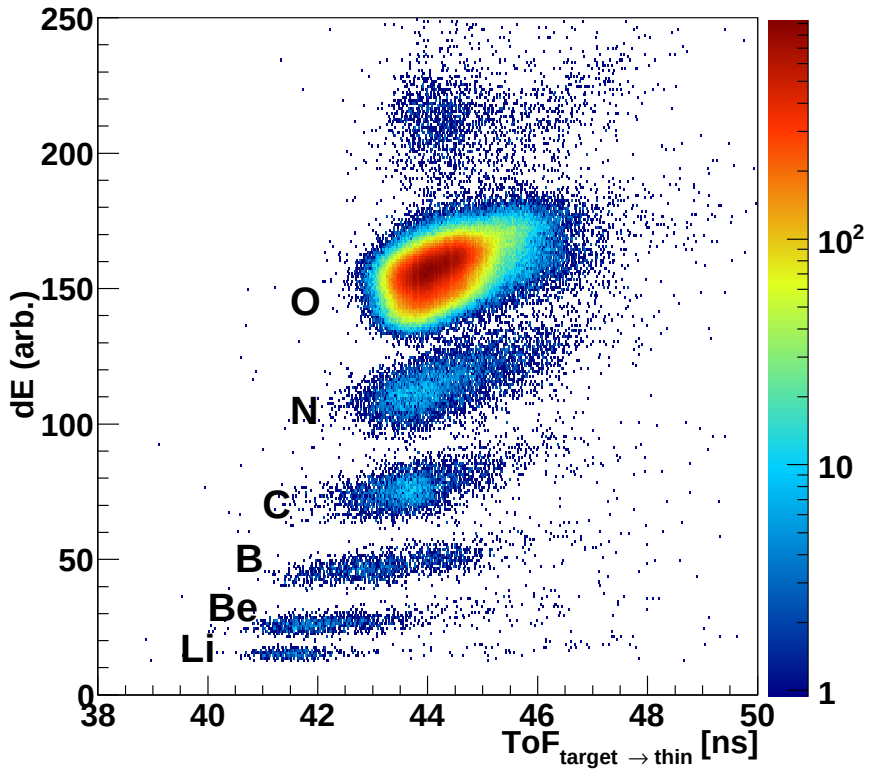

Figure 4.29: dE vs. ToF for reaction products coming from the ^{24}O beam. Coincidence with a neutron is not required.

In practice however, the distributions are broad which makes separation difficult since there is variation in both L and the $B\rho$. This variation arises from several factors including the emittance of the beam, straggling within the target, the nuclear dynamics of the reaction, and the momentum kick from neutron evaporation.

The energy resolution of the hodoscope or the thin scintillator is not sufficient to separate isotopes. However, the rigidity and L of the charged particles are related to their emittance in the sweeper focal plane. To fully untangle the isotopes, it is necessary examine the correlation between the time-of-flight, dispersive angle and position. The convolution between these parameters is most clear for the lightest isotopes and can be seen when plotted in 3D as in Figure 4.30.

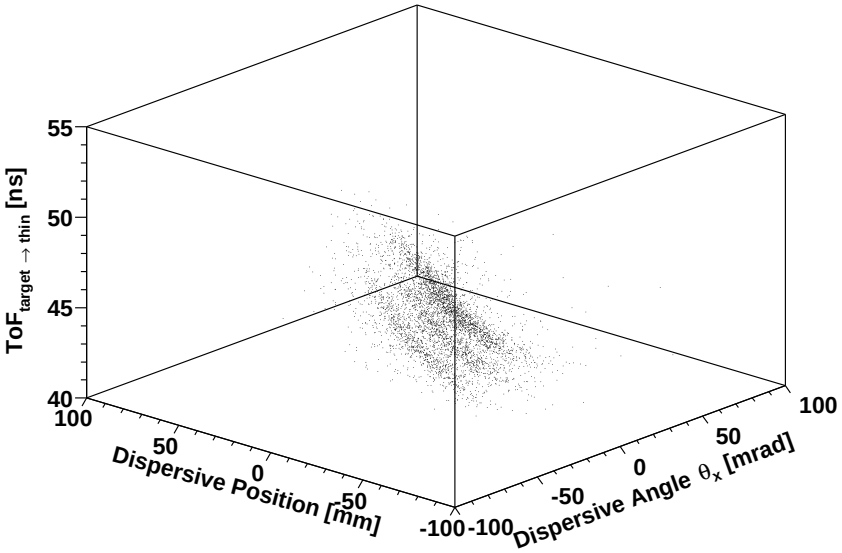

Figure 4.30: 3D correlations for dispersive position, angle, and time-of-flight showing isotope separation for the carbon isotopes.

To untangle this correlation, a projection onto the dispersive angle and position axes is made for a given ToF slice. Contours of iso-time-of-flight are then fit to a quadratic form:

$$f(x) = a_2 * x^2 + a_1 * x + a_0$$

An example of this contour is shown in Fig. 4.31 for the oxygen isotopes. From this quadratic expression a parameter describing both position and angle for constant ToF is constructed:

$$t(x, \theta_x) = \theta_x - f(x)$$

Plotting this parameter against the time-of-flight shows isotope separation (Fig. 4.31). A rotation will give a 1-dimensional parameter to cut on for isotope separation. This is accomplished by a linear fit to one of the isotopes:

$$t_{corr} = t_{target \to thin} + m_0 * t(x, \theta_x)$$

In addition, the large gap of the sweeper creates some dependence on the y-position and y angle. Although it is in the non-dispersive direction, the sweeper field is not completely uniform. The correction can also be taken to higher orders than quadratic making the more general form:

$$t_{corr} = m_0^{-1} * t_{target \to thin} + t(x, \theta_x, y, \theta_y, ...)$$

Where the function $t(x, tx, y, ty, ...)$ is a linear combination of all the terms listed in Table 4.8 with their respective coefficients. While this method provides a corrected time-of-flight for isotope separation, it does not identify the mass. A simple way to determine the mass of the oxygen isotopes is to identify the beam spot, however this luxury does not exist for the other isotopes. Re-examining the Bethe relation and assuming non-relativistic kinematics as well as a constant $B\rho$:

$$\Delta E \propto \frac{Z^2}{v^2}$$

Recall that $B\rho = p/q = mv/Z$, thus $v^2 = Z^2(B\rho^2)/m^2$. Substituting this into the Bethe relation we obtain:

$$\Delta E \propto \frac{Z^2}{v^2} = \frac{Z^2}{Z^2(B\rho)^2} m^2 \propto m^2$$

Hence $\Delta E \propto A^2$. In addition, the time-of-flight is inverse proportional to the velocity thus:

$$ToF \propto \frac{A}{Z}$$

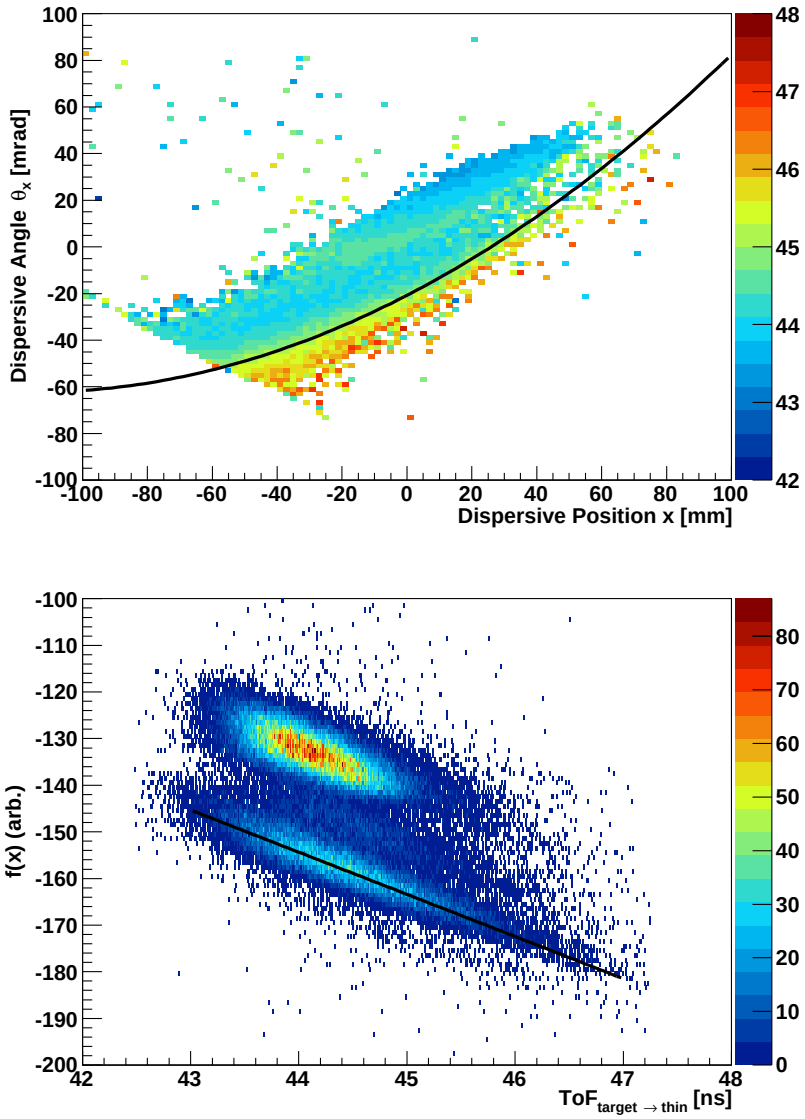

Figure 4.31: Projection of Fig. 4.30 onto the 2D plane of ToF vs. dispersive position for the oxygen isotopes. The contour of iso-time-of-flight is shown in black. This correlation, when plotted against the time-of-flight shows separation for the oxygen isotopes (Right), and can be rotated in this plane for the purposes of making a 1D gate.

Parameter	Coefficient
$t_{target \rightarrow thin}$	7.8231
x	-0.5871
x^2	$-1.7182 * 10^{-3}$
θ_x	0.98959
θ_x^2	$6.1376 * 10^{-4}$
θ_x^3	$-1.51604 * 10^{-5}$
y	$6.04954 * 10^{-2}$
y^2	$5.44903 * 10^{-3}$

Table 4.8: Time-of-flight correction coefficients for isotope separation.

A plot of ΔE vs. ToF_{corr}, should then produce a matrix where each nucleus is uniquely identified since A and Z are discrete. Figure 4.32 shows how nuclei fall in this matrix for various combinations of A and Z (some fictional), with the only constraint being $Z \leq A$.

What is important to notice, is that for integer values of A/Z, different elements fall directly above one-another in a vertical line. Making a plot of ΔE vs. ToF_{corr} shows this behaviour and the isotopes are easily identified. Immediately below the beamspot with the same $A/Z = 3$ is ^{21}N, making the heaviest nitrogen isotope in the acceptance ^{22}N. Continuing along, we see that other heaviest elements are ^{18}C, ^{15}B, and ^{12}Be. A neutron coincidence gate is required in MoNA to reduce the background caused by the unreacted beam. No unbound states in the lithium isotopes can be seen as the statistics are too low. The only lithium isotope in acceptance is ^{9}Li, however there are no neutrons in coincidence with this fragment.

The one-dimensional projections for isotope separation are shown in Figure 4.34 and Figure 4.35 for oxygen and nitrogen respectively. A line is drawn where the gate for the selection of ^{22}O and ^{22}N is placed.

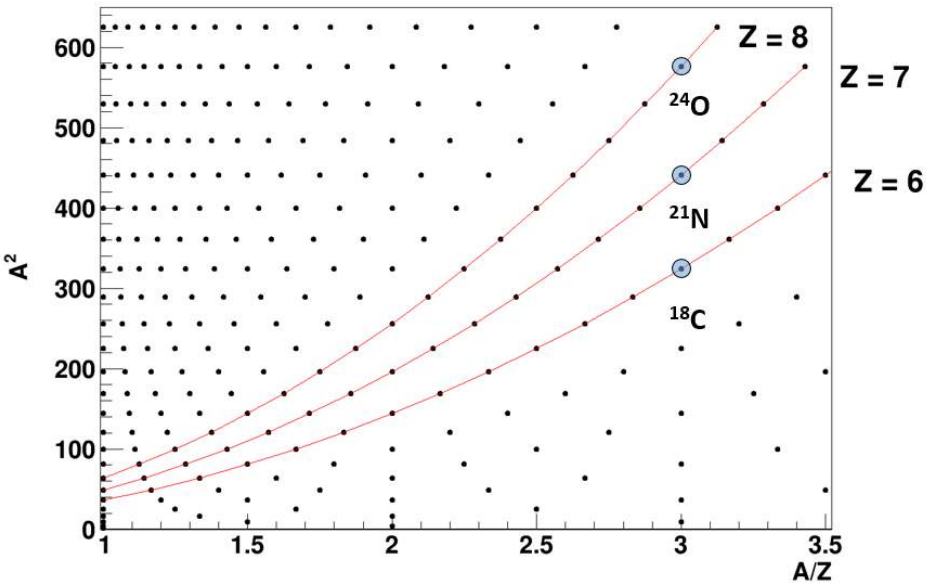

Figure 4.32: Matrix of A^2 vs. A/Z with the condition that $Z \leq A$ up to mass ~ 25. Each point is a separate nucleus (some unphysical).The red lines indicate curves of constant Z.

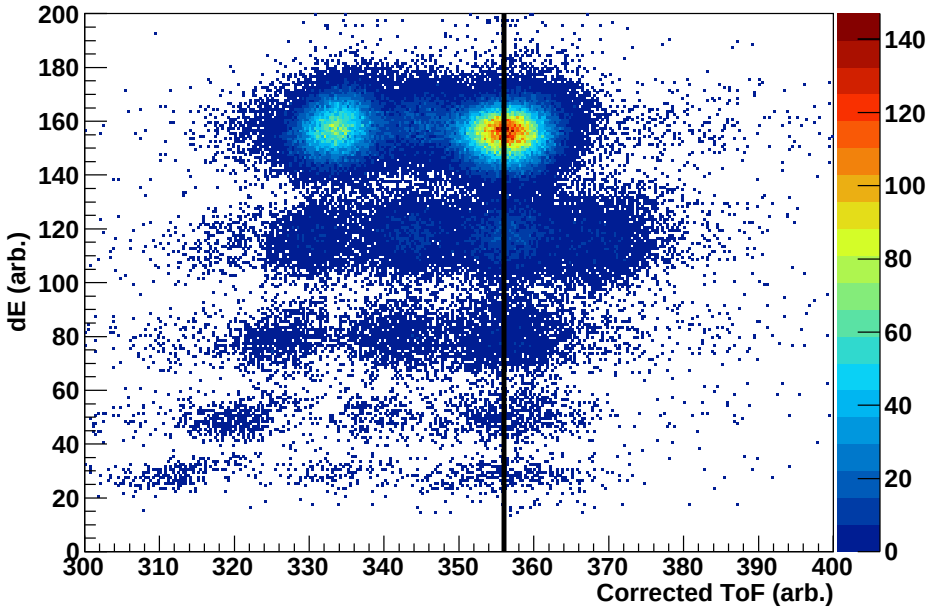

Figure 4.33: Energy loss dE in the ion chamber vs. Corrected time-of-flight showing isotope separation. A coincidence gate with a neutron is required to reduced background from unreacted beam. A vertical line at $A/Z = 3$ is drawn to guide the eye.

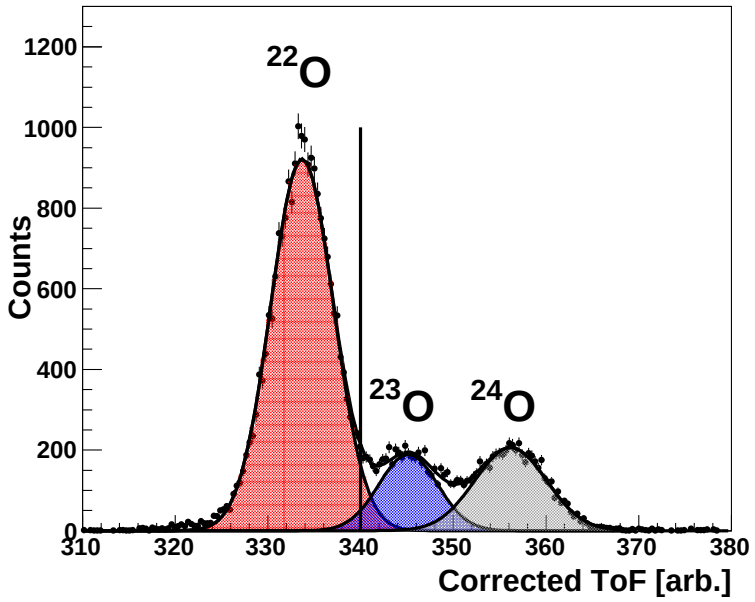

Figure 4.34: One-dimensional particle identification for the Oxygen isotopes. A gate is drawn at the vertical line to select ^{22}O. Neutron coincidence with MoNA-LISA is required to reduce the background from unreacted beam.

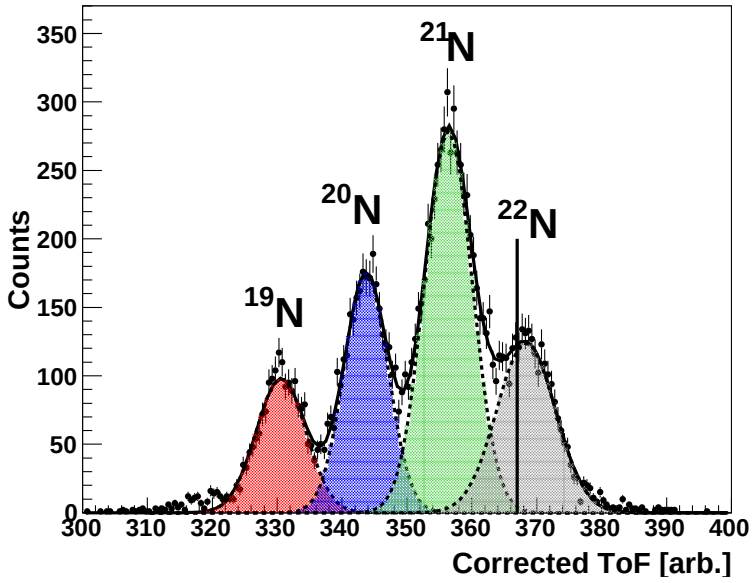

Figure 4.35: One-dimensional particle identification for the Nitrogen isotopes. A gate is drawn at the vertical line to select ^{22}N. Neutron coincidence with MoNA-LISA is required to identify candidates for reconstruction.

4.2.4 Neutron Selection

MoNA-LISA is designed to detect neutrons, but it is also sensitive to background radiation and other events which can cause scintillation. The primary source of background are cosmic muons and γ-rays produced either from the target or in the surrounding environment. Events that correspond to a neutron need to be correctly identified. To ensure that the analysis is being performed on an event which is most likely to be a prompt neutron, each event within the array is time-sorted.

Figure 4.36 shows the neutron time-of-flight in coincidence with ^{22}O in the sweeper. Fig 4.37 shows the correlation between time-of-flight and total charge-deposited. Two peaks are visible in the time of flight spectrum. This is due to the separation of the MoNA-LISA tables. The first peak is from the portion of LISA at 0 degrees (z = 7.5m), while the second is from MoNA which is further back (z = 8.8m). This separation is only visible because ^{23}O has an unbound resonance at a very low decay energy of $E_{decay} = 45$ keV [73, 68, 63]. The off-axis portion of LISA does not see any events from this decay because the "neutron cone" from the decay of ^{23}O does not intersect the detector. A low-energy decay like that in ^{23}O is forward focused in the lab frame. The neutron velocity distribution is narrow enough to distinguish the tables. Larger decays with $E_{decay} \sim 1$ MeV will smear out the time-of-flight distribution, due to a larger forward/backward kick in the center-of-mass frame of the decaying nucleus.

Prompt γ-rays from the target can be seen distinctly at around 25 ns, each peak corresponds to a table in MoNA/LISA. They are gated out by requiring the neutron time-of-flight to be greater than 50 ns. An additional gate is placed at 150 ns, as events beyond this are dominated by random background. Examining the charge-deposited can help improve the

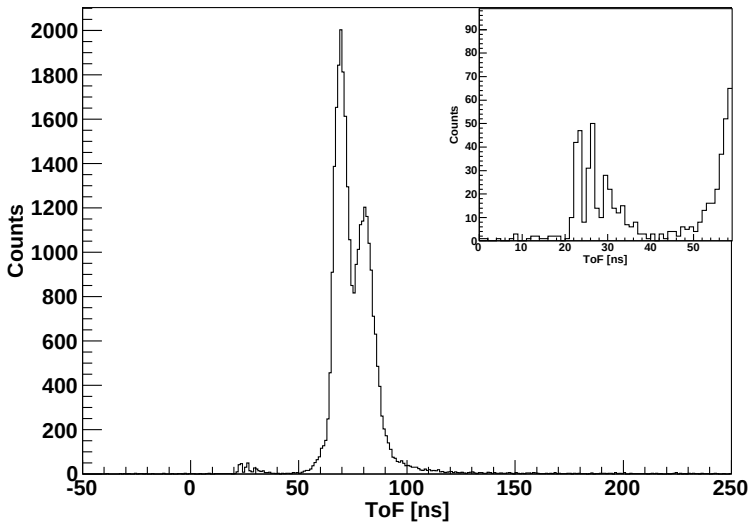

Figure 4.36: Neutron time-of-flight spectrum in MoNA-LISA with ^{22}O coincidence. The splitting is due to the narrow resonance in ^{23}O and the fact that the MoNA-LISA tables are physically separated. The insert shows γ-rays coming from the target.

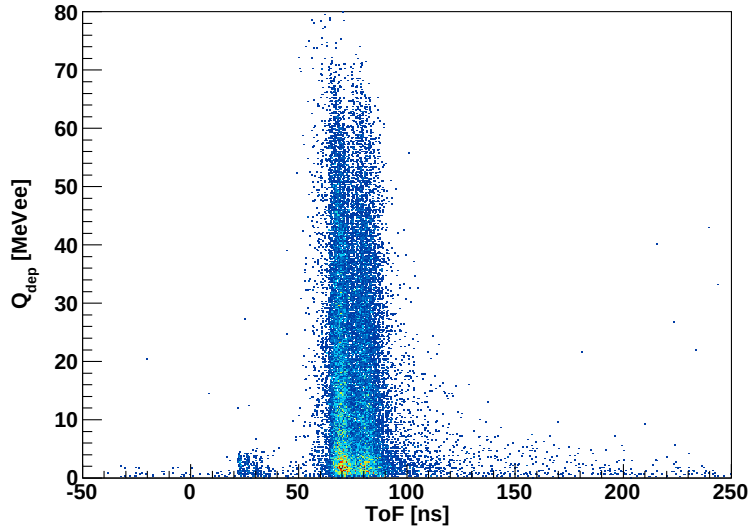

Figure 4.37: Neutron time-of-flight spectrum vs. Charge deposited in MoNA-LISA with ^{22}O coincidence. γ-rays typically deposits < 5 MeVee, while real neutrons can deposit up to the beam energy. No background from cosmic rays is evident.

event selection since the random background from γ-rays deposits little charge (< 5 MeVee). A high threshold of 5 MeVee is used to exclude the vast majority of background events. In addition, a multiplicity, consisting of multiple events within MoNA-LISA above this threshold,

is constructed.

Cosmic rays will deposit around 20 MeVee of energy in the detector and would be uncorrelated in time with a fragment, thus their distribution would be uniform. No such band is visible in the charge vs. ToF spectra for neutrons in coincidence with ^{22}O or ^{22}N, and so this background is negligible.

4.2.4.1 Two-Neutron Selection

When constructing a three-body system, it is crucial to correctly identify events which are true two-neutron events. The fact that MoNA-LISA does not distinguish between one neutron scattering twice from two unique neutrons interacting independently introduces a complication. From a pure-detection point of view, the two situations are identical. However, there is a method for increasing the likelihood that the selection of a multiplicity 2 (and greater) event will consist of true two-neutrons compared to a single neutron scattering twice.

First, a high threshold is required on every hit in MoNA – the energy deposited must be greater than 5 MeVee. This removes events that produce γ-rays from inelasticlly scattering off carbon. For example, a single neutron could undergo a ^{12}C(n,γ) reaction within a bar and scatter out of the detector volume without interacting again. The residual γ-ray can then be detected, and the event will have multiplicity 2 despite there only being one neutron interaction.

Next, a "Causality Cut" is made. This is a cut on the relative velocity V_{12} and distance D_{12} of the first two interactions in MoNA-LISA. This technique has been used to enhance the two-neutron signal in several previous measurements of three-body states [26, 54, 63, 25, 106, 55, 107]. Figure 4.38 shows a simulation, for comparison, of a 1n decay and a 2n decay

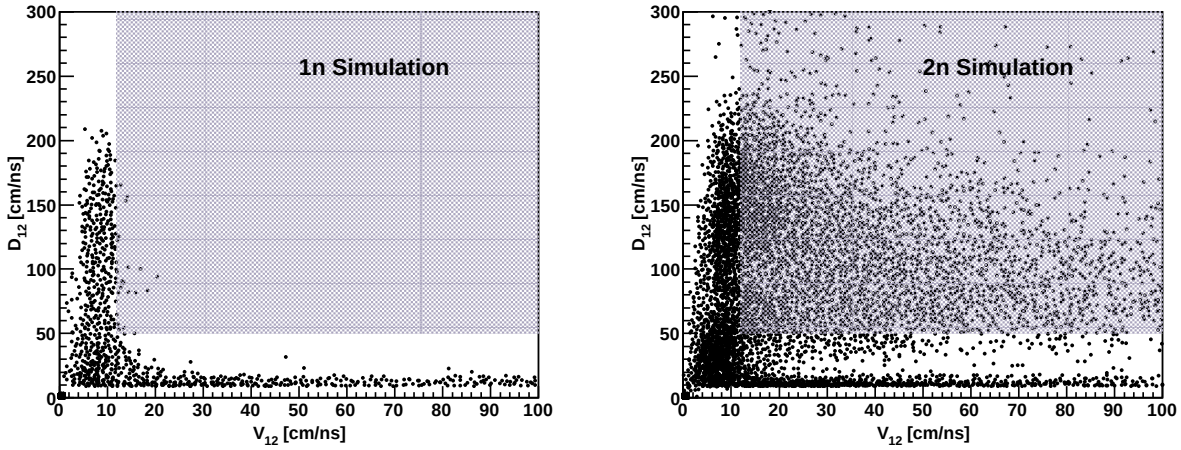

Figure 4.38: Relative distance D_{12} and velocity V_{12} for 1n (Left) and 2n (Right) simulations. The selection for 2n events is shown in by the shaded blue region.

in the D_{12} vs V_{12} phase-space. Events which come from one neutron scattering twice occur primarily in bands along short-distance and high relative velocity or large-distance and low relative velocity.

By requiring a large relative distance $D_{12} > 50$ cm, events which have a clear spatial separation are selected. When a neutron scatters it will lose energy and its relative velocity will be less than that of a separate neutron at beam velocity. To remove these events, a cut is placed on $V_{12} > 12$ cm/ns, which is the beam velocity.

4.3 Inverse Tracking

In order to measure a two- or three-body decay energy it is necessary to know the full 4-vector of the recoiling fragment in addition to the neutron. The 4-vector of the neutron can easily be obtained with knowledge of its time-of-flight and position:

$$\beta_n = \frac{d}{t}$$

$$\gamma_n = \frac{1}{\sqrt{(1-\beta^2)}}$$

from which the total energy and momentum can be obtained. In the case of the fragment however, these quantities are not directly measured. Instead, the position and angle of the fragment after exiting the sweeper are determined by the CRDCs and these variables $(x^{crdc}, \theta_x^{crdc}, y^{crdc}, \theta_y^{crdc})$ must be transformed into the target-frame. The energy is determined by the fragments deviation from the central path of the magnet, which has a known rigidity. Once the energy is known, the momentum can be calculated, and the off-axis components are determined by θ_x^T and θ_y^T:

$$p_{x,y}/p_0 = sin(\theta_{x,y})$$

A full description of the technique is described in Ref. [108, 90], only a summary is presented here. It is possible to calculate ion-optical quantities for a particle as it exits the magnet:

$$\begin{pmatrix} x^{crdc} \\ \theta_x^{crdc} \\ y^{crdc} \\ \theta_y^{crdc} \\ \Delta L \end{pmatrix} = M_f \begin{pmatrix} x^T \\ \theta_x^T \\ y^T \\ \theta_y^T \\ \delta \end{pmatrix}$$

where M_f is a forward transformation matrix. The variable ΔL is the difference between the length the particle traversed, and the length of the central track which is defined as the distance for which the particle is influenced by a magnetic field. This is close to the distance from the target to CRDC1. The drift length L_0 is the theoretical length a particle would

travel if it's $B\rho$ matched the sweeper exactly. The variable δ is the relative energy deviation give by:

$$\delta = \frac{E - E_0}{E_0}$$

Where E_0 is given by the central track and the $B\rho$ setting of the magnet. A hall probe is placed inside the sweeper chamber to provide a measurement of the magnetic field. The field of the dipole has been measured [90, 94], and the field-map is used as an input to the ion-optics code COSY INFINITY [109].

The matrix M_f is useful if the incoming distribution of the beam is known. However, the quantities that are measured experimentally are *after* the dipole. Thus it is necessary to invert the matrix so that the CRDC variables can be used as an input to calculate the appropriate quantities at the target:

$$\begin{pmatrix} \theta_x^T \\ y^T \\ \theta_y^T \\ \Delta L \\ \delta \end{pmatrix} = M_i \begin{pmatrix} x^{crdc} \\ \theta_x^{crdc} \\ y^{crdc} \\ \theta_y^{crdc} \\ x^T \end{pmatrix}$$

However, to do a direct inversion of the matrix the quantity ΔL needs to be known *a priori*. The approach taken by COSY is to calculate an inverse matrix M_i assuming that the x-distribution of the beam is a delta function at $x = 0$ at the target. This allows for a partial inversion of the matrix M_f and the calculation of $(x^T, \theta_x^T, y^T, \theta_y^T)$ and δ at the target allowing the 4-vector of the fragment to be determined. The assumption of $x = 0$, will worsen the resolution of the decay energy but it should not shift the peak of the distribution. If the

beam is not centered, then the reconstructed energy and x angle will also shift. The drift length used for reconstruction was $L_0 = 1.56$ m. The inverse reconstruction can be verified by examining the neutron and fragment energies and angles, as well as by comparing to previous measurement.

4.3.1 Verification

The inverse tracking can be verified by examining the reconstructed neutron and fragment angles and energies. In addition, where possible, several unbound resonances can be compared to previous experiments also performed with the MoNA - Sweeper setup.

4.3.1.1 ^{22}O + 1n

The inverse tracking is verified using the well-known low energy decay of $^{23}\mathrm{O} \rightarrow {}^{22}\mathrm{O} + 1\mathrm{n}$. This resonance has been measured previously multiple times, and is known to be low-lying at $E = 45$ keV. This is an ideal case to check the tracking, as MoNA-LISA has the highest detection efficiency for decays < 100 keV and the full neutron-cone falls within the detectors acceptance. In addition if the decay is reconstructed correctly, the inverse tracked angles of the fragment will match the neutron angles. The centroids of the reconstructed fragment energy and the neutron kinetic energy should also line up and finally, the relative velocity $v_n - v_f$, must be symmetric about zero. These are shown in Figures 4.39 and 4.40, where the neutron and fragment kinetic energy, relative velocity, and angles are compared. The neutron and fragment distributions are shown in blue and black respectively.

As an additional check, the angular distribution of the fragment and the neutron-fragment opening angle can be compared with a previous measurement of the same resonance using the same experimental equipment with similar resolutions [73]. In that experiment ^{23}O

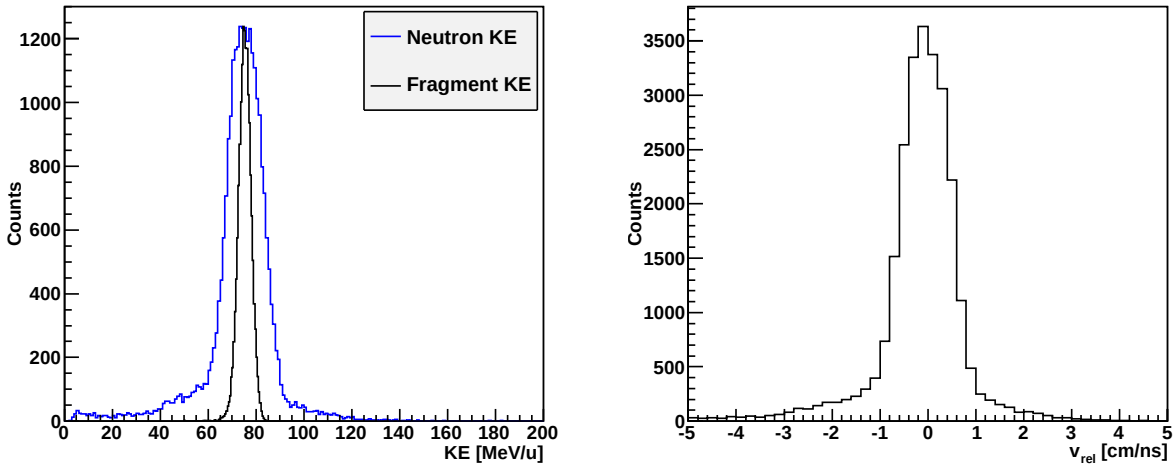

Figure 4.39: Comparison of neutron (blue) and fragment (black) kinetic energy for the decay of ^{23}O. The relative velocity is shown on the right.

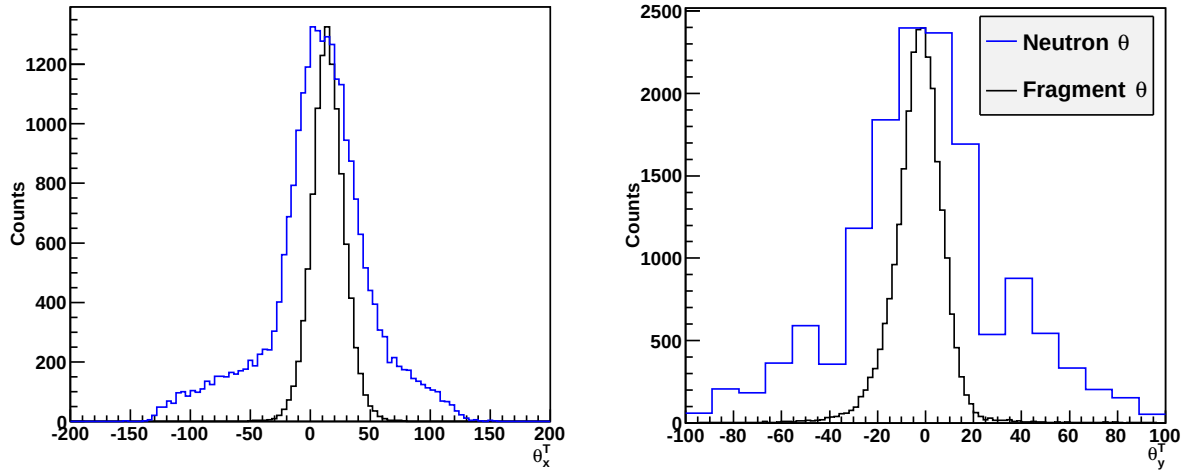

Figure 4.40: Comparison of neutron (blue) and fragment (black) angles at the target. The large binning in θ_Y^T is due to the discretization of the MoNA bars.

was populated via knockout from ^{26}Ne and the low-lying state was observed. While the experimental equipment is similar, there are some differences. For example, the addition of more MoNA bars and their configuration as well as some adjustments in the Sweeper. The width and overall shape of the distribution - which are determined by the decay - agree well. The two-body decay energy for ^{22}O + 1n is shown in Fig. 4.42.

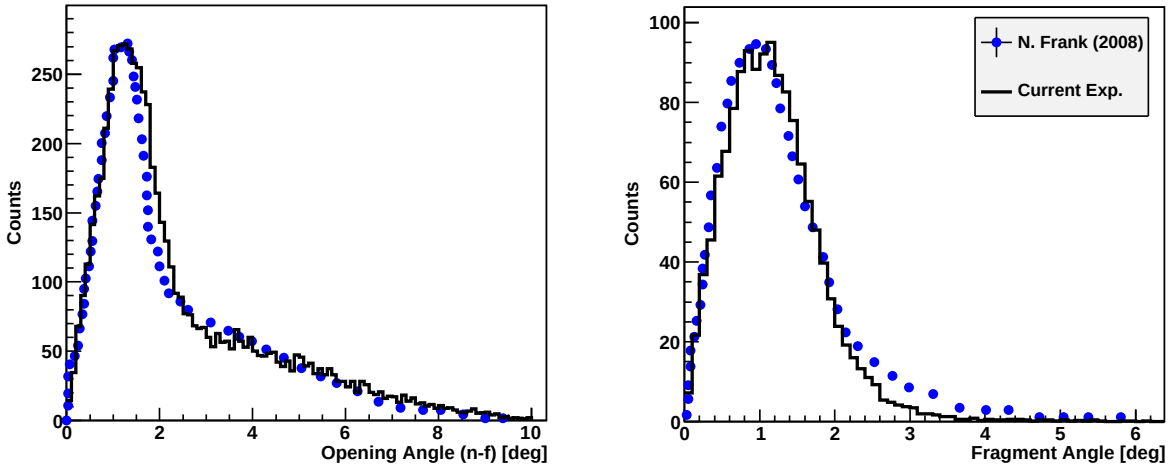

Figure 4.41: Comparison of measured neutron-fragment opening angle θ_{n-f} and fragment angle in spherical coordinates for the decay of ^{23}O $\rightarrow^{22}$O + 1n. In black is the current experiment, shown in blue is a measurement of the same decay using the same experimental apparatus [73] for comparison.

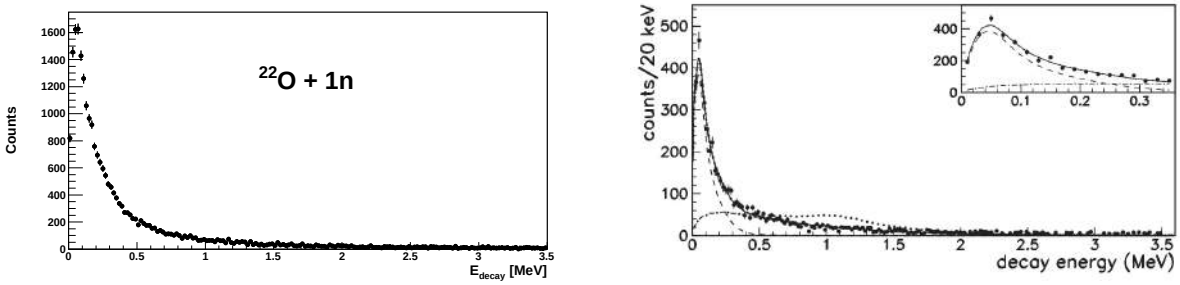

Figure 4.42: 1n E_{decay} spectra for the decay of ^{23}O. (Left) spectrum obtained from the current experiment. (Right) A previous measurement performed on the same experimental apparatus for comparison from Ref. [72]

4.3.1.2 ^{21}N + 1n

In addition to ^{23}N, unbound states in ^{22}N were also populated via 1p1n removal. Gating on ^{21}N in the PID and reconstructing ^{22}N shows a $\sim$ 600 keV peak in good agreement with a previous observation by M.J. Strongman [110] shown in Fig. 4.43.

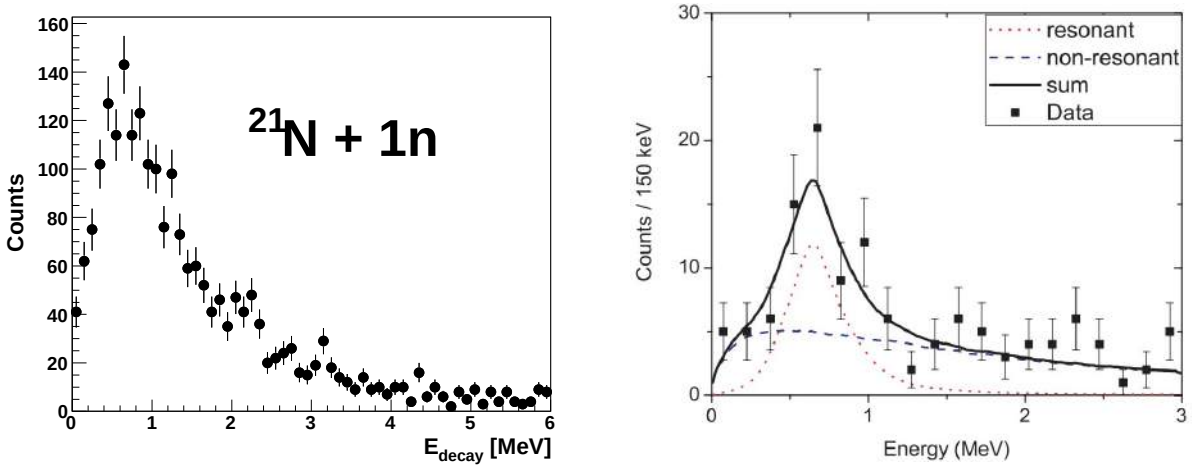

Figure 4.43: E_{decay} spectrum for the decay of ^{22}N $\rightarrow$ ^{21}N + 1n. On the left is the spectrum obtained from the current experiment. (Right) A previous measurement of the same resonance also performed with MoNA [110].

4.3.1.3 ^{23}O + 1n

Unbound states in ^{24}O were populated through inelastic scattering, (d,d'). Previous invariant-mass measurements observed a 2^+ state at 4.70 MeV, and a 1^+ at 5.39 MeV, with decay energies 0.51 and 1.2 MeV, respectively [70, 111].Shown for comparison in Figure 4.44 are the results from this experiment, and those of Hoffman *et al.*[111] which was also measured using MoNA. We are unable to resolve the two states because of the thick deuterium target. Uncertainty in the reaction-point causes a broadening in the reconstruction which worsens the resolution of the decay energy. In the work of Rogers *et al.* [70], it was shown that a thinner target improved the resolution enough to separate the two states.

4.3.1.4 ^{18}C + 1n

Unbound states in ^{19}C have also been previously measured with the MoNA - Sweeper setup, [112] in addition to a RIKEN measurement [114]. A 76 keV resonance was observed in the ^{18}C + 1n system. Figure 4.45. shows the results from this experiment compared to previous

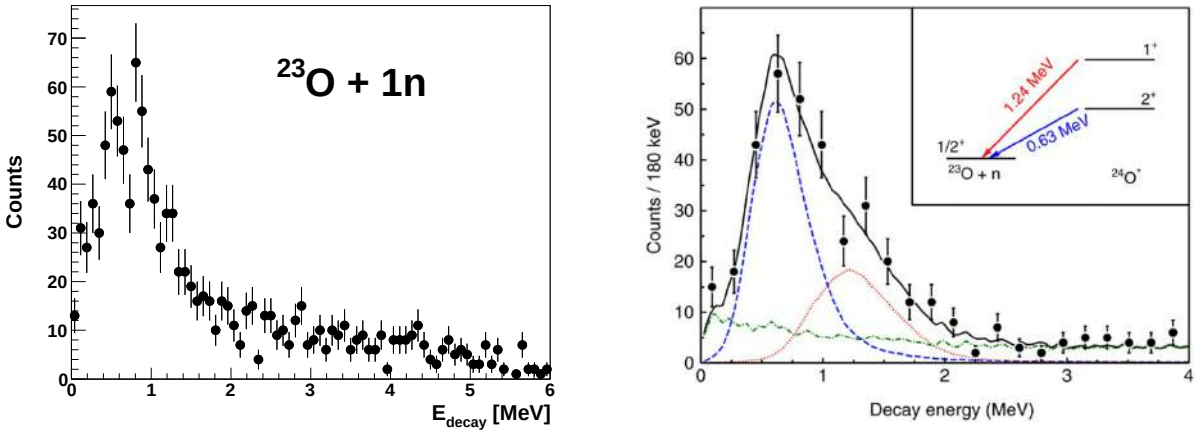

Figure 4.44: E_{decay} spectrum for the decay of ^{24}O $\rightarrow$ ^{23}O + 1n. (Left) spectrum obtained from the current experiment. (Right) A previous measurement of the same resonances using MoNA for comparison. [111]

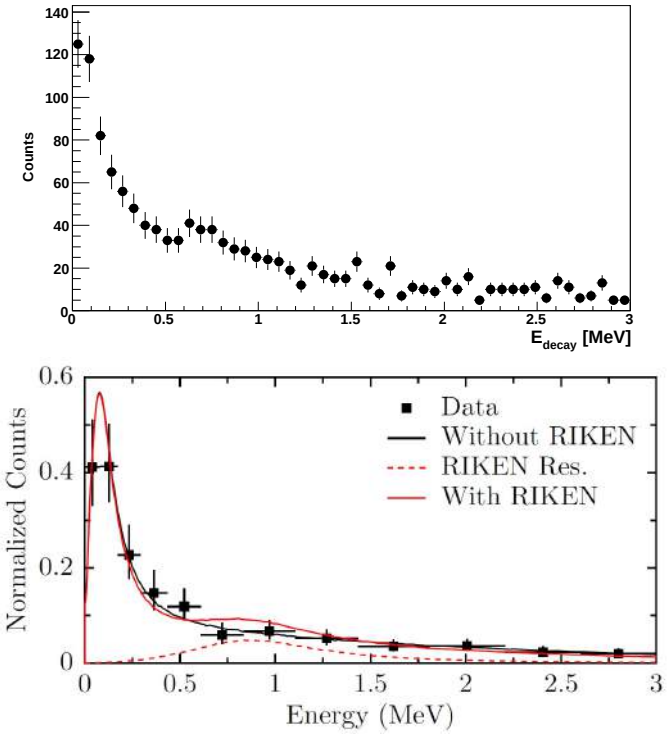

Figure 4.45: (Top) E_{decay} spectrum for the decay of ^{19}C $\rightarrow$ ^{18}C + 1n obtained from the current experiment. (Bottom) A previous measurement of the same resonance using MoNA [112, 113].

[112]. The low-lying resonance is apparent.

The inverse tracking in this experiment is able to reproduce decay energy spectra for at least 4 different unbound systems measured on the same apparatus, giving confidence to the calibrations.

4.4 Modeling and Simulation

Once the data have been calibrated and the spectra of interest generated, the parameters for an observed resonance have to be extracted. This is done by comparison to simulation. An in-house Monte Carlo simulation is used to generate simulated data that are convoluted with the experimental resolution, acceptance and efficiency. The simulations take into account the incoming beam profile, the geometry of the detectors – including the sweeper aperture, as well as the efficiency of MoNA and LISA.

The simulation is divided into multiple steps. The input beam impinges a target of given thickness and the reaction point is randomly chosen within the target. After determining the appropriate energy loss, the reaction mechanism is simulated. In the case of neutron emission, the neutron 4-vectors are determined at the reaction point and passed to GEANT [115]. The remaining charged fragment passes through the rest of the target and through a forward map of the magnet, which determines the distributions of positions at the CRDCs. The CRDC distributions are then folded with their resolution.

The neutron 4-vector is passed to GEANT where interactions in MoNA and LISA are modelled. Using MENATE_R [116], the interaction cross sections for neutrons on carbon and hydrogen are referenced to simulate the interactions in the plastic. In the cases where the angular distribution of a reaction is known (e.g. elastic scattering), this distribution is

used in the center-of-mass frame. However, there are many inelastic processes for which the angular distribution is not known and is assumed to be isotropic. The energy deposited from the neutron interaction is determined by modeling the light collected in the PMTs, and the time of the interaction is determined the same way as in the data.

In the case of multiple neutron simulations, GEANT handles the neutrons independently, but the events are mixed afterward. In a two-neutron decay, the 4-vectors of both neutrons are handled separately to determined the final number of interactions and their interaction times. To make this comparable with data, the interactions from the neutrons are time-sorted to give a single list of interactions that come from either neutron.

Once the interaction position of the neutron is determined and its time-of-flight calculated, the simulated data are taken and passed through the same analysis procedure as the data. In other words, the outputs of the simulation are used as if they were data to construct spectra that can be directly compared.

Various kinds of data are used to constrain simulation. Data taken on a gaseous target is used to fix the beam energy while the beam profile and target thickness are constrained by reproducing the unreacted beam in the focal plane. The reaction parameters are then determined by examining the distribution of events in the CRDCs for a given reaction. The simulation must reproduce the observed neutron kinetic energy, and reconstruct the observed fragment energy. Finally, the decay energies and three-body correlations contrain the resonance parameters.

4.4.1 Incoming Beam Parameters

The incoming beam parameters were set by matching the distribution of the unreacted beam in the focal plane. In addition, they also had to match the inverse-reconstructed

distributions ($\theta_X^T, \theta_Y^T, y^T$) using an energy from the data on a gaseous target. The necessary target thickness in simulation deviates slightly from what is observed. This is because the simulation does not account for the Kapton and Mylar wrapping, or the curvature of the target. Because of this, the thickness is varied in the simulation until the fragment energy is properly reproduced. This ensures that fragments with the correct energy are being transported through the model of the experimental setup. Thus the thickness in the simulation is an effective thickness. A thickness of 650 mg/cm^2 of LD_2 matches the incoming beam distributions very well 4.46. Table 4.9 summarizes the necessary incoming beam distribution to reproduce the unreacted beam in the focal plane.

The A1900 momentum slits were set to 2% $\delta p/p$ which resulted in an energy spread of 1.2%. Given that the magnetic quadrupole before the target was set to a $B\rho = 4.03146$ Tm, this gives a beam energy for ^{24}O of $E_{beam} = 83.4 \pm 1$ MeV/u which is used in simulation.

4.4.2 Reaction Parameters

The $1p$ and $1n$-knockout mechanisms were simulated by removing nucleons from the beam and giving the resulting system a momentum kick in both the parallel and transverse direction. The parallel momentum kick was parameterized based on the Goldhaber [117] model while the transverse kick was taken from Van Bibber's model [118]. In these models, the parallel and transverse kicks are gaussian and defined by widths $\sigma_\perp$, and $\sigma_\parallel$ which are free parameters. The widths are fixed by matching the distribution of fragments in the CRDCs for a given reaction. An additional multiplicative factor is applied to slow the beam within the target and is attributed to dissipative interactions within the target. Table 4.10 summarizes the reactions and the parallel and transverse widths used to reproduce them.

Paramater	Simulation Setting	Significance
eBeam	83.4	Beam enery in MeV/u.
dTarget	650	LD_2 Thickness mg/cm^2.
bSpotCx	0	x centroid of incoming beam.
bSpotCtx	-0.01	θ_x centroid of incoming beam.
bSpotCy	0.0	y centroid of incoming beam.
bSpotCty	-0.001	θ_y centroid of incoming beam.
bSpotDx	0	width of x distribution.
bSpotDy	0.002	width of y distribution.
bSpotDtx	0.007	width of θ_x distribution.
bSpotDty	0.008	width of θ_y distribution.
bSpotCx2	0	x centroid, 2nd beam component.
bSpotCtx2	0.005	θ_x centroid, 2nd beam component.
bSpotCy2	0.003	y centroid, 2nd beam component.
bSpotCty2	0.006	θ_y centroid, 2nd beam component.
bSpotDx2	0.00	width of x distribution, 2nd component.
bSpotDy2	0.01	width of y distribution, 2nd component.
bSpotDtx2	0.005	width of θ_x distribution, 2nd component.
bSpotDty2	0.008	width of θ_y distribution, 2nd component.
normscale1	0.70	relative intensity of 1st component (70%).
normscale2	1	relative intensity of 2nd component (30%).
crdc1MaskLeft	0.15	$+x$ edge of CRDC1 in m.
crdc1MaskRight	-0.15	$-x$ edge of CRDC1 in m.
crdc2MaskLeft	0.15	$+x$ edge of CRDC2 in m.
crdc2MaskRight	-0.1305	$-x$ edge of CRDC2 in m.
crdc2MaskTop	0.15	top edge of CRDC2 in m.
crdc2MaskBot	-0.15	bottom edge of CRDC2 in m.
crdc2dist	1.55	distance between CRDCs in m.
cosymap	"m24O_Jones320A"	inverse and forward map filename.

Table 4.9: Simulation parameters for the incoming beam distribution. Determined by matching unreacted ^{24}O in the focal plane.

Reaction	$\sigma_\perp$ (MeV/c)	$\sigma_\parallel$ (MeV/c)	v_{shift}
^{24}O(-1n)^{23}O	92	64	0.9875
^{24}O(-1p)^{23}N	275	102	0.9550

Table 4.10: Parallel and perpendicular glauber kicks used to reproduce the CRDC distributions.

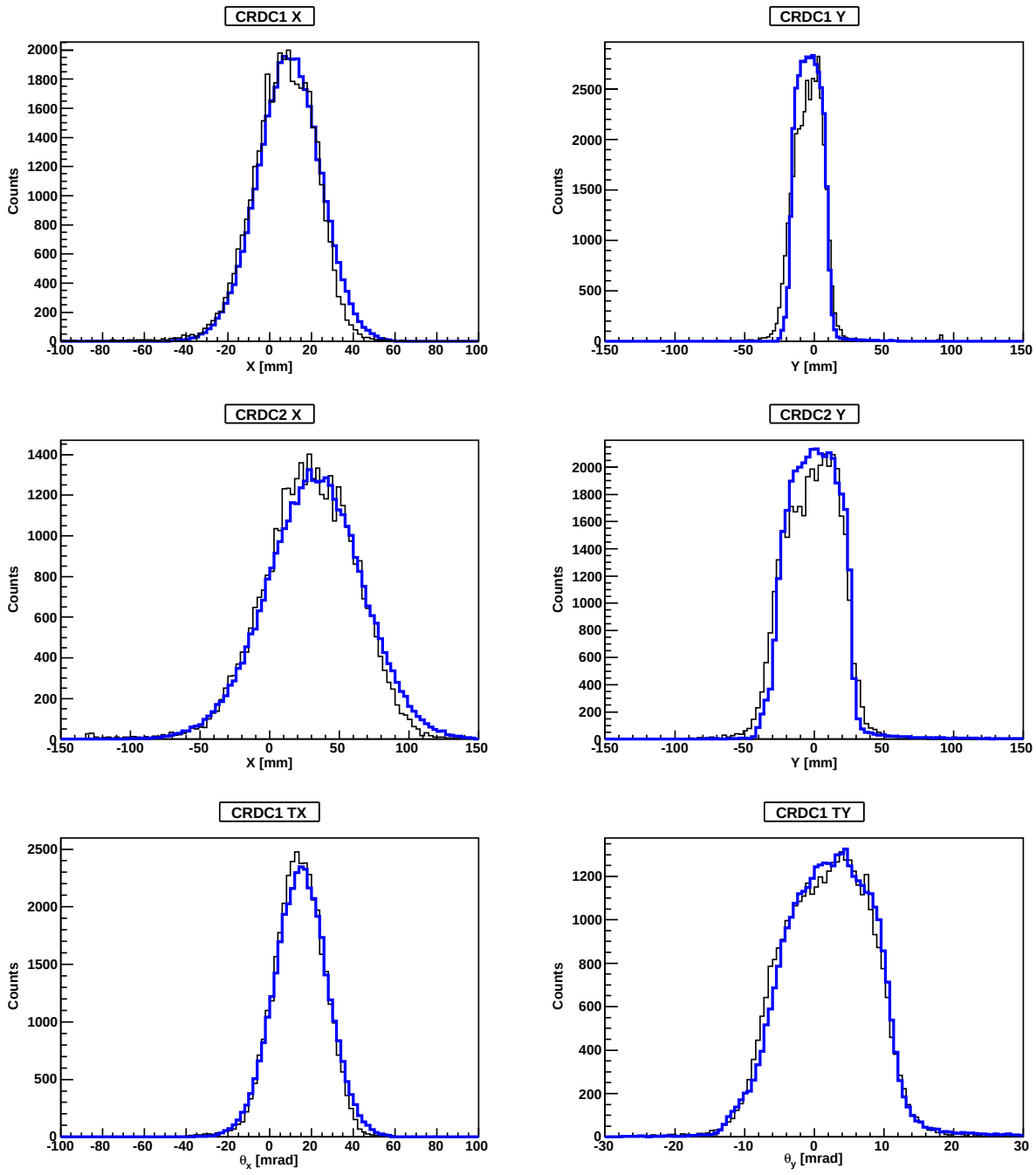

Figure 4.46: Comparison between simulation (blue) and data (black) for the unreacted ^{24}O beam in the focal plane.

4.4.2.1 1n Knockout, Verification ^{22}O

Using the incoming beam settings determined by the unreacted ^{24}O beam setting, the parallel and transverse kicks for modeling the 1n knockout reaction to ^{23}O are constrained by data

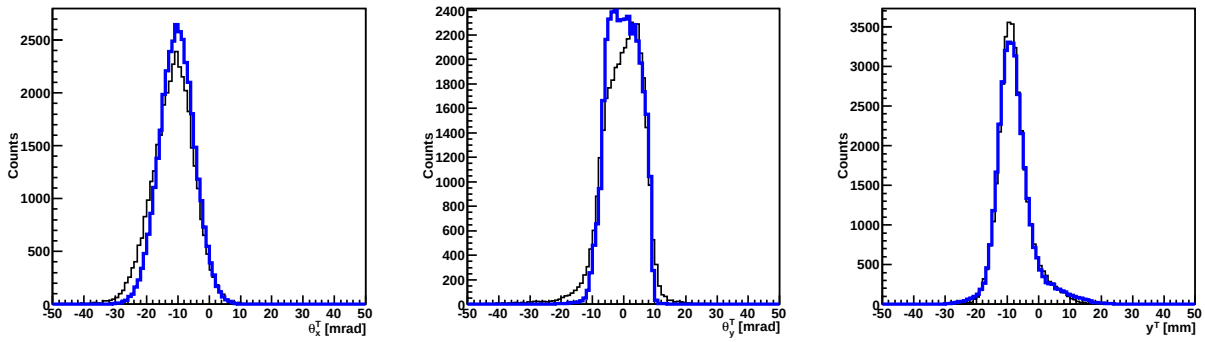

Figure 4.47: Reconstructed angles and target position using a 4-parameter map. The simulation (blue) is compared to data for the unreacted ^{24}O beam (black).

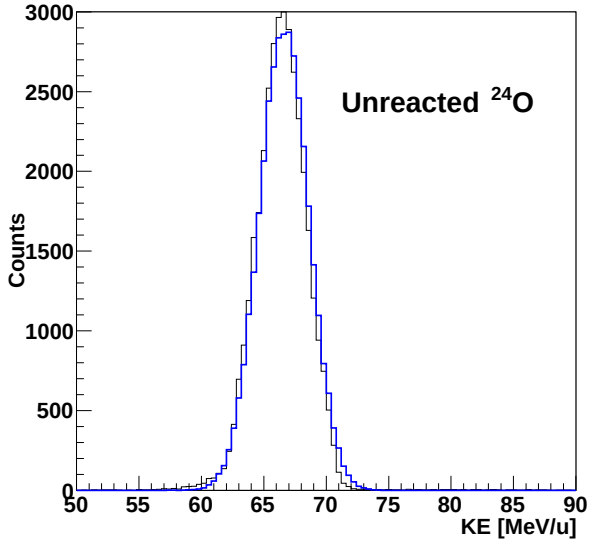

Figure 4.48: Comparison of reconstructed kinetic energy distributions between simulation (blue) and data (black) for the unreacted ^{24}O beam. The reconstructed energy is after passing through the full LD_2 target.

with ^{22}O in coincidence with neutrons as shown in Fig. 4.49. Settings for the beam can be found in Table 4.9, and the reaction parameters in Table 4.10. In order to reproduce the distributions in the CRDCs it was necessary to flip the sign on the incoming θ_x centroid, indicating that the ^{22}O fragments come in at a high angle. It is clear that the momentum distribution of these fragments is not fully in acceptance.

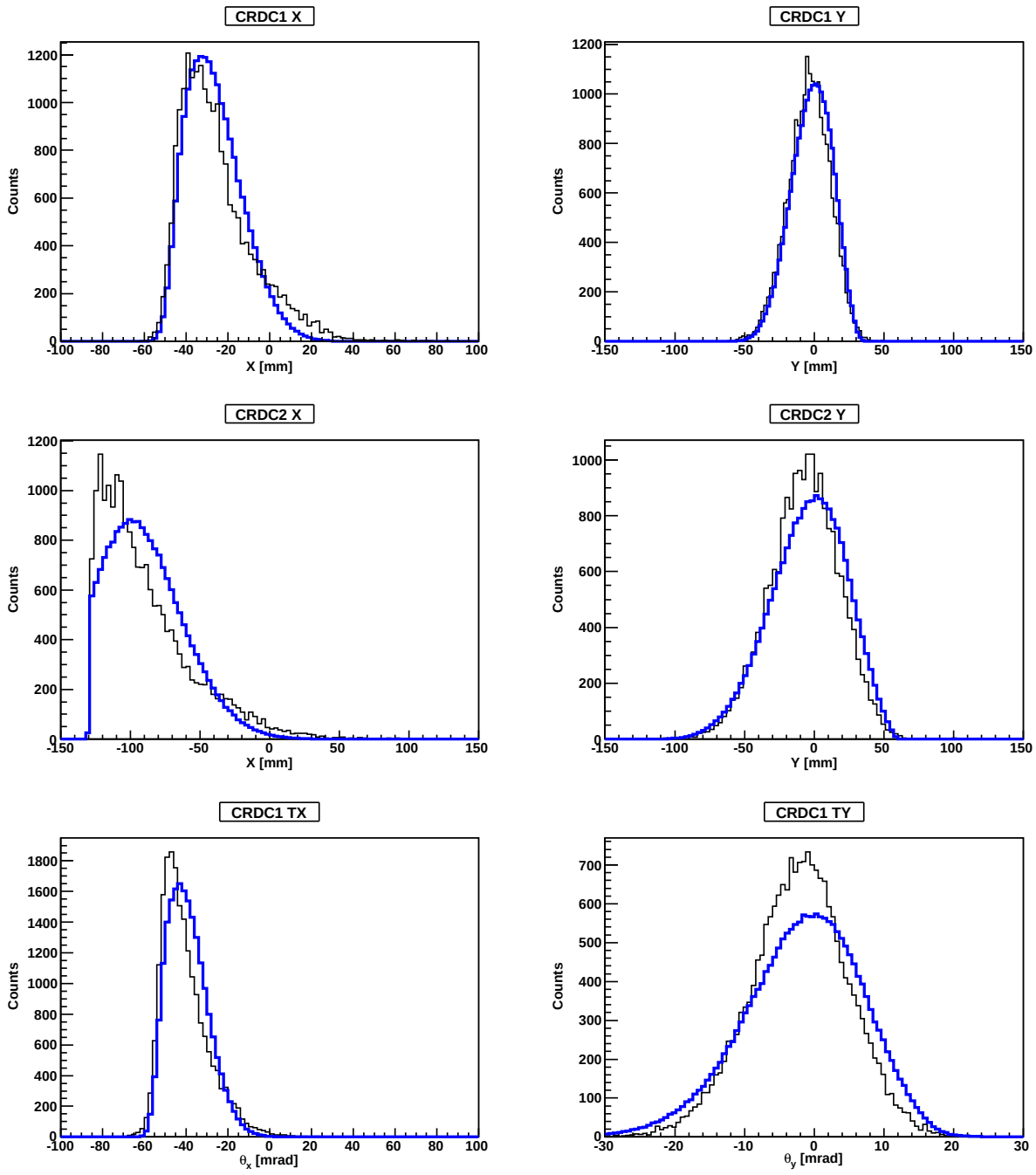

Figure 4.49: Comparison of focal plane position and angles between simulation (blue) and data (black) for 1n knockout to ^{23}O, which then decays to ^{22}O.

4.4.2.2 1p Knockout, Verification ^{22}N

The data for ^{22}N in coincidence with neutrons constrain the parameters for modeling 1p knockout in the simulation. The CRDC distributions for this reaction are shown in Figure

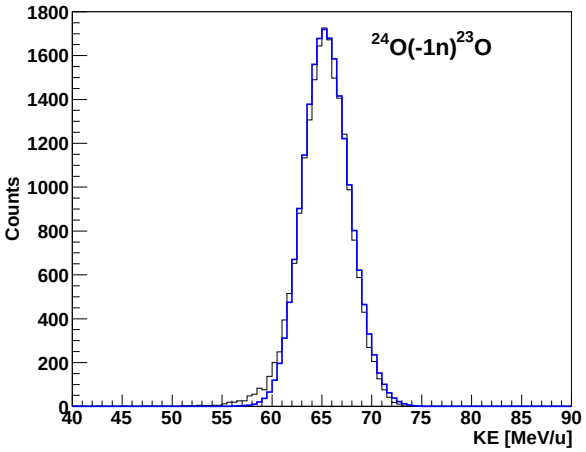

Figure 4.50: Reconstructed kinetic energy for the ^{22}O fragments coming from the 1n knock-out reaction. Simulation results are shown in blue and the data in black.

4.51. Settings for the beam can be found in Table 4.9 and the reaction parameters in Table 4.10.

4.4.2.3 (d,d'), Inelastic Excitation

The (d, d') reaction can be approximated using the global optical models that are available. The angular distribution for inelastic scattering of ^{24}O on D_2 was estimated using FRESCO [119] and a global optical potential for ^{24}O + d [120, 121]. As the deformation length is not known, the deformation length for ^{12}C was used. The differential cross section, $d\sigma/d\Omega$, was calculated for the $0^+ \rightarrow 2^+$ transition in ^{24}O. The angular distribution was then randomly sampled from in the simulation and the reaction kinematics treated as two-body kinematics. The excited ^{24}O then decayed, and the resulting reaction products propagated through the rest of the simulation.

Since the three-body correlations and decay energies are relative measurements, the data are not sensitive to the reaction mechanism. Identical spectra are produced whether or not the reaction mechanism is modelled appropriately. There is no discernable difference between

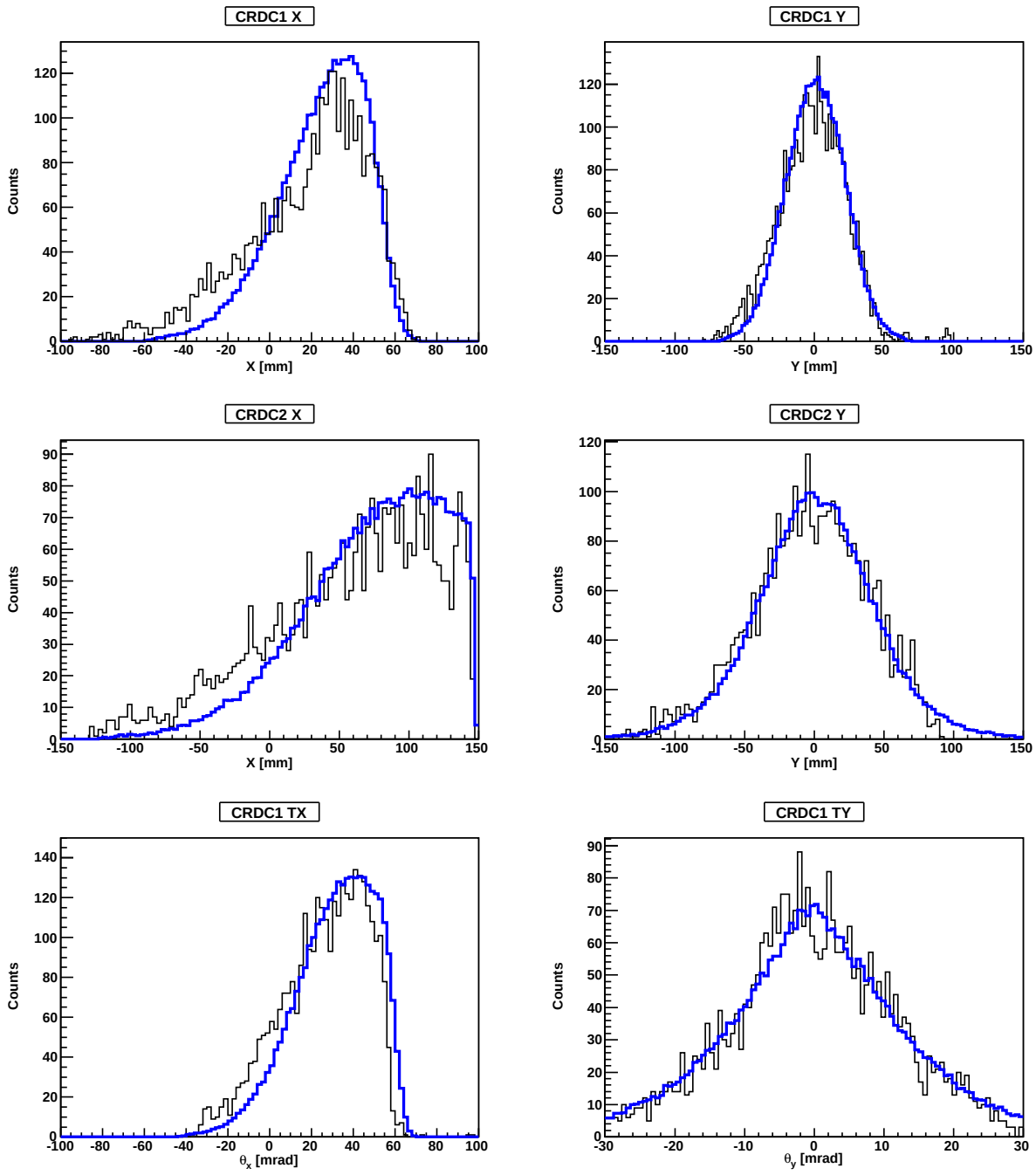

Figure 4.51: Comparison of focal plane position and angles between simulation (blue) and data (black) for 1p knockout to ^{23}N, which then decays to ^{22}N.

using the FRESCO calculation or a glauber-kick without any stripping in the decay energies and Jacobi spectra.

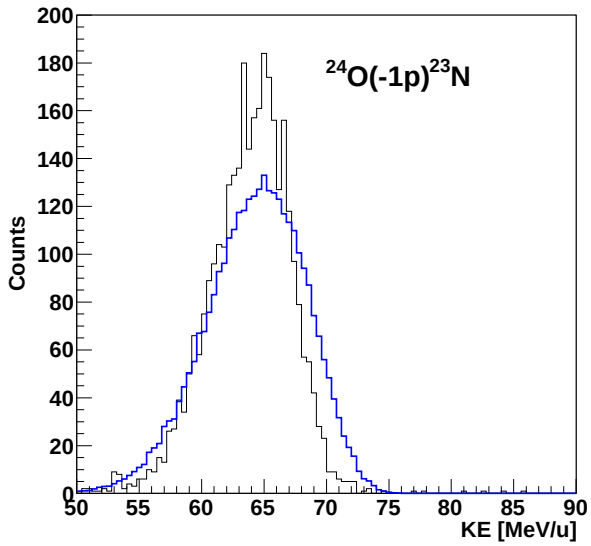

Figure 4.52: Reconstructed kinetic energy for the ^{22}N fragments coming from the proton knockout reaction. Simulation is in blue and data are in black.

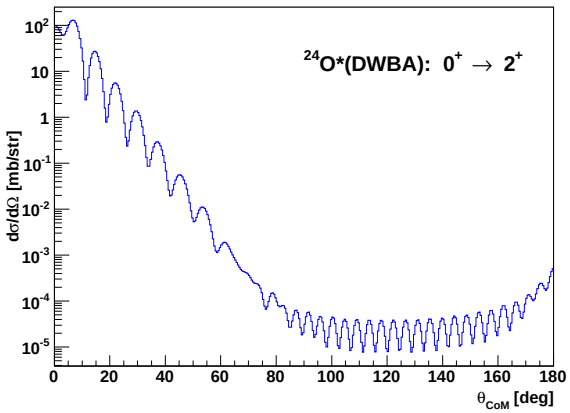

Figure 4.53: Center of mass angular distribution for inelastic scattering of ^{24}O on d at 82.5 MeV/u (lab), estimated with FRESCO, a global optical model, and the deformation length of ^{12}C.

4.4.3 Neutron Interaction and MENATE_R

The neutron interactions are modelled with GEANT [115] and the MENATE_R package [116]. MENATE_R provides cross sections for interactions on hydrogen, carbon, iron, based on previous measurements and the code's ability to reproduce the neutron detection efficiency for plastic scintillators. MENATE_R contains several inelastic processes for neutrons on

carbon, for example ^{12}C$(n, np)^{11}$B, ^{12}C(n,γ) in the energy range of 0 to 100 MeV. However, data for these reactions is scarce and the angular distributions are not known and they are crudely approximated in some cases. For example the ^{12}C(n, γ) interaction is modelled with the emission of only one γ-ray at 4 MeV, when in reality ^{12}C can be excited beyond the first excited state and emit a cascade. Figure 4.54 shows a summary of the inelastic processes included in MENATE_R.

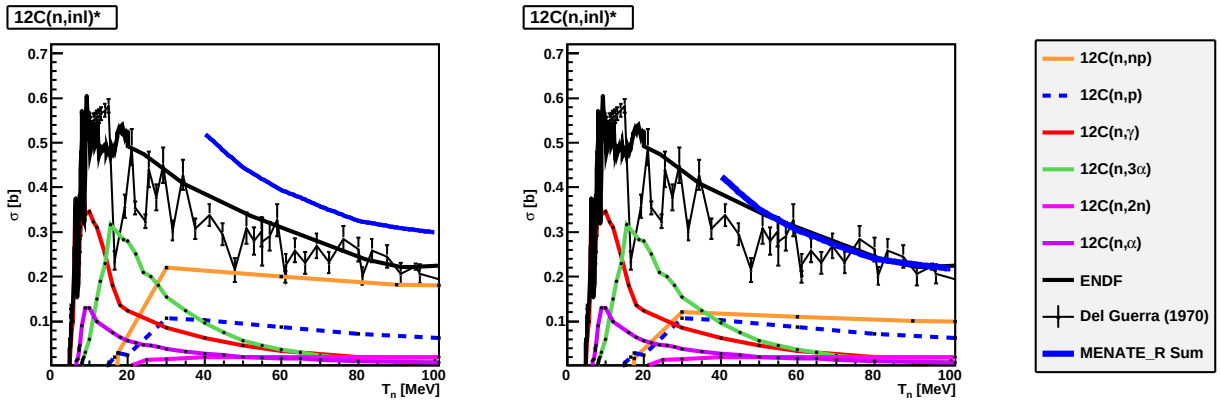

Figure 4.54: Breakdown of ^{12}C(n,*) cross-section in MENATE_R. (Left.) MENATE_R cross sections without any adjustment. The blue curve is the sum of all cross-section in the energy range 40 - 100 MeV. (Right) The total MENATE_R cross-sections after modification compared to the Del Guerra compilation [122] and the ENDF [123] evaluation.

The ^{12}C$(n, np)^{11}$B cross section is overpredicted in the simulation. Summing the components of each inelastic process, the total inelastic cross section is approximately 100 mb too large compared to the 1976 compilation by Del Guerra [122], and the ENDF [123] and JENDL-HE 2007 [124]databases. In addition, the only measurement of this reaction at 90 MeV [125] reported this cross section as a factor 2 lower than what is included in MENATE_R. For this reason, this cross-section was modified in MENATE_R to better agree with the total inelastic cross section. Fig. 4.54.

The high threshold of 5 MeVee removes γ-rays that are produced by ^{12}C(n, γ), which are not appropriately modelled by MENATE_R. The best agreement with MENATE_R is

achieved when this threshold is applied.

4.4.4 Other Parameters

The field maps for the Sweeper magnet are fixed by measurement from a Hall probe inserted in the field of the magnet. The geometric acceptances of the detectors are determined by their geometrical layout in the simulation, which is identical to experiment. The steel vacuum chamber of the magnet is included in the simulation. Resolutions for MoNA and LISA are included as gaussian distributions and the quantization of the bars is also taken into account.

4.4.5 Cuts

Additional cuts were made to the simulation to remove tracks through the magnet that are unphysical. These cuts were made to the emittance, shown in Figure 4.55. The physical aperture of the CRDCs are included in the simulation but hard cuts are made on their acceptance as a redundancy. In addition, the simulated neutrons are required to have physical time-of-flights and be above the 5 MeVee threshold. Identical causality cuts are also made to the simulation. In this way the simulations are made directly comparable to data.

4.4.6 Decay Models

4.4.6.1 One neutron decays

The decay energy for a single neutron decay is given by an energy-dependent Breit-Wigner of the form (described in Section 2.1.1:

$$\sigma_l(E; E_0, \Gamma_0) \propto \frac{\Gamma_l(E; E_0)}{[E_0 - E + \Delta(E; \Gamma_0)]^2 + \frac{1}{4}[\Gamma_l(E; \Gamma_0)]^2}$$

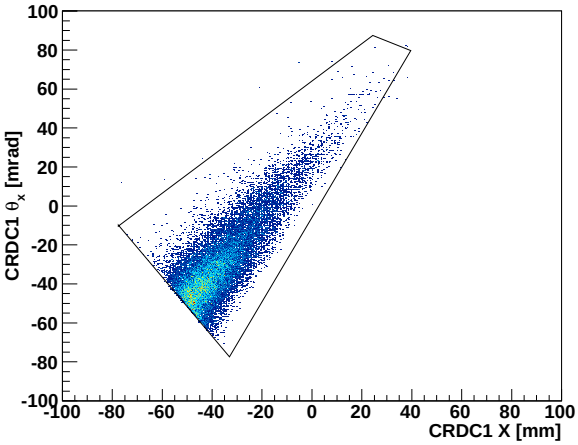

Figure 4.55: CRDC1 X vs. CRDC1 θ_X for all ^{22}O fragments coincident with a neutron. A gate, called an XTX cut, is drawn around the data and applied to simulation. This is to reject fragments which may have a strange emittance in the simulation.

Where the normalization is arbitrary. This model is used to determine the neutron energy and angular momentum ℓ relative to the fragment in the center-of-mass frame, and thus the centroid E_0 and width Γ_0 of the unbound resonance. Both particles are then boosted back into the lab frame in the simulation. This lineshape was used for modeling the 1n decay of ^{23}O and ^{23}N populated by neutron and proton knockout from ^{24}O.

4.4.6.2 Two neutron decays

The decay of the excited state in ^{24}O was modelled as a two-neutron decay to ^{22}O. The decay was modelled as multiple two-body decays using Volya's description [77] for a sequential decay. The intermediate state in ^{23}O is well known and has been measured multiple times, and the energy and width were fixed for the minimization. The total three-body energy was determined by fitting the ^{22}O + 2n spectra with causality cuts. The energy and width were left as free parameters as well as the amplitude. The ℓ value is undetermined, as there was no observable change in the lineshape between $\ell = 1$, or $\ell = 2$ once resolutions were folded

with the simulation. In addition, Volya's model assumes that both neutrons decay with the same ℓ value and come from the same single particle orbtial. Although this is not entirely the case in the present decay, as discussed in Chapter 5, it is sufficient to describe the data. Since the low-lying intermediate state in ^{23}O decays by emission of a $d_{5/2}$ neutron, the ℓ value was taken to be 2 for both decays.

For the phase-space model, the TGenPhaseSpace class was used as implemented in ROOT [126]. This model uniformly samples the phase space of invariant mass of the fragment-neutron and neutron-neutron pairs (M^2_{f-n} vs. M^2_{n-n}) given the masses of each particle and total n-body energy and width as an input. It is used as a baseline for the scenario with no correlations since this model assumes no interaction.

For the di-neutron decay, the two neutrons are assumed to be in a $^1S_0$ configuration with a scattering length of $a = -18.7$ fm. In this model, the di-neutron cluster separates from the core and then proceeds to break up with the a relative energy. The distribution for the total three-body energy as well as the $n-n$ relative energy is determined by Volya's di-neutron model described in Section 2.2.2. In both the di-neutron and sequential models, the two-neutrons are emitted isotropically in the rest frame of the neutron - core/two-body-subsystem. Additional details on two-neutron decays can be found in Section 2.2.

After folding with resolutions and acceptance, all experimental observables of interest are modeled in the simulation under different assumptions and the best-fit values determined by log-likelihood ratio described in the next section.

4.4.7 Fitting and Likelihood Ratio

For poisson errors, the log-likelihood function is written as:

$$\mathcal{L} = -Ln\left[\lambda\right] = -\sum_i Ln\left(\frac{\mu_i^{n_i} e^{-\mu_i}}{n_i!}\right) = \sum_i Ln(n_i!) + \mu_i - n_i Ln(\mu_i)$$

Since we are only concerned with finding the set of μ_i generated by a hypothesis for which the likelihood is maximum, the absolute magnitude is irrelevant. Thus we can add any constant to this expression without affecting the minimization. Consider the likelihood of n_i given the expectation of n_i:

$$-Ln\left[\lambda\right] = -\sum_i Ln\left(\frac{\mu_i^{n_i} e^{-\mu_i}}{n_i!}\right) + \sum_i Ln\left(\frac{n_i^{n_i} e^{-n_i}}{n_i!}\right) = -Ln\left[\frac{\lambda(n_i;\mu_i)}{\lambda(n_i;n_i)}\right]$$

Which is the likelihood ratio. This expression reduces to:

$$-Ln\left[\lambda\right] = \sum_i \mu_i - n_i + n_i Ln\left(\frac{n_i}{\mu_i}\right)$$

This quantity is distributed as $\chi^2/2$ in the limit of large n. In this case the null hypothesis H_0 is the set of μ_i whose probability distribution is determined by theory (resonance parameters), and the alternative hypothesis H_1 is the set of data points n_i under the assumption that they too are sampled from a probability distribution (the "true" resonance parameters). The data are assumed to be poisson distributed. Let θ_i denote the resonance parameters which determine the probability distribution of μ_i. The minimization:

$$-\frac{\partial L}{\partial \theta_i} = 0$$

gives the parameters for which the likelihood is maximum (i.e. the "best-fit").

Once the simulated distributions are made comparable to data by folding with resolution, acceptances, and efficiencies, the log-likelihood ratio can be calculated for a given set of energies and widths, or under different models (e.g. di-neutron, phase-space). Plotting $-Ln\left(\lambda\right)$ as a function of these parameters then defines the statistical boundaries via rejection/acceptance within a critical region. In the case of χ^2 this is often the p value.

In some cases it is useful to minimize on a linear combination of $-Ln\left[\lambda\right]$ to better constrain the simulation. For example, fitting on the sum of the mult ==1 and mult==2 gated spectra will force the model to reproduce the ratio of multiplicities whereas fitting on a single spectrum alone can cause over-prediction of the other (and vice versa). The optimum combination of spectra depends on the problem at hand and can vary depending on what one wants to accomplish. In the case of multiple free parameters, the critical region can be determined by:

$$\theta_i \in \left\{ \theta \;\middle|\; \chi^2 < \chi^2_{min} + \Delta\chi^2(\nu) \right\}$$

Where ν is number of free parameters in the fit, and $\Delta\chi^2(\nu)$ is the change in χ^2 from the minimum such that integration over the χ^2 probability distribution function gives the appropriate σ limits. Using Wilk's Theorem, the statistic $-Ln\left[\lambda\right]$ is distributed as $\chi^2/2$ in the limit of sample size N approaching infinity. For simplicity, one can approximate the critical region for $-Ln\left[\lambda\right]$ with the critical region of $\chi^2/2$, although Monte Carlo methods will more accurately find this boundary.

Chapter 5

Results and Discussion

5.1 ^{22}O + 2n

The two- and three-body decay energy spectra for ^{23}O and ^{24}O are shown respectively in Fig. 5.2. Also shown is the three-body decay energy spectrum for ^{24}O with causality cuts applied. The spectra shown require that the neutron time-of-flight fall between 50 and 150 ns. However, the requirement of good time-of-flight and multiplicity ≥ 2 is not sufficient to separate two-neutron events from one-neutron events. To accomplish this, two cuts are necessary: (1) the causality cut, and (2) a high threshold of 5 MeVee on each interaction.

The causality cuts are cuts on relative velocity V_{12} and distance D_{12} between the first two interactions in MoNA. By requiring a large relative distance, nearby scatter is removed. An additional cut on V_{12} will also remove scattering events as a scattered neutron will lose energy. More information on the causality cuts can be found in Section 4.2.4.1.

The reason for this high threshold is because ^{22}O is populated in multiple ways in this experiment, with the dominant contribution coming from one-neutron knockout from ^{24}O which directly populates ^{23}O as illustrated in Fig. 5.4. This results in an overwhelming contribution of 1n events which need to be suppressed. The 5 MeVee threshold eliminates events where a neutron interacts in the plastic and produces a γ-ray which can interact in another location giving the appearance of two neutron interactions. It was observed through simulation that applying this threshold greatly reduced the contribution of 1n scatter events

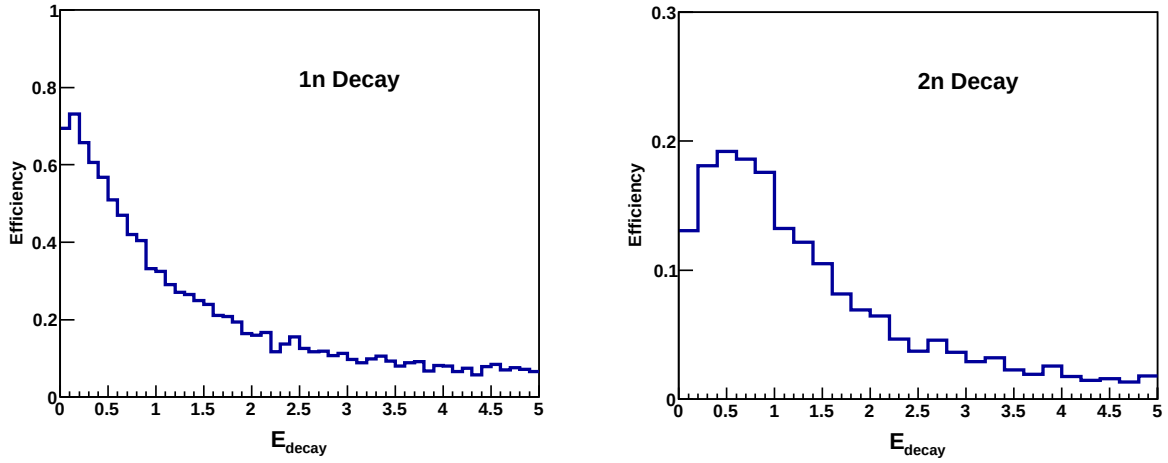

Figure 5.1: (Left) Acceptance of MoNA-LISA for a 1n decay as a function of E_{decay}. (Right) Acceptance for a 2n decay with causality cuts applied.

within the causality cuts.

The low-energy peak in ^{23}O is evident in the two-body spectrum, corresponding to the decay of a $5/2^+$ hole state. It is consistent with previous measurement [63]. The three-body spectrum for ^{24}O with causality cuts shows an apparent broad peak at $\sim$ 1 MeV which is significantly higher than the previously reported value of $\sim$600 keV. However, here one must be careful, as the acceptance of the causality cuts depends strongly on the configuration of MoNA and LISA. Unlike the 1n efficiency, the 2n efficiency does not peak at zero decay energy as shown in Fig. 5.1, and so a proper minimization is necessary to determine the energy.

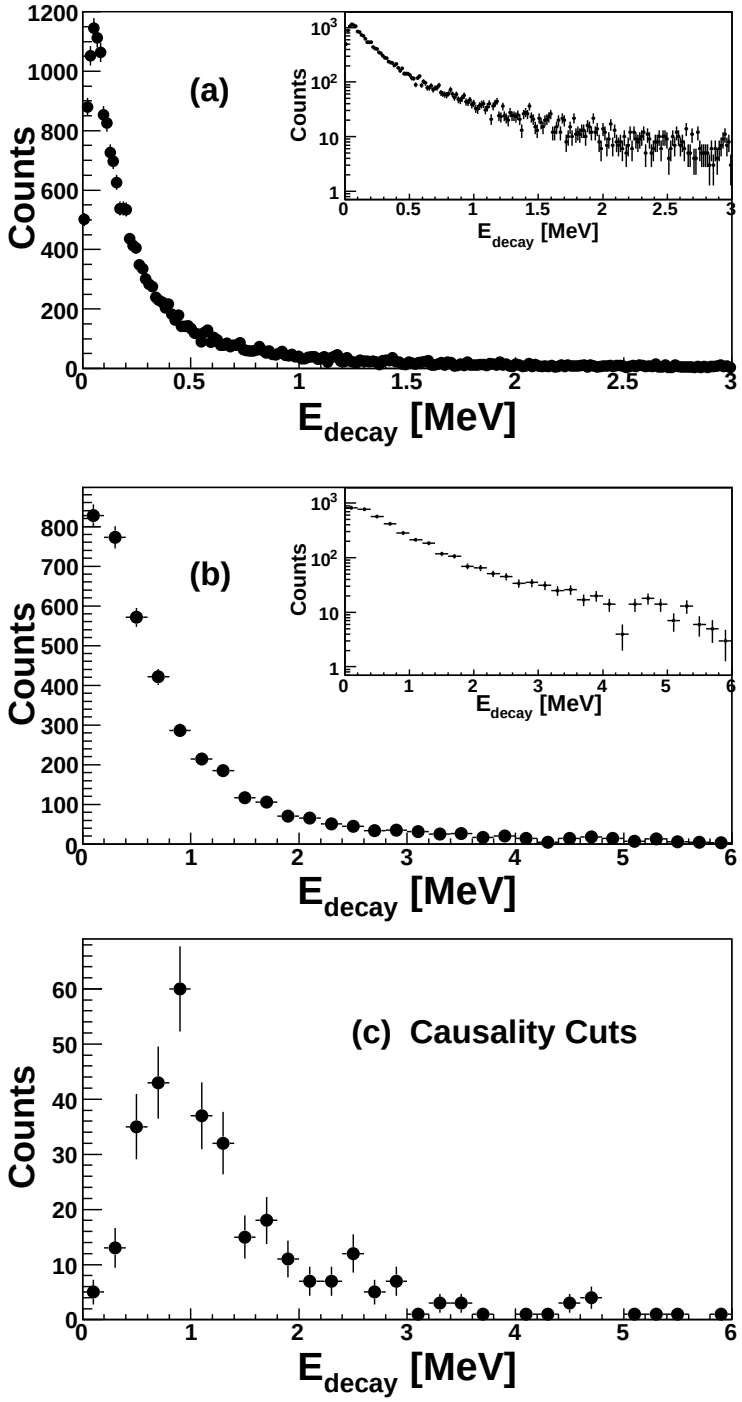

Figure 5.2: (a) 1n decay energy spectra for ^{23}O with contributions from neutron-knockout and inelastic excitation. (b) The three-body decay energy for ^{22}O + 2n for all multiplicities $\geq$ 2. (c) The three-body decay energy with causality cuts applied. The inserts show a logarithmic view.

Figure 5.3 shows the three-body correlations for the ^{22}O + 2n system in the **T** and **Y** Jacobi coordinate systems. The spectra have the causality cuts applied, as well as an additional requirement that $E_{3body} < 4$ MeV.

Even without a fit, there are several features that indicate a sequential decay. The relative energy in the **Y**-system, which represents the neutron-core energy, peaks around 0 and 1. This is indicative of an uneven sequential decay where one neutron is high-energy, and the other low. In addition the relative angle in the **T**-system peaks strongly at -1 and 1 with a valley in between. This is also the result of two neutrons with disparate energies. The **T**-system is constructed in the center-of-mass frame. Since one neutron imparts a bigger kick than the other, when the less energetic particle is boosted into the frame of the more-energetic one, its direction appears backward (even though it is isotropically emitted in the n-core + n frame). This results in peaks at -1 and 1, or 0 and 180 degrees.

Note also that the spectra lack the features one would expect from a di-neutron decay. The ratio E_x/E_T in the **T**-system does not peak at 0, but rather at $\sim 1/2$ implying that the neutron-neutron energy is large relative to the total available energy. However, the spectra do not contain 100% true 2n signals, and one must rely on simulation to estimate the amount of contamination from 1n scatter.

As previously mentioned, ^{22}O can be populated by multiple paths: (1) direct population of ^{23}O via 1n knockout from ^{24}O , and (2) inelastic excitation to ^{24}O* which decays by two-neutron emission. Figure 5.4 illustrates these two population paths.

Since both paths may contribute, it is important to consider both the one and two-neutron decay energy spectra in Fig. 5.2 simultaneously. This is done by a simultaneous minimization of the log-likelihood ratio, $-Ln[\Lambda]$ on (a) the ^{22}O + $1n$ decay energy, (b) the ^{22}O + 2n decay energy, (c) and the ^{22}O + 2n decay energy with causality cuts. This

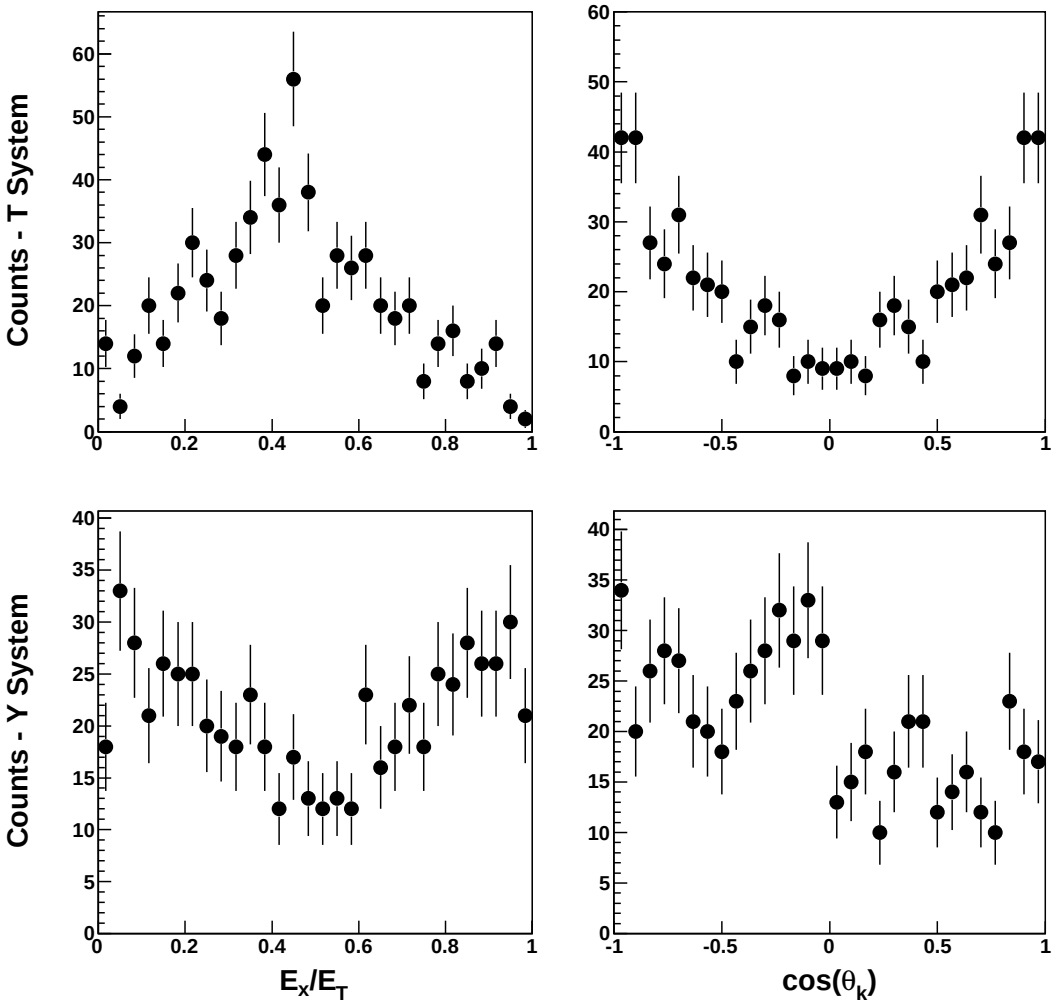

Figure 5.3: Jacobi relative energy and angle spectra in the **T** and **Y** systems for the decay of ^{24}O $\rightarrow$ ^{22}O + 2n with the causality cuts applied and the requirement that $E_{decay} < 4$ MeV.

method provides additional constraints over fitting each spectra independently by requiring the model to appropriately reproduce the ratio of 1 to 2 multiplicity events. For example a pure 1n model will fit the low-lying peak in ^{23}O but will unable to also fit the causality cuts provided a real 2n signal is present.

To allow for the direct population of ^{23}O the decay of two previously reported states was included: the low-lying sharp resonance at 45 keV [73, 68, 72, 63] and the first-excited

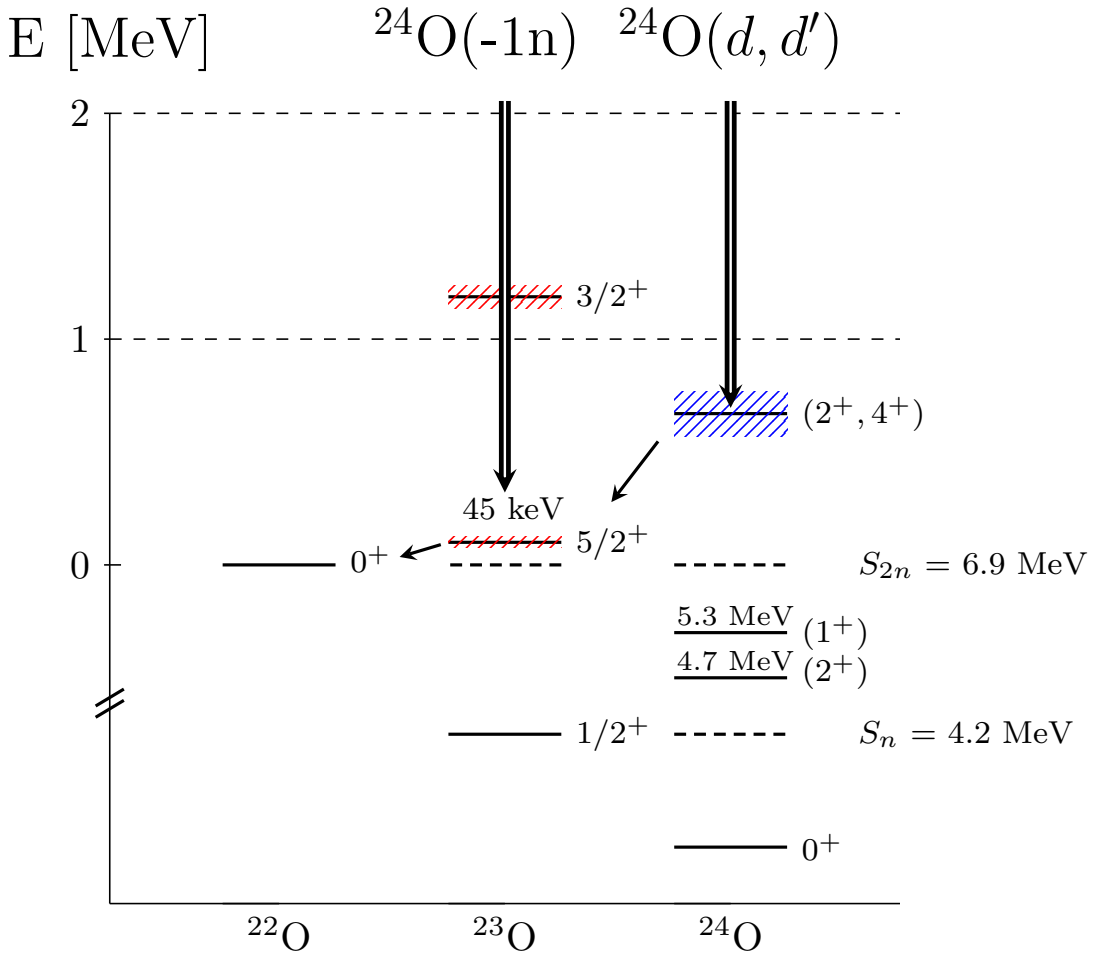

Figure 5.4: Level scheme for the population of unbound states in ^{23}O and ^{24}O from neutron-knockout and inelastic excitation. Hatched areas indicate approximate widths.

state at 1.3 MeV [74]. The one-neutron decays use the Breit-Wigner lineshape discussed in Section 2.1.1. The two-neutron decay was modelled using the formalism of Volya [127], detailed in Section 2.2.2.The best fit for the decay of ^{23}O and ^{24}O is shown in Fig. 5.5.

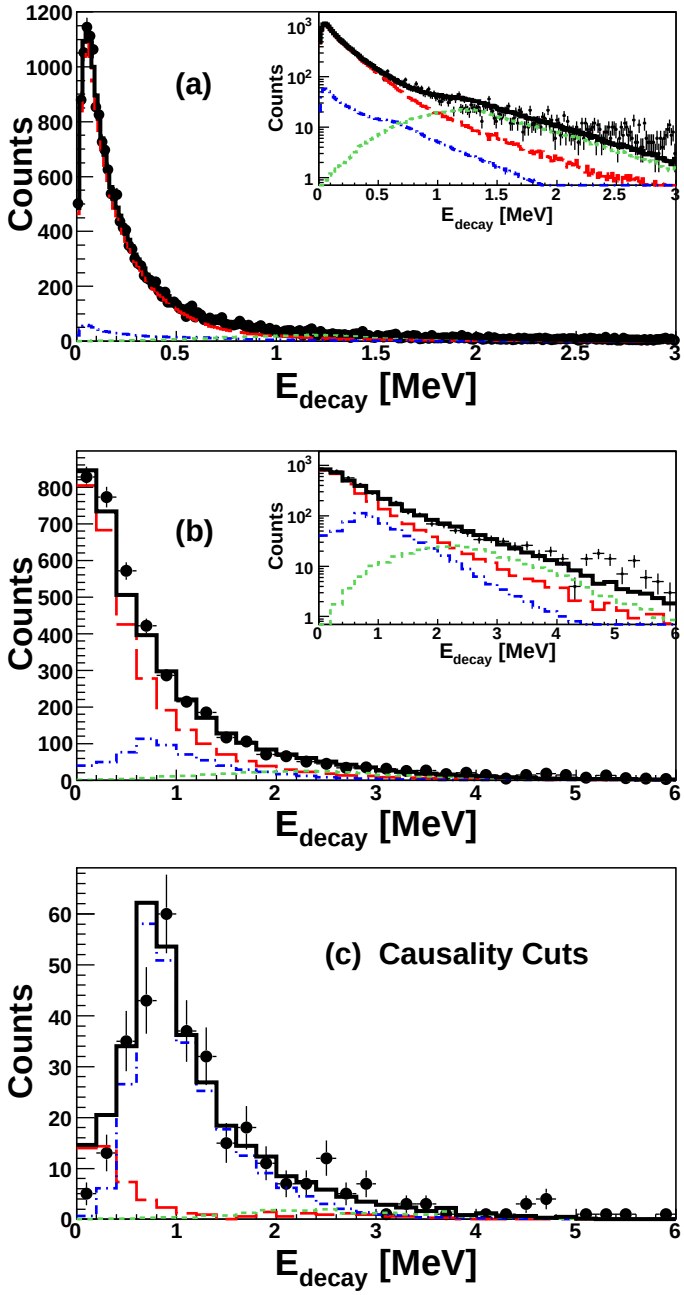

Figure 5.5: (a) 1n decay energy spectra for ^{23}O with contributions from neutron-knockout and inelastic excitation. (b) The three-body decay energy for ^{22}O + 2n for all multiplicities ≥ 2. (c) The three-body decay energy with causality cuts applied. Direct population of the $5/2^+$ state and $3/2^+$ state in ^{23}O are shown in dashed-red and dashed-green respectively. The 2n component coming from the sequential decay of ^{24}O is shown in dashed-blue and decays through the $5/2^+$ state. The sum of all components is shown in black. The inserts show a logarithmic view.

Parameter	Deviation in E_{3body} $\sigma = \sqrt{V}$ [keV]
Input Beam θ_x in Sim. ($\pm$15 [mrad])	14
Target E_{loss} ($\pm$5% $\sim$ 10 [MeV])	10
Drift Length dL (1.56 vs. 1.7 [m])	40
CRDC1 X offset ($\pm$1 [mm])	2
CRDC2 X offset ($\pm$1 [mm])	8
Global t_{mean} for MoNA-LISA ($\pm$0.2 [ns])	6
Total	45

Table 5.1: Error budget for the three-body decay energy. The dominant contribution is the drift length, dL.

Using previously reported values for the states in ^{23}O [73, 68, 72, 63, 74] we obtain good agreement with the data. The best-fit for the three-body decay gives an energy of $E = 715 \pm 110(stat.) \pm 45(sys.)$ keV, which agrees with previous measurement [63], although the central value is approximately 100 keV higher. The systematic error was determined by adjusting several calibration parameters and repeating the minimization to obtain the fluctuations in the minimum energy. The error budget is given in Table 5.1.

Only an upper-limit can be placed on the width with $\Gamma < 2$ MeV, as the width is dominated by the experimental resolution and the Breit-Wigner lineshape saturates at large Γ. Within Volya's description, even an input width of $\Gamma = 6$ MeV produced a resonance with a FWHM of $\sim$ 400 keV. The best fit is shown using the single-particle width $\Gamma_{spdw} = 120$ keV. Using $S_{2n} = 6.93 \pm 0.12$ MeV [8], we obtain an excitation energy for the three-body state at 7.65 ± 0.2 MeV with respect to the ground state of ^{24}O. No branching through the $3/2^+$ state in ^{23}O was necessary to fully describe the data. All three spectra in Figure 5.5 are well described by a single state in ^{24}O. Even though the data are dominated by 1n contributions from direct population of ^{23}O, a one-neutron hypothesis cannot describe the causality cuts as evidenced by its low amplitude in the causality cut spectrum of Fig. 5.5 (red line).

It is possible to fit the three-body energy with any of the two-neutron models considered in this analysis. Since that spectrum only contains relative energy information, the orientation of the nucleons is unimportant so long as their energy adds up to the three-body state. The Jacobi correlations however, offer a powerful tool for discriminating between the different possible decay modes. Figure 5.6 shows the experimental data in the **T** system next to the predictions for each three-body model. Shown here are the same data in Figure 5.3 however now one can see how the relative enegy E_x/E_T is correlated with angle $\cos(\theta)$. The amplitudes of the simulation are set to twice the integral of the three-body spectrum with causality cuts.

It is immediately evident by Figure 5.6 that a di-neutron or phase-space model will be unable to describe the data. Both models have the incorrect inflection in $\cos(\theta)$, and do not reproduce the bell shape in E_x/E_T around $\sim 1/2$. However, comparison to the phase-space model is still useful, as it serves to illustrate what the "base-line" looks like in the case where no correlations are present. The di-neutron is shown as well. Even though it is not expected based on the structure of the energy levels, in principle the decay is an interference of both a di-neutron and sequential emission. It's inclusion demonstrates that the observed correlations are distinct from di-neutron emission which other 2n unbound nuclei are interpreted as emitting [51, 26, 54]. While the sequential model describes the valley in $\cos(\theta)$, and bell-shape in E_x/E_T, it predicts the valley to be deeper than is observed. This can be explained by contamination from 1n events from the decay of ^{23}O.

Figure 5.9 shows the prediction of the best-fit of the decay energy spectra on top of the observed Jacobi spectra. These spectra are reproduced and not fit. Here we assume the decay is a sequential process passing through the low-lying intermediate state in ^{23}O. The agreement is very good. Shown in dashed-blue is the contribution from the sequential decay,

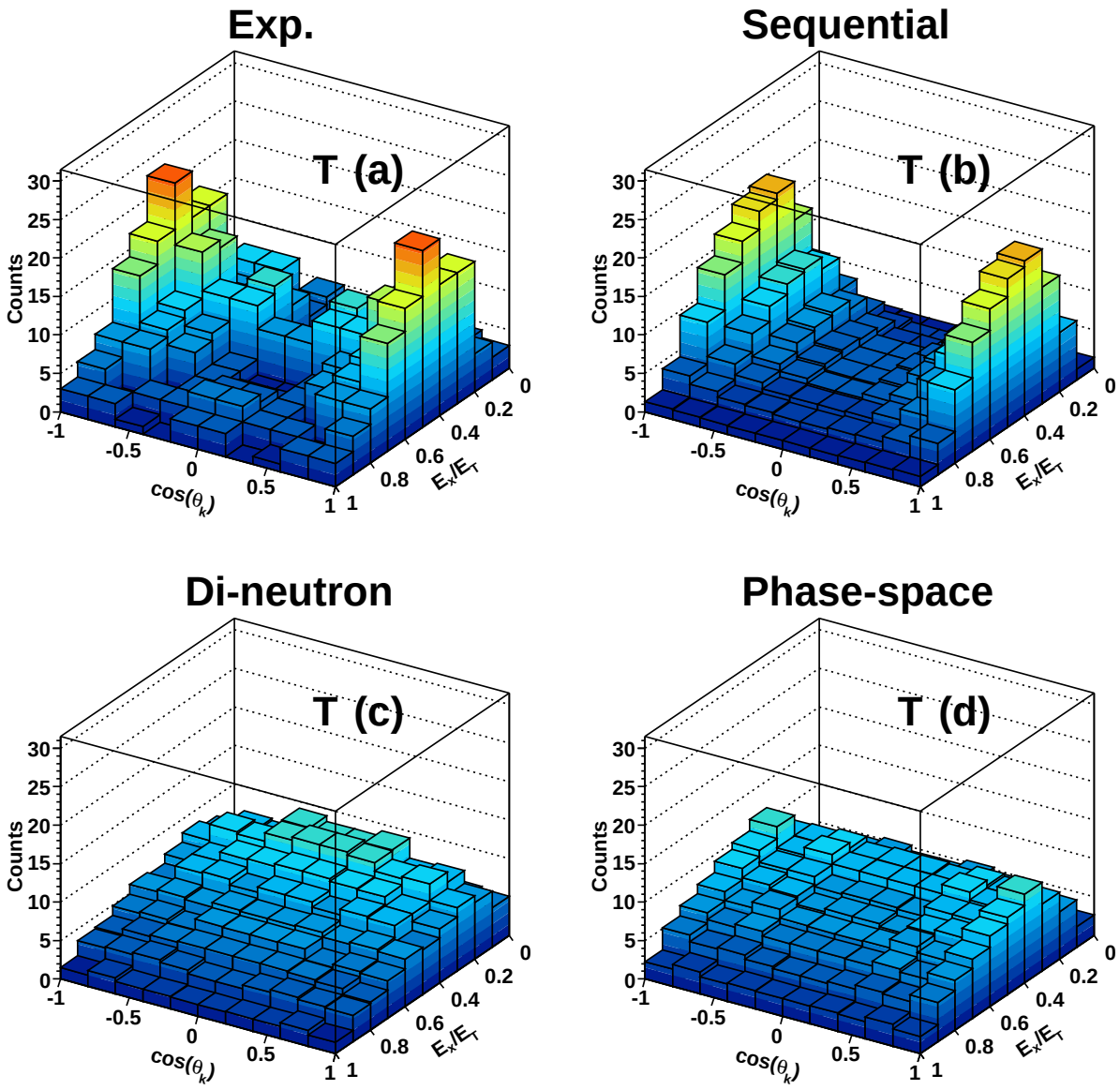

Figure 5.6: Jacobi relative energy and angle spectra in the **T** system for the decay of ^{24}O $\rightarrow$ ^{22}O + 2n with the causality cuts applied and the requirement that $E_{decay} < 4$ MeV. Shown for comparison are simulations of several three-body decay modes. A sequential decay (b), a di-neutron decay with $a = -18.7$ fm (c), and (d) a phase-space decay. The amplitudes are set by twice the integral of the three-body spectrum with causality cuts.

and in gray is the contribution from the 1n decay of ^{23}O. The observed shape of the Jacobi spectra are what we expect give that the intermediate state in ^{23}O is low-lying and narrow. In the two-proton decay of ^{6}Be [43] it was observed that the sequential decay mechanism was suppressed until the decay energy satisfied the following relation:

$$E_{3body} > 2 * E_{2body} + \Gamma_{2body}$$

which is certainly fulfilled here. It is interesting however, that a full three-body calculation is not necessary to describe the decay observed here. On the proton drip-line, several two-proton emitting nuclei show signs of sequential emission competing with true three-body processes [30, 43, 44].

The sequential decay is also supported within the shell model. The $(d, d^{'})$ reaction mechanism will populate particle-hole states in ^{24}O. Such a configuration is illustrated in Figure 5.7 and would be a particle-hole state with spin-parity 2^{+} or 4^{+}. The USDB hamiltonian predicts a 2^{+} and 4^{+} roughly 300 keV apart above the two-neutron separation energy. It is possible that the observed resonance is a superposition of both the 2^{+} and 4^{+} states, however a single resonance is sufficient to describe the data. If the observed peak corresponds to the 4^{+}, then the agreement with the USDB interaction would be very good as shown in Figure. 5.8. A 0^{+} is also predicted to be nearby in energy at 7.5 MeV. However, the 0^{+} would be a two-particle two-hole excitation which cannot be made by $(d, d^{'})$. In addition, another state has been observed above the two-neutron separation energy in ^{24}O at 7.3 MeV. This state however, was observed to undergo a one-neutron decay and was concluded to have $\nu(1s_{1/2})^{-1}\nu(fp)^{1}$ configurations with negative parity [71].

In this picture, the first neutron decays from the $\nu 0d_{3/2}$ orbital, and the second from

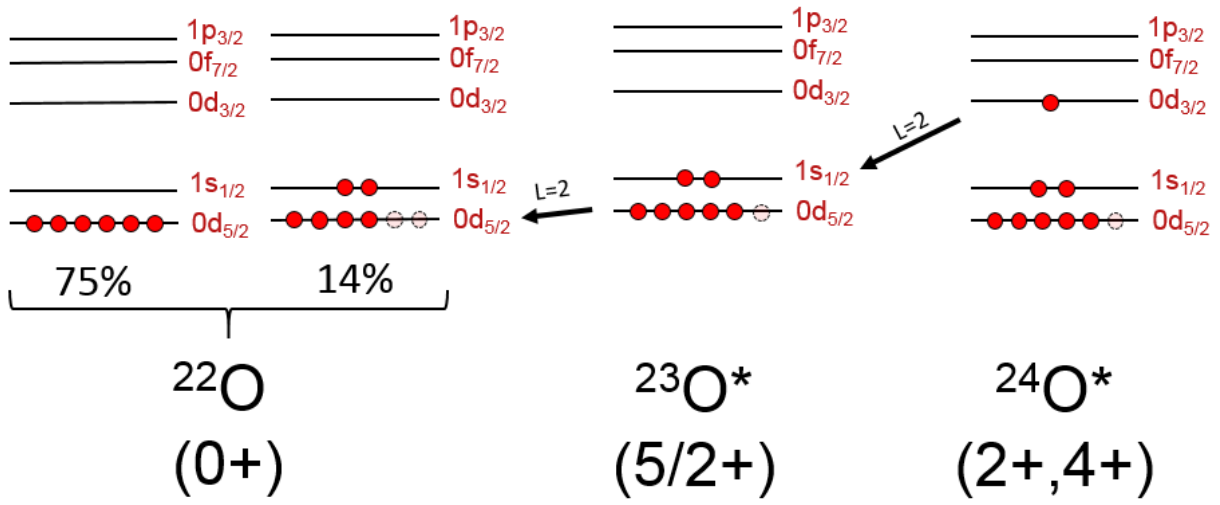

Figure 5.7: Neutron configurations for the two-neutron sequential decay. Filled circle represent particles and faded circles represent holes. The 2^+ or 4^+ configuration of ^{24}O is shown on the far right and is a particle-hole excitation. The $5/2^+$ state in ^{23}O is a hole state which decays to the two-particle two-hole configuration of ^{22}O which is a small component of the ground state wavefunction.

the $\nu 0d_{5/2}$, with the final-step being a decay to a two-particle two-hole configuration of the ground state of ^{22}O. Although the spectroscopic factor for the final step is small, it is finite, as the ground state of ^{22}O contains a mixture of the $\nu(1s_{1/2})^2\nu(0d_{5/2})^{-2}$ configuration at roughly 14% as illustrated in Figure 5.7

It is expected that the neutrons have angular distributions reflective of the fact that they both have $\ell = 2$. It is at this point that Volya's model breaks down, as it is assumed that the neutrons originate from the same orbital, carry the same angular momentum, and are emitted isotropically. At present, the angular distributions of the neutrons are left as isotropic and the J^+ of the state is tentatively assigned to 2^+ or 4^+. This does not affect the decay energy measurement as it is a scalar. A full three-body calculation that properly includes the angular distributions could provide valuable insight into the decay mechanism.

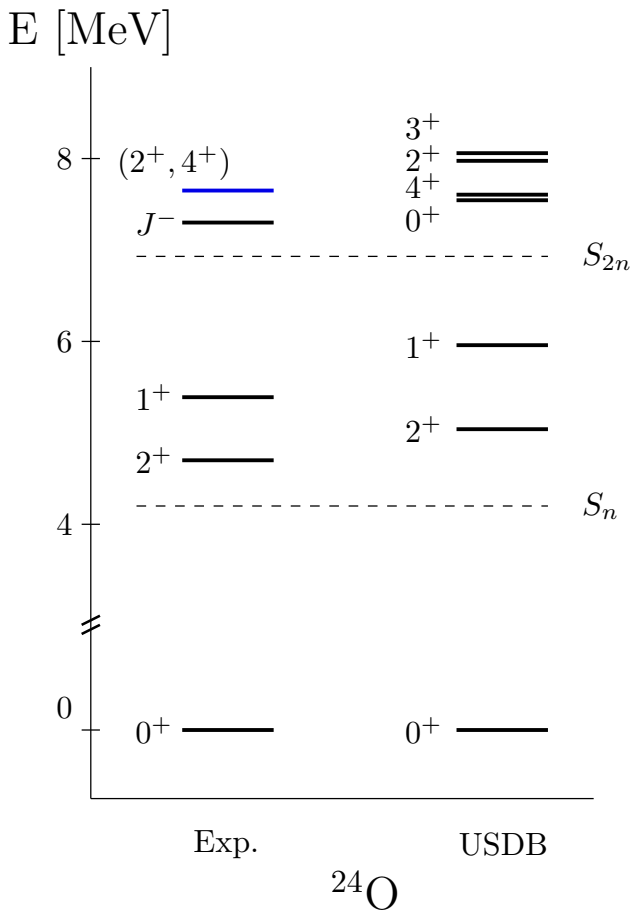

Figure 5.8: Comparison of experimentally measured states in ^{24}O with USDB shell model predictions. Data taken from Refs. [70, 71]. The state observed in the present work is shown in blue.

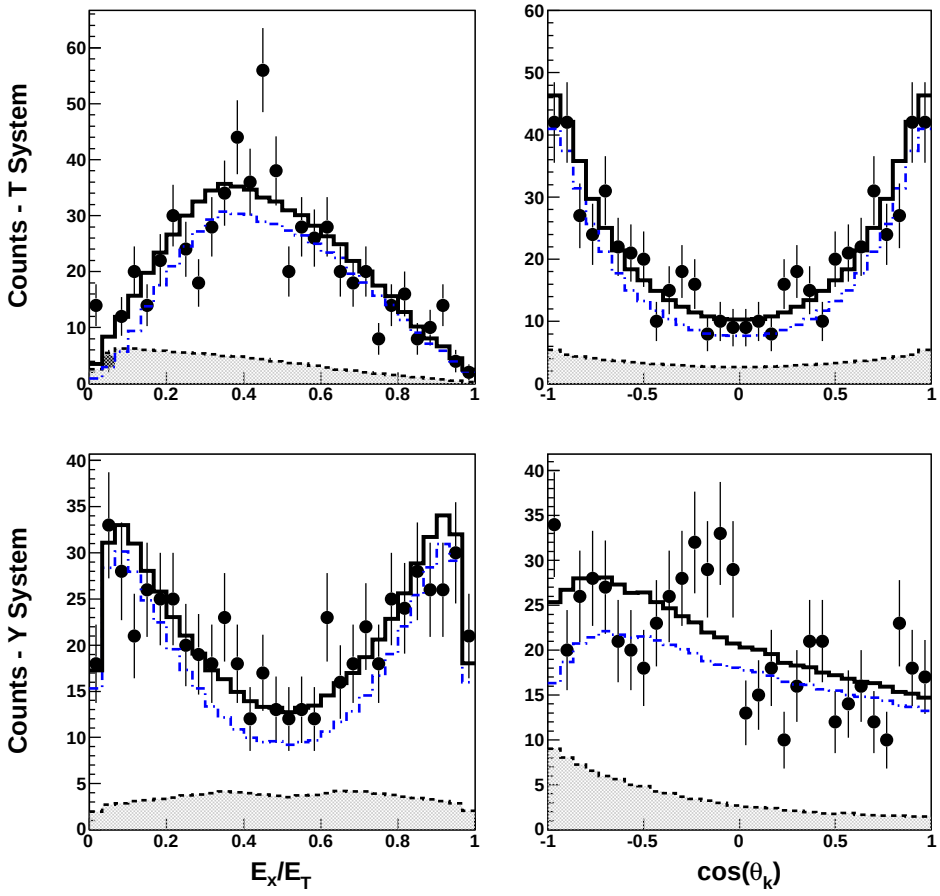

Figure 5.9: Jacobi relative energy and angle spectra in the **T** and **Y** systems for the decay of ^{24}O $\rightarrow$ ^{22}O + 2n with the causality cuts applied and the requirement that $E_{decay} < 4$ MeV. In dashed-blue is the sequential decay through the $5/2^+$ state in ^{23}O. The remaining false 2n components from the 1n decay of ^{23}O are shown in shaded-grey. The sum of both components is shown in solid-black

5.2 ^{22}N + 1n

In addition to observing the sequential decay of ^{24}O, unbound states in ^{23}N were also populated via one-proton knockout. The two-body decay energy for ^{23}N is shown in Figure 5.10 after selection of ^{22}N in the focal plane and requiring a valid neutron in MoNA-LISA.

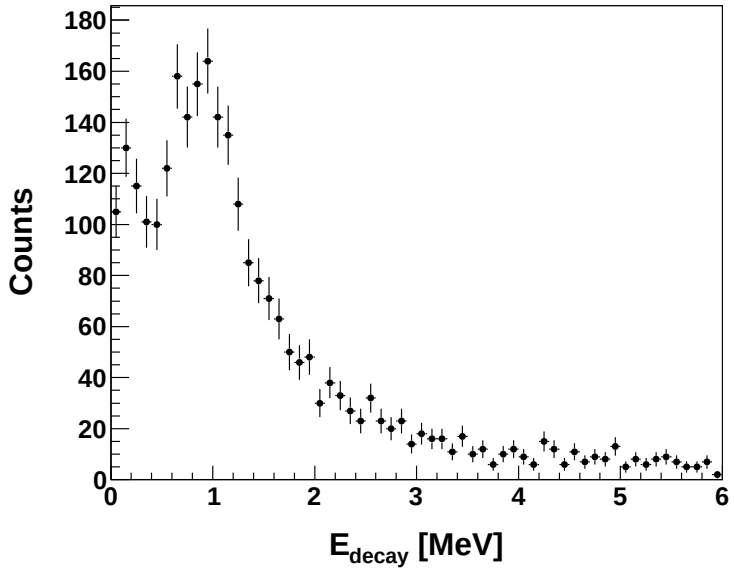

Figure 5.10: Two-body decay energy for ^{22}N + 1n.

As of present, there are no reports of unbound states in ^{23}N although it is known to have a bound ground state [128] with a half-life of about 14 ms [129]. In addition, there are no reports of any bound excited state. The data show two peaks around $\sim$ 100 keV and $\sim$ 1 MeV, both of which are less than the 2n separation threshold in ^{23}N, which is at $S_{2n} = 3.07$ MeV [8] and corresponds to 1.3 MeV in Figure 5.10. If the $\sim$ 1 MeV peak decays to the ground state of ^{22}N, it would correspond to a state at approximately 2.8 MeV with respect to the ground state of ^{23}N. Due to the drop-off in efficiency (Fig. 5.1), the intensity of the $\sim$ 1 MeV peak is nearly $3 - 10$ times higher than the lower-energy peak.

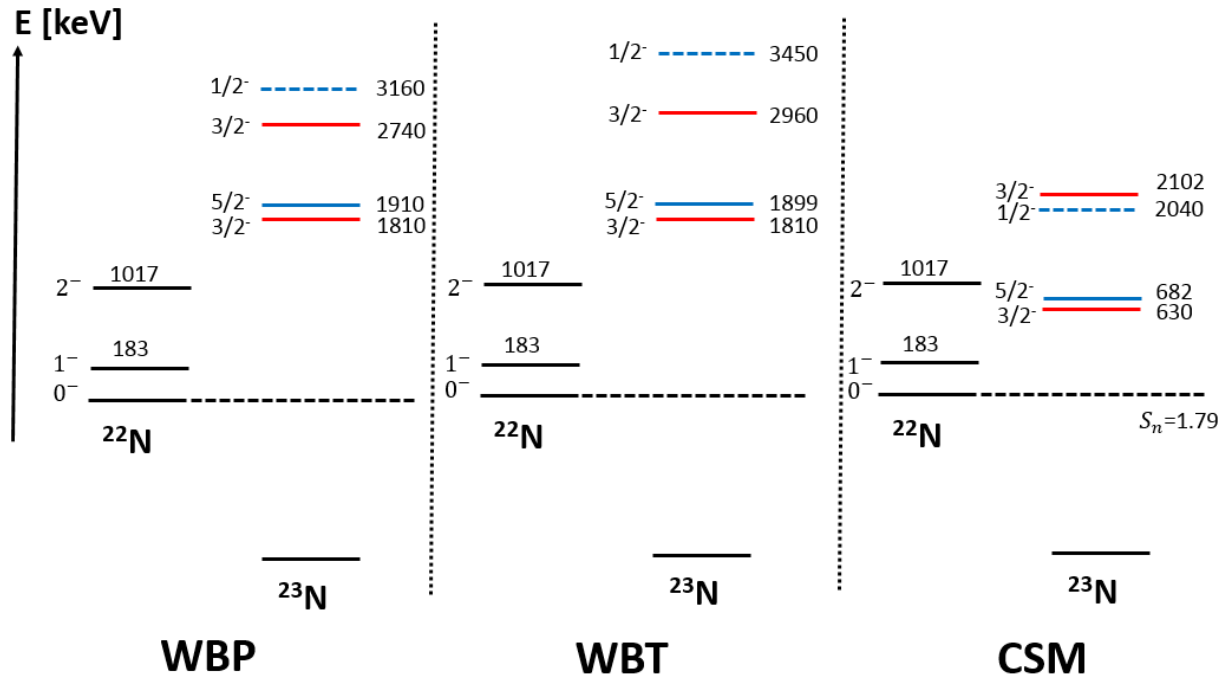

Figure 5.11: Shell model predictions for ^{23}N with the WBP and WBT Hamiltonians as well as the Continuum Shell Model.

5.2.1 Interpretation

It is important to note that ^{22}N has two bound excited states that the neutron decay of ^{23}N could branch to. A study of in-beam γ-ray spectroscopy of ^{22}N observed a 183 keV and an 834 keV transition in coincidence, which have been interpreted as the level scheme in Figure 5.11. Although the spin and parity of the ground and excited states of ^{22}N are tentative, both the WBTM and WBT interactions predict an ordering of $0^-, 1^-$, and 2^- for the ground, first, and second excited states, respectively. It is then possible, that the observed decay energy is not the true energy of a state in ^{23}N, but rather the difference in energy between a state in ^{23}N and an excited state in ^{22}N. In order to distinguish the two, it would be necessary to have γ-ray detection around the target. Such detectors have been used with MoNA in the past, e.g. CAESAR, however this measurement was not within the original scope of the experiment. Thus, no γ-ray information is present in the current data.

Because of this ambiguity, many level schemes and degeneracies are possible. At best, one can only speculate while guided by theoretical calculations.

It is not likely to populate a $5/2^-$ state in ^{23}N by proton knockout from ^{24}O, which has a the ground state configuration of 0^+. To populate a $5/2^-$ state requires an $\ell = 3$ component of the wavefunction and the ground state configuration of ^{24}O has none. A $3/2^-$ state can be populated by removal of a $\pi 0p_{1/2}$ proton, in which case the single proton left in the $\pi 0p_{1/2}$ orbit couples to a 2^+ configuration of neutrons ($\nu 1s_{1/2} \otimes \nu 0d_{3/2}$). Additionally, a $3/2^-$ state is more easily made by simply removing a $\pi 0p_{3/2}$ proton. While more tightly bound, there are a greater number of protons in the $p_{3/2}$ orbital compared to the $p_{1/2}$ orbital, and populating the $3/2^-$ in this way would not require re-arranging the neutrons. Calculations with the WBP and WBT hamiltonian as well as the continuum shell model (CSM), predict the lowest excited states in ^{23}N to be $3/2^-$ and $5/2^-$ in the vicinity of $2 \sim 4$ MeV as shown in Fig. 5.11. The first excited $1/2^-$ does not appear until around 5 MeV of excitation. Thus $3/2^-$ is the most likely candidate for the spin and parity of the state(s) populated in ^{23}N.

If one assumes that the $E \sim 1$ MeV peak does not originate from a transition to the 2^- state in ^{22}N, then the set of possible level schemes is reduced. This is a reasonable assumption, since a decay to this state would imply observing a resonance above the two-neutron separation threshold in ^{23}N that undergoes a one-neutron decay. However, simply being above S_{2n} does not prevent 1n emission. For example, such a decay has been observed in ^{24}O [68] where a state above the two-neutron separation energy underwent a 1n decay to ^{23}O. Under this assumption the possible ordering for these states is shown in Figure 5.12.

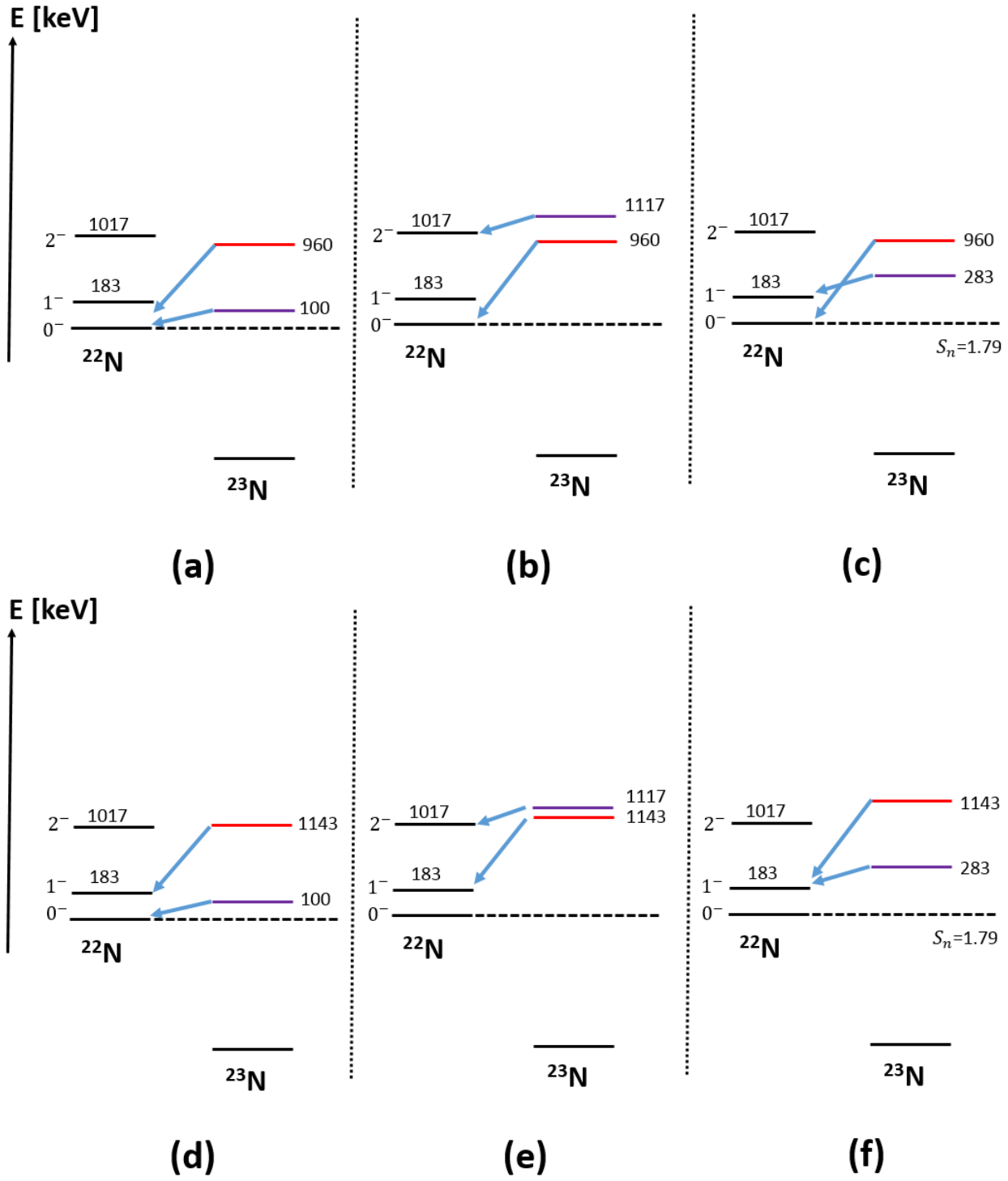

Figure 5.12: Possible level schemes that could give rise to the observed two-body decay energy for ^{23}N. Case (a) is the "Ground State Decay," while the "Two State" scenario is case (b), and the "Single State" case (e). The single state interpretation could also be two states close together. Cases (c), (d), and (f) are excluded due to the weak intensity of the 100 keV transition.

5.2.1.1 Ground State Decay

First, in order to determine the energy, consider the "Ground State Decay" where each peak consists of only a single contribution and represents an independent state in ^{23}N. If we assume the 1 MeV peak is not an overlap of two states, then the best-fit is shown in Figure 5.13. The best description was obtained with two $\ell = 2$ Breit-Wigners at $E_1 = 100 \pm 20$ and $E_2 = 960 \pm 30$ keV. The width is dominated by the experimental resolution and does not minimize. The χ^2 asymptotes around 500 keV at a value within 1σ. For this reason, the single-particle widths of $\Gamma_1 = 2$ keV and $\Gamma_2 = 115$ keV are used for the first and second $3/2^-$ respectively. This scenario, as well as many other possibilities in Fig. 5.12 can be excluded by examining the spectroscopic overlaps C^2S between ^{23}N and ^{24}O. These are summarized in Table 5.2 for the WBT and WBP hamiltonians.

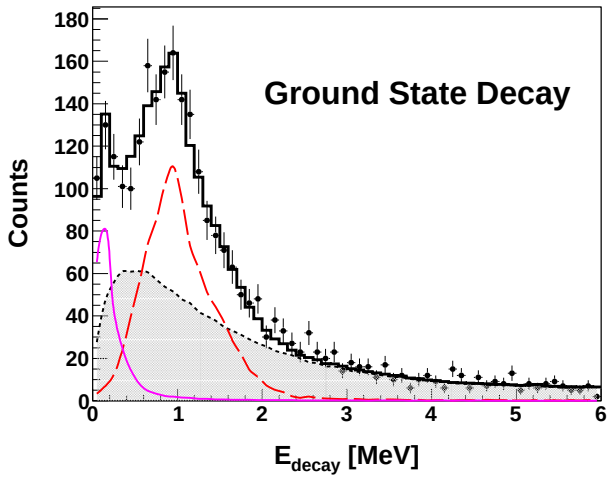

Figure 5.13: Best fit of the two-body decay energy for ^{23}N based on the "Ground State Decay" interpretation. The purple curve indicates the 100 keV transition, the dahsed red is the 960 keV transition. The 2n background is shown in shaded gray.

According to the WBP interaction, the lowest $3/2^-_1$ has the strongest overlap, by about a factor of ~ 2 compared to the second $3/2^-$. The WBT interaction predicts slightly larger overlap for the $3/2^-_2$. If we interpret the ~ 100 keV peak as coming from a state below the

$\sim$ 1 MeV peak, then we reach a contradiction between the data and shell model. Due to our efficiency, the $\sim$ 1 MeV peak is approximately $3 \sim 10$ times more intense than the lower energy peak implying $C^2S(3/2^-_2) > C^2S(3/2^-_1)$, which is not what the WBP interaction predicts. Although the WBT interaction does predict the overlap to the second $3/2^-$ to be greater, it is still about a factor of 4 too small. The intensity of the $\sim$ 100 keV peak in any fit will always be smaller than the $\sim$ 1 MeV peak due to the acceptance of MoNA. To be consistent with the spectroscopic factors the $\sim$ 100 keV transition can originate from either the same state as the $\sim$ 1 MeV transition or a state above it. This leaves a couple possibilities, referred to as the "Single State" and "Two State" scenarios: (1) A single state at 1.1 MeV (or an unresolved doublet), and (2) a state at 1.1 MeV, and another below it at 960 keV.

5.2.1.2 Single State

The data can also be fully described by a single state at $E = 1.1$ MeV. In this scenario, the $\sim$ 100 keV transition is an $\ell = 0, 2$ decay to the 2^- state in ^{22}N, and the observed peak is a superposition of a 960 keV decay to the 1^- state and a 1100 keV decay to the ground state of ^{22}N. Table 5.3 shows the ratio of intensities of each contribution in the fit, which is

WBP				WBT			
E_{calc} (MeV)	E_{decay} (MeV)	J^π	$\langle ^{23}N \vert ^{24}O\rangle$ C^2S	E_{calc} (MeV)	E_{decay} (MeV)	J^π	$\langle ^{23}N \vert ^{24}O\rangle$ C^2S
0	-	$1/2^-_1$	1.9328	0	-	$1/2^-_1$	1.9529
4.961	3.161	$1/2^-_2$	0.0025	5.257	3.457	$1/2^-_2$	0
3.610	1.810	$3/2^-_1$	1.4645	3.610	1.810	$3/2^-_1$	0.6893
4.525	2.725	$3/2^-_2$	0.6480	4.764	2.964	$3/2^-_2$	1.0483

Table 5.2: Spectroscopic overlaps for various states in ^{23}N with the ground state of ^{24}O. E_{decay} is calculated assuming the state decays directly to the ground state of ^{22}N.

Intesntiy Ratio I_i/I_{0^-}	WBP $C^2S_i/C^2S_{0^-}$	WBT $C^2S_i/C^2S_{0^-}$	Single State 1100 keV
I_{1^-}/I_{0^-}	~ 0	0.002	4.52
I_{2^-}/I_{0^-}	0.326	0.058	0.821

Table 5.3: Ratio of intensities in the single state interpretation compared to the equivalent ratio formed from spectroscopic overlaps for possible initial states in ^{23}N with final states in ^{22}N using the WBP and WBT interactions.

proportional to the partial width. The weakest intensity is the transition to the 2^-, while the other two decays ($\ell = 0$, and $\ell = 2$) share their intensity in roughly a 4:1 ratio in favor of the $\ell = 0$ decay. The WBP interaction is consistent with such a scenario. Also compared in Table 5.3 are the ratios of spectroscopic overlaps for $\langle {}^{22}N|{}^{23}N\rangle$ for both the WBP and WBT interactions. Although they predict the s-wave decays ($3/2^- \rightarrow 1^-$) to have almost no overlap, a small spectroscopic factor does not eliminate the possibility. Case (e) of Figure 5.12 illustrates the level scheme in ^{23}N for the "Single State" scenario.

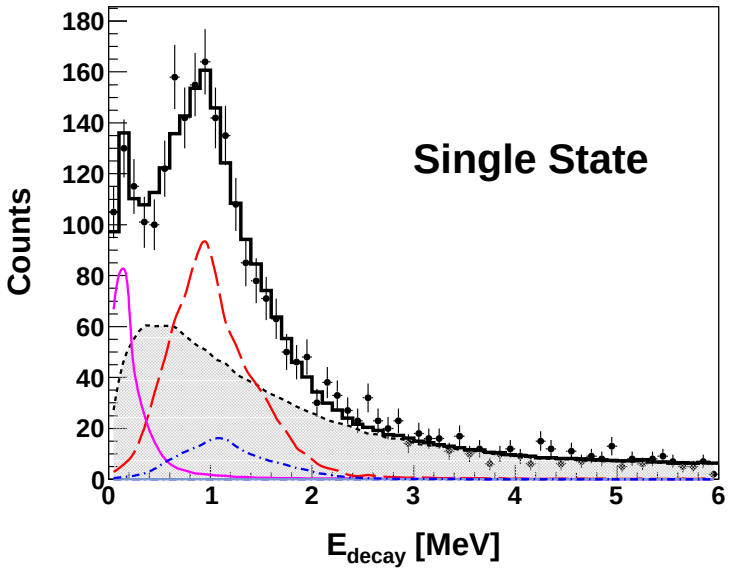

Figure 5.14: Best fit of the two-body decay energy for ^{23}N based on the "Single State" interpretation. The purple curve indicates the 100 keV transition, the dahsed red is the 960 keV transition, and the dashed blue is the 1100 keV transition. The 2n background is shown in shaded gray.

Transition $J_i^\pi \to J_f^\pi$	WBP $C^2S\,\langle {}^{22}N \vert {}^{23}N\rangle$	WBT $C^2S\,\langle {}^{22}N \vert {}^{23}N\rangle$	Two State 1100 keV + 950 keV	G.S. Decay 100 keV + 950 keV
$3/2_1^- \to 0^-$	0.4792	0.6867	0.0209 (degenerate)	0.0049
$3/2_2^- \to 0^-$	0.2926	0.0564	0.0054	0.025
$3/2_1^- \to 1^-$	$\sim$0	0.0013	-	-
$3/2_2^- \to 1^-$	0.0304	0.0220	-	-
$3/2_1^- \to 2^-$	0.1562	0.0401	-	-
$3/2_2^- \to 2^-$	0.0301	0.0492	0.0051	-

Table 5.4: Spectroscopic overlaps for possible initial states in ^{23}N with final states in ^{22}N using the WBP and WBT interactions. For comparison are the intensities for the best-fits of the data.

5.2.1.3 Two State

There is another interpretation consistent with shell model. It is possible that the 100 keV transition originates from a state above a separate state at 960 keV. In this case we observe that the lowest $3/2^-$ is most strongly populated and the second one is weakly populated. This configuration would create another 960 keV transition which would be degenerate in our spectrum, as well as a $\sim$ 700 keV transition. However, these would be s-wave decays. Figure 5.15 shows the best fit in this scenario, which is similar to the "Ground State Decay" interpretation but there is a small contribution from the 1.1 MeV decay. This case is referred to as the "Two State" scenario. No s-wave component is necessary. Table 5.4 shows the spectroscopic overlaps for possible initial states in ^{23}N with final states in ^{22}N compared to the best-fit intensities of the "Ground State" and "Two State" scenarios. Both the WBP and WBT interaction predict overlaps for the $\ell = 0$ transitions to be very small < 0.002. The small amplitude of the 1.1 MeV transition is also consistent with the WBT interactions which predicts a small overlap for the decay of $3/2_2^- \to 0^-$. The strongest intensity is from the 960 keV transition, which is interpreted as a direct decay to the ground state from the lowest $3/2_1^-$ and is consistent with both the WBP and WBT interactions.

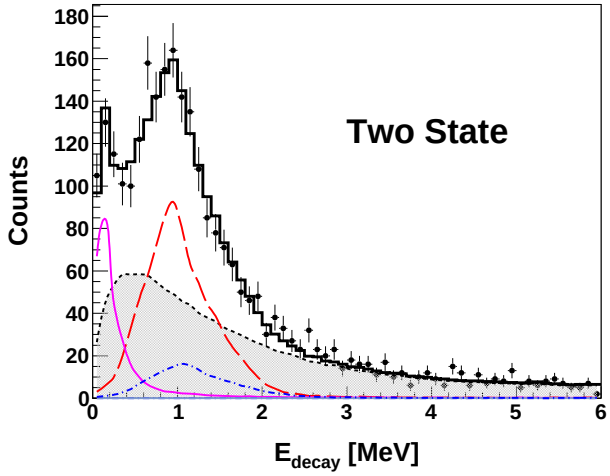

Figure 5.15: Best fit of the two-body decay energy for ^{23}N based on the "Two State" interpretation. The purple curve indicates the 100 keV transition, the dahsed red is the 960 keV transition, and the dashed blue is the 1100 keV transition. The 2n background is shown in shaded gray.

5.2.1.4 Background Discussion - Search for ^{24}N

There is a high-energy tail in the data, and some background contribution is necessary. This tail cannot be described by increasing the width of the $E_2 = 960$ keV peak, as the width of this distribution saturates. A variety of line-shapes can describe this background and provide an adequate fit. The inclusion of another state at 3 MeV, a broad gaussian at 10 MeV, or a thermal distribution with $T = 4$ MeV all describe the high-energy tail.

The proton knockout reaction mechanism should be clean. The necessisty of some background in an otherwise clean reaction mechanism suggests the presence of another reaction channel. In principle, charge-exchange from ^{24}O to ^{24}N could have occurred in this experiment. ^{24}N, being unbound, would decay to ^{23}N which was unfortunately not within the acceptance of the sweeper. However, if the charge-exchange populated a two-neutron unbound excited state then ^{22}N could be produced creating a background in the one neutron spectrum of ^{23}N (Figure 5.10). Figure 5.16 shows the reconstructed two- and three-body energies using either a 1n or 2n thermal background. The multiplicity is also shown for

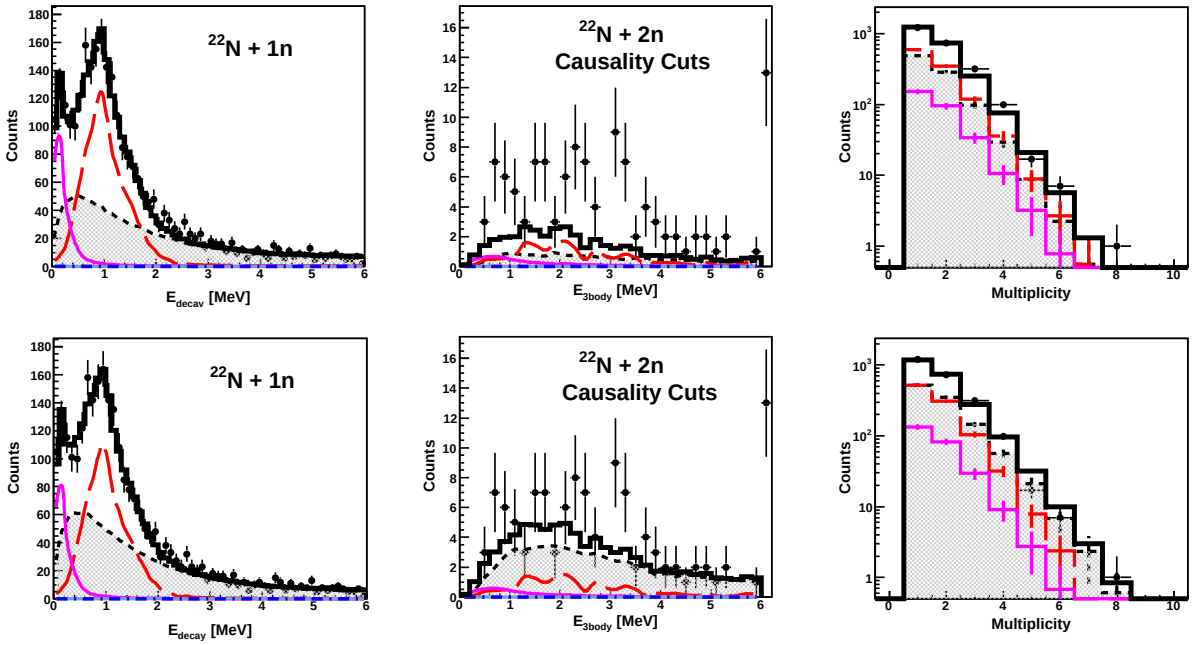

Figure 5.16: Comparison between a 1n thermal background (Top) and a 2n background (Bottom). On the left is the two-body decay energy. The middle panels shown the three-body spectrum for ^{24}N with causality cuts, and the far right panels show the multiplicity. The purple line is the $E_1 = 100$ keV Breit-Wigner, the dashed red is the $E_2 = 960$ keV resonance. The background contribution is shown in shaded gray.

comparison. The multiplicity in combination with the two- and three-body decay energies has been shown to be a useful way of determining the number of neutrons emitted in a decay. Previous studies with MoNA demonstrated this sensitivity in searches for 4n and 3n emission in the reactions ^{14}Be(-2p2n)^{10}He [130], and ^{17}C(-2p)^{15}Be [131].

While the 1n thermal background reproduces the the two-body decay energy, it fails to describe the observed counts in the three-body spectrum with causality cuts. In addition, the simulation underpredicts multiplicities 3 and 4. A 2n thermal background can better describe all three spectra simultaneously. The reduced χ^2/ν for the causality-cut spectrum is good at $\sim 7.7/5$, compared to $\chi^2/\nu \sim 27/5$ for the 1n hypothesis, and the multiplicity is better reproduced. A variety of two-neutron lineshapes were considered, including phase-space and di-neutron decays, however they do not reproduce the two-body spectrum. The 2n

thermal background, with $T = 3$ MeV, is used in this analysis as it provides a simultaneous description of all observables.

5.2.2 Conclusions

It is important to note that the interactions discussed here do not reproduce the experimentally observed energies in both ^{22}N and ^{23}N, although they are within 1 MeV. As ^{23}N is at the dripline, continuum effects and three-body forces may begin to play a significant role, and these effects were not considered in this analysis. Experimentally, we cannot distinguish between any number of cases or degeneracies that produce the energy differences observed in the decay energy. Ultimately a repeat measurement with γ detection is necessary to clarify the structure of ^{23}N.

Chapter 6

Summary and Conclusions

In this dissertation, measurements of neutron unbound states in ^{24}O and ^{23}N have been reported. These states were populated by reactions from an ^{24}O beam provided by the Coupled Cyclotron Facility at the NSCL. Unbound states in ^{24}O were populated by inelastic excitation on a liquid deuterium target, and states in ^{23}N were populated via one-proton knockout. These states were measured by invariant mass spectroscopy, which required a kinematically complete measurement of both the charged fragment and the neutrons emitted in the decay of the unbound state. The resulting charged fragments were bent by the sweeper magnet into a suite of charged particle detectors which measured their position and angle, providing isotope separation. The neutrons, unaffected by the magnetic field, travelled straight toward MoNA-LISA – an array of plastic scintillators that measured the neutron position and time of flight. With the information provided by MoNA-LISA and the sweeper, the invariant mass of the compound nucleus of interest was measured. In the case of two-neutron emission, three-body correlations were examined to determine the decay mechanism.

Unbound states were observed in ^{23}N for the first time. It is known that in this region of the nuclear chart, Mayer and Jensen's magic numbers breakdown and new shell-closures appear. This shift has been attributed to the NN tensor force, three-body forces, and continuum effects. ^{24}O is doubly magic with $Z = 8$ and $N = 16$. ^{23}N should also exhibit the $N = 16$ shell gap although one expects it to be reduced. For example, the $N = 14$ sub-shell gap in ^{22}O was observed to disappear by the time one reaches ^{20}C. Thus, identification of

states in ^{23}N could help better constrain the tensor force and provide a better understanding of shell evolution.

The two-body decay energy for ^{23}N shows prominent peaks at $E_1 = 100 \pm 20$ keV and $E_2 = 960 \pm 30$ keV. ^{22}N has two bound states that the decay of ^{23}N could branch to, implying that the observed decay does not necessarily populate the ground state of ^{22}N. Rather it could be a transition to an excited state in. However, due to the lack of γ-ray detection in the experiment, one cannot make a definitive statement on the structure of ^{23}N with the current data. Shell model calculations with the WBP and WBT interactions lead to several interpretations. A single state at 1.1 MeV above S_n, or 2.9 MeV with respect to the ground state of ^{23}N, is consistent with data and theory as well as two states at 2.9 MeV and 2.75 MeV, respectively. A repeat measurement with γ-ray detection is necessary to clarify the structure of ^{23}N.

In addition to ^{23}N, a state above the two-neutron separation energy was observed in ^{24}O. It decays by emission of two-neutrons with a three-body energy of $E_{3body} = 715 \pm 110$ (stat) ± 45 (sys) keV, placing it at $E = 7.65 \pm 0.2$ MeV with respect to the ground state. The three-body correlations in the **T** and **Y** Jacobi coordinate systems show clear evidence of a sequential decay through a narrow state in ^{23}O. A phase-space or di-neutron hypothesis were unable to describe the observed correlations. This constitutes the first measurement of a sequential decay, exposed by energy and angular three-body correlations in a $2n$ unbound system. The measurement demonstrates the ability to distinguish experimentally, a di-neutron signal from a different decay mode in addition to providing valuable information about few-body physics at the neutron drip line. The three-body correlations were not sensitive to the ℓ value of the decay leaving the spin-parity of this state undetermined. A separate measurement is necessary to determine the angular momentum of this state.

BIBLIOGRAPHY

BIBLIOGRAPHY

[1] Kenneth Krane. *Introductory Nuclear Physics*. John Wiley & Sons, Oregon State University, USA, 1987.

[2] M. Pfützner, M. Karny, L. V. Grigorenko, and K. Riisager. Radioactive decays at limits of nuclear stability. *Rev. Mod. Phys.*, 84:567–619, Apr 2012.

[3] J. Erler, N. Birge, M. Krtelainen, W. Nazarewicz, E. Olsen, A. Perhac, and M. Stoitsove. The limits of the nuclear landscape. *Nature*, 486:509–512, 2012.

[4] M. Thoennessen. Discovery of isotopes with $Z \leq 10$. *Atomic Data and Nuclear Data Tables*, 98(1):43 – 62, 2012.

[5] G. T. Seaborg. Superheavy elements. *Contemporary Physics*, 28(1):33–48, 1987.

[6] T. Yamazaki, Y. Kuramashi, and A. Ukawa. Helium nuclei in quenched lattice qcd. *Phys. Rev. D*, 81:111504, Jun 2010.

[7] Steven Weinberg. Phenomenological lagrangians. *Physica A: Statistical Mechanics and its Applications*, 96(12):327 – 340, 1979.

[8] M. Wang, G. Audi, A.H. Wapstra, F.G. Kondev, M. MacCormick, X. Xu, and B. Pfeiffer. The AME2012 atomic mass evaluation. *Chinese Physics C*, 36(12):1603, 2012.

[9] Robert Hofstadter. Electron scattering and nuclear structure. *Rev. Mod. Phys.*, 28:214–254, Jul 1956.

[10] Alex Brown. *Lecture Notes in Nuclear Structure Physics*. National Superconducting Cyclotron Laboratory and Department of Physics and Astronomy, East Lansing, MI, USA, 2005.

[11] Nobel gas. `https://en.wikipedia.org/wiki/Noble_gas`. Accessed: 2015-10-5.

[12] Maria Goeppert Mayer. Nuclear configurations in the spin-orbit coupling model. I. empirical evidence. *Phys. Rev.*, 78:16–21, Apr 1950.

[13] Otto Haxel, J. Hans D. Jensen, and Hans E. Suess. On the "Magic Numbers" in nuclear structure. *Phys. Rev.*, 75:1766–1766, Jun 1949.

[14] M. Stanoiu, D. Sohler, O. Sorlin, F. Azaiez, Zs. Dombrádi, B. A. Brown, M. Belleguic, C. Borcea, C. Bourgeois, Z. Dlouhy, Z. Elekes, Zs. Fülöp, S. Grévy, D. Guillemaud-Mueller, F. Ibrahim, A. Kerek, A. Krasznahorkay, M. Lewitowicz, S. M. Lukyanov, S. Mandal, J. Mrázek, F. Negoita, Yu.-E. Penionzhkevich, Zs. Podolyák, P. Roussel-Chomaz, M. G. Saint-Laurent, H. Savajols, G. Sletten, J. Timár, C. Timis, and A. Yamamoto. Disappearance of the $N = 14$ shell gap in the carbon isotopic chain. *Phys. Rev. C*, 78:034315, Sep 2008.

[15] C. R. Hoffman, T. Baumann, D. Bazin, J. Brown, G. Christian, P. A. DeYoung, J. E. Finck, N. Frank, J. Hinnefeld, R. Howes, P. Mears, E. Mosby, S. Mosby, J. Reith, B. Rizzo, W. F. Rogers, G. Peaslee, W. A. Peters, A. Schiller, M. J. Scott, S. L. Tabor, M. Thoennessen, P. J. Voss, and T. Williams. Determination of the $N = 16$ shell closure at the oxygen drip line. *Phys. Rev. Lett.*, 100:152502, Apr 2008.

[16] R. Kanungo, C. Nociforo, A. Prochazka, T. Aumann, D. Boutin, D. Cortina-Gil, B. Davids, M. Diakaki, F. Farinon, H. Geissel, R. Gernhäuser, J. Gerl, R. Janik, B. Jonson, B. Kindler, R. Knöbel, R. Krücken, M. Lantz, H. Lenske, Y. Litvinov, B. Lommel, K. Mahata, P. Maierbeck, A. Musumarra, T. Nilsson, T. Otsuka, C. Perro, C. Scheidenberger, B. Sitar, P. Strmen, B. Sun, I. Szarka, I. Tanihata, Y. Utsuno, H. Weick, and M. Winkler. One-neutron removal measurement reveals ^{24}O as a new doubly magic nucleus. *Phys. Rev. Lett.*, 102:152501, Apr 2009.

[17] E. K. Warburton, J. A. Becker, and B. A. Brown. Mass systematics for A =29∼44 nuclei: The deformed A ∼32 region. *Phys. Rev. C*, 41:1147–1166, Mar 1990.

[18] S. M. Brown, W. N. Catford, J. S. Thomas, B. Fernández-Domínguez, N. A. Orr, M. Labiche, M. Rejmund, N. L. Achouri, H. Al Falou, N. I. Ashwood, D. Beaumel, Y. Blumenfeld, B. A. Brown, R. Chapman, M. Chartier, N. Curtis, G. de France, N. de Sereville, F. Delaunay, A. Drouart, C. Force, S. Franchoo, J. Guillot, P. Haigh, F. Hammache, V. Lapoux, R. C. Lemmon, A. Leprince, F. Maréchal, X. Mougeot, B. Mouginot, L. Nalpas, A. Navin, N. P. Patterson, B. Pietras, E. C. Pollacco, A. Ramus, J. A. Scarpaci, I. Stefan, and G. L. Wilson. Low-lying neutron fp-shell intruder states in ^{27}Ne. *Phys. Rev. C*, 85:011302, Jan 2012.

[19] Takaharu Otsuka, Toshio Suzuki, Rintaro Fujimoto, Hubert Grawe, and Yoshinori Akaishi. Evolution of nuclear shells due to the tensor force. *Phys. Rev. Lett.*, 95:232502, Nov 2005.

[20] Takaharu Otsuka. Exotic nuclei and nuclear forces. *Physica Scripta*, 2013(T152):014007, 2013.

[21] G. Hagen, M. Hjorth-Jensen, G. R. Jansen, R. Machleidt, and T. Papenbrock. Continuum effects and three-nucleon forces in neutron-rich oxygen isotopes. *Phys. Rev. Lett.*, 108:242501, Jun 2012.

[22] Isao Tanihata. Effects of Tensor Forces in Nuclei. *Physica Scripta*, 2013(T152):014021, 2013.

[23] H.T. Johansson, Yu. Aksyutina, T. Aumann, K. Boretzky, M.J.G. Borge, A. Chatillon, L.V. Chulkov, D. Cortina-Gil, U. Datta Pramanik, H. Emling, C. Forssn, H.O.U. Fynbo, H. Geissel, G. Ickert, B. Jonson, R. Kulessa, C. Langer, M. Lantz, T. LeBleis, K. Mahata, M. Meister, G. Mnzenberg, T. Nilsson, G. Nyman, R. Palit, S. Paschalis, W. Prokopowicz, R. Reifarth, A. Richter, K. Riisager, G. Schrieder, N.B. Shulgina, H. Simon, K. Smmerer, O. Tengblad, H. Weick, and M.V. Zhukov. Three-body correlations in the decay of ^{10}He and ^{13}Li. *Nuclear Physics A*, 847(12):66 – 88, 2010.

[24] S. I. Sidorchuk, A. A. Bezbakh, V. Chudoba, I. A. Egorova, A. S. Fomichev, M. S. Golovkov, A. V. Gorshkov, V. A. Gorshkov, L. V. Grigorenko, P. Jalůvková, G. Kaminski, S. A. Krupko, E. A. Kuzmin, E. Yu. Nikolskii, Yu. Ts. Oganessian, Yu. L. Parfenova, P. G. Sharov, R. S. Slepnev, S. V. Stepantsov, G. M. Ter-Akopian, R. Wolski, A. A. Yukhimchuk, S. V. Filchagin, A. A. Kirdyashkin, I. P. Maksimkin, and O. P. Vikhlyantsev. Structure of ^{10}He low-lying states uncovered by correlations. *Phys. Rev. Lett.*, 108:202502, May 2012.

[25] Z. Kohley, J. Snyder, T. Baumann, G. Christian, P. A. DeYoung, J. E. Finck, R. A. Haring-Kaye, M. Jones, E. Lunderberg, B. Luther, S. Mosby, A. Simon, J. K. Smith, A. Spyrou, S. L. Stephenson, and M. Thoennessen. Unresolved question of the ^{10}He ground state resonance. *Phys. Rev. Lett.*, 109:232501, Dec 2012.

[26] Z. Kohley, E. Lunderberg, P. A. DeYoung, A. Volya, T. Baumann, D. Bazin, G. Christian, N. L. Cooper, N. Frank, A. Gade, C. Hall, J. Hinnefeld, B. Luther, S. Mosby, W. A. Peters, J. K. Smith, J. Snyder, A. Spyrou, and M. Thoennessen. First observation of the ^{13}Li ground state. *Phys. Rev. C*, 87:011304, Jan 2013.

[27] M. F. Jager, R. J. Charity, J. M. Elson, J. Manfredi, M. H. Mahzoon, L. G. Sobotka, M. McCleskey, R. G. Pizzone, B. T. Roeder, A. Spiridon, E. Simmons, L. Trache, and M. Kurokawa. Two-proton decay of ^{12}O and its isobaric analog state in ^{12}N. *Phys. Rev. C*, 86:011304, Jul 2012.

[28] R. A. Kryger, A. Azhari, M. Hellström, J. H. Kelley, T. Kubo, R. Pfaff, E. Ramakrishnan, B. M. Sherrill, M. Thoennessen, S. Yokoyama, R. J. Charity, J. Dempsey, A. Kirov, N. Robertson, D. G. Sarantites, L. G. Sobotka, and J. A. Winger. Two-proton emission from the ground state of ^{12}O. *Phys. Rev. Lett.*, 74:860–863, Feb 1995.

[29] I. Mukha, L. Grigorenko, L. Acosta, M. A. G. Alvarez, E. Casarejos, A. Chatillon, D. Cortina-Gil, J. M. Espino, A. Fomichev, J. E. García-Ramos, H. Geissel, J. Gómez-Camacho, J. Hofmann, O. Kiselev, A. Korsheninnikov, N. Kurz, Yu. A. Litvinov, I. Martel, C. Nociforo, W. Ott, M. Pfützner, C. Rodríguez-Tajes, E. Roeckl, C. Scheidenberger, M. Stanoiu, K. Sümmerer, H. Weick, and P. J. Woods. New states in ^{18}Na and ^{19}Mg observed in the two-proton decay of ^{19}Mg. *Phys. Rev. C*, 85:044325, Apr 2012.

[30] I. Mukha, L. Grigorenko, K. Sümmerer, L. Acosta, M. A. G. Alvarez, E. Casarejos, A. Chatillon, D. Cortina-Gil, J. M. Espino, A. Fomichev, J. E. García-Ramos, H. Geissel, J. Gómez-Camacho, J. Hofmann, O. Kiselev, A. Korsheninnikov, N. Kurz, Yu. Litvinov, I. Martel, C. Nociforo, W. Ott, M. Pfützner, C. Rodríguez-Tajes, E. Roeckl, M. Stanoiu, H. Weick, and P. J. Woods. Proton-proton correlations observed in two-proton decay of ^{19}Mg and ^{16}Ne. *Phys. Rev. C*, 77:061303, Jun 2008.

[31] P. Voss, T. Baumann, D. Bazin, A. Dewald, H. Iwasaki, D. Miller, A. Ratkiewicz, A. Spyrou, K. Starosta, M. Thoennessen, C. Vaman, and J. A. Tostevin. ^{19}Mg two-proton decay lifetime. *Phys. Rev. C*, 90:014301, Jul 2014.

[32] Y.B. Zeldovish. The existence of new isotopes of light nuclei and the equation of state of neutrons. *Journal of Experimental and Theoretical Physics*, 1960.

[33] V.I. Goldansky. On neutron-deficient isotopes of light nuclei and the phenomena of proton and two-proton radioactivity. *Nuclear Physics*, 19:482 – 495, 1960.

[34] J. Giovinazzo, B. Blank, M. Chartier, S. Czajkowski, A. Fleury, M. J. Lopez Jimenez, M. S. Pravikoff, J.-C. Thomas, F. de Oliveira Santos, M. Lewitowicz, V. Maslov, M. Stanoiu, R. Grzywacz, M. Pfützner, C. Borcea, and B. A. Brown. Two-proton radioactivity of ^{45}Fe. *Phys. Rev. Lett.*, 89:102501, Aug 2002.

[35] M. J. Chromik, P. G. Thirolf, M. Thoennessen, B. A. Brown, T. Davinson, D. Gassmann, P. Heckman, J. Prisciandaro, P. Reiter, E. Tryggestad, and P. J. Woods. Two-proton spectroscopy of low-lying states in ^{17}Ne. *Phys. Rev. C*, 66:024313, Aug 2002.

[36] I. Mukha, K. Sümmerer, L. Acosta, M. A. G. Alvarez, E. Casarejos, A. Chatillon, D. Cortina-Gil, J. Espino, A. Fomichev, J. E. García-Ramos, H. Geissel, J. Gómez-Camacho, L. Grigorenko, J. Hoffmann, O. Kiselev, A. Korsheninnikov, N. Kurz, Yu. Litvinov, I. Martel, C. Nociforo, W. Ott, M. Pfutzner, C. Rodríguez-Tajes, E. Roeckl, M. Stanoiu, H. Weick, and P. J. Woods. Observation of two-proton radioactivity of ^{19}Mg by tracking the decay products. *Phys. Rev. Lett.*, 99:182501, Oct 2007.

[37] C. Dossat, A. Bey, B. Blank, G. Canchel, A. Fleury, J. Giovinazzo, I. Matea, F. de Oliveira Santos, G. Georgiev, S. Grévy, I. Stefan, J. C. Thomas, N. Adimi, C. Borcea, D. Cortina Gil, M. Caamano, M. Stanoiu, F. Aksouh, B. A. Brown, and L. V. Grigorenko. Two-proton radioactivity studies with ^{45}Fe and ^{48}Ni. *Phys. Rev. C*, 72:054315, Nov 2005.

[38] B. Blank, A. Bey, G. Canchel, C. Dossat, A. Fleury, J. Giovinazzo, I. Matea, N. Adimi, F. De Oliveira, I. Stefan, G. Georgiev, S. Grévy, J. C. Thomas, C. Borcea, D. Cortina, M. Caamano, M. Stanoiu, F. Aksouh, B. A. Brown, F. C. Barker, and W. A. Richter. First observation of ^{54}Zn and its decay by two-proton emission. *Phys. Rev. Lett.*, 94:232501, Jun 2005.

[39] D. F. Geesaman, R. L. McGrath, P. M. S. Lesser, P. P. Urone, and B. VerWest. Particle decay of ^{6}Be. *Phys. Rev. C*, 15:1835–1838, May 1977.

[40] O. V. Bochkarev, A.A. Korsheninnikov, E.A. Kuz'min, I.G. Mukha, A.A. Oglobin, L.V. Chulkov, and G.B. Yan'kov. Two-proton decay of ^{6}Be. *JETP Letters*, 40:969.

[41] A. Azhari, R. A. Kryger, and M. Thoennessen. Decay of the ^{12}O ground state. *Phys. Rev. C*, 58:2568–2570, Oct 1998.

[42] V.A. Karnaukhov and L. Hsi-T'ing. An experimental attempt to detect two-proton decay of ^{16}Ne. *Soviet Physics JETP*, 20:860–861, 1965.

[43] I. A. Egorova, R. J. Charity, L. V. Grigorenko, Z. Chajecki, D. Coupland, J. M. Elson, T. K. Ghosh, M. E. Howard, H. Iwasaki, M. Kilburn, Jenny Lee, W. G. Lynch, J. Manfredi, S. T. Marley, A. Sanetullaev, R. Shane, D. V. Shetty, L. G. Sobotka, M. B. Tsang, J. Winkelbauer, A. H. Wuosmaa, M. Youngs, and M. V. Zhukov. Democratic decay of ^{6}Be exposed by correlations. *Phys. Rev. Lett.*, 109:202502, Nov 2012.

[44] L.V. Grigorenko, T.D. Wiser, K. Miernik, R.J. Charity, M. Pftzner, A. Banu, C.R. Bingham, M. wiok, I.G. Darby, W. Dominik, J.M. Elson, T. Ginter, R. Grzywacz, Z. Janas, M. Karny, A. Korgul, S.N. Liddick, K. Mercurio, M. Rajabali, K. Rykaczewski, R. Shane, L.G. Sobotka, A. Stolz, L. Trache, R.E. Tribble, A.H. Wuosmaa, and M.V. Zhukov. Complete correlation studies of two-proton decays: ^{6}Be and ^{45}Fe. *Physics Letters B*, 677(12):30 – 35, 2009.

[45] C.R. Bain, P.J. Woods, R. Coszach, T. Davinson, P. Decrock, M. Gaelens, W. Galster, M. Huyse, R.J. Irvine, P. Leleux, E. Lienard, M. Loiselet, C. Michotte, R. Neal, A. Ninane, G. Ryckewaert, A.C. Shotter, G. Vancraeynest, J. Vervier, and J. Wauters. Two proton emission induced via a resonance reaction. *Physics Letters B*, 373(13):35 – 39, 1996.

[46] R. J. Charity, J. M. Elson, J. Manfredi, R. Shane, L. G. Sobotka, B. A. Brown, Z. Chajecki, D. Coupland, H. Iwasaki, M. Kilburn, Jenny Lee, W. G. Lynch, A. Sanetullaev, M. B. Tsang, J. Winkelbauer, M. Youngs, S. T. Marley, D. V. Shetty, A. H. Wuosmaa, T. K. Ghosh, and M. E. Howard. Investigations of three-, four-, and five-particle decay channels of levels in light nuclei created using a ^{9}C beam. *Phys. Rev. C*, 84:014320, Jul 2011.

[47] B. Blank and M.J.G. Borge. Nuclear structure at the proton drip line: Advances with nuclear decay studies. *Progress in Particle and Nuclear Physics*, 60(2):403 – 483, 2008.

[48] H.O.U. Fynbo, M.J.G. Borge, L. Axelsson, J. yst, U.C. Bergmann, L.M. Fraile, A. Honkanen, P. Hornshj, Y. Jading, A. Jokinen, B. Jonson, I. Martel, I. Mukha, T. Nilsson, G. Nyman, M. Oinonen, I. Piqueras, K. Riisager, T. Siiskonen, M.H. Smedberg, O. Tengblad, J. Thaysen, and F. Wenander. The β2p decay mechanism of ^{31}Ar. *Nuclear Physics A*, 677(14):38 – 60, 2000.

[49] J. Gómez del Campo, A. Galindo-Uribarri, J. R. Beene, C. J. Gross, J. F. Liang, M. L. Halbert, D. W. Stracener, D. Shapira, R. L. Varner, E. Chavez-Lomeli, and M. E. Ortiz. Decay of a resonance in ^{18}Ne by the simultaneous emission of two protons. *Phys. Rev. Lett.*, 86:43–46, Jan 2001.

[50] G. Raciti, M. De Napoli, G. Cardella, E. Rapisarda, F. Amorini, and C. Sfienti. Two-proton correlated emission from 18ne excited states. *Nuclear Physics A*, 834(14):464c – 466c, 2010. The 10th International Conference on Nucleus-Nucleus Collisions (NN2009).

[51] M. S. Golovkov, L. V. Grigorenko, A. S. Fomichev, S. A. Krupko, Yu. Ts. Oganessian, A. M. Rodin, S. I. Sidorchuk, R. S. Slepnev, S. V. Stepantsov, G. M. Ter-Akopian, R. Wolski, M. G. Itkis, A. S. Denikin, A. A. Bogatchev, N. A. Kondratiev, E. M.

Kozulin, A. A. Korsheninnikov, E. Yu. Nikolskii, P. Roussel-Chomaz, W. Mittig, R. Palit, V. Bouchat, V. Kinnard, T. Materna, F. Hanappe, O. Dorvaux, L. Stuttgé, C. Angulo, V. Lapoux, R. Raabe, L. Nalpas, A. A. Yukhimchuk, V. V. Perevozchikov, Yu. I. Vinogradov, S. K. Grishechkin, and S. V. Zlatoustovskiy. Correlation studies of the ^{5}H spectrum. *Phys. Rev. C*, 72:064612, Dec 2005.

[52] A. Matta et al. *RIKEN Accel. Prog. Rep.*, 45, 2012.

[53] Yu. Aksyutina, T. Aumann, K. Boretzky, M. J. G. Borge, C. Caesar, A. Chatillon, L. V. Chulkov, D. Cortina-Gil, U. Datta Pramanik, H. Emling, H. O. U. Fynbo, H. Geissel, A. Heinz, G. Ickert, H. T. Johansson, B. Jonson, R. Kulessa, C. Langer, T. LeBleis, K. Mahata, G. Münzenberg, T. Nilsson, G. Nyman, R. Palit, S. Paschalis, W. Prokopowicz, R. Reifarth, D. Rossi, A. Richter, K. Riisager, G. Schrieder, H. Simon, K. Sümmerer, O. Tengblad, R. Thies, H. Weick, and M. V. Zhukov. Study of the ^{14}Be continuum: Identification and structure of its second 2^{+} state. *Phys. Rev. Lett.*, 111:242501, Dec 2013.

[54] A. Spyrou, Z. Kohley, T. Baumann, D. Bazin, B. A. Brown, G. Christian, P. A. DeYoung, J. E. Finck, N. Frank, E. Lunderberg, S. Mosby, W. A. Peters, A. Schiller, J. K. Smith, J. Snyder, M. J. Strongman, M. Thoennessen, and A. Volya. First observation of ground state dineutron decay: ^{16}Be. *Phys. Rev. Lett.*, 108:102501, Mar 2012.

[55] E. Lunderberg, P. A. DeYoung, Z. Kohley, H. Attanayake, T. Baumann, D. Bazin, G. Christian, D. Divaratne, S. M. Grimes, A. Haagsma, J. E. Finck, N. Frank, B. Luther, S. Mosby, T. Nagi, G. F. Peaslee, A. Schiller, J. Snyder, A. Spyrou, M. J. Strongman, and M. Thoennessen. Evidence for the ground-state resonance of ^{26}O. *Phys. Rev. Lett.*, 108:142503, Apr 2012.

[56] C. Caesar, J. Simonis, T. Adachi, Y. Aksyutina, J. Alcantara, S. Altstadt, H. Alvarez-Pol, N. Ashwood, T. Aumann, V. Avdeichikov, M. Barr, S. Beceiro, D. Bemmerer, J. Benlliure, C. A. Bertulani, K. Boretzky, M. J. G. Borge, G. Burgunder, M. Caamano, E. Casarejos, W. Catford, J. Cederkäll, S. Chakraborty, M. Chartier, L. Chulkov, D. Cortina-Gil, U. Datta Pramanik, P. Diaz Fernandez, I. Dillmann, Z. Elekes, J. Enders, O. Ershova, A. Estrade, F. Farinon, L. M. Fraile, M. Freer, M. Freudenberger, H. O. U. Fynbo, D. Galaviz, H. Geissel, R. Gernhäuser, P. Golubev, D. Gonzalez Diaz, J. Hagdahl, T. Heftrich, M. Heil, M. Heine, A. Heinz, A. Henriques, M. Holl, J. D. Holt, G. Ickert, A. Ignatov, B. Jakobsson, H. T. Johansson, B. Jonson, N. Kalantar-Nayestanaki, R. Kanungo, A. Kelic-Heil, R. Knöbel, T. Kröll, R. Krücken, J. Kurcewicz, M. Labiche, C. Langer, T. Le Bleis, R. Lemmon, O. Lepyoshkina, S. Lindberg, J. Machado, J. Marganiec, V. Maroussov, J. Menéndez, M. Mostazo, A. Movsesyan, A. Najafi, T. Nilsson, C. Nociforo, V. Panin, A. Perea, S. Pietri, R. Plag, A. Prochazka, A. Rahaman, G. Rastrepina, R. Reifarth, G. Ribeiro, M. V. Ricciardi, C. Rigollet, K. Riisager, M. Röder, D. Rossi, J. Sanchez del Rio, D. Savran, H. Scheit, A. Schwenk, H. Simon, O. Sorlin, V. Stoica, B. Streicher, J. Taylor, O. Tengblad, S. Terashima, R. Thies, Y. Togano, E. Uberseder, J. Van de Walle, P. Velho, V. Volkov, A. Wagner, F. Wamers, H. Weick, M. Weigand, C. Wheldon, G. Wilson, C. Wimmer,

J. S. Winfield, P. Woods, D. Yakorev, M. V. Zhukov, A. Zilges, M. Zoric, and K. Zuber. Beyond the neutron drip line: The unbound oxygen isotopes ^{25}O and ^{26}O. *Phys. Rev. C*, 88:034313, Sep 2013.

[57] Z. Kohley, T. Baumann, D. Bazin, G. Christian, P. A. DeYoung, J. E. Finck, N. Frank, M. Jones, E. Lunderberg, B. Luther, S. Mosby, T. Nagi, J. K. Smith, J. Snyder, A. Spyrou, and M. Thoennessen. Study of two-neutron radioactivity in the decay of ^{26}O. *Phys. Rev. Lett.*, 110:152501, Apr 2013.

[58] L. V. Grigorenko, I. G. Mukha, C. Scheidenberger, and M. V. Zhukov. Two-neutron radioactivity and four-nucleon emission from exotic nuclei. *Phys. Rev. C*, 84:021303, Aug 2011.

[59] L. V. Grigorenko, I. A. Egorova, M. V. Zhukov, R. J. Charity, and K. Miernik. Two-proton radioactivity and three-body decay. v. improved momentum distributions. *Phys. Rev. C*, 82:014615, Jul 2010.

[60] Z Kohley, T Baumann, D Bazin, G Christian, P A De Young, J E Finck, R A Haring-Kaye, J Hinnefeld, N Frank, E Lunderberg, B Luther, S Mosby, W A Peters, J K Smith, J Snyder, S L Stephenson, M J Strongman, A Spyrou, M Thoennessen, and A Volya. Structure and decay correlations of two-neutron systems beyond the dripline. *Journal of Physics: Conference Series*, 569(1):012033, 2014.

[61] Z. Kohley, T. Baumann, G. Christian, P. A. DeYoung, J. E. Finck, N. Frank, B. Luther, E. Lunderberg, M. Jones, S. Mosby, J. K. Smith, A. Spyrou, and M. Thoennessen. Three-body correlations in the ground-state decay of ^{26}O. *Phys. Rev. C*, 91:034323, Mar 2015.

[62] K. Hagino and H. Sagawa. Three-body model calculation of the 2^+ state in ^{26}O. *Phys. Rev. C*, 90:027303, Aug 2014.

[63] C. R. Hoffman, T. Baumann, J. Brown, P. A. DeYoung, J. E. Finck, N. Frank, J. D. Hinnefeld, S. Mosby, W. A. Peters, W. F. Rogers, A. Schiller, J. Snyder, A. Spyrou, S. L. Tabor, and M. Thoennessen. Observation of a two-neutron cascade from a resonance in ^{24}O. *Phys. Rev. C*, 83:031303, Mar 2011.

[64] R. E. Azuma, L. C. Carraz, P. G. Hansen, B. Jonson, K. L. Kratz, S. Mattsson, G. Nyman, H. Ohm, H. L. Ravn, A. Schröder, and W. Ziegert. First observation of beta-delayed two-neutron radioactivity: ^{11}Li. *Phys. Rev. Lett.*, 43:1652–1654, Nov 1979.

[65] R.E. Azuma, T. Bjrnstad, H.. Gustafsson, P.G. Hansen, B. Jonson, S. Mattsson, G. Nyman, A.M. Poskanzer, and H.L. Ravn. Beta-delayed three-neutron radioactivity of 11li. *Physics Letters B*, 96(1):31 – 34, 1980.

[66] J.P. Dufour, R. Del Moral, F. Hubert, D. Jean, M.S. Pravikoff, A. Fleury, A.C. Mueller, K.-H. Schmidt, K. Smmerer, E. Hanelt, J. Frehaut, M. Beau, and G. Giraudet. Beta delayed multi-neutron radioactivity of ^{17}B, ^{14}Be, ^{19}C. *Physics Letters B*, 206(2):195 – 198, 1988.

[67] R J Charity, J M Elson, S Komarov, L G Sobotka, J Manfredi, R Shane, I A Egorova, L V Grigorenko, K Hagino, D Bazin, Z Chajecki, D Coupland, A Gade, H Iwasaki, M Kilbrun, J Lee, S M Lukyanov, W G Lynch, M Mocko, S P Lobastov, A Rodgers, A Sanetullaev, M B Tsang, M S Wallace, J Winkelbauer, M Youngs, S Hudan, C Metelko, M A Famino, S T Marley, D V Shetty, A H Wuosmaa, M J van Goethem, and M V Zhukov. Two-proton decay of the ^{6}Be ground state and the double isobaric analog of ^{11}Li. *Journal of Physics: Conference Series*, 420(1):012073, 2013.

[68] K. Tshoo, Y. Satou, C.A. Bertulani, H. Bhang, S. Choi, T. Nakamura, Y. Kondo, S. Deguchi, Y. Kawada, Y. Nakayama, K.N. Tanaka, N. Tanaka, Y. Togano, N. Kobayashi, N. Aoi, M. Ishihara, T. Motobayashi, H. Otsu, H. Sakurai, S. Takeuchi, K. Yoneda, F. Delaunay, J. Gibelin, F.M. Marqus, N.A. Orr, T. Honda, T. Kobayashi, T. Sumikama, Y. Miyashita, K. Yoshinaga, M. Matsushita, S. Shimoura, D. Sohler, J.W. Hwang, T. Zheng, Z.H. Li, and Z.X. Cao. Neutron occupancy of the orbital and the shell closure in ^{24}O. *Physics Letters B*, 739(0):19 – 22, 2014.

[69] M. Stanoiu, F. Azaiez, Zs. Dombrádi, O. Sorlin, B. A. Brown, M. Belleguic, D. Sohler, M. G. Saint Laurent, M. J. Lopez-Jimenez, Y. E. Penionzhkevich, G. Sletten, N. L. Achouri, J. C. Angélique, F. Becker, C. Borcea, C. Bourgeois, A. Bracco, J. M. Daugas, Z. Dlouhý, C. Donzaud, J. Duprat, Zs. Fülöp, D. Guillemaud-Mueller, S. Grévy, F. Ibrahim, A. Kerek, A. Krasznahorkay, M. Lewitowicz, S. Leenhardt, S. Lukyanov, P. Mayet, S. Mandal, H. van der Marel, W. Mittig, J. Mrázek, F. Negoita, F. De Oliveira-Santos, Zs. Podolyák, F. Pougheon, M. G. Porquet, P. Roussel-Chomaz, H. Savajols, Y. Sobolev, C. Stodel, J. Timár, and A. Yamamoto. $N = 14$ and 16 shell gaps in neutron-rich oxygen isotopes. *Phys. Rev. C*, 69:034312, Mar 2004.

[70] W. F. Rogers et al. Unbound excited states of the $N = 16$ closed shell nucleus ^{24}O. *Phys. Rev. C*, 92:034316, Sep 2015.

[71] K. Tshoo, Y. Satou, H. Bhang, S. Choi, T. Nakamura, Y. Kondo, S. Deguchi, Y. Kawada, N. Kobayashi, Y. Nakayama, K. N. Tanaka, N. Tanaka, N. Aoi, M. Ishihara, T. Motobayashi, H. Otsu, H. Sakurai, S. Takeuchi, Y. Togano, K. Yoneda, Z. H. Li, F. Delaunay, J. Gibelin, F. M. Marqués, N. A. Orr, T. Honda, M. Matsushita, T. Kobayashi, Y. Miyashita, T. Sumikama, K. Yoshinaga, S. Shimoura, D. Sohler, T. Zheng, and Z. X. Cao. $N = 16$ spherical shell closure in ^{24}O. *Phys. Rev. Lett.*, 109:022501, Jul 2012.

[72] A. Schiller, N. Frank, T. Baumann, D. Bazin, B. A. Brown, J. Brown, P. A. DeYoung, J. E. Finck, A. Gade, J. Hinnefeld, R. Howes, J.-L. Lecouey, B. Luther, W. A. Peters, H. Scheit, M. Thoennessen, and J. A. Tostevin. Selective population and neutron decay of an excited state of ^{23}O. *Phys. Rev. Lett.*, 99:112501, Sep 2007.

[73] N. Frank, T. Baumann, D. Bazin, B.A. Brown, J. Brown, P.A. DeYoung, J.E. Finck, A. Gade, J. Hinnefeld, R. Howes, J.-L. Lecouey, B. Luther, W.A. Peters, H. Scheit, A. Schiller, M. Thoennessen, and J. Tostevin. Neutron decay spectroscopy of neutron-rich oxygen isotopes. *Nuclear Physics A*, 813(34):199 – 211, 2008.

[74] Z. Elekes, Zs. Dombrádi, N. Aoi, S. Bishop, Zs. Fülöp, J. Gibelin, T. Gomi, Y. Hashimoto, N. Imai, N. Iwasa, H. Iwasaki, G. Kalinka, Y. Kondo, A. A. Korsheninnikov, K. Kurita, M. Kurokawa, N. Matsui, T. Motobayashi, T. Nakamura, T. Nakao, E. Yu. Nikolskii, T. K. Ohnishi, T. Okumura, S. Ota, A. Perera, A. Saito, H. Sakurai, Y. Satou, D. Sohler, T. Sumikama, D. Suzuki, M. Suzuki, H. Takeda, S. Takeuchi, Y. Togano, and Y. Yanagisawa. Spectroscopic study of neutron shell closures via nucleon transfer in the near-dripline nucleus ^{23}O. *Phys. Rev. Lett.*, 98:102502, Mar 2007.

[75] Ian J. Thompson and Filomena M. Nunes. *Nuclear Reactions for Astrophysics*. Cambridge University Press, The Edinburgh Building, Cambridge CB2 8RU, UK, 2009.

[76] A. M. Lane and R. G. Thomas. R-matrix theory of nuclear reactions. *Rev. Mod. Phys.*, 30:257–353, Apr 1958.

[77] Alexander Volya and Vladimir Zelevinsky. Continuum shell model. *Phys. Rev. C*, 74:064314, Dec 2006.

[78] Alexander, Volya. Physics of unstable nuclei: from structure to sequential decays. *EPJ Web of Conferences*, 38:03003, 2012.

[79] Aage Bohr and Ben Mottelson. *Nuclear Structure Volumes I and II.* World Scientific, River Edge, NJ 07661, USA, 1998.

[80] D. E. Gonzalez Trotter, F. Salinas Meneses, W. Tornow, C. R. Howell, Q. Chen, A. S. Crowell, C. D. Roper, R. L. Walter, D. Schmidt, H. Witała, W. Glöckle, H. Tang, Z. Zhou, and I. Šlaus. Neutron-deuteron breakup experiment at $E_n = 13$ MeV: Determination of the $^1S_0$ neutron-neutron scattering length a_{nn}. *Phys. Rev. C*, 73:034001, Mar 2006.

[81] H. Ryuto et al. *Nucl. Instrum. Methods Phys. Res. A*, 555:1, 2005.

[82] M.D. Bird et al. *IEEE Trans. Appl. Supercond.*, 15:1252, 2005.

[83] B. Luther et al. *Nucl. Instrum. Methods A*, 505:33, 2003.

[84] F. Marti, P. Miller, D. Poe, M. Steiner, J. Stetson, and X. Y. Wu. Commissioning of the coupled cyclotron system at nscl. *AIP Conference Proceedings*, 600(1):64–68, 2001.

[85] D.J. Morrissey, B.M. Sherrill, M. Steiner, A. Stolz, and I. Wiedenhoever. Commissioning the A1900 projectile fragment separator. *Nuclear Instruments and Methods in Physics Research Section B: Beam Interactions with Materials and Atoms*, 204:90 – 96, 2003. 14th International Conference on Electromagnetic Isotope Separators and Techniques Related to their Applications.

[86] Isao Tanihata. Radioactive beam facilities and their physics program. *Nuclear Physics A*, 553:361 – 372, 1993.

[87] R.B. Firestone. Nuclear data sheets for A = 24. *Nuclear Data Sheets*, 108(11):2319 – 2392, 2007.

[88] Experimental physics and industrial control system kernel description. http://www.aps.anl.gov/epics. Accessed: 2015-09-14.

[89] M.D. Jones, J. Pereira, and R.G.T. Zegers. Operational procedure for the gas-handling system of the Ursinus/NSCL Liquid Hydrogen/Deuterium Target in the N2 Vault. https://portal.frib.msu.edu/nsclproject/Shared%20Documents/Projects/LD2%20Target.

[90] Nathan Frank. *Spectroscopy of Neutron Unbound States in Neutron Rich Oxygen Isotopes*. PhD thesis, Michigan State University, 2006.

[91] Glenn Knoll. *Radiation Detection and Measurement*. John Wiley & Sons, University of Michigan, Ann Arbor MI, USA, 2010.

[92] EJ-204 Plastic Scintillator Data Sheet. http://www.eljentechnology.com/images/stories/Data_Sheets/Plastic_Scintillators/ej204%20data%20sheet.pdf.

[93] R.A. Cecil, B.D. Anderson, and R. Madey. Improved predections of neutron detection efficiency for hydrocarbon scintillators from 1 MeV to about 300 MeV. *Nuclear Instruments and Methods*, 161(3):439 – 447, 1979.

[94] Bill Peters. *Study of Neutron Unbound States Using the Modular Neutron Array (MoNA)*. PhD thesis, Michigan State University, 2007.

[95] Gregory Christian. *Spectroscopy of Neutron-Unbound Fluorine*. PhD thesis, Michigan State University, 2011.

[96] Jenna Smith. *Unbound States in the Lightest Island of Inversion: Neutron Decay Measurements of* ^{11}*Li,* ^{10}*Li, and* ^{12}*Be*. PhD thesis, Michigan State University, 2014.

[97] MKS Type PDR 2000 Dual Capacitance Diaphragm Gauge Controller, Instruction Manual. http://orca.physics.unc.edu/RS232/MKS_PDR2000_files/pdr2000man.pdf, 2001.

[98] LakeShore 331S Temperature Controller, User's Manual. http://www.lakeshore.com/ObsoleteAndResearchDocs/331_Manual.pdf, 2009.

[99] Antoine equation parameters for neon. http://webbook.nist.gov/cgi/cbook.cgi?ID=C7440019&Mask=4&Type=ANTOINE&Plot=on#ANTOINE, 2011.

[100] Daniel R. Stull. Vapor pressure of pure substances. organic and inorganic compounds. *Industrial & Engineering Chemistry*, 39(4):517–540, 1947.

[101] E. R. Grilly. The vapor pressures of hydrogen, deuterium and tritium up to three atmospheres. *Journal of the American Chemical Society*, 73(2):843–846, 1951.

[102] O.B. Tarasov and D. Bazin. LISE++: Radioactive beam production with in-flight separators. *Nuclear Instruments and Methods in Physics Research Section B: Beam Interactions with Materials and Atoms*, 266(1920):4657 – 4664, 2008. Proceedings of the XVth International Conference on Electromagnetic Isotope Separators and Techniques Related to their Applications.

[103] Brookhaven National Laboratory Selected cryogenic Data Notebook, Section IV. https://www.bnl.gov/magnets/staff/gupta/cryogenic-data-handbook/Section4.pdf, 1980.

[104] Occupational health and safety guide interm: Glass and plastic window design for pressure vessels, 1989.

[105] J.M. Paul. The density effect and rate of energy loss in common plastic scintillators. *Nuclear Instruments and Methods*, 96(1):51 – 59, 1971.

[106] J. K. Smith, T. Baumann, D. Bazin, J. Brown, S. Casarotto, P. A. DeYoung, N. Frank, J. Hinnefeld, M. Hoffman, M. D. Jones, Z. Kohley, B. Luther, B. Marks, N. Smith, J. Snyder, A. Spyrou, S. L. Stephenson, M. Thoennessen, N. Viscariello, and S. J. Williams. Low-lying neutron unbound states in ^{12}Be. *Phys. Rev. C*, 90:024309, Aug 2014.

[107] T. Nakamura, A. M. Vinodkumar, T. Sugimoto, N. Aoi, H. Baba, D. Bazin, N. Fukuda, T. Gomi, H. Hasegawa, N. Imai, M. Ishihara, T. Kobayashi, Y. Kondo, T. Kubo, M. Miura, T. Motobayashi, H. Otsu, A. Saito, H. Sakurai, S. Shimoura, K. Watanabe, Y. X. Watanabe, T. Yakushiji, Y. Yanagisawa, and K. Yoneda. Observation of strong low-lying $e1$ strength in the two-neutron halo nucleus ^{11}Li. *Phys. Rev. Lett.*, 96:252502, Jun 2006.

[108] N. Frank, A. Schiller, D. Bazin, W.A. Peters, and M. Thoennessen. Reconstruction of nuclear charged fragment trajectories from a large-gap sweeper magnet. *Nuclear Instruments and Methods in Physics Research Section A: Accelerators, Spectrometers, Detectors and Associated Equipment*, 580(3):1478 – 1484, 2007.

[109] K. Makino and M. Berz. *Nucl. Instrum. Methods A*, 558:346, 2005.

[110] M. J. Strongman, A. Spyrou, C. R. Hoffman, T. Baumann, D. Bazin, J. Brown, P. A. DeYoung, J. E. Finck, N. Frank, S. Mosby, W. F. Rogers, G. F. Peaslee, W. A. Peters, A. Schiller, S. L. Tabor, and M. Thoennessen. Disappearance of the $N = 14$ shell. *Phys. Rev. C*, 80:021302, Aug 2009.

[111] C.R. Hoffman, T. Baumann, D. Bazin, J. Brown, G. Christian, D.H. Denby, P.A. DeYoung, J.E. Finck, N. Frank, J. Hinnefeld, S. Mosby, W.A. Peters, W.F. Rogers, A. Schiller, A. Spyrou, M.J. Scott, S.L. Tabor, M. Thoennessen, and P. Voss. Evidence for a doubly magic ^{24}O. *Physics Letters B*, 672(1):17 – 21, 2009.

[112] M. Thoennessen, S. Mosby, N.S. Badger, T. Baumann, D. Bazin, M. Bennett, J. Brown, G. Christian, P.A. DeYoung, J.E. Finck, M. Gardner, E.A. Hook, B. Luther, D.A. Meyer, M. Mosby, W.F. Rogers, J.K. Smith, A. Spyrou, and M.J. Strongman. Observation of a low-lying neutron-unbound state in ^{19}C. *Nuclear Physics A*, 912:1 – 6, 2013.

[113] Shea Mosby. *Spectroscopy of Neutron Unboudn States in Neutron Rich Carbon.* PhD thesis, Michigan State University, 2012.

[114] Y. Satou, T. Nakamura, N. Fukuda, T. Sugimoto, Y. Kondo, N. Matsui, Y. Hashimoto, T. Nakabayashi, T. Okumura, M. Shinohara, T. Motobayashi, Y. Yanagisawa, N. Aoi, S. Takeuchi, T. Gomi, Y. Togano, S. Kawai, H. Sakurai, H.J. Ong, T.K. Onishi, S. Shimoura, M. Tamaki, T. Kobayashi, H. Otsu, Y. Matsuda, N. Endo, M. Kitayama, and M. Ishihara. Unbound excited states in ^{19},^{17}C. *Physics Letters B*, 660(4):320 – 325, 2008.

[115] S. Agostinelli et al. *Nucl. Instrum. Mehtods A*, 506:240, 2003.

[116] B. Roeder. EURISOL Design Study, Report No. 10-25-2008-006-In-beamvalidations.pdf. pages 31 – 44, 2008.

[117] A.S. Goldhaber. Statistical models of fragmentation processes. *Physics Letters B*, 53(4):306 – 308, 1974.

[118] K. Van Bibber, D. L. Hendrie, D. K. Scott, H. H. Weiman, L. S. Schroeder, J. V. Geaga, S. A. Cessin, R. Treuhaft, Y. J. Grossiord, J. O. Rasmussen, and C. Y. Wong. Evidence for orbital dispersion in the fragmentation of ^{16}O at 90 and 120 MeV/nucleon. *Phys. Rev. Lett.*, 43:840–844, Sep 1979.

[119] Ian Thompson. Fresco, version 2.9. `http://www.fresco.org.uk/`, 2006.

[120] Reference input parameter library (ripl-3). `https://www-nds.iaea.org/RIPL-3/`, 2015.

[121] J. Bojowald, H. Machner, H. Nann, W. Oelert, M. Rogge, and P. Turek. Elastic deuteron scattering and optical model parameters at energies up to 100 MeV. *Phys. Rev. C*, 38:1153–1163, Sep 1988.

[122] A. Del Guerra. A compilation of n-p and n-c cross sections and their use in a monte carlo program to calculate the neutron detection efficiency in plastic scintillator in the energy range 1300 MeV. *Nuclear Instruments and Methods*, 135(2):337 – 352, 1976.

[123] Evaluated Nuclear Data Files. `https://www-nds.iaea.org/exfor/endf.htm`, 2015.

[124] Japanese Evaluated Nuclear Data Library. `http://wwwndc.jaea.go.jp/jendl/jendl.html`, 2007.

[125] D. A. Kellogg. Cross sections for products of 90-MeV neutrons on carbon. *Phys. Rev.*, 90:224–232, Apr 1953.

[126] F. James. *Monte Carlo Phase Space, CERN*, 68-16, 1968.

[127] A. Volya. *EPJ Web of Conferences*, 38:03003, 2012.

[128] L. Gaudefroy, W. Mittig, N. A. Orr, S. Varet, M. Chartier, P. Roussel-Chomaz, J. P. Ebran, B. Fernández-Domínguez, G. Frémont, P. Gangnant, A. Gillibert, S. Grévy, J. F. Libin, V. A. Maslov, S. Paschalis, B. Pietras, Yu.-E. Penionzhkevich, C. Spitaels, and A. C. C. Villari. Direct mass measurements of ^{19}B, ^{22}C, ^{29}F, ^{31}Ne, ^{34}Na and other light exotic nuclei. *Phys. Rev. Lett.*, 109:202503, Nov 2012.

[129] K. Yoneda, N. Aoi, H. Iwasaki, H. Sakurai, H. Ogawa, T. Nakamura, W.-D. Schmidt-Ott, M. Schäfer, M. Notani, N. Fukuda, E. Ideguchi, T. Kishida, S. S. Yamamoto, and M. Ishihara. β-decay half-lives and β-delayed neutron multiplicities of the neutron drip-line nuclei ^{19}B, ^{22}C, and ^{23}N. *Phys. Rev. C*, 67:014316, Jan 2003.

[130] M. D. Jones, Z. Kohley, T. Baumann, G. Christian, P. A. DeYoung, J. E. Finck, N. Frank, R. A. Haring-Kaye, A. N. Kuchera, B. Luther, S. Mosby, J. K. Smith, J. Snyder, A. Spyrou, S. L. Stephenson, and M. Thoennessen. Further insights into the reaction $^{14}\mathrm{Be}(\mathrm{CH}_2, X)^{10}$He. *Phys. Rev. C*, 91:044312, Apr 2015.

[131] A. N. Kuchera, A. Spyrou, J. K. Smith, T. Baumann, G. Christian, P. A. DeYoung, J. E. Finck, N. Frank, M. D. Jones, Z. Kohley, S. Mosby, W. A. Peters, and M. Thoennessen. Search for unbound ^{15}Be states in the $3n + ^{12}$ Be channel. *Phys. Rev. C*, 91:017304, Jan 2015.